In the field of energy storage for devices
ranging from EVs to consumer electronics and peak power storage,
we're pioneering the study of new multiple electron (per molecule) storage processes,
to learn to create batteries with greater storage capacity than gasoline.

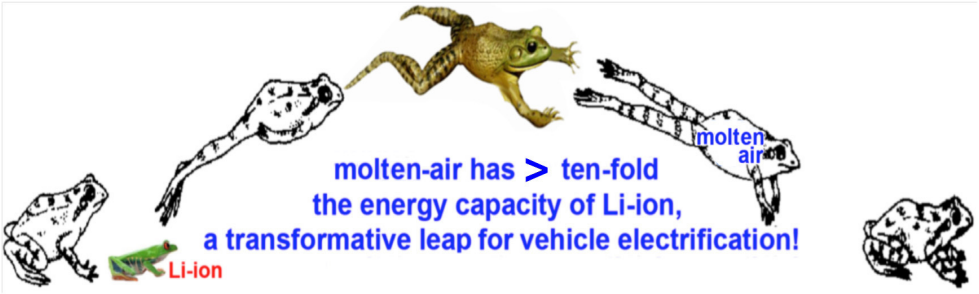

Included are Technical Write-ups of:

1) Molten Air Batteries (selected publications from 2013-onward)

2) The VB_2/Air Battery (selected publications from 2008-onward)

3) Super-iron Batteries (selected publications from 1999-onward)

4) Sulfur Batteries (select publication from 1987-onward)

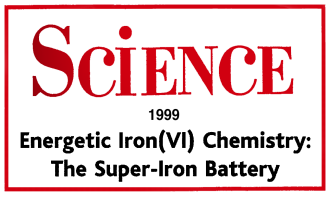

Further information available at Licht research group sites:
http://home.gwu.edu/~slicht/index.html

http://departments.columbian.gwu.edu/chemistry/people/103

The **Licht research group** has taken on the challenge of *a comprehensive solution to climate change*.
We're working towards changing today's fossil fuel, to a renewable chemical, economy,
replacing the largest greenhouse gas emitters,
and discovering new high energy, highest storage capacity batteries.

Energy & Environmental Science

RSC Publishing

PAPER

Molten air – a new, highest energy class of rechargeable batteries†

Cite this: *Energy Environ. Sci.*, 2013, **6**, 3646

Stuart Licht,* Baochen Cui, Jessica Stuart, Baohui Wang and Jason Lau

This study introduces the principles of a new class of high-energy batteries and their fundamental chemistry is demonstrated. These *molten air* batteries use air, a molten electrolyte, are quasi-reversible (rechargeable), have the capability for multiple electrons stored per molecule, and have the highest intrinsic electric energy storage capacities. Here we show three examples of the new battery's electron transfer chemistry. These are the metal, carbon and VB_2 molten air batteries with respective intrinsic volumetric energy capacities of 10 000 (for Fe to Fe(III)), 19 000 (C to CO_3^{2-}) and 27 000 W h l^{-1} (VB_2 to B_2O_3 + V_2O_5), compared to 6200 W h l^{-1} for the lithium air battery. Higher energy capacity, cost effective batteries are needed for a range of electronic, transportation and greenhouse gas reduction power generation devices. Needed greenhouse gas battery reduction applications include overcoming the battery driven "range anxiety" of electric vehicles, and increased capacity energy storage for the electric grid.

Received 5th August 2013
Accepted 12th September 2013

DOI: 10.1039/c3ee42654h

www.rsc.org/ees

Broader context

From which chemistries will new batteries arise? High capacity, cost effective batteries are needed for a range of applications, including applications to reduce greenhouse gases such as overcoming the "range anxiety" of electric vehicles and increased storage capacity for the electric grid. Multiple electron per molecule batteries, such as the eleven electron per VB_2 air battery, have among the highest battery energy capacities. The challenge has been to recharge; to electrochemically reinsert this large number of molecular storage electrons. This study resolves that challenge with a new class of rechargeable batteries, and several of these new molten air battery chemistries are demonstrated. The batteries use a molten electrolyte, are quasi-reversible (rechargeable), and have amongst the highest intrinsic battery storage capacities.

Introduction

High capacity, cost effective batteries are urgently needed for a range of applications, including greenhouse gas reduction applications such as overcoming the battery driven "range anxiety" of electric vehicles, and increased energy capacity storage for the electric grid.[1–3] In this study, the principles of a new class of batteries, rechargeable molten air batteries are introduced, and several *molten air* battery chemistry examples are demonstrated. The batteries use a molten electrolyte, are quasi-reversible (rechargeable), and have amongst the highest intrinsic battery electric energy storage capacities.

In 2008 a zirconia stabilized VB_2 air battery was presented. This $11e^-$ (eleven electron) per molecule, room temperature, aqueous electrolyte battery has the highest volumetric energy capacity for a battery, with an intrinsic capacity greater than that of gasoline and an order of magnitude higher than that of conventional lithium ion batteries.[4–6] The challenge has been to recharge the battery; that is to electrochemically reinsert $11e^-$ into the battery discharge products. Here, this challenge is resolved through the introduction of a new class of *molten air* batteries.

Other classes of molten electrolyte batteries had been investigated. A *molten sulfur* battery has been widely studied, particularly for electric car and grid applications.[2,3,7–9] During discharge, the battery uses sulfur and sodium (or potassium) for the respective cathode and anode storage materials, and these high temperature molten components are kept from chemically reacting by a solid electrolyte beta alumina separator. Both the molten and room temperature class of sulfur cathode batteries,[10,11] are limited by the maximum intrinsic capacity of the $2e^-$ per sulfur (2 Faraday per 32 g sulfur). Another fascinating class of *molten metal* electrolyte batteries utilizes an insoluble, dense, molten cathode during discharge situated below a (less dense) molten metal anode floating on a molten electrolyte. Unlike the molten sulfur battery, this latter class does not require a solid electrolyte separator; but to date has lower capacity. An example of this latter class of batteries is the magnesium-antimony battery with a molten halide electrolyte.[11]

In this study rechargeable molten air batteries are introduced, and several examples of their battery chemistry are

Department of Chemistry, George Washington University, Washington, DC, 20052, USA. E-mail: slicht@gwu.edu; Tel: +1 202 994 6121

† Electronic supplementary information (ESI) available: Consists of carbonate electrolyte stability. See DOI: 10.1039/c3ee42654h

demonstrated. Unlike prior rechargeable molten batteries, the battery is not burdened by the weight of the active chargeable cathode material. The rechargeable *molten air* electrode instead uses oxygen directly from the air to yield high battery capacity. This electrode will be shown to be compatible with several high capacity multiple electron redox couples. Three demonstrated new batteries chemistries are the metal (iron), carbon and VB_2 molten air batteries with intrinsic volumetric energy capacities greater than that of the well known lithium air battery.[12,13] due to the latter's single electron transfer and low density limits.

Electrochemical energy storage with the molten air battery is represented in Scheme 1 in both generalized form and with a specific example (the iron molten air battery). As illustrated for the iron molten air example of the battery, during charging, iron oxide is converted to iron metal *via* a three-electron reduction, and O_2 is released to the air. During discharge iron metal is converted back to iron oxide. We observe that Li_2CO_3, which melts at 723 °C, and lower melting carbonate eutectics are effective electrolytes. Simple steel foil cathodes and nickel foil anodes are effective for either iron oxide[14–18] or carbon dioxide splitting. For example, these anodes and cathodes can sustain high splitting (mA to A cm^{-2}) current densities at low overpotential in molten lithium carbonate. These electrolyses for either iron oxide[14–18] or carbon dioxide splitting can also represent charging of a molten air at high current density and low potential.

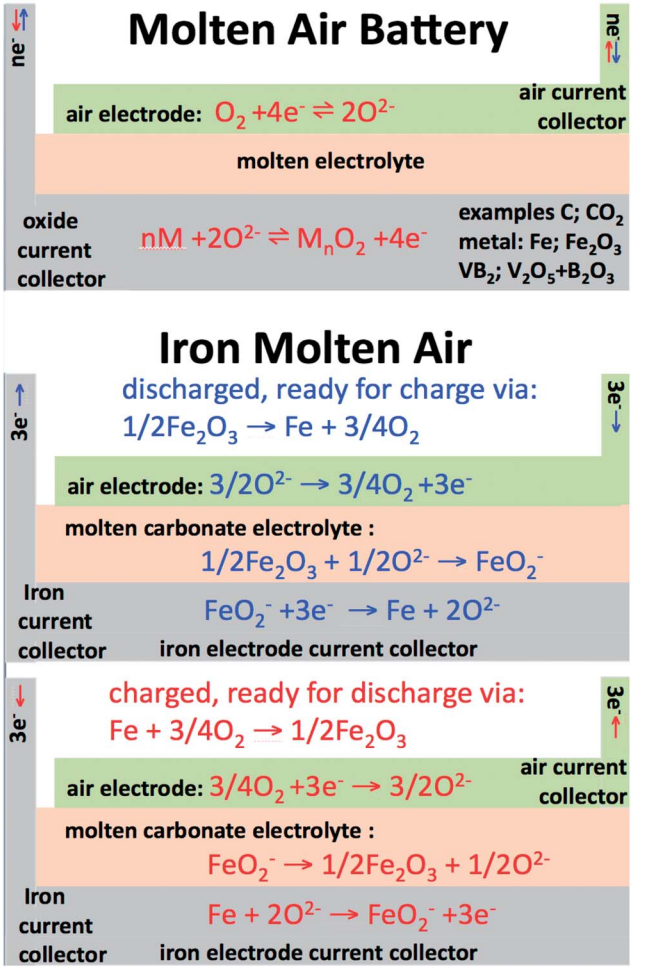

Scheme 1 Top: the molten air battery. Bottom: the iron molten air battery; illustration of the charge/discharge in molten carbonate. The charging or discharging process is indicated by red or blue text & arrows.

Experimental

Lithium carbonate utilized is (Li_2CO_3, Alfa Aesar, 99%), ferric oxide is Fe_2O_3 (99.4%, JT Baker), Li_2O (Alfa 99.5%), 1 mm and 2 mm Ni wire (Alfa 99.5%) and Ni foil (McMaster pure Ni 200 shim), $Ce(NO_3)_3 \cdot 6H_2O$ (STREM 93-43831) crucibles: nickel (VWR AA35906-KY), Fe wire (Anchor dark annealed annealed), steel foil (McMaster 75 μm 316 steel), crucibles: nickel (VWR AA35906-KY), high purity alumina (AdValue Technology AL-2100, OD 40 mm, height 95 mm, Pflatz & Bauer, 99%), boron oxide (B_2O_3, 99.98%, Alfa Aesar 89964), V_2O_5 (99.6%, Alfa Aesar 89964), $LiVO_3$ (99.9%, Alfa Aesar 39358) & anhydrous lithium metaborate ($LiBO_2$, 99.9%, Alfa Aesar 12591).

Splitting oxides electrochemically, carbon & iron syntheses

Iron metal synthesis in molten carbonates are conducted *via* constant current electrolyses. As shown in the left side of Fig. 1, we have found that iron oxide (as hematite, Fe_2O_3, or magnetite, Fe_3O_4) readily electrolyzes to iron which forms on an iron or platinum cathode.[14–18] Post electrolysis, iron deposited on an extracted cathode is shown with an overlay of electrolyte in the top left of Fig. 1. The deposit is easily peeled from the cooled cathode, and after peeling, the post electrolysis steel foil cathode is shown (middle photo) ready for a repeat electrolysis. A cross-section of the cathode deposit is shown in the right photo, and the iron deposit is evident. The high coulombic efficiency of the deposited iron, as well as the high purity of iron in the layers adjacent to the cathode is delineated in ref. 17.

The top of Fig. 2 presents various carbonate electrolytes, cooled and extracted after pressed iron oxide (Fe_2O_3) on a cathode current collector (a coiled steel wire) is reduced to iron. The nickel air anode is highly stable and unaffected by the electrolysis (shown the right side of the top row of photographs as extracted subsequent to electrolysis, still with a small coating of solidified electrolyte). The next row of photos shows the Fe_2O_3 before and after electrolytic reduction and conversion to iron metal. The mechanism of dissolution and charging of iron oxide to iron metal in carbonates has been studied in depth.[15,16] Unlike in sodium or potassium carbonates, iron oxides are highly soluble in molten lithiated carbonates such as Li_2CO_3 or Li_2CO_3 mixes with alkali earth, or with other alkali carbonates. Both Fe_2O_3 (hematite) and Fe_3O_4 (magnetite) are highly soluble in Li_2CO_3.[14] Cyclic voltammetry (CV) of Fe_3O_4 in molten lithium carbonate exhibits two distinct reduction peaks, while CV of dissolved Fe_2O_3 exhibits a single reduction peak indicative of the direct reduction of Fe(III) to Fe(0).[14] The Fe_2O_3 in carbonate, iron electrolysis product has been analyzed by quantitative analysis under a wide variety of electrolysis conditions,[17] and other than electrolyte and a few percent of partially reduced iron

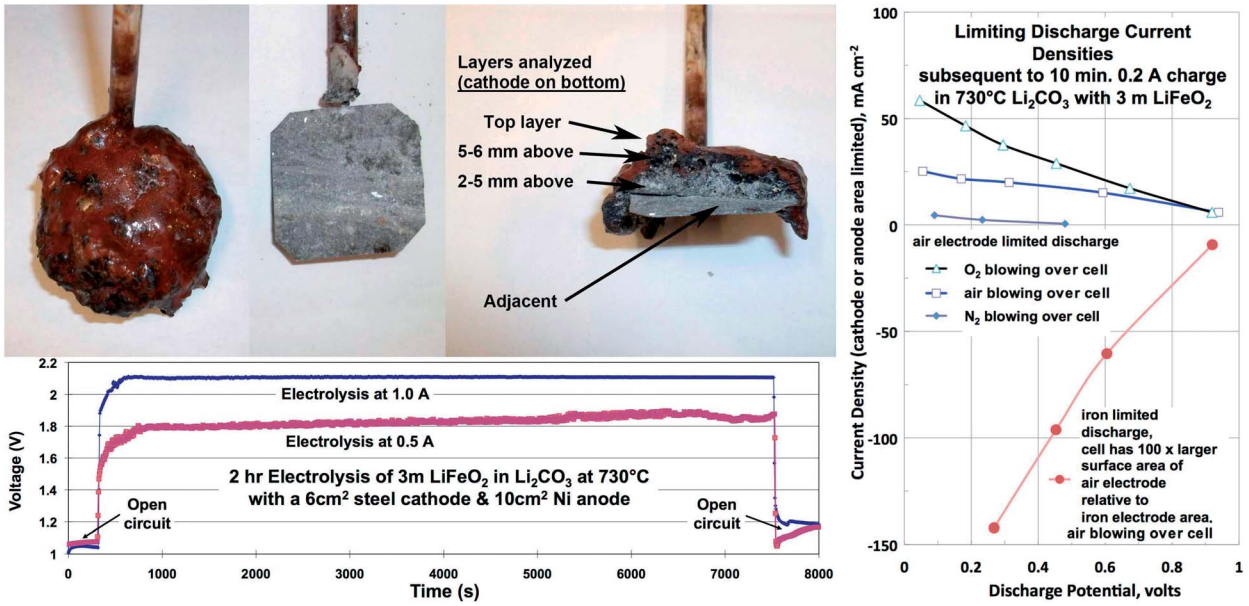

Fig. 1 Sustainable charge (left) and discharge (right) rates for the iron molten air battery. Left: facile, high rate charging of the iron molten air battery forms a thick iron layer on the cathode. Right: discharge polarization (following electrochemical charge to form iron) of the air electrode (planar Ni, a planar disk of wound Ni wire, or planar Ir yield highly similar same results) and the iron electrode (planar steel shim or a planar disk of wound iron wire yield highly similar results) in 730 °C molten lithium carbonate with $LiFeO_2$ (formed by dissolution of equimolar Fe_2O_3 & Li_2O). Right side data (this paper); left side data from our ref. 17.

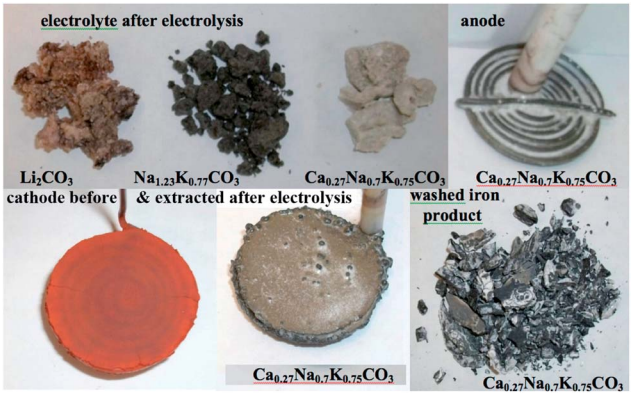

Fig. 2 Left: the iron molten air battery starting with an (uncharged) pressed Fe_2O_3 pellet cathode bottom left photo in several molten carbonate electrolytes. Fe_2O_3 is soluble in Li_2CO_3 (as $LiFeO_2$, with addition of Li_2O), but not in sodium or potassium carbonates. A variety of carbonates can promote iron electrodeposition, without Fe(III) lithiation dissolution, such as the $Ca_{0.27}Na_{0.7}K_{0.73}CO_3$ (shown).[17] Bottom: two photographs of the battery cell configuration.

(Fe^{2+}), the iron formed near the cathode (Fig. 1 photo) or after washing to remove electrolyte (Fig. 2 photo) is pure iron.[17]

This study probes both charge *and* discharge conditions of iron or carbon molten air batteries, and also investigates the electrochemistry of molten borate/vanadate mixes. Generalized cell conditions for molten air battery charge are shown at the top of Scheme 1. The electrochemical conditions for iron[17] and carbon syntheses[18–20] in molten carbonates, including optimization of the electrode and electrolyte configuration has been previously detailed. These syntheses equate to charging of the iron and carbon molten air batteries. In the study here, the full charge/discharge cycle is probed.

Battery cycling

The electrochemical charge cycling cell utilizes an orthogonal (vertical) wall alumina or nickel crucible cell to prevent electrolyte migration, with various specified molten electrolytes and containing an air electrode with either an iron, carbon or VB_2 electrode. Charge cycling is at a constant charging current followed by a constant resistive load discharge. To isolate anode or cathode overpotential trends (and *in lieu* of trying to define a quasi-reference electrode relevant to each new molten electrolyte) the polarization is measured using a counter electrode with 100 fold larger surface area.

Results and discussion

Iron has been widely explored for battery storage due to its availability as a resource and its capability for multiple electron charge transfer. Retention of the intrinsic *anodic* storage capacity of these batteries has been an ongoing challenge. Room temperature aqueous iron batteries continue to be explored today.[21] In 2010 we introduced the molten carbonate electrolytic conversion of iron oxide to iron as a CO_2-free synthesis alternative to the conventional greenhouse gas intensive industrial production of iron metal.[14–18] The unexpected, high solubility of iron oxide in lithiated molten carbonate electrolytes[14] was demonstrated to lead to the facile splitting of iron oxide to iron metal with the concurrent release of oxygen.[15–18] Here, we consider this unusual electrolytic splitting as a battery "charging". We couple this with the known primary discharge of the air cathode as used in the widely studied molten carbonate fuel cell, including those using coal as a fuel,[22–26] to explore the first example of a molten air

rechargeable battery. In lieu of iron we also explore the alternative use of carbon and VB_2 as alternative high capacity discharge redox couples for these rechargeable cells. Electrochemical storage in these iron, carbon or VB_2 molten air batteries are in accord with:

$$\text{iron molten air, } 3e^- \text{ battery: } Fe + 3/4O_2 \rightleftharpoons 1/2Fe_2O_3 \quad (1)$$

$$\text{carbon molten air, } 4e^- \text{ battery: } C + O_2 \rightleftharpoons CO_2 \quad (2)$$

$$VB_2 \text{ molten air battery, } 11e^-\text{: } VB_2 + 11/4O_2 \rightleftharpoons B_2O_3 + V_2O_5 \quad (3)$$

The right column of Table 1 compares the intrinsic capacity of these batteries, which is *one to two orders of magnitude greater* than that of the volumetric energy capacity of conventional Li ion batteries. Lithium (metal) air also has a lower volumetric energy capacity. While Li's gravimetric charge capacity (3860 A h kg^{-1}) is similar to that of VB_2 (4060 A h kg^{-1}), it has a lower 6200 W h l^{-1} volumetric capacity due to a low density (0.534 kg l^{-1}), and single, rather than multiple, electron charge transfer.

Metal molten air battery

We have previously introduced the wide iron oxide concentration and temperature domains in which nickel and iridium are effective air (anode) electrodes, and steel, iron and platinum are effective iron (cathode) electrodes for the synthesis of iron metal from a range of molten carbonates. Interestingly as seen in the right side of Fig. 1, the same simple electrodes, that is Ni as the air electrode and steel wire as the iron electrode, are also effective for the reverse mode, that is the reduction of oxygen to oxides and the oxidation of deposited iron to iron oxide. In addition, noble metals – iridium as the air electrode and platinum as the iron electrode, are also effective and exhibit similar polarization currents. As seen in the figure the oxygen reduction electrode is rate limiting. That is, the oxygen reduction reaction incurs with a several fold higher overpotential (lower current density at equivalent electrolysis potentials) than the cathode iron oxidation discharge reaction. As expected, in the absence of oxygen (under nitrogen in the figure) the current disappears, while pure O_2, rather than air, increases the current density establishing the basis for electrochemical discharge of the cell. A nickel air electrode, air or oxygen, and a lithium electrolyte are used in this study to demonstrate the simplicity and cost effectiveness of the cell, and the results are repeated with the noble metal iridium, to demonstrate that the air, and not the air cathode, reversibly stores charge. We have previously observed that the addition of lithium oxide to a carbonate electrolyte (i) increases cell potential and (ii) prevents molten carbonate decomposition, favouring reactant rather than products in the equilibrium:[16–18]

$$Li_2CO_3 \rightleftharpoons Li_2O + CO_2 \quad (4)$$

Figure 3 presents the charge cycling of the iron molten air battery in a lithium carbonate (2 g Li_2CO_3) electrolyte containing 3 M $LiFeO_2$ and 1.5 M Li_2O (the excess Li_2O is to prevent electrolyte loss (as Li_2CO_3 decomposition)). Although cycling is evident, it is seen in the figure that this cell with equal surface area air and counter electrodes exhibits substantial hysteresis (significant losses of the charging compared to the discharge voltage, as well as a rapid decline in the discharge potential), The large hysteresis is consistent with the polarizations losses of the air electrode during discharge seen on the right side of Fig. 1.

Iridium is used as an air electrode in Fig. 3 discharges to present a first quasi-reversible molten air battery with a noble metal air electrode. We have previously observe that during several hundred hours of oxygen evolution at an iridium electrode in molten carbonates, the iridium exhibits no evident physical changes, no visible coating, nor change in thickness.[16] Iridium was used here (in Fig. 3 battery results), rather than nickel (in Fig. 4 battery results), to establish that this current collector for the air electrode is not consumed during charge cycling, but both Ni (wound wire, perforated foil or mesh) and Ir are effective as the air electrodes. We have previously quantified that nickel is highly stable as an air anode in a variety of lithium oxide containing electrolytes;[10–14,27] a nickel oxide layer quickly forms and stabilizes the electrode.[16] Replacement of the iridium with the same surface area of nickel results in a battery discharge highly similar to that seen with iridium in Fig. 3. Also, platinum was used in the discharged cell in Fig. 3 as the counter electrode, rather than steel, to establish in this experiment that

Table 1 The charged intrinsic energy storage capacity of various molten air rechargeable batteries. Volumetric energy capacity, E_{vol}, is calculated from the number of electrons stored, n, the density d, the Faraday constant, $F = 26.80$ A h mol^{-1}, the formula weight, FW, and $E°$ in accord with eqn (1) and (2) or 3 as $E_{vol} = ndE°F/FW$. The cell potential at unit activity, $E°$, is temperature dependent. For example, while constant over a wide temperature range at 1.0 V for the carbon anode, $E°$ decreases for the iron anode from 1.2 to 0.9 V with temperature increase from 25 °C to 850 °C.[21] The theoretical storage capacity of air batteries is traditionally calculated based on the mass or volume of the reduced active anode material (such as zinc in a zinc air battery) as oxygen is freely available from the air. However, in practice the mass and volume of air battery systems increases with the uptake of oxygen during discharge, and the limiting capacities may be better represented by a form half way between the charged and discharged state. Hence, the final mass, volume and capacity of lithium air batteries need to include the oxygen to form the oxidized product, Li_2O. This effect is large for lithium air batteries as a mole of Li increases from 6.9 g to a discharged mass of 14.9 g ($1/2Li_2O$), and relatively less for iron which increases from a molar mass of 55.8 g to a discharged mass of 79.8 g ($1/2Fe_2O_3$). Table 1 calculates air battery capacities in the traditional manner, but we note that this provides only an upper limit to the capacity of such air batteries when fully charged

Anode	Formula weight, kg mol^{-1}	e^-s stored	Charge capacity, A h kg^{-1}	d, kg l^{-1}	$E°$, V *vs.* O_2	Energy capacity gravimetric, W h kg^{-1}	Energy capacity volumetric, W h l^{-1}
Iron	0.05585	$3e^-$	1440	7.2	1.0	1400	10 000
Carbon	0.01201	$4e^-$	8930	2.1	1.0	8900	19 000
VB_2	0.07256	$11e^-$	4060	5.1	1.3	5300	27 000

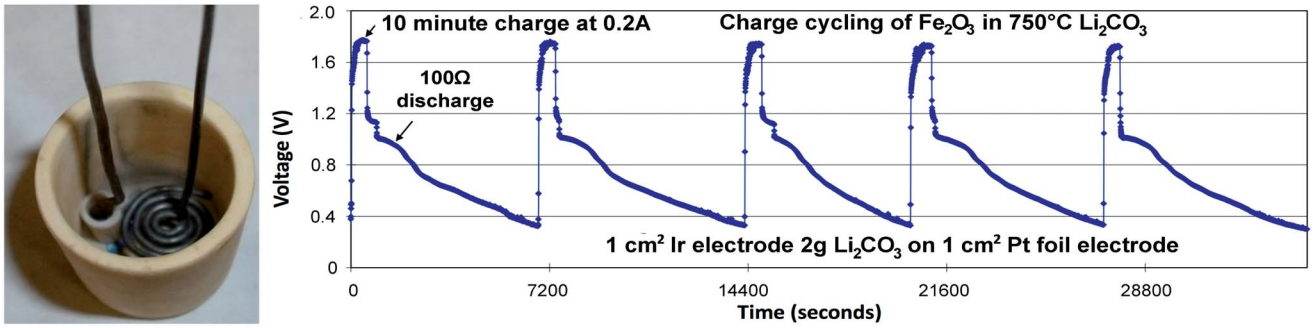

Fig. 3 Cycling characteristics of an iron molten air battery exhibiting large hysteresis. The battery characteristics are similar whether the respective air and counter electrodes are composed of iridium and platinum (as shown) or equal surface areas of nickel and steel. The lithium carbonate electrolyte contains 3 M Fe_2O_3 and 3 M Li_2O. The battery cycling consists of repetition of a charge at a constant current of 0.2 A for 10 minutes, followed by discharge at a constant load of 100 ohm. Left (photo): cell configuration with wound wire air electrode (visible in the photo) above the iron counter electrode, prior to addition of the electrolyte. A space maintained between the electrodes and the crucible walls prevents trapping/splashing of air bubbles. Less than two grams of molten electrolyte is sufficient to cover the electrodes.

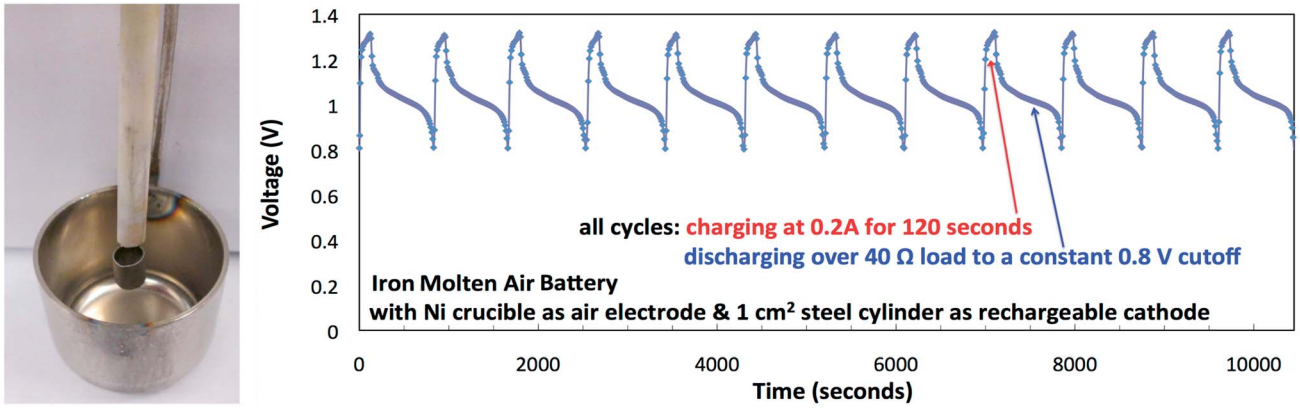

Fig. 4 Left photograph: cycling characteristics of an iron molten air battery exhibiting small hysteresis. The low polarization cell configuration of the molten air iron battery uses a nickel crucible (3.3 cm diameter, 2.9 cm depth, straight wall Ni crucible Alfa Aesar #35962) as both electrolyte case and air electrode, and a 1 cm^2 steel (1.67 cm high cylinder with a circumference of 0.6 cm) rechargeable counter. Electrodes are shown prior to the addition of the electrolyte. Right: Cycling of this cell at 730 °C containing a Li_2CO_3 electrolyte with 3 M dissolved Fe(III). Cell is charge at 0.2 A for 120 seconds and discharged over 40 Ω to 0.8 V cut-off.

iron from Fe_2O_3, rather iron from the current collector, is deposited during charge and oxidized during discharge. However, replacement of the platinum by steel in the counter electrode does not result in a voltage loss during discharge, or a corrosion or change during repeated cycling of the battery.

Several molten carbonate fuel cell studies have shown that higher air electrode discharge current densities (of up to 100 mA cm^{-2}) with lower polarization losses are observed when supported by air electrodes in which the electrolyte is bound within pores in solid lithium aluminate matrices.[23,24,26] This allows a high surface area air interface in contact with the molten electrolyte. Although molten carbonate fuel cells have not previously been shown to be electrochemically rechargeable, prior MCFC studies[15–19] suggest certain modified electrolytes and modified electrodes, such as those employed in the metal molten air battery sections, will improve gas access to the air electrode, decrease the discharge polarization and improve the sustainable current densities by several fold. Such cell configurations are not readily available, and *in lieu* of these structures, in this study several effective cell configurations employing a high surface area of air electrode relative to the counter electrode are presented and utilized in our subsequent iron, carbon and VB_2 molten air batteries.

One of the simplest of our high surface area air electrode configurations exhibits low hysteresis is shown in Fig. 4–6. The configuration utilizes a nickel crucible, *in lieu* of the alumina crucible, to act not only as the electrolyte encasement, but also as a large surface area air electrode. As seen in Fig. 5, the battery exhibits low polarization losses during discharge. Down to a 20 Ω load discharge is supported without significant potential drop when compared to the 1.1 V open circuit battery potential. That is, there is little polarization losses up to discharge current densities of 50 mA cm^{-2} (1 V/20 Ω) through the (1 cm^{-2}) steel electrode. At higher current densities, a significant potential drop occurs (at resistive loads of 10 Ω or less). As presented in Fig. 5, this configuration of the iron molten air battery exhibits substantially less hysteresis than was seen in Fig. 3, and as shown in Fig. 6 stable cycling behaviour. The voltage efficiency of the cell is 84% (1.05 V discharge/1.25 V charge) and the coulombic efficiency is 75% (=18 coulombs discharge/the injected charge of 0.2 A × 120 seconds) to a discharge cut-off voltage of 0.8 V. The coulombic efficiency increases to over 85%

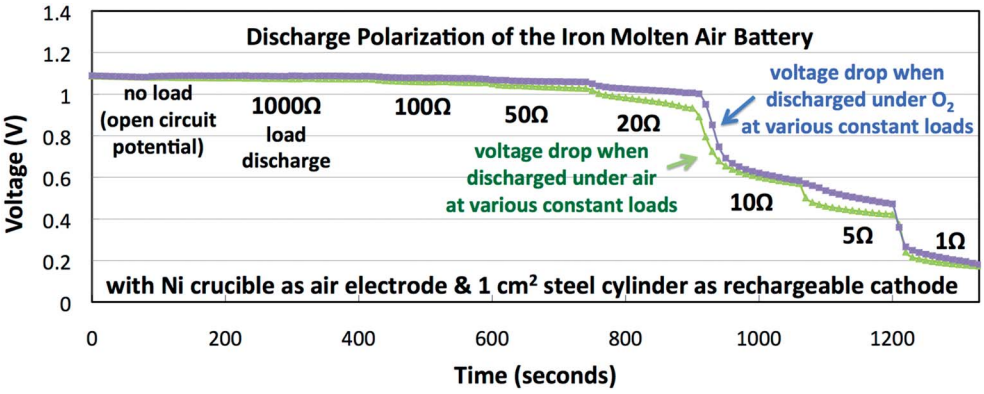

Fig. 5 Battery potential at open circuit, and the discharge potential under load, of Fig. 4 iron molten air battery, at 730 °C containing a Li_2CO_3 electrolyte with 3 M dissolved Fe(III) in a Ni crucible with a 1 cm^2 steel electrode.

when the cell is discharged to a cut-off voltage of 0.7 V, as shown in Fig. 6 to include a portion of a second voltage plateau which is seen to occur at that potential. This lower voltage plateau discharge can be attributed to either the partial discharge of Fe^{2+} to Fe^{3+} as we have previously observed by cyclic voltammetry,[14] or to a solid carbon discharge as seen in the next section of this study. A future paper will seek to discriminate which of these secondary discharges is dominant in the iron molten air battery.

Carbon molten air battery

As we have previously observed during electrolysis of lithium carbonate mix electrolytes,[19,20] and as seen in the photos of Fig. 7 in a barium/lithium carbonate mix at 750°, that a voluptuous layer of carbon forms on the (steel) cathode side facing the air electrode. When extracted, cooled washed and weighed the carbon mass approaches the theoretical mass calculated by the 100% coulombic efficiency of the $4e^-$ reduction of carbonate. The photo is the cathode extracted after 4 hours of 1

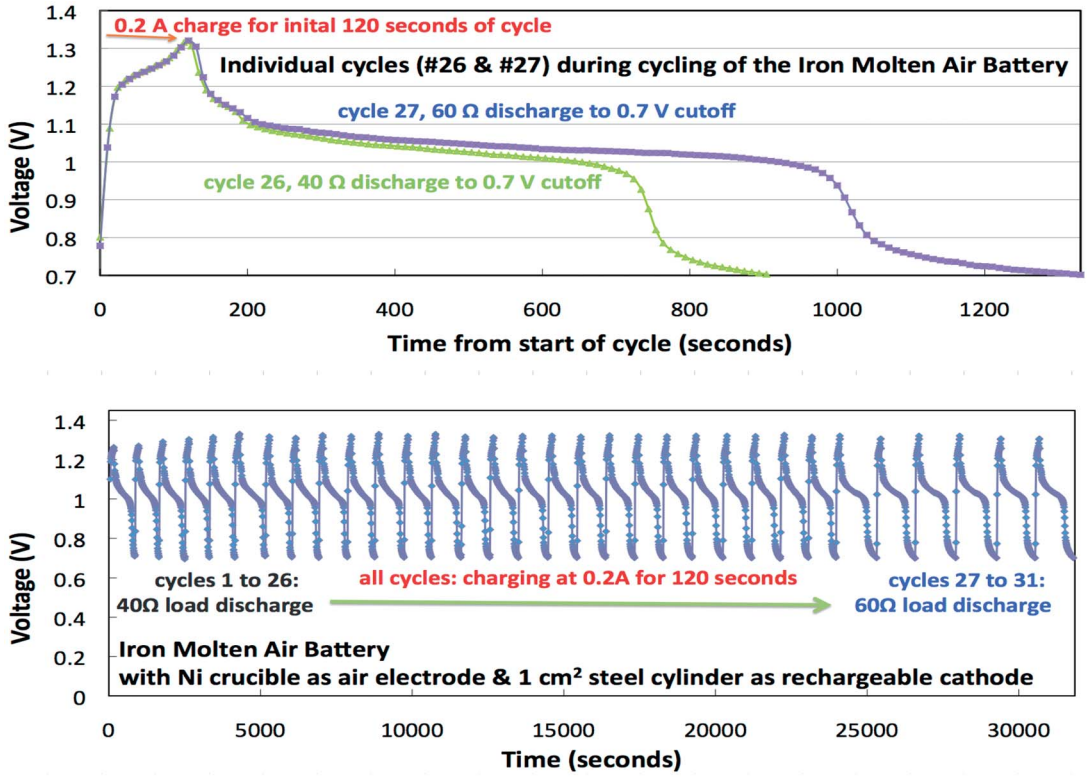

Fig. 6 Cycling characteristics of the iron molten air battery presented in Fig. 4 exhibiting low hysteresis (the average discharge potential of 1.05 V compares favourably with the average charging potential of 1.25 V, and the discharge potential does not decrease rapidly). The battery is charged at 0.2 A constant current for 120 seconds, followed by discharge at the indicated constant resistance loads.

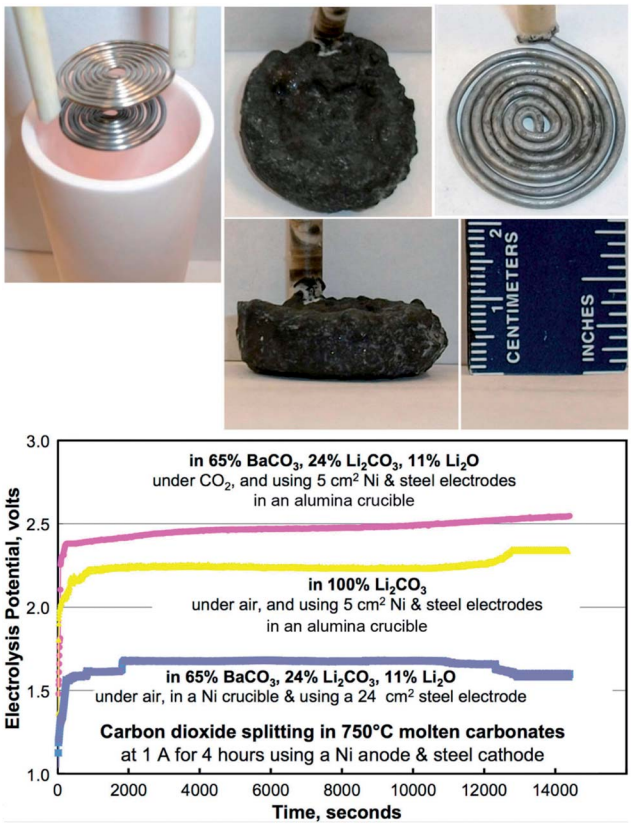

Fig. 7 Charging the carbon molten air battery. Photos: coiled 5 cm^2 nickel (air) & steel (C) electrodes prior to electrode insertion as used in the pink and yellow labeled charge reactions below. Right: the post-electrolysis reusable air electrode. Middle: the thick carbon layer formed on the 5 cm^2 steel cathode by a 4 hour, 1 A charge in molten carbonate. Electrodes are photographed after extraction and without washing. Bottom: the electrolysis potential of carbonate electrolysis in various molten carbonates under various conditions.

A electrolysis in a barium mix electrolyte denoted as the pink electrolysis potential *versus* time plot in Fig. 7. As seen in the figure as the grey curve, the charging potential falls to ~1.6 when an oversized Ni air electrode (the Ni crucible) is used in the carbonate (to carbon) splitting. As summarized in Fig. 9, the charging potential decreases to ~1.2 V at low current densities (<100 mA cm^{-2}) Similar carbon depositions are observed during a 4 A electrolysis in 1 hour (albeit at higher potential), and during an electrolysis in a pure Li_2CO_3, rather than a Li–$BaCO_3$ mix electrolyte (although the proclivity to absorb CO_2 is greater in the latter electrolyte as delineated in the ESI†).

As calculated from the temperature dependence of the thermochemical enthalpy and entropy of the constituents,[28–30] and as delineated in the ESI,† molten carbonates can be highly stable at elevated temperatures. Increasing the temperature above 800 °C in molten Li_2CO_3 (ref. 21) favors CO *via* the Boudouard reaction, eqn (5). If not collected, this CO gas, instead of solid carbon product, leads to a parasitic charge loss for the carbon battery *via* the evolution of carbon monoxide gas.

$$2CO \rightleftharpoons C + CO_2 \quad (5)$$

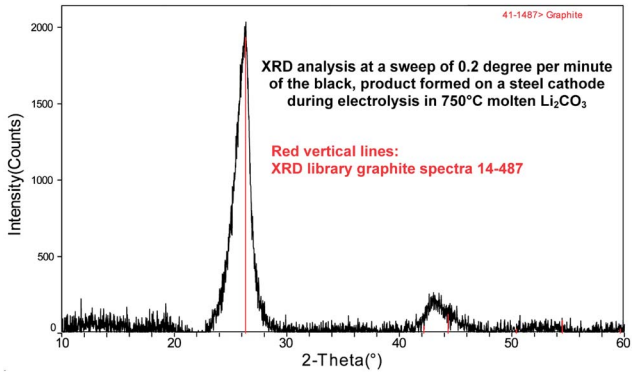

Fig. 8 XRD analysis of the black product formed on a steel cathode during electrolysis in 750° molten Li_2CO_3 electrolysis. XRD analysis is conducted at a sweep rate of 0.2 degree per minute on a Rigaku Miniflex diffractometer and analyzed with the Jade software package (JADE, 6:1; Materials Data, Inc. Livermore, CA, 2002).

Carbon formation during molten carbonate electrolysis here provides charging of the carbon/molten air battery. Molten carbonate cells have been widely probed as robust fuel cells, and we had previously demonstrated that the reverse of this process (electrolysis) provides opportunities for carbon capture. Combined, these two processes provide new opportunities for high capacity reversible battery storage. XRD of our post-electrolysis, black cathode product is shown in Fig. 8 (after washing to remove excess electrolyte). As shown, the measured XRD matches the library XRD of pure graphite. We observe that graphite is deposited as the cathode product from molten lithium carbonate, molten alkali mixes, and molten lithium and alkali earth carbonate mixes, and at temperatures below 800 °C remains the carbon product, independent of current density, or whether the product is electrodeposited onto a steel or nickel cathode.

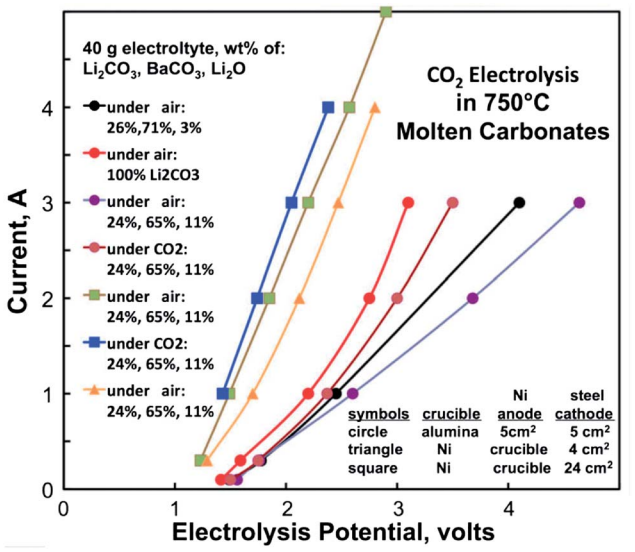

Fig. 9 The carbon molten air electrolysis, charging potential as a function of current in various, indicated, carbonate electrolytes at 750 °C and under either air or pure CO_2.[17]

Fig. 7 summarizes the variation of charging potential in time at high current densities sustained by the carbon molten air battery using a variety of cell configurations and carbonate electrolytes (the yellow curve is in pure Li_2CO_3, while the other curves are in Ba–Li mix electrolytes). Fig. 9 compares the polarization during charge with a variety of electrolyte and cell conditions. As described in the ESI,† $BaCO_3$ is more facile in CO_2 uptake for carbon capture. However, pure Li_2CO_3, which also forms a robust carbon overlayer, is more conductive for batteries. Hence, for this carbon molten air battery example we focus on the latter, Li_2CO_3, electrolyte.

As presented in the right side of Fig. 1, due to the large polarization of the air electrode during discharge in lithium carbonate, we expect a substantial hysteresis when cycling a carbon molten air battery with the same sized air and counter electrodes. This is observed in Fig. 10 in which equal surface area sandwiched electrodes in a pure Li_2CO_3 molten electrolyte were used to demonstrate the rechargeable battery. This carbon molten air cell contains molten lithium carbonate with an upper, planar 1.0 cm^2 nickel electrode exposed to the air, and separated by the molten carbonate from a lower, 1.0 cm^2 planar Pt electrode. Platinum is again used to demonstrate the current collector metal is not involved in oxidation or reduction, but only as a conduit for charge transfer, but steel is also effective. The energy efficiency of this battery configuration is low, as the cell is charged at 2 V and discharged at only 0.5 V. However, the current extracted during discharge is similar to the current injected during charge, indicative of the high coulombic efficiency (albeit at low voltage efficiency using Fig. 10 cell configuration) of the carbon molten air battery. The ~300 coulombs of charge injected during the two charge cycles in the lower portion of Fig. 6 is approached by the 270 coulombs of discharge generated over the load, prior to depletion, during the two discharge cycles. Hence, the cell exhibits high coulombic efficiency (the coulombs generated during discharge is over 90% of the coulombs inject during charging).

A carbon molten air battery that exhibits improved energy efficiency is shown in Fig. 11. The improvements include the addition of Li_2O to the electrolyte (to prevent carbonate decomposition), a large surface area of air electrode relative to the rechargeable cathode (to minimize the hysteresis), an alkali mix carbonate electrolyte, and a cathode of nickel (rather than steel). We choose the alkali mix electrolyte based on a Li–Na–K carbonate eutectic, and add 25 wt% cesium carbonate. Cesium carbonate has been shown to improve oxygen solubility which can further decrease the air electrode polarization losses.[23] Whereas a steel electrode tends to corrode in molten alkali mix carbonate, we find that nickel is stable. As with steel, the analyzed cathodic charging product on nickel is graphite, as determined by XRD analysis.

As seen in Fig. 11, the improved carbon molten air battery of Fig. 10 exhibits good charge cycling, and low polarization (supporting current densities of over 50 mA cm^{-2}). As measured in Fig. 10 to an 0.3 V discharge cutoff, the energy efficiency (average 0.7 V discharge/0.95 V charge) is 74%, and the coulombic efficiency (comparing 28 coulombs generated to 30 C injected) is over 90%. Further optimization of the electrode morphology, and cell configuration may further increase these values.

VB_2 molten air battery

The foundation of understanding of the electrochemical VB_2 molten air system is small; there is little or no prior information pertaining to an electrochemical path for recharge of the eqn (3) molten vanadate (V_2O_5) and molten borate (B_2O_3) discharge products. Our prior attempts at aqueous, room temperature recharge of the systems were not successful.[31] Here, we provide a path towards recharge of the VB_2 air battery. The studies are less advanced due to the scarcity of prior fundamental electrochemical knowledge of the molten system.

The electrochemical discharge products of VB_2, B_2O_3 (mp 450 °C, white, melts clear) and V_2O_5 (mp 690 °C, yellow/brown) have a low melting point compared to VB_2 (mp 2450 °C, black). We observe that molten B_2O_3 and V_2O_5 salts are miscible, whereas the charged product, VB_2, does not appear to be soluble in the molten B_2O_3–V_2O_5 mix. Due to its higher density, VB_2 descends in the molten mixture. This B_2O_3–V_2O_5 molten phase is without significant ionic dissociation, and hence is an electrochemical insulator. Alone, the melt cannot be electrochemically charged. However, dissolution of an oxide such as Li_2O,

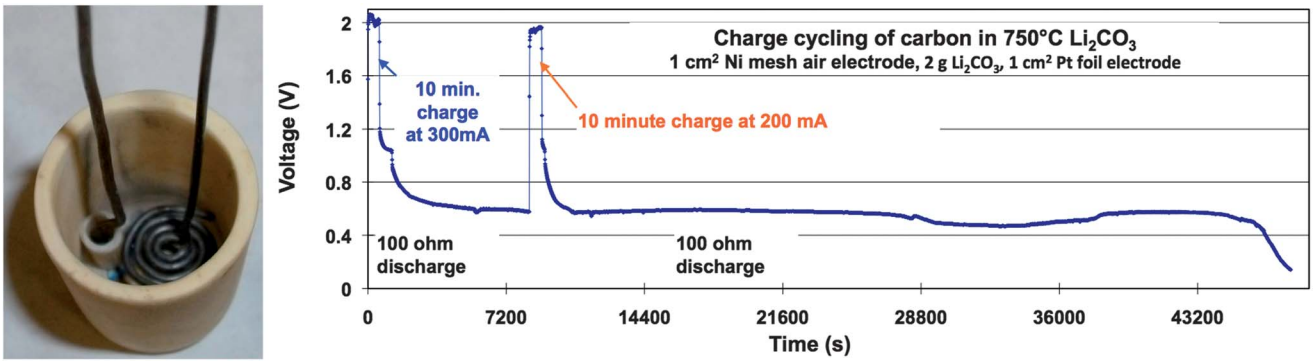

Fig. 10 Cycling of a carbon molten air battery exhibiting high voltage hysteresis, but good charge efficiency. Cell configuration: the cell contains an air electrode which is a 1 cm^2 Ni electrode (Ni mesh, Ni foil, and wound nickel wire, or a 1 cm^2 Ir electrode yields similar results), over a 1 cm^2 Pt electrode (or a 1 cm^2 steel yields similar results) immersed in 2 g of 750 °C molten Li_2CO_3 in an alumina crucible with vertical walls.

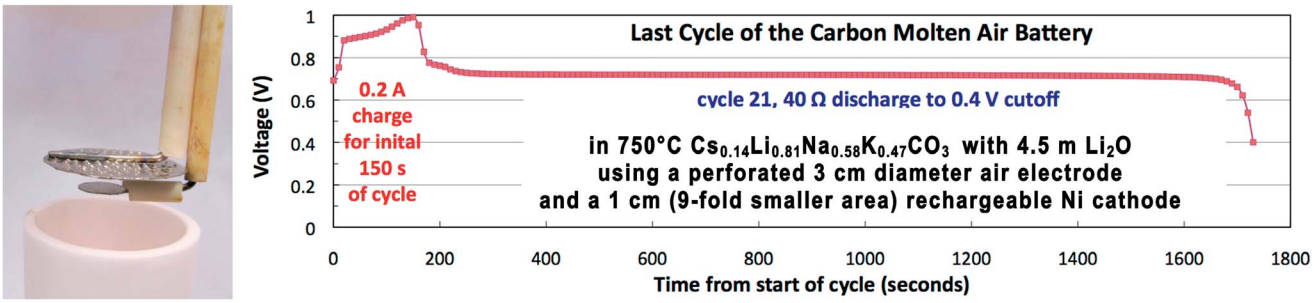

Fig. 11 Cycling of a carbon molten air battery exhibiting low hysteresis, and good charge efficiency. Cell configuration: the cell contains an air electrode with 3 cm diameter perforated Ni foil electrode, 9-fold times larger than the 1 cm diameter Ni foil rechargeable cathode, immersed in a 750 °C alkali mix carbonate electrolyte ($Cs_{0.14}Li_{0.81}Na_{0.58}K_{0.47}CO_3$) in an alumina crucible with vertical walls. Shown: the last cycle (cycle no. 21) of the recharge experiment in the lower panel of Fig. 12.

into the B_2O_3–V_2O_5 melt provides adequate ionic conductivity for charging. In this mix, we will provide preliminary evidence that electrolysis and charging of the oxide mix occurs.

The high temperature (molten) phase of the Li_2O–B_2O_3–V_2O_5 system has not been previously explored, but ionic conductivity range of this system in the solid phase at temperatures up to 250 °C has been established.[32] At higher temperature, the simpler, binary system of B_2O_3 (mp 450 °C) and Li_2O (mp 1438 °C, white, dissolves clear) presents a complex phase diagram with an extensive homogenous liquid phase above 767 °C.[33,34] Fig. 13 presents the liquid domain and complexity of the binary Li_2O–B_2O_3 (wt%) system. Domains of this diagram that we have probed are indicated by the "Liquid" sections in the top of the figure. A comparable phase diagram of the trinary system including V_2O_5, or the quaternary system also including CaO is not available, although we note that each of the following electrolytes is liquid and appears to be homogeneous at 800 °C: the molar ratios of V_2O_5–B_2O_3–Li_2O–CaO of 1 : 2 : 2 : 0, 1 : 7 : 12 : 0 and 1 : 2 : 4 : 3.

Fig. 14 includes a photo of an initially bare, coiled steel wire electrode, after electrolysis in the molten vanadate, borate, lithium mixture. The extracted electrode exhibits evidence of VB_2 on steel subsequent to charging in a 767 °C 1 : 2 : 0.67 V_2O_5, B_2O_3, Li_2O mix electrolyte. Charging is accomplished with a coiled nickel wire oxygen generating anode, situated above the coiled steel wire cathode, in an alumina crucible containing the electrolyte, and yields a thick black deposit on the cathode. The charging product is examined by extraction, cooling, and

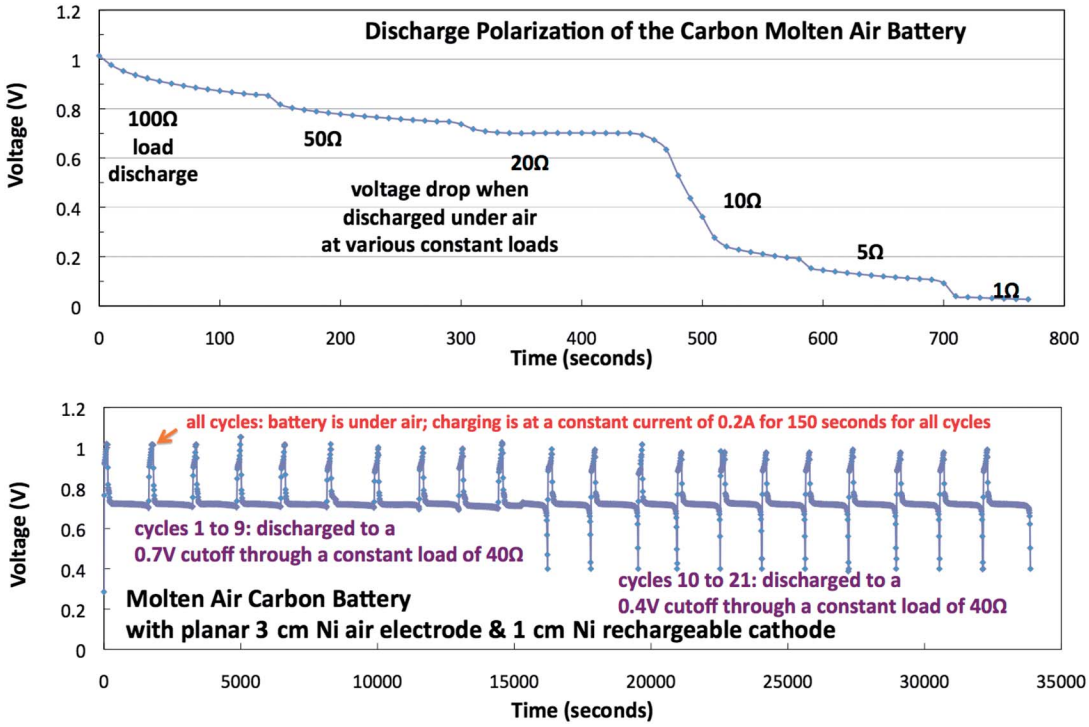

Fig. 12 Polarization and cycling characteristics of the carbon molten air battery presented in Fig. 11. High discharge potentials are maintained down to a load of 20 Ω (through the 1 cm diameter cathode and 3 cm diameter air electrode), and reproducible charge/discharge cycles to either a 0.7 V or 0.4 V cut-off, in which the battery has been charged at a 0.2 A constant current for 150 seconds, followed by discharge over a 40 Ω resistance load.

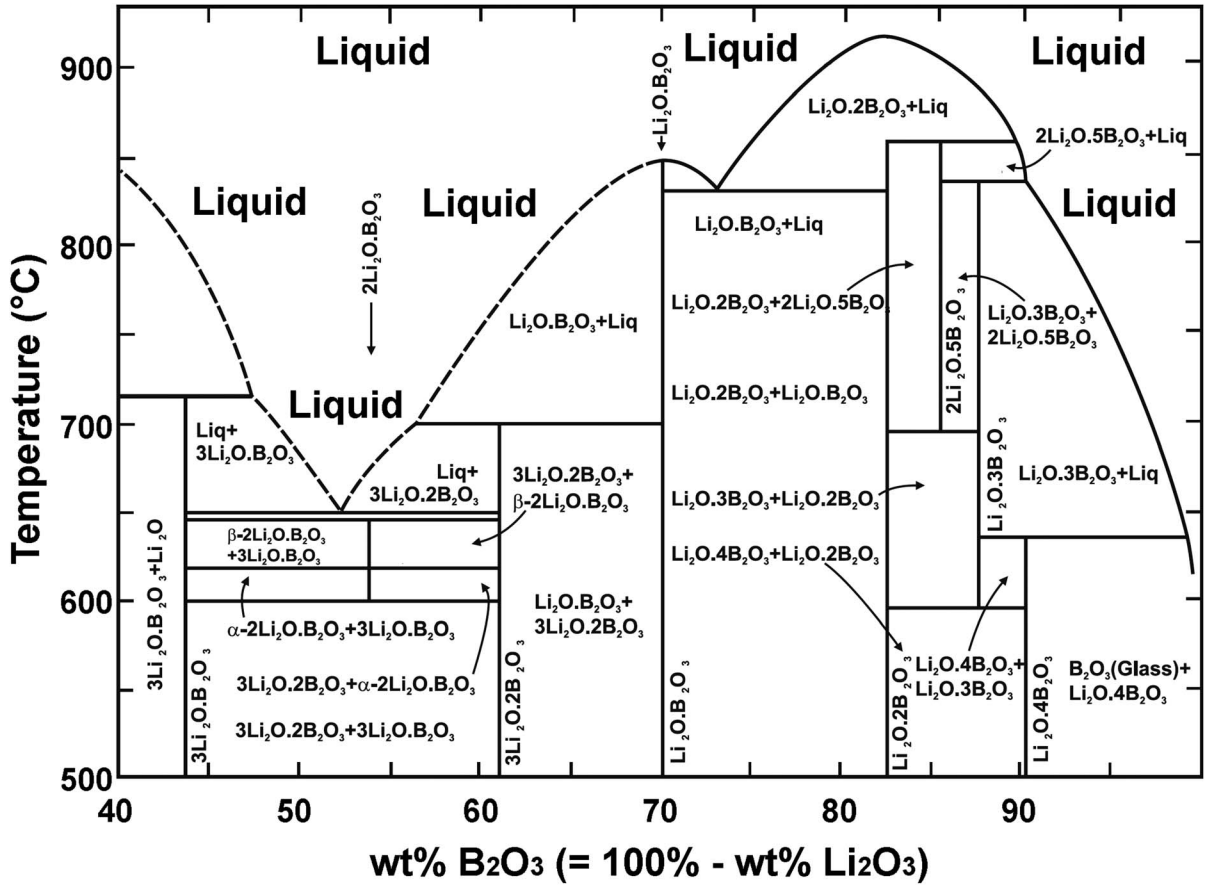

Fig. 13 The liquid component of the binary Li_2O–B_2O_3 (wt%) system (modified from ref. 34).

Fig. 14 The VB_2 molten air battery. Photo: VB_2 formed on the steel wire cathode, extracted following an 8.5 hour charge at 0.2 A in a Li_2O–V_2O_5–B_2O_3 electrolyte. FTIR analysis of this electrode is described in the text. Right: 100 ohm discharge potential subsequent to a 0.2 A charging for 10 minute, in 2 g of various 800 °C vanadate borate electrolytes sandwiched between a coiled disc nickel (4 cm^2 area coiled 1.0 mm diameter wire) electrode above and a coiled disc steel (3 cm^2 area coiled 1.2 mm diameter wire) electrode.

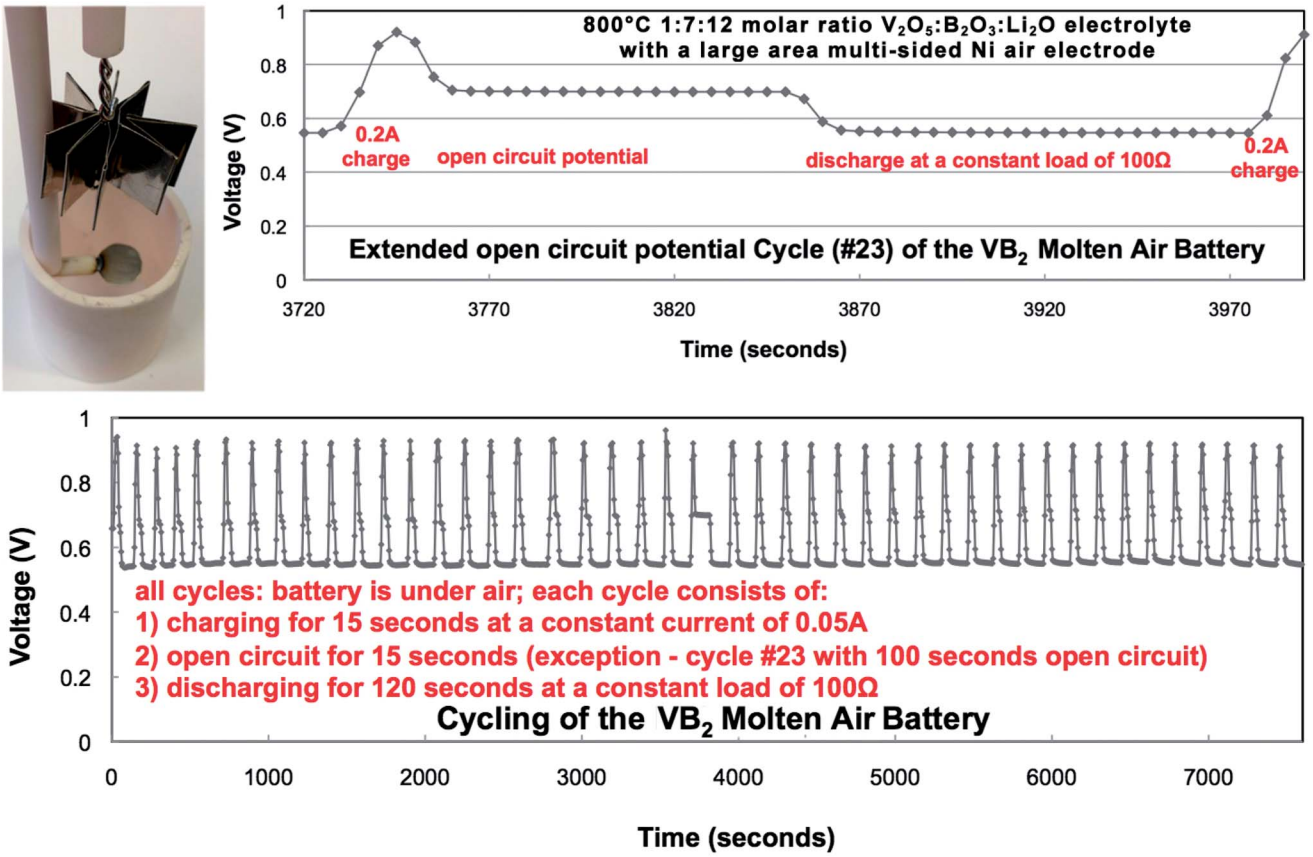

Fig. 15 The VB_2 molten air battery using a large surface area Ni air electrode. Photo: the multi-side Ni electrode formed from folded (25 cm × 2 cm) Ni and the 1 cm diameter steel rechargeable cathode prior to addition of the molten electrolyte in a vertical wall alumina crucible. Lower panel: cycling of the battery with a repeated 0.05 A 15 second charge, followed by discharge over a 100 Ω load to a 0.55 V cutoff. The middle cycle includes an extended period at open circuit, and this cycle is expanded in the top panel of the figure.

acid wash of the cathode to remove soluble components. FTIR of the product exhibits absorption peaks at 1640 and 3470 cm^{-1} that coincide with that of commercial VB_2 (from NOAH high purity chemicals). A more extensive (2 A charge for 6 hour) charge results in a mass loss of 1.5 g, only ~40% of the expected mass loss due to oxygen evolution *via* eqn (3) (in the charging, reverse mode). Electrolytes prepared from mixtures of $LiVO_3$ and $LiBO_2$ (rather than non-lithiated salts mixed with Li_2O) also yield similar results.

The right side of Fig. 14 includes the extended discharge of a VB_2 molten air batteries containing other electrolytes composed to improve the cell discharge potential; the discharge is subsequent to a 0.2 A charge for 10 min. For example, a higher fraction of added Li_2O is added to improve ionic conductivity (and increase the discharge potential under load); while additions of CaO or increases were added to observe their effect on potential. As can be seen, the electrolyte that after charging exhibited the highest discharge voltage is the 1 : 7 : 12 ratio V_2O_5–B_2O_3–Li_2O (without CaO). Further increases in the relative B_2O_3 or Li_2O concentrations were observed to decrease the discharge voltage. Although a relatively light load (100 Ω) is utilized, and although the air electrode has a higher surface area (4 cm^2), in all three cases the discharge potential is significantly less than the charging potential. To present a preliminary effective demonstration of a VB_2 molten air battery with less hysteresis, a very large surface area (50 cm^2) air electrode was prepared by folding a 25 cm × 2 cm Ni shim into the multiple sided configuration shown in Fig. 15. As seen in the lower panel of the figure, starting with a cell in the discharged (molten borate and vanadate) condition, the VB_2 molten air system can repeatedly inject and release charge The hysteresis is large, although not significantly different than observed in many hydrogen fuel cells. This is evident in the difference between charging (0.9 V at 0.2 A) and discharging (0.55 V over a 100 Ω load) voltages, but the discharge voltage is stable, and as can be seen in the middle cycle (cycle number 23 as expanded in the upper part of the figure), the open circuit potential is 0.7 V. It is evident in the repeated recharge cycles that electrochemical storage has been achieved, but that more studies are needed to better understand and optimize this last demonstrated form of a molten air battery.

Conclusions

The foundation, experimental demonstration, and proof of principle of a new class of molten air batteries is established. The iron molten and carbon molten air batteries exhibit high rate charging capability and quasi reversibility (rechargeability).

An extensive range of experimental parameters (electrolyte and gas composition, electrode morphology, temperature, and cycle rates) next need to be explored to optimize the mechanism and cycling characteristics of these batteries. For example, while these experiments have been conducted in the 700 °C to 800 °C temperature range, the molten carbonate electrolyte has a wide range of electrolyte opportunities, such as through the use of mixed alkali carbonate eutectics which exhibit a minimum melting point below 400 °C. Enhancements of the morphology and modifications of the electrocatalytic nature of the air electrode should improve energy efficiency of the cell. A range of cell configurations with lower polarization (with similar discharge potentials, but supporting significantly higher current density) will be reported in a future study.

Acknowledgements

We are grateful to the United States National Science Foundation award DMR 1006568 for partial support of this work. Graduate student Jessica Stuart contributed to the VB_2 molten air battery data.

Notes and references

1 R. Shapira, G. D. Nessin, T. Zimrin and D. Aurbach, *Energy Environ. Sci.*, 2013, **6**, 734.
2 B. Dunn, H. Kamath and J. M. Tarascon, Electrical Energy Storage for the Grid: A Battery of Choices, *Science*, 2011, **334**, 928–935.
3 J. B. Goodenough, Rechargeable batteries: challenges old and new, *J. Solid State Electrochem.*, 2012, **16**, 2019.
4 S. Licht, H. Wu, X. Yu and Y. Wang, *Chem. Commun.*, 2008, 3257.
5 S. Licht, S. Ghosh, B. Wang, D. Jiang, J. Asercion and H. Bergmann, *Electrochem. Solid-State Lett.*, 2011, **14**, A83.
6 S. Licht, C. Hettige, J. Lau, U. Cubeta, H. Wu, J. Stuart and B. Wang, *Electrochem. Solid-State Lett.*, 2012, **15**, A12.
7 K. B. Hueso, M. Armand and T. Rojo, *Energy Environ. Sci.*, 2013, **6**, 734.
8 X. Lu, B. W. Kirby, G. Li, J. Y. Kim, J. P. Lemmon, V. L. Sprenkle and Z. Yang, *Energy Environ. Sci.*, 2013, **6**, 299.
9 D. Peramunage and S. Licht, *Science*, 1993, **261**, 1029.
10 R. Demir-Cakan, M. Morcerette, B. Gangul, A. Gueguen, R. Dedryvere and J. Tarascon, *Energy Environ. Sci.*, 2013, **6**, 176.
11 D. J. Bradwell, H. Kim, H. C. Sirk and D. R. Sadoway, *J. Am. Chem. Soc.*, 2012, **134**, 1895.
12 J. Christensen, P. Abertus, R. S. Xanches-Varrera, T. Lohmann, B. Kozinsky, R. Liedtke, J. Ahmed and A. Kojic, A Critical Review of Li/Air Batteries, *J. Electrochem. Soc.*, 2012, **159**, R1.
13 Y.-C. Lu, M. M. Gallant, D. G. Kwabi, J. R. Hrding, R. R. Mitchell, M. S. Whittingham and Y. Shao-Horn, *Energy Environ. Sci.*, 2013, **6**, 750.
14 S. Licht and B. Wang, *Chem. Commun.*, 2010, **46**, 7004, with online 6 page supplement.
15 S. Licht, H. Wu, Z. Zhang and H. Ayub, *Chem. Commun.*, 2011, **47**, 3081, with online 7 page supplement.
16 S. Licht and H. Wu, *J. Phys. Chem. C*, 2011, **115**, 25138.
17 B. Cui and S. Licht, *Green Chem.*, 2013, **113**, 881.
18 S. Licht, *Adv. Mater.*, 2011, **47**, 5592.
19 S. Licht, *J. Phys. Chem. C*, 2009, **113**, 16283.
20 S. Licht, B. Wang, S. Ghosh, H. Ayub, D. Jiang and J. A. Ganley, *J. Phys. Chem. Lett.*, 2010, **1**, 2363.
21 A. K. Manohar, S. Malkhandi, B. Yang, C. Yang, G. K. S. Prakash and S. R. Narayanan, A High-Performance Rechargeable Iron Electrode for Large-Scale Battery Based Energy Storage, *J. Electrochem. Soc.*, 2012, **159**, A1209.
22 A. Kulami and S. Giddey, *J. Solid State Electrochem.*, 2012, **16**, 3123.
23 D. D. Smith and J. Winnick, Cesium-containing electrolyte for the molten carbonate fuel cell, *Electrochem. Solid-State Lett.*, 1999, **2**, 207.
24 M. R. Predtechensky, Y. D. Varlamov, S. N. Ul'yankin and Y. Dubov, Direct conversion of solid hydrocarbons in a molten carbonate fuel cell, *Thermophys. Aeromech.*, 2009, **16**, 601.
25 A. C. Rady, S. Giddey, S. P. S. Badwal, B. P. Ladewig and S. Bhattacharya, Review of Fuels for Direct Carbon Fuel Cells, *Energy Fuels*, 2012, **26**, 1472.
26 L. Kouchachvi and M. Ikura, Performance of direct carbon fuel cell, *Int. J. Hydrogen Energy*, 2011, **36**, 10263.
27 S. Licht, *arXIV*, arXiv: 2112, 1209.3512 [physics.chem-ph], 1, http://arxiv.org/pdf/1209.3512v1.pdf.
28 M. W. Chase, *J. Phys. Chem. Ref. Data*, 1998, **9**, 1.
29 U.S. NIST ChemWeb online thermochemical, http://webbook.nist.gov/chemistry/form-ser.html.
30 Glenn Research Center NASA, ThermoBuild access to NASA Glenn thermodynamic CEA database, 2006, http://www.grc.nasa.gov/WWW/CEAWeb/ceaThermoBuild.htm.
31 S. Licht and X. Yu, *Electrochim. Acta*, 2007, **52**, 8138.
32 Y. Lee, J. Lee, S. Hong and Y. Park, Li-ion conductivity in Li_2O–B_2O_3–V_2O_5 glass system, *Solid State Ionics*, 2004, **175**, 687.
33 P. Pasierb, R. Gajerski, M. Rokita and M. Rekas, Studies on the binary system Li_2CO_3-$BaCO_3$, *Physica B*, 2001, **304**, 463–476.
34 E. B. Ferreira, E. Zanotto, S. Feller, G. Lodden, J. Banerjee, T. Edwards and M. Affatigat, Critical Analysis of Glass Stability Parameters and Application to Lithium Borate Glasses, *J. Am. Ceram. Soc.*, 2011, **94**, 3833.

View Article Online
DOI: 10.1039/C3EE42654H

Electronic Supplementary Information for

Molten Air - A new, highest energy class of rechargeable batteries

Stuart Licht*, Baochen Cui and Jessica Stuart
Department of Chemistry, George Washington University, Washington, DC, 20052, USA. E-mail: slicht@gwu.edu

Supplementary Information:
Carbonate electrolyte stability

Carbonate electrolyte stability. We have recently shown that under many conditions molten lithium carbonate readily absorbs atmospheric carbon dioxide, providing a facile route to decrease CO_2 in the atmosphere. As summarized in the CO_2/carbonate equilibrium diagram in Figure S-1, we now calculate from the known variation of standard enthalpies and entropies with temperature[23-25] that barium carbonate has an even larger affinity for CO_2 capture than lithium carbonate.

The equilibrium curves in the figure summarize the partial pressure of CO_2 and dissolved oxide concentration relative to carbonate in which CO_2 absorption occurs (above the line) or carbonate decomposition occurs (below the line). This equilibrium can be controlled through cation and temperature choice, and the concentration of oxide in the melt. Molten carbonate can gain or lose mass through CO_2 absorption or emission, and the concentration of carbon dioxide maintained above the melt is in accord with the equilibrium:

$$MCO_3 \rightleftharpoons MO + CO_2;\ M= Li_2, Na_2, K_2, Ba, \text{etc} \qquad \text{(S-1)}$$

Barium carbonate is solid at lithium carbonate's 723°C melting point. However as summarized in the Figure S-1 inset, barium carbonate readily dissolves in lithium carbonate, and a eutectic comprised of 69% by mass barium to lithium carbonate melts at 609°C.

View Article Online
DOI: 10.1039/C3EE42654H

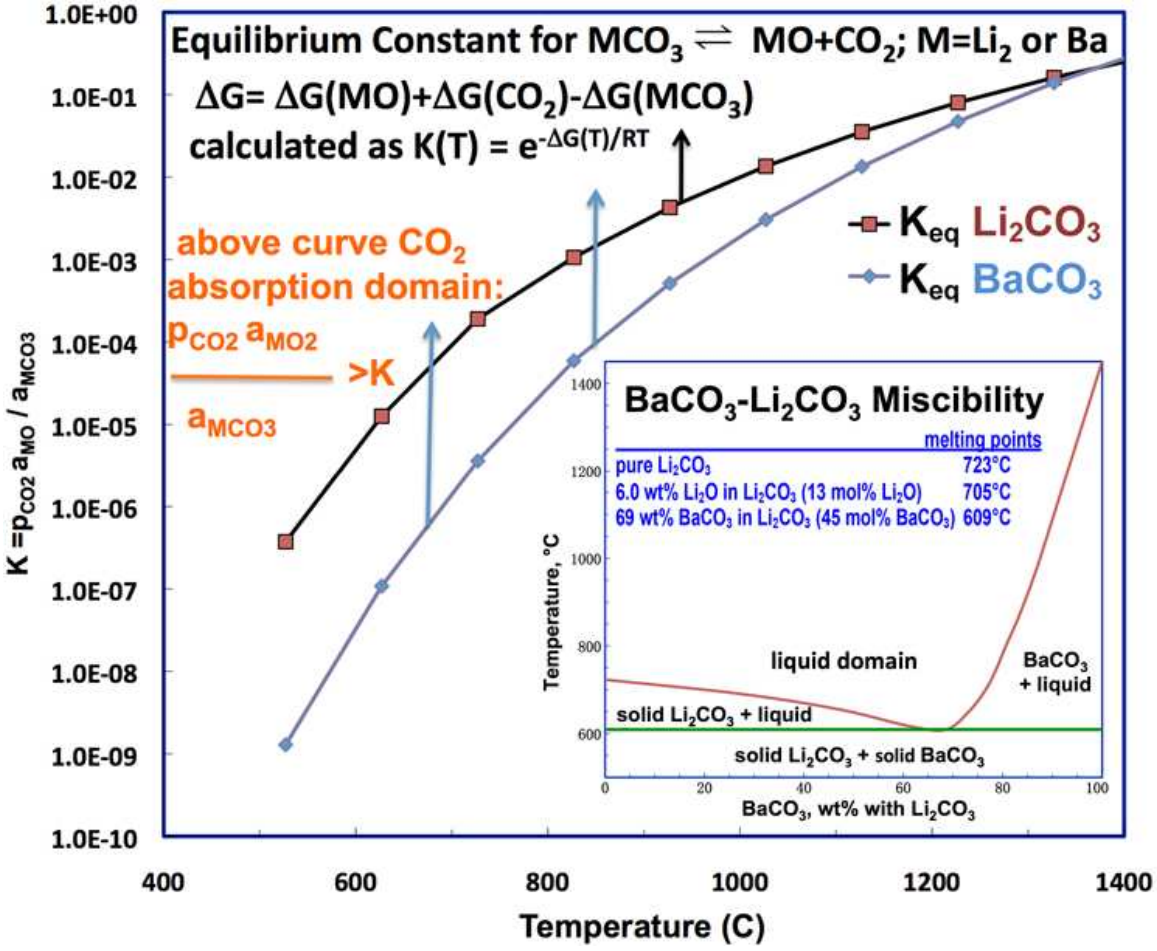

Figure S-1. Comparison of the equilibrium constant for Li_2CO_3 and $BaCO_3$, decomposition or absorption of CO_2 as calculated from the thermochemistry of the carbonate, carbon dioxide and oxide components. Inset: Phase diagram of the $BaCO_3$ - Li_2CO_3 system (100% or 0% respectively indicate pure barium or lithium carbonate); modified from reference *33*. The 705°C Li_2O/Li_2CO_3 mix melting point is noted for comparison, but not shown on the curve.

Journal of Materials Chemistry A

PAPER

A low temperature iron molten air battery†

Cite this: J. Mater. Chem. A, 2014, 2, 10577

Received 15th March 2014
Accepted 2nd May 2014

DOI: 10.1039/c4ta01290a

www.rsc.org/MaterialsA

Baochen Cui‡ and Stuart Licht*

A molten air battery was demonstrated to work at temperatures favourable for EV applications. Molten air battery is a new class of rechargeable batteries with the highest-density energy storage capability, consisting of three parts: a discharging air cathode, molten electrolyte and multi-electron anode. A eutectic electrolyte with soluble $LiFeO_2$ and optimized cell configuration lowered the battery operating temperatures by >100 °C. In the eutectic electrolyte at 600 °C, the cycling of iron molten air battery averaged 60% coulombic efficiency at 1.3 V charge and 1.0 V constant load discharge, and 92% coulombic efficiency at a lower cut-off voltage of 0.5 V.

Higher energy density batteries are urgently needed for today's medical and consumer electronics and for the functioning of low CO_2 emitting technologies.[1–4] The latter category includes higher capacity batteries to reduce the range anxiety of electric vehicles and to improve storage for wind and solar-generated electricity.

Recently, we introduced a new class of rechargeable batteries, the molten (electrolyte) air batteries, which exhibit amongst the highest reversible electrical energy storage capabilities of any battery. When discharging these batteries, each utilizes an air cathode, a molten electrolyte and a high capacity multi-electron anode.[1] The discharge of rechargeable molten air batteries couples the cathodic reduction of O_2 from air with anodic multi-electron/molecule oxidation to yield an intrinsic storage capacity on the order of 10^4 W h per liter, which is greater than that of Li–air and over ten-fold greater than that of Li-ion.[1]

To date, molten air battery chemistries have been demonstrated in the temperature range from 730 °C to 800 °C using anodes discharging (i) the $11e^-$ oxidation of VB_2 (with a vanadate/borate electrolyte), (ii) the $4e^-$ carbon or (iii) the $3e^-$ iron (each with a carbonate electrolyte).[1] Lower-temperature battery chemistries would greatly expedite their utility for EV (electric vehicle) applications (as discussed in the ESI†).

In this study, we probed one example, the iron molten air batteries. We probed the sustainable current densities and discharge efficacy and demonstrated a pathway to lower the temperature in a rechargeable iron molten air battery. The reactions in the iron molten air battery are represented by eqn (1), including eqn (1a) showing the dissolution of Fe_2O_3 by Li_2O to form a lithiated iron oxide, $LiFeO_2$,[5] followed by quasi-reversible charge/discharge of $LiFeO_2$ to iron, shown in eqn (1b).

Global $3e^-$ iron molten air battery charge/discharge:

$$1/2Fe_2O_3 \rightleftharpoons Fe + 3/4O_2 \quad (1)$$

Molten electrolyte dissolution:

$$1/2Fe_2O_3 + 1/2Li_2O \rightleftharpoons LiFeO_2 \quad (1a)$$

$3e^-$ cycling:

$$LiFeO_2 \rightleftharpoons Fe + 1/2Li_2O + 3/4O_2 \quad (1b)$$

Four configurations of the iron molten air cell battery are shown in the top panel of Fig. 1, each photographed prior to the insertion of the molten electrolyte. Each of the cells exhibits similar, reproducible charge/discharge behaviour. A sampling of the repeated charge/discharge cycling behaviour for the battery with a nickel crucible configuration is shown in the bottom panel of Fig. 1, and the measured full cell voltage is presented as voltage (V). In the leftmost photograph, the crucible is made of nickel. The adjacent photograph shows an alumina configuration, where the upper electrode is a McMaster 200 pure Ni shim perforated with holes to facilitate oxygen escape, and the electrolyte is contained in a (white) alumina crucible, while in the other two configurations, the electrolyte is retained by either a Ni or a Ni-alloy container that also functions as the air electrode. Rather than using pure Ni for the cell case and air electrode, the U- and V-shaped configurations shown are made of Inconel Ni alloy, which results in the same battery voltage, cycling performance and stability, and exhibits better stability in contact with externally heated oxygen.

In the photos in Fig. 1, the counter electrode is always 1 cm^2 of 316 stainless steel shim (McMaster), either flat or curved into the indicated cylindrical shape, and situated in the middle of and/or below the air electrode. In the absence of Fe(III), the cell

Department of Chemistry, George Washington University, Ashburn, Virginia 20147, USA. E-mail: slicht@gwu.edu; Tel: +1 703 726 8215

† Electronic supplementary information (ESI) available: (1) Molten air mechanism of action, (2) electrochemistry of iron in molten carbonates. See DOI: 10.1039/c4ta01290a

‡ Current address: College of Chemistry and Chemical Engineering, Northeast Petroleum University, Daqing, 163318, PR China.

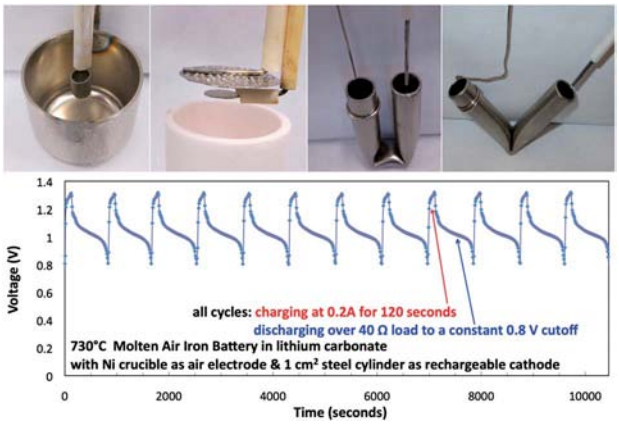

Fig. 1 Cycled charge/discharge of the 730 °C iron molten air battery with 1.5 m Fe_2O_3 and 3 m Li_2O in Li_2CO_3 electrolyte. The photographed batteries utilize a 1 cm^2 stainless steel 316 electrode located inside Ni (leftmost) or Inconel (right) or under Ni (second photo). In all except the second configuration, the encasement also acts as the air electrode. In the second photo, the encasement is an AdValue AL-2100 (OD 40 mm, height 95 mm) alumina crucible. Inconel is a McMaster 600 tubing (1.1 cm ID). The Ni crucible in the leftmost photo is a 20 mL Alfa 35952. In the two right photos, the "U" or "V" shape seals the cell bottom and provides contact to the inner wall of the air electrode.

acts as a carbon molten air battery, and charging results in graphite deposition on the steel. Carbon molten air battery discharges in the 0.3–0.7 V range (and is capable of being charged at potentials as low as 1 V).[1] Only when Fe(III) is added to the iron molten air battery, the charging product in molten carbonate becomes a loose, electrodeposited iron layer on the steel.[6,7] This discharges in the 0.8–1.2 V range. When iron molten air battery is discharged to a lower cut-off voltage, it can also approach a second low voltage graphite discharge plateau after this high voltage plateau.

We have previously demonstrated that the iron molten air battery exhibits a high degree of reversibility.[1] Fig. 2 shows the discharge voltage for the iron molten air battery in the Li_2CO_3 electrolyte at 730 °C. The battery exhibits a 5–100 mA cm^{-2} discharge current density, evident by comparing the voltage to the load normalized by the steel electrode area. These moderate currents, combined with the high intrinsic molten air battery capacity (approaching 10^4 mA h g^{-1}), can lead to days or weeks of discharge times, which are a challenge to compare in a reasonable time frame.

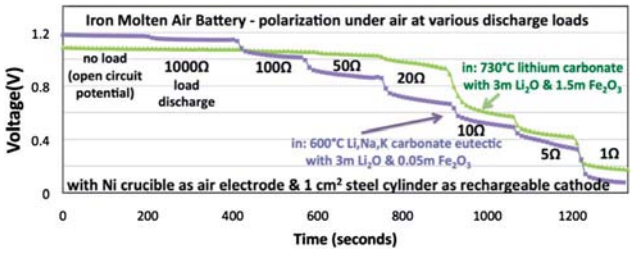

Fig. 2 Comparison of the iron molten air battery potentials in open circuit and the discharge potential under load in a battery with $Li_{0.87}Na_{0.63}K_{0.50}CO_3$ electrolyte at 600 °C or the Li_2CO_3 electrolyte at 730 °C.

As predicted by our prior thermodynamic calculations (ESI†), a temperature decrease should increase the open circuit potential for the endothermic iron oxide reduction in the iron molten air battery. Pure Li_2CO_3 melts at 723 °C. $Li_{0.87}Na_{0.63}K_{0.50}CO_3$ eutectic melts at ~393 °C, permitting the study of the iron molten air battery in low-temperature molten electrolytes. Fig. 2 compares the measured battery potentials of similar iron molten air batteries, with the first containing lithium carbonate at 730 °C as the electrolyte, and the second a battery with a lower working temperature, which contained the eutectic carbonate at 600 °C as the electrolyte. As predicted, the lower-temperature battery has a higher open circuit potential. Compared with the 730 °C battery, the 600 °C battery exhibits higher polarization losses, as lower temperature will increase electrolyte resistivity and impede charge transfer kinetics.

Originally, we studied 1.5 m $LiFeO_2$ (m ≡ moles kg^{-1} carbonate) batteries.[1] In this study, we probed the opposite domain, *i.e.* a low concentration of dissolved Fe(III) to accelerate discharge probes of the cell. When the dissolved iron concentration was decreased to 0.05 m Fe_2O_3 in the molten Li_2CO_3 electrolyte, the intrinsic capacity in the battery was lowered to 333 coulombs of Fe(III). This is a sufficiently small storage capacity that the cell may be charged/discharged in hours rather than days or weeks.

Each iron molten air battery configuration shown in Fig. 1 exhibits highly similar charge/discharge curves. Other factors probed (Fig. 3) showed impacts on battery chemistry. The coulombic efficiency is measured by comparing the extent of discharge as a percentage of the constant charge input during each cycle, as well as cells purposely discharged to a lower cut-off voltage (to 0.5 V rather than 0.8 V) to effectuate the comparison of charge efficiency. During charging, iron oxide is converted back to iron and oxygen. During this charging, we observed oxygen forming at the air electrode (the nickel or monel wall), rising and leaving the cell. As seen in Fig. 3A, if the steel electrode is too close to the air electrode, then the charge will be lost. The iron molten air charge coulombic efficiency decreases from 100% to <70% if the iron electrode is located too close to the air cathode. The chemical self-discharge loses stored charge as

$$3Fe + 2O_2 \rightarrow Fe_3O_4 \quad (2)$$

This loss in charge efficiency is avoided by the spatial removal of evolving O_2 from the iron deposited on the inner steel. The discharge plateau observed below 0.7 V represents a loss of voltage efficiency but not charge efficiency. As previously delineated[1] and elaborated in the ESI,† this is due to the competing formation and discharge of graphite from the carbonate electrolyte at lower potentials:

$4e^-$ battery charge/discharge:

$$Li_2CO_3 \rightleftharpoons C_{graphite} + Li_2O + O_2 \quad (3)$$

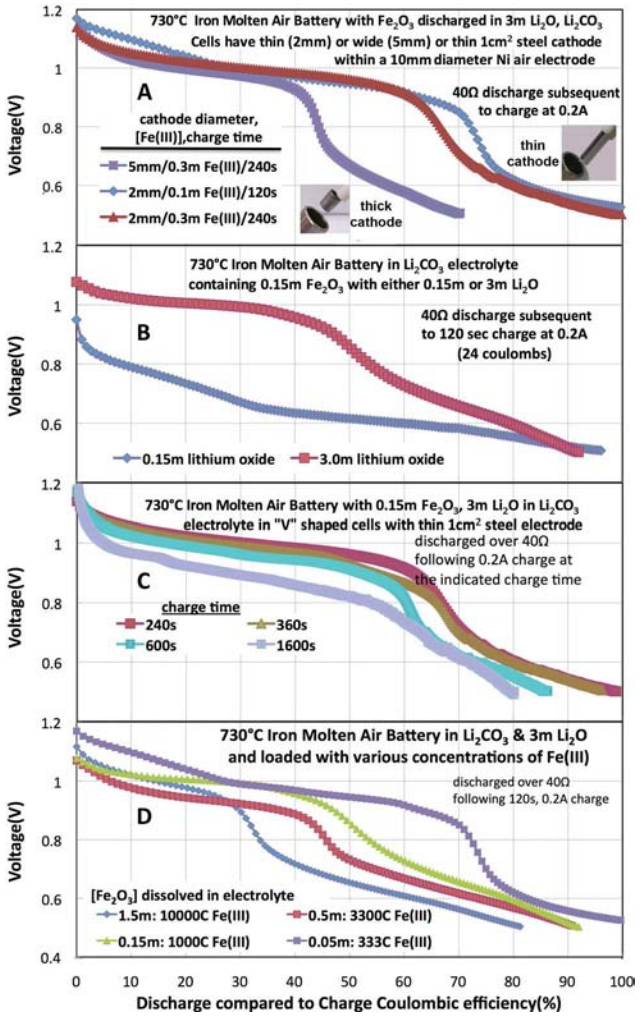

Fig. 3 730 °C iron molten air battery variation of the discharge voltage with charge Coulomb efficiency as affected by (A) proximity of the inner steel electrode to the outer air electrode (using the V-shaped configuration in Fig. 1). (B) The [Li_2O] in the molten carbonate electrolyte. (C) The charge duration during battery cycling. (D) The [Fe(III)] in the molten carbonate electrolyte.

Dissolved iron represents a substantial electrical storage capacity, and the iron molten air battery can contain a large fraction of rechargeable iron. A low concentration ratio of Li_2O to Fe_2O_3 limits the molten carbonate solubility of the ferric species, as shown in eqn (1a), and results in discharge overpotential. Fig. 3B illustrates that the Li_2O concentration affects the iron molten air battery; on the other hand, in the case of 0.15 m Fe_2O_3 dissolved in 0.15 m Li_2O, the regeneration of iron oxide by the oxidation of iron metal occurs at substantial overpotential losses during discharge. This loss does not occur when excess Li_2O (3 m) is added to the electrolyte.

Fig. 3C compares the discharge subsequent to constant current (0.2 A) charge for different durations. Charges prior to each discharge range from 320 coulombs (0.2 A × 1600 s) to 24 coulombs. The efficiency of discharge to a 0.5 V cut-off remains high; however, the average upper plateau discharge voltage diminishes from 1.1 V for the short charge duration (240 s) to 0.9 V for the longer charge duration (1600 s). Note that the discharge time over the 40 Ω load is quite long following the 1600 s charge; in this case, the discharge to the 0.5 V cut-off occurs over >13 000 seconds.

We probed the effect of dissolved Fe(III) concentrations on coulombic efficiency (Fig. 3D). When the concentration is decreased to 0.05 m Fe_2O_3, the intrinsic capacity of Fe(III) in the battery is lowered to 333 coulombs. As shown in Fig. 3D, the discharge voltage improves as the Fe(III) concentration in the battery is lowered, going from 10 000 to 3300 to 1000 to 333 coulombs. In the latter case, 100% coulombic efficiency is reached (according to voltage) with ~80% contribution from iron oxidation (in the 1 V domain) and 20% contribution from the iron/graphite oxidation transition towards 0.5 V. This is a sufficiently small storage capacity that the cell may be discharged in a reasonably short time period (<one day).

Fig. 3 establishes that a Fe(III) limited iron molten air battery with a high coulombic efficiency can be prepared with 0.05 m Fe_2O_3 and 3 m Li_2O in Li_2CO_3 at 730 °C. An analogous, but lower-temperature battery was prepared with $Li_{0.87}Na_{0.63}K_{0.50}CO_3$ eutectic with a lower melting point. At 395 °C, the polarization is high, and a 0.04 A cm^{-2} constant charge voltage is excessive at 2.8(±0.1) V, which precludes cycling. The 0.04 A charge voltage decreases to 1.6(±0.2) V at 500 °C or 600 °C to only 1.5(±0.1) V.

As seen in Fig. 4, the eutectic iron molten air battery cycles effectively at 600 °C (lower three rows) but exhibits excessive polarization at 500 °C (top row showing 7 cycles). At 500 °C over a 100 Ω load, a small shoulder is observed at 0.8 V. At 600 °C, this shoulder potential increases to ~1 V and increases further

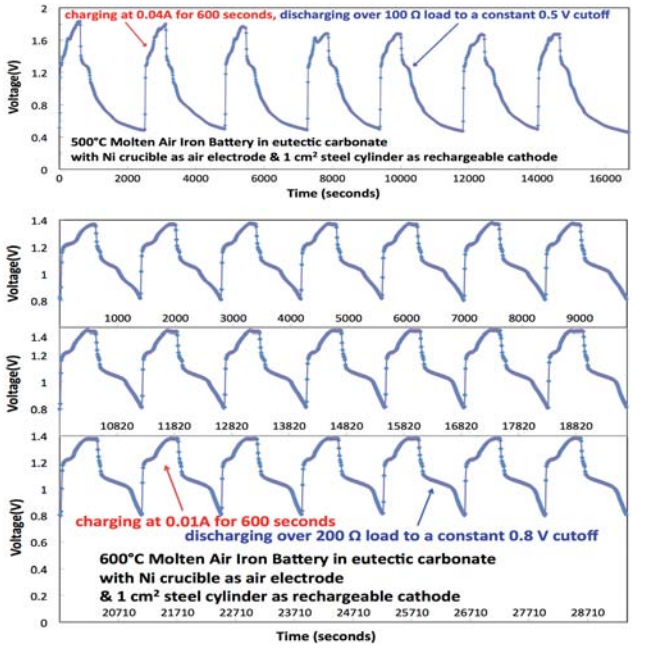

Fig. 4 Cycled charge/discharge behaviour of the $Li_{0.87}Na_{0.63}K_{0.50}CO_3$ iron molten air battery with 3 m Li_2O and 0.05 m Fe_2O_3 at 500 °C (top row) or 600 °C (bottom three rows). The 500 °C cycle charges at 0.04 A and discharges over a 100 Ω load, while the 600 °C battery cycle charges at 0.01 A and discharges over a 200 Ω load.

to ~1.1 V over a 200 Ω load. At heavier load, the polarization is larger. Over a 10 Ω constant load, the discharge voltage is 0.1 V, 0.2 V and 0.5 V at 395 °C, 500 °C and 600 °C, respectively. At 600 °C and a lower constant current of 0.01 A, the charging voltage further decreases to 1.3(±0.1) V.

The lower three rows in Fig. 4 present 21 cycles of the 600 °C iron molten $Li_{0.87}Na_{0.63}K_{0.50}CO_3$ air battery. The ~1.1 V discharge plateau is high compared to the 1.3(±0.1) V voltage at the 0.01 A charge. The cell is discharged reproducibly to a 0.8 V cut-off yielding 60% coulombic efficiency of the injected charge. A separate 600 °C battery is cycled to 0.5 V discharge cut-off (not shown) discharged to 92% of injected charges and includes a low voltage plateau. Variation of other rates during discharge will be presented in a future study. The increase of overpotential with load is highlighted by a decrease in voltage (Fig. 2); a discharge under pure O_2 marginally improves the voltage.[1] The variation of molten salt resistance with carbonate cation and temperature has been highlighted in our previous studies.[6,12] At 600 °C, the reversible cycling of the iron molten air battery performance shows 60% coulombic efficiency with a constant current average charge at 1.3 V and a constant load average discharge at 1.0 V, and 92% coulombic efficiency when the battery is discharged to a lower (0.5 V) cut-off voltage.

Conclusions

Optimization of temperature, current density, electrolyte composition and cell configuration led to rechargeable behaviour approaching 100% coulombic efficiency for the iron molten air battery. The operational temperature rechargeable molten air battery is decreased from 700–800 °C to 600 °C or less with a low melting point $Li_{0.87}Na_{0.63}K_{0.50}CO_3$ eutectic. High voltage efficiency and cycling are observed at 600 °C, but polarization is excessive at 395 °C. The low temperature advantage of the eutectic electrolyte is offset by two disadvantages: Li_2CO_3 is more conductive than electrolytes containing Na_2CO_3 or K_2CO_3,[8,9] and Li_2O is more stabilizing than Na_2O or K_2O in carbonates[10] or chlorides.[11] We hope to explore if a new $BaCO_3$ additive[12] can offset the disadvantages.

Acknowledgements

We are grateful to the ONR award N14-13-1-0791 for partial support of this study.

Notes and references

1 S. Licht, B. Cui, J. Stuart, B. Wang and J. Lau, *Energy Environ. Sci.*, 2013, **6**, 3646.
2 R. Shapira, G. D. Nessin, T. Zimrin and D. Aurbach, *Energy Environ. Sci.*, 2013, **6**, 734.
3 B. Dunn, H. Kamath and J.-M. Tarascon, *Science*, 2011, **334**, 928.
4 J. B. Goodenough, *J. Solid State Electrochem.*, 2012, **16**, 2019.
5 S. Licht, H. Wu, Z. Zhang and H. Ayub, *Chem. Commun.*, 2011, **47**, 3081.
6 B. Cui and S. Licht, *Green Chem.*, 2013, **15**, 881.
7 S. Licht and B. Wang, *Chem. Commun.*, 2010, **46**, 7004.
8 *Principles of Molten Salt Electrochemistry*, ed. M. Zhang and Z. Wang, Chem. Industry Press, Beijing, 2006, p. 191.
9 T. Kojima, Y. Miyazaki, K. Nomura and K. Tanimoto, *J. Electrochem. Soc.*, 2008, **155**, F150.
10 S. Licht, arXiv: physics. chem-ph arXiv:1209.3512v1, 2012.
11 Y. D. Yang, I. D. Sommerville and A. McLean, *Trans. Indian Inst. Met.*, 2006, **59**, 655.
12 S. Licht, B. Cui and B. Wang, *J. CO_2 Utilization*, 2013, **2**, 58.

Electronic Supplementary Information (ESI) for:

A Low Temperature Iron Molten Air Battery

Baochen Cui[a] and Stuart Licht*[,a]

ESI contains:

1) Molten Air mechanism of action (reproduced in part, reproduced with permission from S. Licht, B. Cui, J. Stuart, B. Wang and J. Lau[a], *Energy & Environmental Science*, 2013, **6,** 3646.)

2) Electrochemistry of iron in molten carbonates (reproduced with permission from S. Licht, H. Wu, Z. Zhang and H. Ayub, *Chem. Comm.*, 2011, **47,** 3081.)

1) Molten Air mechanism of action:

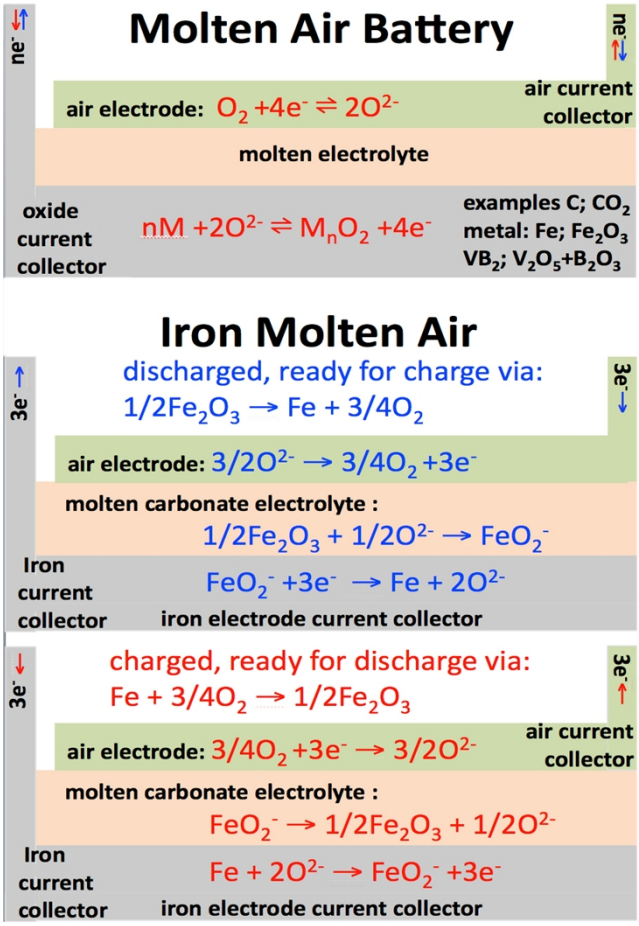

Scheme 1-ESI Top: The molten air battery. Bottom: The iron molten air battery; illustration of the charge/discharge in molten carbonate. The charging or discharging process is indicated by red or blue text & arrows.

Recently rechargeable molten air batteries are introduced, and several examples of their battery chemistry demonstrated.[1] Unlike prior rechargeable molten batteries, the battery is not burdened by the weight of the active chargeable cathode material. The rechargeable molten air electrode instead uses oxygen directly from the air to yield high battery capacity. This electrode was shown to be compatible with several high capacity multiple electron redox couples. Three demonstrated new batteries chemistries are the metal (iron), carbon and VB_2 molten air batteries.

Other classes of molten electrolyte batteries had been investigated. A molten sulfur battery has been widely studied, particularly for electric car and grid applications.[13-16] During discharge, the battery uses sulfur and sodium (or potassium) for the respective cathode and anode storage materials, and these high temperature molten components are kept from chemically reacting by a solid electrolyte beta alumina separator. Both the molten[13-16] and room temperature class of sulfur cathode batteries,[17,18] are limited by the maximum intrinsic capacity of the 2 electron per sulfur (2 Faraday/ 32g sulfur), while the new Molten Air batteries are independent of this mass limitation.

Internal combustion engines driven by gasoline (petrol) typically reach temperatures of 700°C, higher temperatures occur within the manifold and at the catalytic converter. Internal combustion engines driven by diesel typically reach temperatures of 600°C or higher. Here we study Molten Air Batteries that can operate at temperatures $\leq$ 600°C and demonstrate this aspect of EV (electric vehicle) compatibility. Molten Air electrochemical energy storage with is represented in Scheme 1-ESI in both generalized form and with a specific example (the Iron Molten Air battery). As illustrated for the Iron Molten Air example, during charging, iron oxide is converted to iron metal via a three-electron reduction, and O_2 is released to the air. During discharge iron metal is converted back to iron oxide.

To date, Molten Air Battery chemistries were demonstrated using anodes discharing (i) the 11e⁻ oxidation of VB_2 (with a vanadate/borate electrolyte), (ii) the 4e⁻ Carbon or (iii) the 3e⁻ Iron (each with carbonate electrolyte). Each only at temperatures of 730°C or higher.[1] Lower temperature battery chemistries would greatly expedite their utility for electric vehicle applications. In this study we probe one example, Iron Molten Air, which includes a lower temperature battery chemistry.

Table 1. The charged intrinsic energy storage capacity of various molten air rechargeable batteries. Volumetric energy capacity, E_{vol}, is calculated from the number of electrons stored, n, the density d, the Faraday constant, F = 26.80 Ah mol^{-1}, the formula weight, FW, and E° in accord with Eqs. 1, 2 or 3 as $E_{vol} = ndE°F / FW$. The cell potential at unit activity, E°, is temperature dependent. For example, while constant over a wide temperature range at 1.0 V for the carbon anode, E° decreases for the iron anode from 1.2 to 0.9 V with temperature increase from 25°C to 850°C.[21] The theoretical storage capacity of air batteries is traditionally calculated based on the mass or volume of the reduced active anode material (such as zinc in a zinc air battery) as oxygen is freely available from the air. However, in practice the mass and volume of air battery systems increases with the uptake of oxygen during discharge, and the limiting capacities may be better represented by a form half way between the charged and discharged state. Hence, the final mass, volume and capacity of lithium air batteries need to include the oxygen to form the oxidized product, Li_2O. This effect is large for lithium air batteries as a mole of Li increases from 6.9g to a discharged mass of 14.9g ($1/2Li_2O$)), and relatively less for iron which increases from a molar mass of 55.8 g to a discharged mass of 79.8g ($1/2Fe_2O_3$). Table 1 calculates air battery capacities in the traditional manner, but we note that this provides only an upper limit to the capacity of such air batteries when fully charged.

Anode	Formula Weight kg mol^{-1}	e⁻s stored	Charge Capacity Ah/kg	d, kg l^{-1}	E°, V vs O_2	Energy Capacity gravimetric Wh kg^{-1}	Energy Capacity volumetric Wh liter^{-1}
Iron	0.05585	3e⁻	1,440	7.2	1.0	1,400	10,000
Carbon	0.01201	4e⁻	8,930	2.1	1.0	8,900	19,000
VB_2	0.07256	11e⁻	4,060	5.1	1.3	5,300	27,000

The right column of Table 1 compares the intrinsic capacity of these batteries, which is *one to two orders of magnitude greater*

than that of the volumetric energy capacity of conventional Li ion batteries. Lithium (metal) air also has a lower volumetric energy capacity. While Li's gravimetric charge capacity (3860 Ah/kg) is similar to that of VB_2 (4,060 Ah/kg), it has a lower 6,200 Wh liter^{-1} volumetric capacity due to a low density (0.534 kg liter^{-1}), and single, rather than multiple, electron charge transfer.

Accelerated testing of the VB_2 or Carbon molten air batteries presents fundamental challenges avoided by the Iron Molten Air Battery. In each case of the three cases the storage capacity is high, and it is a challenge to limit the storage reactant availability. Constraining the high intrinsic capacity of the VB_2 molten air cell requires thin cross sections of electrolyte to limit the high capacity, which is an interesting, but longer-term challenge. In the VB_2 Molten Air Battery the reactant is comprised from (and not added to) a molten vanadate and borate electrolyte and are charged to form the VB_2 storage product:

VB_2 molten air battery, 11e$^-$: $VB_2 + 11/4O_2 \rightleftharpoons B_2O_3 + V_2O_5$ (1)

The Carbon Molten Air Battery provides the greatest challenge to constrain its high capacity for accelerated testing purposes. The battery reactant is formed via the molten carbonate electrolyte from air borne CO_2. In the presence of CO_2, the electrolyte need not be consumed during discharge. This cell uses only atmospheric oxygen and atmospheric CO_2 during cycling (while one of the mobile ions during charge cycling is electrolytic carbonate, carbonate involved in the individual electrode reactions balances out in the global reaction). The mass of the electroactive storage materials are "free (or zero)" in the context of the conventional battery energy density calculation, in that they are available in the air and are not carried within, or stored externally, to the battery. This is evident by comparing the mechanism when the cell is charged and discharged in either the absence, or presence of CO_2. While many carbonates are available, for clarity, a single carbonate (lithium carbonate) is used in the mechanism below:

global 4e- Carbon Molten Air charge/discharge:

$$CO_2 \rightleftharpoons C + O_2 \quad (2)$$

CO_2 dissolution into electrolyte: $Li_2O + CO_2 \rightarrow Li_2CO_3$ (2a)

4e$^-$ battery cycling $Li_2CO_3 \rightleftharpoons C + Li_2O + O_2$ (2b)

In a manner analogous to the VB_2 molten air cell, in the absence of atmospheric CO_2 the Carbon Molten Air Battery capacity is limited by the electrolyte. Constraining the high intrinsic capacity of this carbonate molten air cell also requires thin cross sections of electrolyte to limit the high capacity, which is an interesting, but longer-term challenge. Without external CO_2 the Carbon Molten Air Battery capacity is limited by the carbonate electrolyte, such as lithium carbonate:

global 4e$^-$, carbonate limited, Carbon Molten Air charge/discharge:

$$Li_2CO_3 \rightleftharpoons C + Li_2O + O_2 \quad (3)$$

Unlike the challenges to study of the Carbon or VB_2 Molten Air Batteries by constraining their intrinsic capacity, the capacity of an Iron Molten Air Battery can be controlled by limiting the iron added to the cell. As one example of the recently introduced molten air battery class, we probe here the rechargeable nature of the Iron Molten Air Battery. Of the three examples of molten air batteries provided to date,[1] the Iron Molten Air example provides the easiest route to purposely restrict the battery capacity by limiting the iron reactant (by allowing free flow entry of air, but by constraining the concentration of dissolved iron salt in the electrolyte). We will probe sustainable current densities and discharge efficacy, and then demonstrate a pathway to lower temperature rechargeable Iron Molten Air batteries. The Iron Molten Air battery is represented by Eq. 4, and is facilitated by the Eq. 4a dissolution of Fe_2O_3 with Li_2O to form lithiated iron oxide, $LiFeO_2$,[5] followed by quasi-reversible charge/discharge of $LiFeO_2$ to iron, Eq 4b.

global 3e$^-$ Iron Molten Air charge/discharge:

$$1/2Fe_2O_3 \rightleftharpoons Fe + 3/4O_2 \quad (4)$$

molten dissolution: $1/2Fe_2O_3 + 1/2Li_2O \rightleftharpoons LiFeO_2$ (4a)

3e$^-$ cycling: $LiFeO_2 \rightleftharpoons Fe + 1/2Li_2O + 3/4O_2$ (4b)

As elaborated on in section 3 (Temperature effects on thermodynamics & voltage of iron in molten carbonates), lithiated ferric iron oxides are extremely soluble in lithium ion containing carbonates. For example, 14 m (m is molal = mols solute / kg solvent) Fe(III) can dissolve in Li_2CO_3.[5,7] For the Iron Molten Air Battery, even higher amounts of iron are available for storage by maintaining a buffer of solid Fe_2O_3. This becomes soluble when existing dissolved Fe(III) is reduced to iron metal during the battery charging. This provides unusually high battery storage capacities.

The intrinsic volumetric energy capacity of the Iron Molten Air Battery, E_{vol}, is calculated from, n, the 3 electrons stored in the reduction to iron, the iron density d=7.2 kg/ l^{-1}, the Faraday constant, F = 26.80 Ah mol^{-1}, the formula weight, FW=0.05585 kg mol^{-1}. As Q=nF / FW this to gives a charge capacity of 1,440 Ah kg^{-1}, and based on an observed open circuit potential of E°=1.2V, yields a gravimetric energy capacity of E_{grav} = QE° and a volumetric energy capacity of E_{vol} = dQE this gives a gravimetric energy capacity of 1,728 Wh kg^{-1}, and a volumetric capacity of 12,0000 Wh liter^{-1}. This is *one to two orders of magnitude greater* than the volumetric energy capacity of conventional Li ion batteries. The theoretical storage capacity of air batteries is traditionally calculated based on the mass or volume of the reduced active anode material (such as zinc in a zinc air battery) as oxygen is freely available from the air. However, in practice the mass and volume of air battery systems increases with the uptake of oxygen during discharge, and the limiting capacities may be better represented by a form half way between the charged and discharged state. Hence for example if we were to consider a lithium air battery, the final mass, volume and capacity of these batteries need to include the oxygen to form the oxidized product, Li_2O. This effect is large for lithium air batteries as a mole of Li increases from 6.9g to a discharged mass of 14.9g (1/2Li_2O)), and relatively less for iron which increases from a molar mass of 55.8 g to a discharged mass of 79.8g (1/2Fe_2O_3).

We observe that Li_2CO_3, which melts at 723°C, and lower melting carbonate eutectics are effective electrolytes. Simple steel foil cathodes and nickel foil anodes are effective for either iron oxide[14-18] or carbon dioxide splitting. In addition to nickel, the nickel alloy inconel can simultaneously act as the air electrode and cell container. These anodes and cathodes can sustain high splitting (mA to A per cm^{-2}) current densities at low overpotential in molten lithium carbonate. These electrolyses for either iron oxide[1,6,7,12,19] or carbon dioxide splitting[1,20-21] can also represent charging of a molten air at high current density and low potential.

2) Electrochemistry of iron in molten carbonates

In the electrolyte Fe(III) originates from dissolved ferric oxides, such as $LiFeO_2$ or $LiFe_5O_8$. The potential for the three electron reduction to iron varies in accord with the general Nerstian expression, for a concentration [Fe(III)], at activity coefficient, α:

$$E_{Fe(III/0)} = E°_{Fe(III/0)} + (RT/nF) \log(\alpha_{Fe(III)} [Fe(III)])^{1/3} \quad (S\text{-}4)$$

Fig. 1-ESI summarizes the thermochemical calculated potentials constraining iron production in molten carbonate. The decrease in electrolysis potential with increasing Fe(III) varies as $6.6x10^{-5}$VxT(electrolysis,K)/K (=RT/nF), which is accentuated by high temperature. Hence, from the thermodynamic perspective with a simple assumption of unit activity coefficient, a 14 molal iron concentration will decrease the 1223 K (950°C) electrolysis potential by a further 0.1 V. Higher activity coefficient, $\alpha_{Fe(III)} > 1$, would further decrease the thermodynamic potential to produce iron. In various concentrated electrolytes, activity coefficients, α, an order of magnitude, or more, higher than unity have been observed.

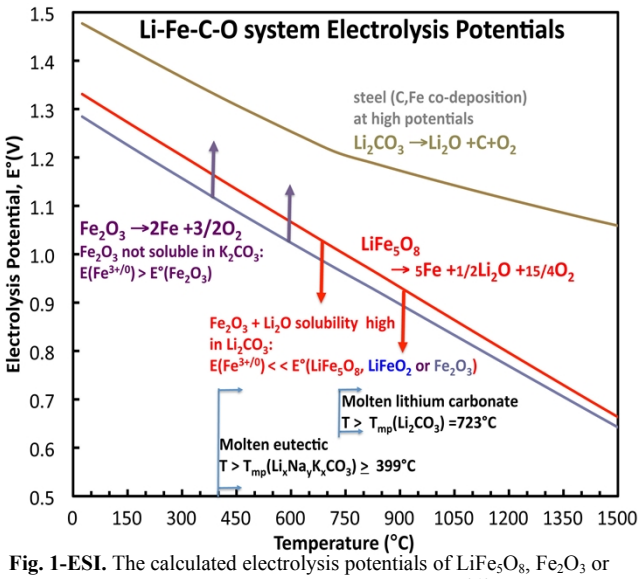

Fig. 1-ESI. The calculated electrolysis potentials of $LiFe_5O_8$, Fe_2O_3 or Li_2CO_3 at unit activity from the thermochemical data.[9,10] Vertical arrows indicate Nernstian shifts at high or low Fe(III) solubilities. $\Delta G(T)$ are better described for $LiFe_5O_8$ compared to $LiFeO_2$; hence as indicated, $LiFe_5O_8$ calculations are included in the figure.

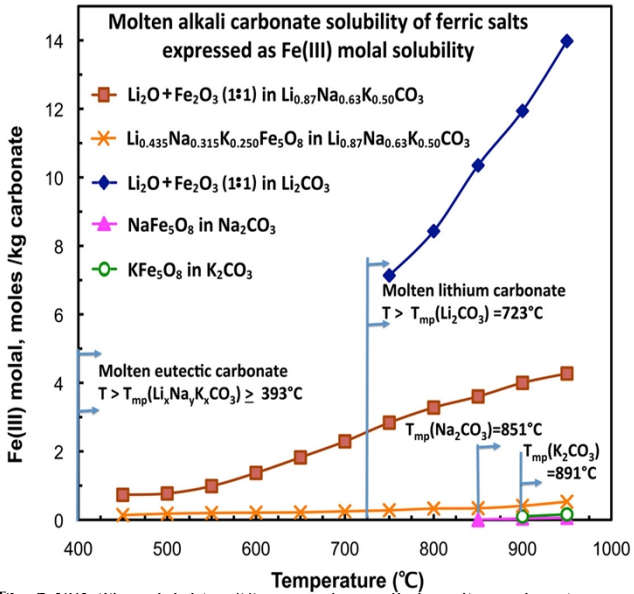

Fig. 2-ESI. The solubility of ferric oxides in alkali molten carbonates.

Fig. 2-ESI, presents the wide solubility variation of Fe(III) in different alkali carbonates, Fe(III) is not soluble up to over 950°C in either molten Na_2CO_3 or K_2CO_3. The addition of a 1:1 equivalent ratio of Li_2O to Fe_2O_3 dissolves in Li_2CO_3 without the reactive formation of CO_2, as $LiFeO_2$. As seen, the solubility of this Fe(III) dissolved as $LiFeO_2$ (by the addition of $Li_2O + Fe_2O_3$) in the alkali carbonate eutectic, $Li_{0.87}Na_{0.63}K_{0.50}CO_3$, is high, and at 750°C approaches half the solubility of the high solubility in the pure lithium carbonate electrolyte. The eutectic has the distinction of a greater molten temperature range (extending several hundred degrees lower than the pure lithium system). Solubility of this lithiated ferric oxide in the $Li_xNa_yK_zCO_3$ mixes provides an alternative molten media for the iron molten air battery, which compared to pure lithium carbonate, has the disadvantage of lower conductivity, but the advantage of even greater availability, and a wider operating temperature domain.

Also evident in Fig. 2-ESI, while the solubility of the lithiated ferric oxide in the eutectic carbonate is high, the solubility of a mixed alkali penta-iron octa-oxide salt, synthesized as $Li_{0.435}Na_{0.315}K_{0.250}Fe_5O_8$, is low, reaching a maximum concentration of only 0.5 m Fe(III) at 950°C.

The measured electrolysis (charging) potential is presented in Figure 3-ESI for dissolved Fe(III) in molten lithium carbonate. As seen, the charging potential increases with i) decreasing temperature, (ii) decreasing concentration of dissolved Fe(III), and (iii) an increasing charge density. As expected at low (< 0.A cm^{-2}) charge density, the measured potentials in the figure are considerably less than the room temperature 1.3V thermodynamic potential required to convert Fe_2O_3 to iron and oxygen.

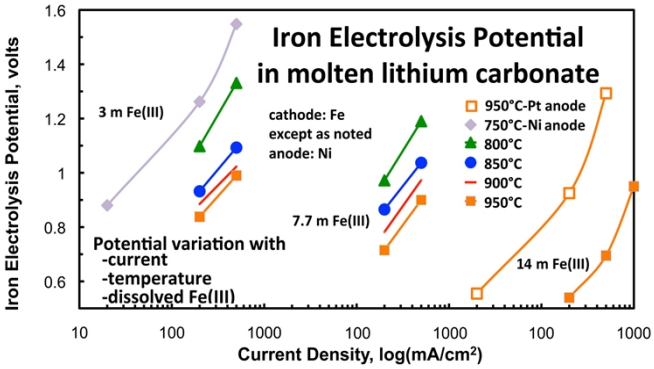

Fig. 3-ESI. The measured electrolysis potentials of iron, for dissolved Fe(III) in molten Li_2CO_3, as a function of the electrolyte temperature and the concentration of dissolved iron. The cell electrolysis potentials are measured as a function of constant current, with current density constrained by the cathode surface area.

Additional references

13. B. Dunn, H. Kamath and J. M. Tarascon, J. M. Electrical Energy Storage for the Grid: A Battery of Choices. *Science,* 2011, **334**, 9280935.
14. J. B. Goodenough, Rechargeable batteries: challenges old and new, *J. Solid State Electrochem.,* 2012, **16**, 2019.
15. K. B. Hueso, M. Armand and T. Rojo, *Energy Environ. Sci.,* 2013, **6**, 734.
16. X. Lu, B. W. Kirby, G. Li, J. Y. Kim, J. P. Lemmon, V. L. Sprenkle and Z. Yang, *Energy Environ. Sci.,* 2013, **6**, 299.
17. D. Peramunage and S Licht, *Science*, 1993, **261**, 1029.
18. R. Demir-Cakan, M. Morcerette, Gangulbabu, A. Gueguen, R. Dedryvere and J. Tarascon, *Energy Environ. Sci.,* 2013, **6**, 176.
19. S. Licht and H. Wu, *J. Phys. Chem. C.*, 2011, **115**, 25138.
20. S. Licht and B. Wang, *J. Phys. Chem. Lett.,* 2010, **1**, 2363.
21. S. Licht, *Advanced Materials,* 2011, **27,** 2993.

Renewable highest capacity VB_2/air energy storage†

Stuart Licht,*[ab] Huiming Wu,[b] Xingwen Yu[b] and Yufei Wang[b]

Received (in Cambridge, UK) 9th May 2008, Accepted 2nd June 2008
First published as an Advance Article on the web 17th June 2008
DOI: 10.1039/b807929c

The first renewable electrochemical energy system which stores more energy than gasoline is presented, and with an order of magnitude higher capacity than lithium-ion batteries, VB_2 opens a pathway towards electric vehicles with a viable driving range.

A fundamental impediment to electric, *versus* gasoline, vehicles has been the lower volumetric capacity of electrochemical energy, which had limited the vehicle driving range, and which is directly related to the practical capacity of gasoline (2.7 kWh L^{-1}) compared to state of the art Li-ion (0.5 kWh L^{-1}). The volumetric energies are compared in Fig. 1, and include Zn/air cells which exhibit among the highest volumetric energy of commercialized electrochemical systems. Zn/air was demonstrated with an alkaline carbon air(O_2) anode in 1932.[1] Zinc, FW (Formula Weight) = 0.0654 kg mol^{-1}, d (density) = 7.1 kg L^{-1}, releases 2 F (Faraday) mol^{-1} stored charged, for a capacity Q(zinc) = 5.82 kAh L^{-1}. With a thermodynamic 1.6 V potential, the intrinsic capacity of the cell is 9.4 kWh L^{-1}. Commercial zinc air cells using external air and internal zinc have been referred to as both battery and fuel cell, and with a practical cell voltage of 1.3 V, currently have a practical 1.75 kWh L^{-1} cell capacity, inclusive of the carbon anode and all other cell components.[2]

Borides can exhibit even higher charge and energy capacities than zinc. VB_2 undergoes an oxidation of both the tetravalent transition metal ion, V ($+4 \rightarrow +5$), and each of the two boron's $2 \times$ B ($-2 \rightarrow +3$), for an exceptional $11e^-$ per molecule oxidation. Hence, VB_2 has an intrinsic gravimetric capacity of 4060 Ah kg^{-1}, five-fold higher than that of the Zn anode electrode, and with d = 5.10 kg L^{-1}, has a volumetric capacity of $Q(VB_2)$ = 20.7 kAh L^{-1}.

In this study, we have considered a variety of borides including TaB, TaB_2, MgB_2, CrB_2, CoB_2, Ni_2B and LaB_6 as alternative active anode materials for alkaline electrochemical storage cells. The two tantalum boride salts exhibit alkaline anodic charge storage capacity, although less than that of the zinc anode. The other borides did not exhibit significant primary discharge behavior due to their high solubility in alkaline solution or their excessive reactivity with an alkaline electrolyte. In 2004, Yang and co-workers reported the discharge of VB_2, but also documented the extended domain in which VB_2 is susceptible to corrosion in alkali media.[3] In 2007, we reported that a zirconia overlayer on VB_2 prevents this corrosion[4] and provides an effective alkaline anode counterpart to a super-iron cathode.[5–7]

Stabilization studies of the boride anode, as used in the super-iron boride battery,[4] can be advanced towards a boride air fuel cell. In this study we present a renewable boride air fuel cell, which utilizes a conventional air cathode and a zirconia stabilized vanadium boride anode. The standard redox potential we observe for the $11e^-$ VB_2 alkaline anodic redox reaction is:

$$VB_2 + 11OH^- \rightarrow \tfrac{1}{2}V_2O_5 + B_2O_3 + \tfrac{11}{2}H_2O + 11e^- \qquad (1)$$
$$E = 0.9 \text{ V } \textit{vs.} \text{ SHE}$$

The eqn (1) oxidation products are generalized as B_2O_3 and V_2O_5, which are the respective anhydride salts of boric acid (H_3BO_3 with p$K_{1,2,3}$ = 9.1, 12.7 and 13.8) and vanadaic acid (H_3VO_4 with p$K_{1,2,3}$ = 3.8, 7.8 and 13.0). In solution, the products will vary with hydroxide concentration and depth of discharge, including hydrogen and metal cation containing species, such as in either a KOH or NaOH electrolyte: $K_xH_zBO_3^{3-x-z}$ or $Na_xH_zBO_3^{3-x-z}$ (where x ranges from 0 to 3, and z from 0 to $3 - x$), as well as polymeric species, such as related to the boric condensation reaction forming borax species: $Na_yB_4O_7^{2-y}$, $K_yB_4O_7^{2-y}$, and analogous vanadium species, *etc.*

The VB_2 cell reaction for an $11e^-$ boride air fuel cell couples eqn (1) with reduction at an oxygen/air cathode, eqn (2), to yield

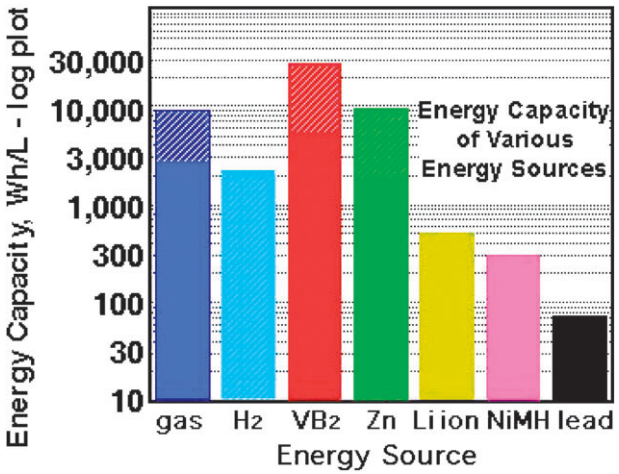

Fig. 1 Energy capacity comparison of gasoline (petrol), hydrogen and electrochemical energy sources. The intrinsic energy of gasoline yields a maximum practical efficiency of 30% due to Carnot and friction losses. Air fuel cells do not have this Carnot inefficiency, and have practical capacities instead constrained by overpotential losses, and the requisite volume of the air anode and all other cell components. Volumetric capacity of liquid H_2 is constrained by its density of 0.0708 kg L^{-1}. Shaded superimposed on solid, colors, compare intrinsic and practical capacities.

[a] *Division of Chemistry, National Science Foundation, 4201 Wilson Blvd, Arlington, VA 22230, USA. E-mail: slicht@NSF.gov; Fax: +1 703 292 9037; Tel: +1 703 292 9037*
[b] *Department of Chemistry, University of Massachusetts, 100 Morrissey Blvd, Boston, MA 02125, USA. Fax: +1 617 287 6030; Tel: +1 617 287 6130*

† Electronic supplementary information (ESI) available: Optimization studies. See DOI: 10.1039/b807929c

the vanadium boride air cell discharge:

$$O_2 + 2H_2O + 4e^- \rightarrow 4OH^- \; E = +0.4 \text{ V } \textit{vs.} \text{ SHE} \quad (2)$$

$$VB_2 + \tfrac{11}{4}O_2 \rightarrow B_2O_3 + \tfrac{1}{2}V_2O_5 \; E_{cell} = 1.3 \text{ V} \quad (3)$$

Consistent with eqn (3), the VB_2/air cell has an intrinsic volumetric energy capacity of (1.3 V) × (20.7 kAh L^{-1}) = 27 kWh L^{-1} (= 97 MJ L^{-1} = 5.3 kWh kg^{-1}). As shown in Fig. 1, the vanadium boride air cell intrinsic volumetric energy capacity is substantially greater than that of gasoline, hydrogen, or a zinc air fuel cell, and is an order of magnitude greater than that of all rechargeable batteries, including Li ion, metal hydride or lead acid. Practical, compared to intrinsic, energy electrochemical capacity is limited by the delivered energy and system mass, incorporates all voltage losses, air cathode size, and all other cell components. For example, the practical energy of a small, portable commercial zinc air cell exceeds 18% of the intrinsic energy capacity,[2] and can be higher in an optimized, large fuel cell configuration. The relative practical capacity of the VB_2/air cell can be estimated as similar to that of the well studied Zn/air system (electrolytes and cathodes are similar). Based on this analog, the practical vanadium boride fuel has a lower limit of 18% of its intrinsic 27 kWh L^{-1}, for an estimated vanadium boride air practical storage capacity of 5 kWh L^{-1}.

As recently as 1997 it was noted that basic physical chemical properties of VB_2 are scarce.[8] Boride corrosion is not only a chemical loss of the electrochemical capacity, but evolved hydrogen is flammable, and the evolved gas can swell or even crack a cell. Zirconia is highly stable in aqueous alkaline media, maintaining effective charge transfer during boride anodic discharge. A zirconia coating may be readily applied to a boride salt, for example in this study *via* $ZrCl_4$ (AR grade, ACROS®), which is dissolved in ether (Fisher®). The VB_2 (insoluble in ether) is stirred as a suspension in this solution for 30 min, followed by vertex suction, then vacuum removal of the remaining solvent, and air drying overnight. The Zr^{2+} equivalents, in the coating solution, control the weight percent and thickness of the coating. As is evident in the inset of Fig. 2, ZrO_2 is readily distinguished from VB_2 *via* its IR absorbance. With this, the extent of ZrO_2 coating on VB_2 is observed using ATR/FTIR (Attenuated Total Reflectance Fourier Transform Infrared) as we have detailed in references 4, 7 and 9. The effects of corrosion are accelerated at higher temperature, and this domain is used to accelerate long-term anode stability studies. Stored at 45 °C for one week, and then discharged at room temperature, the uncoated VB_2 alkaline anode loses 10% of its original charge capacity, but with a 1% ZrO_2 coating retains 100% of that capacity. Similarly, stored at 70 °C for 1 week, the uncoated VB_2 retains only 65% of its original capacity, but with a 1% ZrO_2 coating retains 85% of that charge capacity (thicker coatings further improve stability[9]).

A series of impediments to effective discharge of the vanadium boride fuel cell have been overcome. The supplementary information contains extended, systematic optimization studies.† As summarized by the optimization studies in Fig. 3, the vanadium boride air cell can be efficiently discharged. This figure compares the discharge of these cells under a variety of anode, capacity and load conditions. As is evident in the black curve, the substantial capacity of VB_2 is experimentally realized (89% of the theoretical capacity; this $11e^-$ efficiency is the measured integrated charge to

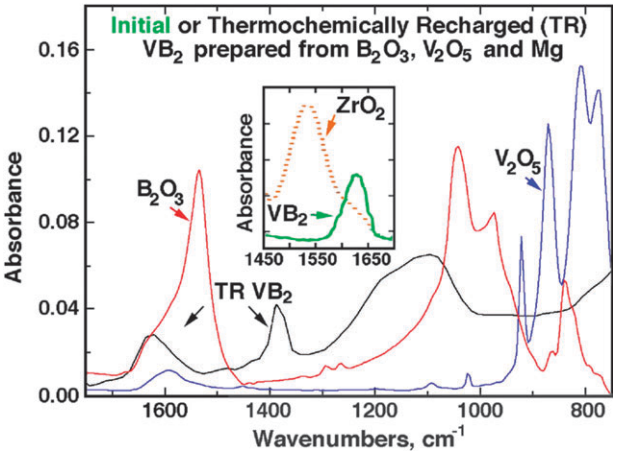

Fig. 2 Inset: IR spectra of pure VB_2 or ZrO_2. Main figure: The IR of thermochemically recharged (TR) VB_2, prepared as described in the text, is comparable to that of the initial VB_2, and is distinct from that of the vanadate and borate fuel cell discharge products.

a discharge cutoff of 0.6 V, compared to the 4260 mAh g^{-1} intrinsic capacity of VB_2). As seen in the blue and green curves, anode additives, of up to 10 wt% solid NaF or NaOH, can improve both coulombic efficiency and potential, although at higher weight fractions these salts are deleterious to the observed discharge. The observed VB_2 $11e^-$ anode efficiency consistently improves with either an increase in added anodic graphite or in the discharge load, or a decrease in the anode thickness (example: efficiency is 30, 76, or 89%, respectively for otherwise equivalent 50, 15 or 5 mAh capacity cells). Hence, the VB_2/air cell is limited by the rate of charge transfer or resistance to the anodic current collector. As seen in the violet and bronze curves, this limitation is overcome by decreasing the VB_2 particle size. Ground (ball milled) VB_2 exhibits higher anodic discharge efficiencies. When separated by particle size, the smallest particle (<28 μm) VB_2 anode discharges to the highest (82%) coulombic efficiency and exhibits a higher initial discharge potential.

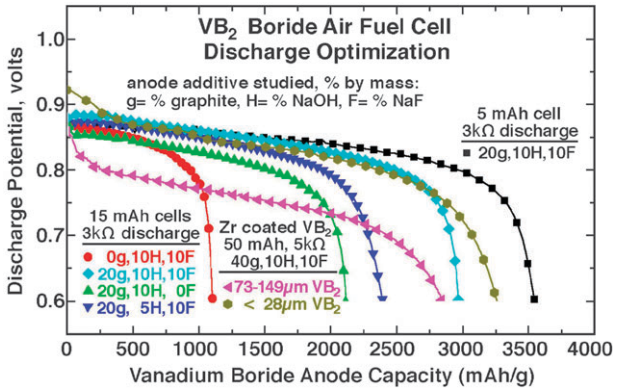

Fig. 3 Optimization of the vanadium boride air cell anode capacity as a function of the indicated anode composition, capacity, and discharge load conditions. The measured integrated discharge current is normalized by VB_2 mass in a 1 cm^2 cell, consisting of a zinc air coin (McMaster 1015K13 IEC PR44), with saturated NaOH electrolyte, in which the zinc anode is replaced with boride. The higher capacity (50 mAh) cells are prepared with ball milled VB_2 (of either <25 μm, or 73–149 μm particle size as indicated on the figure) which has been coated with an overlayer of (1%) zirconia. The lower capacity (5 and 15 mAh) cells are prepared with VB_2 which has been neither milled nor coated.

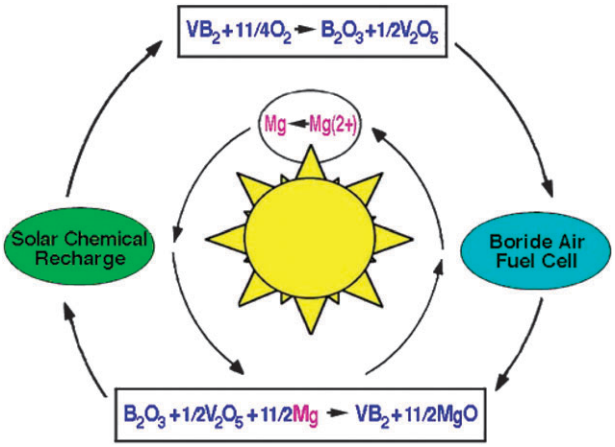

Scheme 1 Discharge and solar chemical charge of the VB_2 air cell.

Over a 1 kΩ discharge load, a thick (150 mAh) anode comprised of <28 μm VB_2 with 30% graphite sustains a higher coulombic efficiency and a higher discharge potential than a thinner (50 mAh) anode comprised of unsorted, ground, VB_2 containing 40% graphite. The uncoated smaller particle VB_2 tends to be less stable in the alkaline electrolyte, which is prevented by the zirconia coating. It is evident that smaller particles will be useful for efficient, high rate discharge, if thicker VB_2 anodes are needed. It is expected that a further decrease in particle size, by two orders of magnitude or more (to the submicron domain), can be available through conventional high energy ball milling techniques, and also as alternative VB_2 synthesis strategies are developed.

The boride air fuel cell exhibits electrochemical irreversibility. We present a viable alternative pathway to regenerate the vanadium boride fuel cell, as represented in Scheme 1. In the first (irreversible) electrochemical discharge cycle, the alkaline vanadium boride electrode approaches the intrinsic VB_2 anode capacity. However upon subsequent electrochemical charge/discharge cycles, and independent of charging conditions, we observe the anode yields less than 10% of this intrinsic capacity after the first discharge/charge cycle.

Chemical regeneration of VB_2 is explored here through Mg reduction of the fuel cell discharge products. Solar thermal and photothermal processes can regenerate metals from their salts.[10] An efficient solar powered laser has been reported to generate Mg from its oxide and/or chloride salts, including:[11,12]

$$MgCl_2 + h\nu(\text{solar}) \rightarrow Mg(l) + Cl_2(g) \qquad (4)$$

Traditionally, vanadium boride was prepared by high-temperature reaction of boron with metals,[8,13] or *via* carbothermal reduction of V_2O_5 and B_2O_3 above 1600 °C,[14] or as a self-propagating high-temperature reaction between VCl_3 and MgB_2.[15] To probe the feasibility of the chemical regeneration of the fuel cell discharge products in eqn (3), we explore here a Mg-assisted formation of vanadium boride, as expressed by eqn (5). Magnesium is sufficiently energetic to regenerate vanadium boride from its discharge products. Following chemical regeneration of VB_2, MgO is removed by dissolution in HCl (to $MgCl_2$ in H_2O):

$$B_2O_3 + \tfrac{1}{2}V_2O_5 + \tfrac{11}{2}Mg \rightarrow VB_2 + \tfrac{11}{2}MgO \qquad (5)$$

Specifically, V_2O_5, B_2O_3 and Mg were added in accord with eqn (5) and ball milled for 24 h in an argon atmosphere at room temperature. Impurities (including the MgO product and residual reactants) were removed by leaching the as-milled powder with a 10% HCl solution for 1 h. The solution was decanted after leaching, the solid product was washed with deionized water, and finally vacuum dried. The secondary product, $MgCl_2$, is available for solar recharge to magnesium, as in eqn (4). The primary product, chemically recharged VB_2, sustains an electrochemical discharge at the expected potential, and exhibits characteristic IR absorptions matching commercial VB_2 (including at 1097, 1391, 1630, and 3401 cm^{-1}), and as seen in Fig. 2 is distinct from the discharge products and synthesis reactants.

The zirconium stabilized boride air cell is based on the unusual 11 electron per molecule storage capacity of VB_2, and is the first electrochemical system with a practical energy storage capacity comparable to that of gasoline. This high storage capacity is liberated at a uniform, single discharge potential plateau when the VB_2 is protected by a zirconia overlayer which prevents corrosion of the boride anode, stabilizes alkaline charge transfer chemistry, and is applied to form a functional, highest energy capacity VB_2/air cell. A stepwise optimization of the vanadium boride/air fuel cell is presented, and then a viable solar photochemical pathway is shown, which regenerates the vanadium boride to recharge the fuel cell. The large volumetric capacity of the fuel cell, and the pathway for a renewable (solar) energy recharge, are positive attributes of this novel vanadium boride air cell. Systems aspects will continue to be analyzed and optimized. Liquid (higher temperature, solar driven), rather than solid, Mg, should facilitate the recharge formation of VB_2 in eqn (5). The discharge studies indicate that sub micron particle size VB_2, as available following high energy ball milling, can further improve anodic kinetics and coulombic efficiency.

This material was based on work supported in part by the United States National Science Foundation, with research support to Stuart Licht while working at the Foundation.

Notes and references

1. K. Kinoshita, *Electrochemical Oxygen Technology*, Wiley-Interscience, Hoboken, NJ, USA, 1992, pp. 259–260.
2. *Zinc Air Technical Bulletin*, Duracell, 2005, http://www.duracell.com/oem/primary/Zinc/zinc_air_tech.asp.
3. H. X. Yang, Y. D. Wang, X. P. Ai and C. S. Cha, *Electrochem. Solid-State Lett.*, 2004, **7**, A212.
4. S. Licht, X. Yu and D. Qu, *Chem. Commun.*, 2007, 4341.
5. S. Licht, B. Wang and S. Ghosh, *Science*, 1999, **285**, 1039.
6. S. Licht and R. Tel-Vered, *Chem. Commun.*, 2004, 628.
7. S. Licht, X. Yu and D. Zheng, *Chem. Commun.*, 2006, 4341.
8. C. Bulfon, A. Leithe-Jasper, H. Sassik and P. Rogl, *J. Solid State Chem.*, 1997, **133**, 113.
9. S. Licht, X. Yu and Y. Wang, *J. Electrochem. Soc.*, 2008, **155**, A1.
10. S. Licht, *Chem. Commun.*, 2005, 4341.
11. T. Yabe, S. Uchida, K. Ikuta, K. Yoshida, C. Baasandash, M. Mohamed, Y. Sakurai, Y. Ogata, M. Tuji, Y. Mori, Y. Satoh, T. Ohkubo, M. Murahara and A. Ikesue, *Appl. Phys. Lett.*, 2006, **89**, 261107.
12. T. Yabe, T. Ohkubo, S. Uchida, K. Yoshida, M. Nakatsuka, T. Funatsu, A. Mabuti, A. Oyama, K. Nakagawa, T. Oishi, K. Daito, B. Behgol, Y. Nakayama, M. Yoshida, S. Motokoshi, Y. Sato and C. Baasandash, *Appl. Phys. Lett.*, 2007, **90**, 261120.
13. L. Y. Markovskii, *Poroshk. Metall.*, 1969, **77**, 13.
14. H. Blumenihal, *J. Am. Chem. Soc.*, 1952, **74**, 2942.
15. L. Rao, E. G. Gillan and R. B. Kaner, *J. Mater. Res.*, 1995, **10**, 353.

Electrochemical and Solid-State Letters, **15** (1) A12-A14 (2012)
1099-0062/2012/15(1)/A12/3/$28.00 © The Electrochemical Society

Nano-VB_2 Synthesis from Elemental Vanadium and Boron: Nano-VB_2 Anode/Air Batteries

Stuart Licht,[*,z] Chaminda Hettige,[*] Jason Lau,[**] Ulyana Cubeta,[**] Hongjun Wu,[*] Jessica Stuart,[**] and Baohui Wang[a]

Department of Chemistry, George Washington University, Washington, DC 20052, USA

A straightforward synthetic route to nano-VB_2 particles, via planetary ball milling of elemental vanadium and boride in a 1:2 equivalent ratio is presented. Variation of the mechanochemical synthesis milling speed and milling time is used to optimize this nano-VB_2 for use as a high capacity anode material with enhanced charge transfer and increase voltage. VB_2 releases, via electrochemical oxidation, an unusual 11 electrons per molecule at a favorable, highly level electrochemical potential. Coupled with an air cathode, this anode with volumetric and gravimetric capacity of 20.7 kAh/L and 4.1 kAh/kg, has energy density greater than that of gasoline.
 [DOI: 10.1149/2.018201esl]

Manuscript submitted August 31, 2011; revised manuscript received October 7, 2011. Published November 21, 2011.

Higher energy density batteries are needed for applications ranging from consumer electronics, industrial, medical, military applications, to hybrid and electric vehicles. The quest for a long, uninterrupted power supply has focused on lithium-ion batteries for a number of years, but recently an alternative material, vanadium diboride (VB_2) has been introduced as a potential high capacity anode, with a VB_2 air battery (utilizing an air-O_2 cathode) shown to have an order of magnitude higher capacity than lithium-ion batteries.[1] In an unusual multiple electron process, each VB_2 releases up to eleven electrons at a level discharge potential, which does not exhibit separate voltage plateaus. While electrochemically recharging this eleven electron anode is challenging,[2] the system has been demonstrated to be chemically rechargeable.[1] Using the VB_2 air battery has a theoretical discharge potential of 1.55 V, as calculated[3] from the thermodynamic free energy of the cell reactants and products:[4,5]

$$\text{Anode}: \quad VB_2 + 11OH^- \rightarrow {}^1/_2V_2O_5 + B_2O_3 + 11/2\,H_2O + 11e^- \qquad [1]$$

$$\text{Cathode}: \quad O_2 + 2H_2O + 4e^- \rightarrow 4OH^- \qquad [2]$$

$$\text{Cell}: \quad VB_2 + 11/4O_2 \rightarrow B_2O_3 + V_2O_5 \quad E_{cell} = 1.55\,V \qquad [3]$$

With a density of 5.10 kg/l, the 11 electron per molecule VB_2 oxidation reaction provides a theoretical intrinsic volumetric and gravimetric capacity of 20.7 kAh/l and 4.1 kAh/kg and an intrinsic volumetric energy density of 32 kWh/l, which is higher than that of gasoline (~10 kWh/l). Experimental discharge has yielded 3.7 kAh/kg to a 0.4 V discharge cutoff.[1] VB_2 corrodes at a slow rate in alkaline media, releasing hydrogen. However, we have demonstrated that a zirconia coating stabilizes VB_2, when in contact with alkaline electrolytes, to minimize this self discharge reaction for alkaline batteries containing a VB_2 anode.[6,7]

Traditionally, vanadium boride was prepared by high-temperature reaction of boron with metals,[8,9] or via carbothermal reduction of V_2O_5 and B_2O_3 above 1600°C.[10] There have been a variety of other synthesis methods proposed for the formation of vanadium diboride, including a self-propagating high temperature synthesis from the elemental forms of vanadium and boron,[11] a nanocrystalline synthesis of VB_2 from the 650°C solid state reaction VCl_4, $NaBH_4$ and Mg,[12] as well as a mechanochemical procedure that utilized VCl_3, LiH and $LiBH_4$.[13] With the latter synthesis, VB_2 impurities prevent effective anodic discharge, but were sufficient to demonstrate that the nano- VB_2 yields higher open circuit potentials compared to macroscopic (micron dimensioned, rather than nano-scale particles) VB_2.[3] We have shown that milling of macroscopic VB_2 in the presence of saturated fatty acids can lead to restructuring and the formation of VB_2 nanorods, which exhibit both the higher discharge potential, as well as the enhanced rates of charge transfer expected from the increased surface to volume ratio of the nano-materials.[3] Recently, a mechanochemical synthesis of vanadium monoboride (VB_x, exploring the range x = 0 to 1) was reported in which different ratios of elemental vanadium and boron were ball milled to form different borides of vanadium, with a demonstrated capacity up to 2.1kAh/kg (to 0.4V) .[14] The study characterized the disappearance of vanadium, as VB was formed.

We report here a synthesis of vanadium diboride mechanochemical process from elemental vanadium and boron, and it will be shown that the resultant nano-VB_2 exhibits higher anodic discharge potential and capacity compared to the monoboride. We have utilized a mixture of 1:2 equivalent ratio of the elements V:B for the synthesis of VB_2, while ratios of 1:1 and 1:0.5 have been studied for the purpose of comparison with previous work[14]. In the high temperature synthesis, it was previously shown that the combination of the elemental vanadium and boron in the ratio of 1:2 primarily formed VB_2,[8] which suggests that the mechanochemical reaction of the elements in a 1:2 ratio would primarily form VB_2.

For the synthesis procedure introduced here, elemental vanadium (99.5%, −325 Mesh, Alfa Aesar) and boron (98%, −325 Mesh, Alfa Aesar) were used to prepare VB_2. A set amount of 0.5g of vanadium was used for all synthesis, with the amount of boron varying depending on the molar ratio of the synthesis desired. Self-ignition of boron in air was prevented by confining the boron, or mixture, to an argon atmosphere, and the mixture placed into a 50 mL tungsten carbide ball milling jar (Retsch part number 01.462.0156) along with ten tungsten carbide bearings that had a diameter of 10mm. As previously discussed, the material is milled in a tungsten carbide vessel, as the hardness of VB_2 is greater than that of a conventional steel vessel.[3] The jar containing the bearings and vanadium and boron mixture was sealed in an argon atmosphere and transferred to a Retsch PM 100 ball milling machine. Initial results were obtained by milling the material at 600 RPM for 4 hours continuously. One set of experiments focused on varying the milling time at a fixed rotation speed (600 RPM) and another focused on varying rotation speed at a fixed milling time (4 hours). Upon completion of the ball milling program, the temperature of the jar was allowed to return to room temperature and the powdered material was collected in an argon atmosphere. The nano-VB_2 formed in ball milling was evaluated as an anode material in VB_2 air batteries as well as with x-ray powder diffraction analysis (XRD) and Transmission electron microscopy (TEM).

* Electrochemical Society Active Member.
** Electrochemical Society Student Member.
[a] Present address: College of Chemistry & Chemical Engineering, Northeast Petroleum University, Daqing, China.
[z] E-mail: slicht@gwu.edu

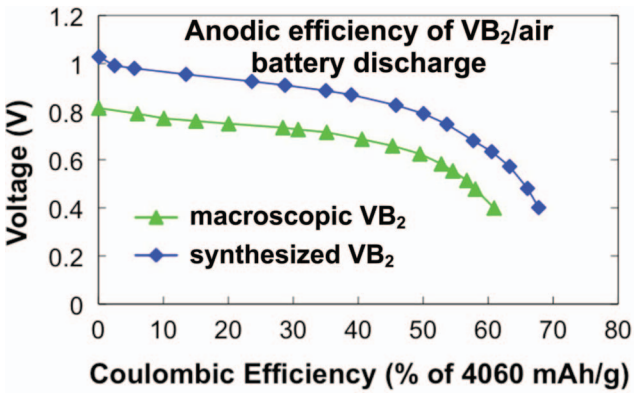

Figure 1. Discharge curves from VB_2-air cells. 10 mAh cells were discharged over 3000 Ω loads. Synthesized material was prepared by ball milling a mixture of V:B = 1:2 ratio in a Retsch PM 100 ball mill in Argon atmosphere for 4 hours at 600 RPM.

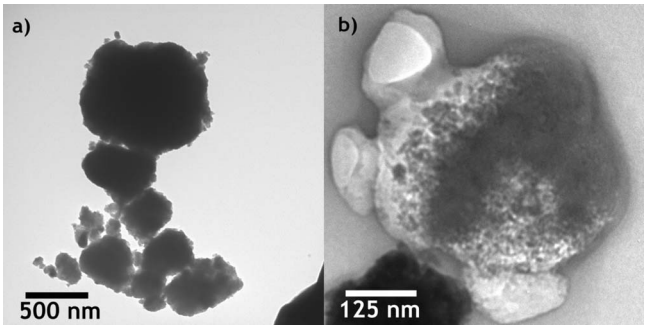

Figure 2. (a) A TEM image of Vanadium diboride prepared by milling elemental boron and vanadium in a 1:2 ratio for 20 minutes at 600RPM. (b) A TEM image of a sample of Vanadium Diboride prepared by milling elemental boron and vanadium in a 1:2 ratio for 4 hours at 600RPM.

Panasonic 675 Zinc Air batteries (Panasonic Corporation, Japan) with 1 cm^2 anode surface area were used to fabricate the cells. The anode from the Panasonic battery was replaced with a mixture of the synthesized VB_2 and 2 micron graphite powder in a ratio such that 20% of the total weight of the mixture was graphite. A solution mixture of 5M each KOH and NaOH was used as the electrolyte and the loading of the anode material for each cell was 10 mAh. VB_2 cells were discharged across a resistor loading of 3000 Ω and the battery discharge data was recorded using a DAQ module (National Instruments NI-USB-6211) and LabVIEW software. For the purpose of comparison of results, we have fabricated equivalent cells using macroscopic VB_2 purchased from American Elements, U.S.A with a purity of 99.999%.

VB_2 mechanochemically synthesized here from the elements, exhibits a higher discharge capacity than macroscopic commercial vanadium diboride as shown in Figure 1, and discharges to a majority of the intrinsic 4060 mAh/g capacity. The discharges of the synthesized material also exhibit a higher discharge voltage that is characteristic of nano-sized VB_2,[2] and is ∼0.2 V (25%) higher than reported for vanadium monoboride mechanochemically synthesized from the elements.[14] Note that the cells under 3000 ohm discharge load require ∼a day to discharge. At 1000 ohm discharge load (not shown) the coulombic efficiency is only modestly impacted, but the average discharge potential decreases by ∼0.05 V. As expected, an increase in the carbon fraction in the anode improves both efficiency and discharge potential. Under the same discharge conditions, pure boron provides no observable discharge, while pure vanadium discharges at a lower potential than the VB_2 product. Pure vanadium discharges at a level potential (starting at ∼0.6V and terminating at 0.4 V) to an experimental capacity of 2.1 kAh/kg, approaching the 2.6 kAh/kg theoretical intrinsic capacity for the 5 electron oxidation (of V(0 → +5) of vanadium (element weight = 50.94 g/mol).

Figure 2 presents TEM images of the milled mix of 1:2 elemental vanadium and boron measured with a JOEL JEM-1200 EX Transmission Electron Microscope. Prior to milling, the vanadium and boron particles consist of 325 mesh (up to 44 micron particles). After only 20 minutes of 600 RPM ball milling the vanadium boron mix consist of a heterogeneous distribution of submicron particles in the 100 to 400 nm range (Figure 2a), although agglomerates of larger particles are also evident. Extended milling, such as after a 4 hour mill under the same conditions (Figure 2b), does not significantly alter the particle size or distribution, but as will be indicated from both XRD and electrochemical evidence, provides time required for a more complete reaction to VB_2. The lack of crystalline character or shape evident in Figure 2b is also typical of this high capacity anode material, and subsequent XRD suggests that the majority phase present is VB_2. FTIR analysis, as conducted in accord with our prior experiments,[1,7,15] provides further evidence that the product of this mechanochemical stoichiometric reaction of elemental V and B is VB_2 and includes a prominent absorption at 1630 cm^{-1}. Further details of this analysis will be provided in an expanded study.

When the V: B ratio was changed to 1:1, it was previously suggested that VB is formed, and when the V: B ratio was changed to 1:0.5, excess, unreacted vanadium was observed.[14] With its lower discharge capacity the presence of VB (2.6 kAh/kg for a 6 electron oxidation), should cause a decrease in the anodic coulombic efficiency (coulombic efficiency is the measured percentage of the theoretical charge), and would remain low in presence of unreacted vanadium. This expected result is confirmed in the top portion of Figure 3 comparing discharge of cells containing a 1:0.5, 1:1 or 1:2 ratio of mixed, milled V: B. The new 1:2 (VB_2) material exhibits both higher potential and considerably higher discharge capacity than the 1:0.5 or 1:1 materials. The discharge potential of the 1:0.5 and 1:1 material is comparable to that previously observed, and while the absolute columbic efficiencies of these two materials are lower than previously observed, their relative capacities are comparable.[14] Note that the decreased anodic efficiency of the 1:1 or lower ratio materials, compared to the 1:2 material, does not rule out the possibility that for those lower ratio materials the majority product may have been vanadium diboride plus excess vanadium, rather than vanadium monoboride. The expected discharge plateau which would occur, for unreacted vanadium of ∼0.5 V was not observed in the top portion of Figure 3, but is observed at lower milling speed or at shorter milling time conditions in the middle and lower portions of the figure, and will be seen to correlate with the observation of unreacted vanadium via XRD in Figure 4.

In prior results of macroscopic VB_2 anodes, used in conjunction with a Fe(VI), rather than air, cathode, we have shown that systematic variation of preparation parameters can substantially improve VB_2 anode characteristics.[15] In order to optimize the mechanochemical process the synthesis mill time was varied between 10 minutes and 5 hours. The anodic discharge efficiency of these materials is compared in the middle portion of Figure 3, and improved for times longer than 20 minutes, with a peak efficiency was observed at ∼ 4 hours of mill time. Over milling (5 hours) led to decreased anodic efficiency. Studies of mill velocity variation provide evidence that better coulombic efficiencies were also linked to higher mill speeds. As shown in the lower portion of Figure 3, discharge efficiencies continually increased with increasing RPM. At 200 RPM the discharge efficiencies observed were lower than 40% and the highest efficiencies were noticed for 600 RPM. Limitations of the Retsch PM 100 did not allow us to study mixtures synthesized above 600 RPM.

The ball milling process requires sufficient thermal energy and impact conditions to impart the energy to VB_2 from the elemental metals. This idea is supported by the observation that using low energy conditions such as low RPM, formation of VB_2 led to lower columbic efficiencies in the cells. XRD data, shown in Figure 4, corroborate this fact as at increasing milling times the peak that is the predominant peak for VB_2, which is located at $2\theta = 45.8$, increases in size. Neither

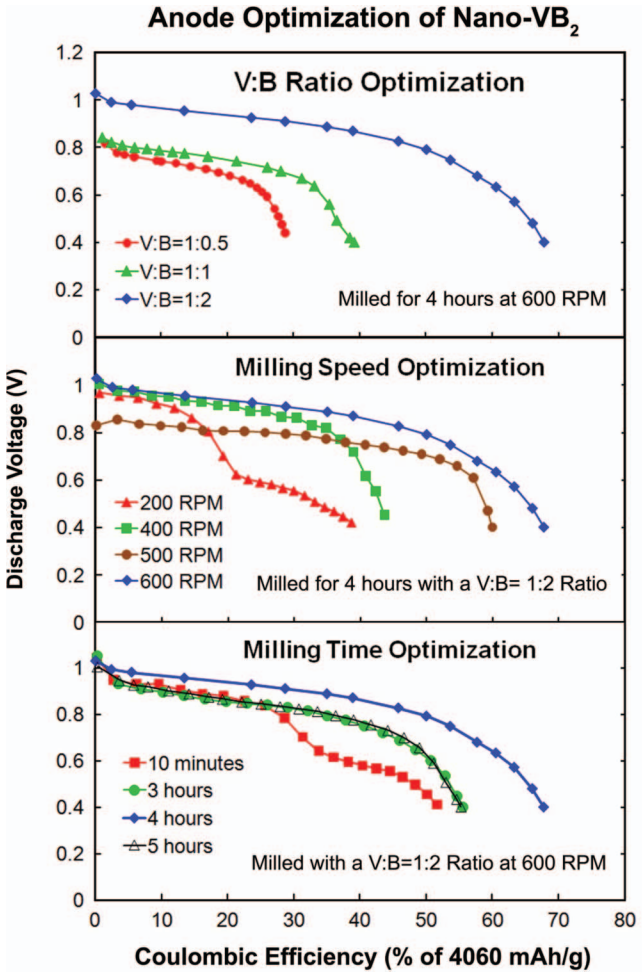

Figure 3. Discharge curves of cells made with Retsch PM 100 ball milled mixtures of elemental vanadium and born in an equivalent ratio of V:B = x:y. Cells of 10 mAh capacity were discharged over 3000 Ω loads. Top: Variation of V:B ratio. V:B = 1:2, V:B = 1:1 or V:B = 1:0.5. Mixtures were milled at 600 RPM for 5 hours in an argon atmosphere with a mill. Middle: Variation of mill time with V:B = 1:2 mixtures at fixed 600RPM. Bottom: Variation of mill velocity with V:B = 1:2 mixtures for a fixed 4 hours milling time.

elemental vanadium nor boron exhibit a significant XRD intensity at this value of 2θ. This increase in peak size follows the similar pattern of discharge efficiencies as a function of milling time. The observed XRD peaks of ball milled material are generally broad, which we attribute to an increase in reflections of smaller grains of varied shape and size dominated by short range order that occurs during the ball milling synthesis process. As seen in the figure, the XRD data from macroscopic and mechanochemical synthesized nano VB_2 match the peaks corresponding to the VB_2 standard library spectra, while incomplete reaction due to slow milling speed and short milling times leads to an XRD dominated by the elemental vanadium peak; the small, but evident, shoulder in the 600 RPM XRD at $2\theta = 42$ indicates that a potential vanadium impurity is present in the final mix.

The mechanochemical synthetic process of ball milling of elemental vanadium and boron is a straightforward method for synthesis of VB_2 and has been shown to produce a material that has a very high discharge efficiency. This efficiency is a result of the fact that this method does not involve other chemicals beyond the elemental metals

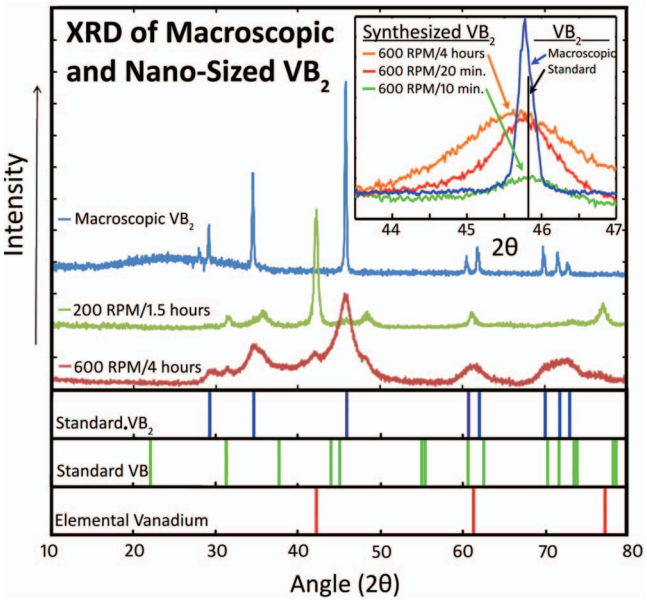

Figure 4. XRD data of various ball mill synthesized and macroscopic vanadium diboride. All synthesized materials started with a mixture of 1:2 V: B elemental ratio and are milled at 600 RPM. Commercial (macroscopic) vanadium diboride was purchased from American Elements. The vertical lines in the lower portion of the figure, as well as the line at 45.8° in the inset, corresponds to the Inorganic Crystal Structure Database standard for VB_2.

of vanadium and boron so that VB_2 of high purity can be obtained via optimization of reaction conditions at high yields. The macroscopic VB_2 consists of 1 to 5 micron particles.[3] VB_2 synthesized by the alternative elemental route are tenfold smaller. With a particle as sphere simple assumption, a tenfold radius decrease, increases the relative surface area and decreases the overpotential, by decreasing the surface current density and enhancing contact to the anode current collector.

Acknowledgments

This work was funded by in part NSF DMR award 1006568.

References

1. S. Licht, H. Wu, X. Yu, and Y. Wang, *Chem. Commun. (Cambridge)*, **2008**, 3527 (2008).
2. X. Yu and S. Licht, *Electrochmica Acta*, **52**, 8138 (2007).
3. S. Licht, S. Ghosh, and B. Y. Wang, *Electrochem. Solid St. Lett.*, **14**, A83 (2011).
4. B. R. Emrich, Literature Survey on Synthesis, Properties and Applications of Selected Boride Compounds, *Air Force Systems Command,* **37**, 441 (1962).
5. NIST-Chemweb Thermochemical Data, data interactively available at: http://webbook.nist.gov/chemistry/form-ser.html.
6. S. Licht, X. Yu, and D. Zheng, *Chem. Commun. (Cambridge)*, **2006**, 4341 (2006).
7. S. Licht, X. Yu, and D. Qu, *Chem. Commun. (Cambridge)*, **2007**, 2753 (2007).
8. C. Bulfon, A. Leithe-Jasper, H. Sassik, and P. Rogl, *J. Solid State Chem.*, **133**, 113 (1997).
9. L. Y. Markovskii, *Poroshk. Metall.*, **77**, 13 (1969).
10. H. Blumenithal, *J. Am. Chem. Soc.*, **74**, 2942 (1952).
11. C. L. Yeh and H. J. Wang, *J. Alloy. Compd.*, **509**, 3257 (2011).
12. L. Shi, Y. Gu, L. Chen, Z. Yang, J. Ma, and Y. Qian, *Mater. Lett.*, **58**, 2890 (2004).
13. J. W. Kim, J.-H. Shim, J.-P. Ahn, Y. W. Cho, J.-H. Kim, and K. H. Oh, *Mater. Lett.*, **62**, 2461 (2008).
14. Y. Wang, X. Y. Guang, Y. L. Cao, X. P. Ai, and H. X. Yang, *J. Alloy. Compd.*, **501**, L12 (2010).
15. S. Licht, X. Yu, Y. Wang, and H. Wu, *J. Electrochem. Soc.*, **155**, A297 (2008).

Journal of Power Sources 239 (2013) 244–252

Contents lists available at SciVerse ScienceDirect

Journal of Power Sources

journal homepage: www.elsevier.com/locate/jpowsour

Evaluation of properties and performance of nanoscopic materials in vanadium diboride/air batteries

Christopher Rhodes [a,*], Jessica Stuart [b], Ruben Lopez [a], Xuguang Li [a], Mahesh Waje [a], Matthew Mullings [a], Jason Lau [b], Stuart Licht [b,**]

[a] Lynntech, 2501 Earl Rudder Fwy S, College Station, TX 77845, USA
[b] Department of Chemistry, The George Washington University, 2121 Eye Street NW, Washington, DC 20052, USA

HIGHLIGHTS

- VB_2/air batteries containing nanoscopic VB_2 anodes have significantly higher voltages and capacities than cells containing macroscopic VB_2 anodes.
- The nanoscale thickness of the zirconia layer on the VB_2 nanomaterial may facilitate rapid discharge through the coating.
- The higher performance of the VB_2 nanoscopic material may result from the combination of the nanomaterial's higher surface area and higher electronic conductivity.
- Electrochemical impedance analysis showed that charge transfer resistance increases from charge to discharge for cells containing both macroscopic and nanoscopic VB_2.

ARTICLE INFO

Article history:
Received 22 October 2012
Received in revised form
13 March 2013
Accepted 15 March 2013
Available online 28 March 2013

Keywords:
Vanadium diboride/air batteries
Nanomaterials
Electrochemical properties
High energy density power sources

ABSTRACT

The unique eleven electron per molecule electrochemical oxidation of vanadium diboride (VB_2) combined with an air cathode provides VB_2/air batteries that have extremely high theoretical energy densities. Testing of VB_2/air cells at various discharge times showed that VB_2/air batteries containing nanoscopic VB_2 anodes provide higher capacities and voltages than cells containing macroscopic VB_2 anodes. The structure and properties of nanoscopic VB_2 were compared with those of macroscopic VB_2 to provide further insight into the enhanced electrochemical performance of the nanomaterial. From nitrogen physisorption and electrical conductivity measurements, we determined that the higher performance of the nanoscopic VB_2 material compared with the macroscopic VB_2 material may result from the combination of the nanomaterial's higher surface area and higher electronic conductivity. The thickness of the zirconia layer applied to prevent corrosion in alkaline electrolyte was shown by transmission electron microscopy and energy dispersive X-ray spectroscopy to be ca. 3–40 nm which may allow rapid discharge through the coating. Electrochemical impedance spectroscopy results showed that for cells containing both the macroscopic and the nanoscopic materials the resistance associated with charge transfer increases during the discharge process. The results provide a basis for further development of high energy and power density VB_2/air batteries.

1. Introduction

For over a century, metallic zinc has been predominantly used as an anode material in almost all aqueous primary systems due to zinc metal's high two-electron oxidation capacity. The zinc–carbon battery, known as the Leclanché cell, was first introduced in the 19th century, as a low-cost solution for early energy storage needs. The zinc cell, which produced approximately 65 Wh kg^{-1}, was ideal only for low rate discharges. Precipitation of side reaction products creates an increase in cell resistance and contributes to cell leakage, resulting in instability [1,2]. Until the development of the zinc/alkaline/manganese dioxide battery and the zinc/air cell, there was little improvement in primary batteries. The alkaline Zn/MnO_2 cell has since dominated primary electrochemical storage, offering 145 Wh kg^{-1}. Although more expensive than the zinc–carbon battery, the alkaline cell improved performance by increasing energy densities and power capabilities. The zinc/air battery, similar to a fuel cell, offered further improvements exhibiting the highest

* Corresponding author. Tel.: +1 979 764 2313; fax: +1 979 764 2343.
** Corresponding author. Tel.: +1 703 726 8225; fax: +1 202 994 5873.
E-mail addresses: christopher.rhodes@lynntech.com, cprhodes@suddenlink.net (C. Rhodes), slicht@gwu.edu (S. Licht).

0378-7753/$ – see front matter © 2013 Elsevier B.V. All rights reserved.
http://dx.doi.org/10.1016/j.jpowsour.2013.03.071

energy density of many primary systems. The zinc/air cell is limited in power output by the air cathode. For a wide range of electronic devices, it would be useful to achieve even higher energy densities than that of the zinc/air battery [3]. Most metal/air batteries to date, including the zinc/air cell, have been unsuccessful in reaching the high energy densities possible by multi-electron oxidations, due to material passivation or chemical instabilities [4].

To provide high energy density cells, in recent years there has been an immense effort to successfully develop a high capacity anode through multi-electron charge storage processes [5]. Vanadium diboride (VB_2) undergoes an extraordinary multiple electron oxidation process, which to its completion involves an 11 electron per molecule oxidation, including oxidation of the tetravalent transition metal ion, V($+4 \rightarrow +5$), and each of the two boron's $2 \times B(-2 \rightarrow +3)$ [6]. VB_2 has an intrinsic gravimetric capacity of 4060 Ah kg^{-1} which is five-fold higher than that of the Zn anode electrode (820 Ah kg^{-1}). The intrinsic volumetric anodic capacity of the VB_2 anode (20.7 kAh L^{-1}) is ten-fold higher than that of the lithium anode (2.06 kAh L^{-1}).

The VB_2 anode can be coupled with available air to provide extremely high energy density VB_2/air batteries [6]. The anode half cell, cathode half cell, and full cell reactions based on generalized discharge products [7] are as follows:

$$\text{Anode: } VB_2 + 11OH^- \rightarrow 1/2V_2O_5 + B_2O_3 + 11/2H_2O + 11e^- \quad (1)$$

$$\text{Cathode: } O_2 + 2H_2O + 4e^- \rightarrow 4OH^- \quad (2)$$

$$\text{Cell: } 2VB_2 + 11/2O_2 \rightarrow 2B_2O_3 + V_2O_5 \quad E_{cell} = 1.55\ V \quad (3)$$

The VB_2/air battery has a theoretical discharge potential of 1.55 V, as calculated from the thermodynamic free energy of the cell reactants and products [7]. The VB_2/air cell's intrinsic volumetric energy density of 32 kWh L^{-1} is substantially greater than that of gasoline (<10 kWh L^{-1}) [6,8]. VB_2/air batteries have an intrinsic specific energy of 5300 kWh kg^{-1}, which is four times higher than the theoretical specific energy of zinc/air batteries (1353 kWh kg^{-1}).

The VB_2/air couple uses an alkaline electrolyte of KOH/NaOH, and oxygen from the air reacts at the cathode similar to that of the zinc/air cell [1]. While concentrated aqueous hydroxide electrolytes ranging from 8 M to saturated in NaOH or KOH yield a similar electrochemical discharge in the VB_2/air cell, we have recently observed that a mixture of NaOH and KOH yields marginally improved high rate performance [7] compared to the earlier pure NaOH electrolyte [6,8] and have continued with this mixed electrolyte in this study. The VB_2/air cell shows an experimental open circuit potential of ~1.3 V, and under load, the cell can release its capacity over a flat, remarkably singular discharge potential plateau. Previous work by Licht et al. has shown that although VB_2 is susceptible to corrosion in alkali media, a zirconia overlayer on VB_2 prevents this corrosion [6]. Prior work demonstrated that thin zirconia coatings on macroscopic alkaline battery materials do not impede charge transfer at rates tested, but provide significant stability benefits [6,9–11]. Therefore, coating the anode material with a zirconia layer has been developed as a strategy to stabilize VB_2 against corrosion in the alkaline electrolyte.

Recently, Licht et al. have developed nanoscopic VB_2 materials prepared using mechanochemical processes and showed that at slow discharge times of between eight and ten hours cells containing nanoscopic VB_2 exhibited higher voltages and discharge capacities compared with cells containing macroscopic VB_2 [7]. Operating at slow discharge times is useful for many applications such as portable electronics and hearing aids. However, for many applications operating at rapid discharge times is needed for full discharge, partial discharge or high power pulses. Achieving cells that provide high performance at high discharge rates requires material properties and an electrode structure designed for high power operation.

Preliminary results from previous works established by Licht et al. suggest that zirconia-coated nanoscopic VB_2 will outperform the uncoated and macroscopic materials [5–7]. Based on the improved performance of the nanoscopic VB_2 at slow discharge times we postulated that at high discharge rates nanoscopic VB_2 would provide improved performance compared with macroscopic VB_2.

In this study, we explored the properties and performance of nanoscopic VB_2 materials and compared the results obtained with macroscopic VB_2 materials. Electrochemical testing was performed to determine the performance of nanoscopic VB_2 at rapid discharge times. Material properties were investigated using microscopy, electrical measurements, nitrogen physisorption, and electrochemical impedance spectroscopy to determine the reason for the improved performance of cells containing the nanomaterials. The specific material properties of the nanoscopic VB_2 have not been previously studied, and a greater understanding of the VB_2/air system provides the ability to further improve the performance of this interesting multi-electron charge storage material [6].

2. Experimental

2.1. Vanadium diboride synthesis

Nanoscopic VB_2 was synthesized mechanochemically using vanadium powder (Alfa Aesar) and boron powder (Alfa Aesar) based on results previously published by Licht et al. [7]. In a controlled argon atmosphere glovebox system (Vacuum Atmospheres, Nexus-II), 0.500 g of vanadium and 0.212 g of boron power were measured and transferred into a tungsten carbide milling chamber along with ten tungsten carbide balls, ten millimeters in diameter. The milling vessel was sealed, removed from the glovebox, and placed into a Retsch PM 100 planetary ball mill set to 600 rpm and allowed to run for four hours. After the vanadium diboride cooled to room temperature, the material was then collected in the glovebox into a round bottom flask, and the mass was measured. A zirconium oxide layer was formed by adding 3.5% by weight (or as noted in the text) zirconium chloride (Acros Organics), following the procedure outlined by Licht et al. with the exception of adding ten milliliters diethyl ether to the round bottom flask; the 3.5 wt% $ZrCl_4$ addition forms a 1.9 wt% ZrO_2 overlayer [9]. After one hour of mixing on a stir plate, the ether was evaporated using a rotary evaporator and collected. For comparison, macroscopic VB_2 was obtained from American Elements and was coated in a similar manner as described above.

2.2. Electrochemical testing

Panasonic 675 Zinc/Air batteries (Panasonic Corporation, Japan) were used for cell fabrication. The Zn anode of the Panasonic cells was removed by opening the existing cell and removing the anode active material. The separator and cathode were used as received for the VB_2/air battery as further described in Supplemental data. The VB_2 anode was fabricated by mixing 30 wt% carbon black (Timcal Super-C65) with 70 wt% VB_2 (as synthesized coated nanoscopic material or macroscopic material) and spread on the cap with isopropyl alcohol. The electrode area was approximately 0.57 cm^2. For all cells, the mass loading was 1.2 ± 0.1 mg, with the exception of the nanoscopic cells discharged at 3000 Ω, which had an average mass loading of 0.8 mg. The electrolyte, 27 μL of a mixture of 4 M KOH and 4 M NaOH, was applied to the separator. Excess electrolyte was removed using a cotton swab prior to closing each cell. The cell was then closed with the cap in reverse so that

the anodic material was in contact with the electrolyte. Once the fabrication process had been completed, cells were placed on a holder and discharged at constant loads of 3000 Ω, 1000 Ω, 600 Ω, and 200 Ω using an Arbin Instruments battery tester controlled by MITS Pro software. The discharge of each cell contained an initial rest step of 10 min during which the cells were allowed to equilibrate. At the end of the equilibration step, the open circuit potential was recorded. The equilibrated cells were then discharged under a constant load. Coulombic efficiency was calculated as the percentage of the measured capacity compared to the theoretical anode eleven electron discharge capacity of 4060 Ah kg^{-1}.

The average theoretical cell capacity was 4.5 mAh based on the measured amount of VB_2 and the theoretical specific capacity of VB_2. The average experimentally determined capacity was 2.5 mAh using the mass of VB_2 and the measured capacities. VB_2/air cells with theoretical capacities of between 5 mAh and 50 mAh have been previously reported by the authors [6–8]. The lower end of these capacities was selected for initial testing of the rate capabilities to allow measurement of the properties of VB_2 within relatively thin electrode films ($\sim$26 μm-thick). The information obtained provides a basis for designing thicker electrodes which could be used for cells with practical capacities required for various devices.

2.3. Microscopy and energy dispersive X-ray analysis

Transmission electron microscopic (TEM) measurements were performed using a FEI Tecnai G2 F20 transmission electron microscope, equipped with Schottky-type field emission gun, X-twin objective lenses, an energy dispersive X-ray spectrometer (EDS), and a scanning TEM (STEM) unit with high-angle annular dark-field (HAADF) detector operating at 200 kV. Samples were prepared by sonication of the VB_2 material in ethanol for 10 min and dropwise addition of the sample onto a carbon-coated 400 mesh Cu grid followed by solvent evaporation in air.

2.4. Electrical conductivity measurements

A two-electrode powder conductivity measurement apparatus, fabricated as per the design developed by Holmberg and Yan [12], was used for the measurement of the electrical conductivity of the VB_2 materials. Powder samples were loaded in small cylinders (φ = 0.159 cm) which were contacted by two electrodes (gold-plated stainless steel rods) on either side. The powders were loaded and measurements were taken in an inert atmosphere glovebox in order to eliminate potential effects of atmospheric exposure. The powder was compressed to a torque of 2.26 N-m by tightening the fixture screws, corresponding to a pressure of 189–283 MPa on the powder samples. The length of sample within the cylinders was between 0.4 and 0.6 cm. The resistance of the powder sample was then measured with an Agilent milliohmmeter 4338B (1 kHz). Data was also obtained using potentiostatic two electrode electrochemical impedance spectroscopy measurements (Princeton Applied Research, VersaStat) to validate the results obtained using the milliohmmeter. As a reference, the conductivity of Vulcan XC-72 carbon was obtained and compared to reported values. The electrical conductivity, σ, expressed in the unit S cm^{-1} was obtained from the experimentally determined resistance, the area, and the measured length using the equation:

$$\sigma = \frac{l}{RA} \tag{4}$$

where l is the compressed length of the sample in cm, R is the measured resistance in Ω, and A is the cross-sectional area of the electrodes.

2.5. Nitrogen physisorption measurements

Nitrogen physisorption measurements were obtained using a Micromeritics Tristar 3000 surface area porosity analyzer. Samples were prepared and loaded within an inert atmosphere glovebox. Initial weights were taken of sample material before degassing for cross-reference. Samples were degassed at two stages. The samples were taken from ambient temperature to 30 °C using a 10 °C min^{-1} ramp rate and held at 30 °C for 10 min. The second stage involved heating at 10 °C min^{-1} to either 50 °C or 100 °C followed by hold a temperature of either 50 °C or 100 °C for 4 h. Samples were then reweighed, recorded and analyzed.

2.6. Electrochemical impedance spectroscopy (EIS)

Two-point probe electrochemical impedance spectroscopy (EIS) measurements were obtained for the VB_2/air cells using a Princeton Applied Research (PAR) VersaStat MC potentiostat operated with VersaStudio software. An applied root mean square amplitude of 50 mV was used over the frequency range of 1.0 MHz–0.1 Hz, and data was taken at open circuit potential in either the charged or discharged state. The experimental impedance data was fit using ZSimpWin software (version 3.21, Princeton Applied Research) with an equivalent circuit described in the text.

3. Results and discussion

3.1. Electrochemical analysis

Electrochemical testing was performed to determine the performance of VB_2/air cells containing either 1.9 wt% ZrO_2-coated macro-VB_2 or 1.9 wt% ZrO_2-coated nano-VB_2 material at different discharge times ranging from 13 h (3000 Ω) to less than 1 h (200 Ω). Data obtained for relatively slow discharge times of 8–13 h (3000 Ω) and 4 h (1000 Ω) are shown in Fig. 1. The results obtained for multiple cells provide evidence for reproducibility of the cell performance. Relatively small differences in the voltages and capacities observed for repeated cells may result from small mass differences, as well as from using cell configuration that did not result in uniform pressure applied to each cell.

From the data presented in Fig. 1, it is evident that at relatively low discharge times of between 4 and 13 h the nanoscopic VB_2 anode cells show significantly higher discharge voltages and greater discharge capacities compared with the macroscopic VB_2 anode cells. A relatively flat, discharge voltage is also evident during the discharge at low rates (specifically at 3000 Ω), occurring without voltage steps to a columbic efficiency of over 70%. This is indicative of a nearly complete oxidative charge transfer of the full VB_2 capacity of eleven electrons.

Shown in Fig. 2 are the discharge curves obtained for faster discharge times of 2 h (600 Ω) to less than 1 h (200 Ω). As evidenced by the data in Fig. 2, at higher discharge rates, the nanoscopic material also exhibits significantly higher voltages compared to the macroscopic material, similar to the results obtained at lower discharge rates. Interestingly, although the voltages are significantly higher, the capacities of the nanoscopic and macroscopic VB_2 are similar at higher discharge times. In addition, as expected the capacities for the cells at higher rates (Fig. 2) were lower than those at lower rates (Fig. 1). A number of factors including surface area and the coating may affect the reaction and influence the high rate capacities, as discussed further below.

The discharge times, voltages, specific capacities, and specific energies for the macroscopic and nanoscopic VB_2 materials at different loads are compared in Table 1. The data shows the significantly higher voltages and specific energies (anode mass

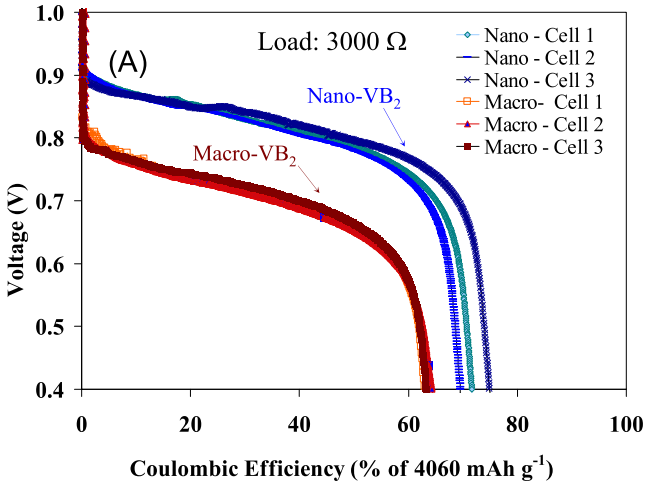

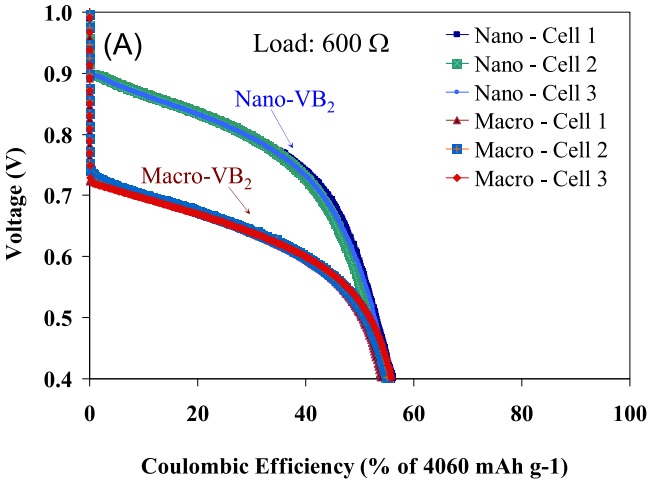

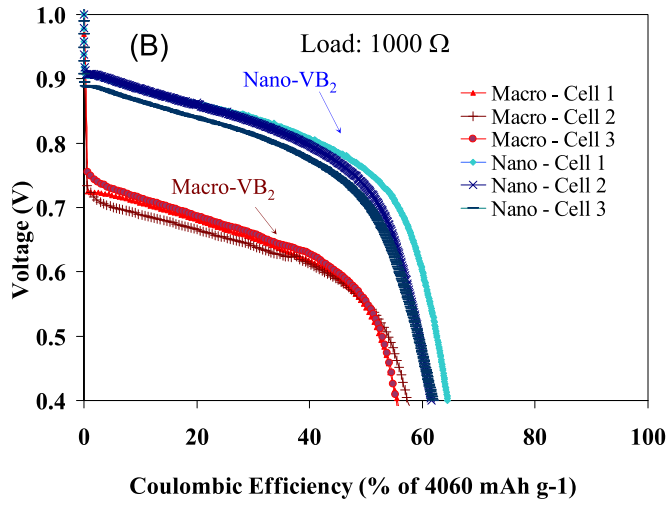

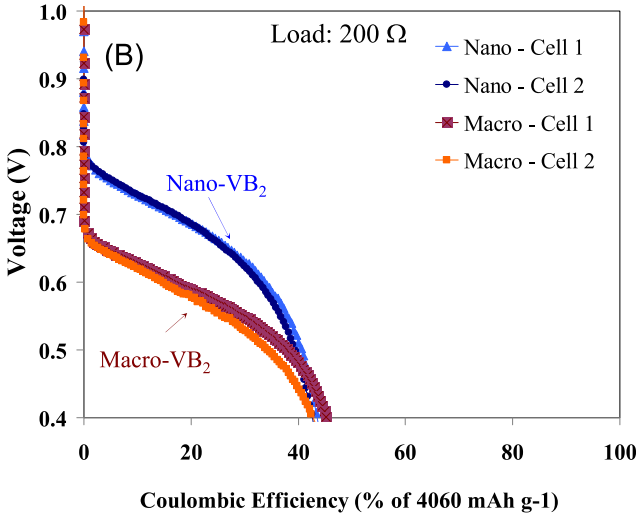

Fig. 1. Comparison of macroscopic vs. nanoscopic 1.9% ZrO_2-coated VB_2 anodes. (A) Discharge profile comparison of nanoscopic to macroscopic VB_2 for VB_2/air cells with a capacity of 5 mAh at a constant load of 3000 Ω. (B) Discharge profile comparison of nanoscopic to macroscopic VB_2 for VB_2/air cells with a capacity of 5 mAh at a constant load of 1000 Ω.

Fig. 2. Comparison of macroscopic vs. nanoscopic 1.9% ZrO_2-coated VB_2 anodes. (A) Discharge profile comparison of nanoscopic to macroscopic VB_2 for VB_2/air cells with a capacity of 5 mAh at a constant load of 600 Ω. (B) Discharge profile comparison of nanoscopic to macroscopic VB_2 for VB_2/air cells with a capacity of 5 mAh at a constant load of 200 Ω.

only) of the nanoscopic compared with the macroscopic material. The comparison of the ratios of the specific energies of the macro-VB_2 and nano-VB_2 shows that at lower discharge rates, the nano-VB_2 exhibits a higher degree of improvement in specific energy compared with the ratio observed at higher rates.

3.2. Microscopy analysis

A coating that protects the VB_2 is critical to maintaining the structure and chemical integrity of the anode material within the highly alkaline environment. The uncoated VB_2 is unstable in the alkaline environment and corrosion results in evolved hydrogen from the decomposition reaction and loss of the electrochemical capacity [6]. Zirconia is highly stable in aqueous alkaline media and maintains effective charge transfer during boride anodic discharge, preventing vanadium boride decomposition. Previous work demonstrated that for uncoated macroscopic material VB_2, stored at 45 °C for one week in contact with the electrolyte, and then discharged at room temperature loses 10% of its charge capacity, however with a 1% zirconia coating retains 100% of that capacity [6].

The morphology and thickness of the coating play an important role in the stability and electrochemical performance of the VB_2 anode and may influence performance at high discharge rates. Since the nature of the coating on the VB_2 had not been previously characterized, analysis was performed to determine the thickness and morphology of the zirconia coating on the nano-VB_2 material. For the base VB_2 material, previous work established that the uncoated nanoscopic material prepared using the mechanochemical process (high energy ball milling) results in a distribution of submicron particles in the 100–400 nm range with agglomerates of larger particles also evident [7].

To characterize the zirconia coating on the base nano-VB_2 material, transmission electron microscopic (TEM) measurements and energy dispersive X-ray spectra (EDS) were obtained. Based on the limitations of the instrument to obtain high quality images on micron-scale particles, TEM images were obtained only for the nanoscopic-coated VB_2 rather than the macroscopic-coated VB_2 since the later is composed of large micron-scale particles.

A representative TEM image of the nanoscopic VB_2 coated with 1.9 wt% ZrO_2 layer is shown in Fig. 3A. The VB_2 base material can be clearly observed in the darker region with the ZrO_2 coating layer in

Table 1
Comparison of the electrochemical performance of zirconia-coated macroscopic VB_2 and zirconia-coated nanoscopic VB_2 at various loads from 3000 Ω to 200 Ω. Values were obtained from averages of multiple cells. The specific capacity utilized the mass of the active VB_2, and the specific energy included the experimental cell voltage and the mass of the anode material only.

Load (Ω)	Material	Discharge time (h)	Voltage (V)	Specific capacity (mAh g^{-1})	% of theoretical capacity (4060 mAh g^{-1})	Specific energy (Wh kg^{-1}) (anode material)	Ratio of specific energy (nanoscopic/macroscopic)
3000	Macroscopic VB_2	13.67	0.68	2600	63	1800	1.3
	Nanoscopic VB_2	8.49	0.79	2700	72	2300	
1000	Macroscopic VB_2	3.57	0.64	2300	56	1400	1.4
	Nanoscopic VB_2	4.32	0.73	2500	63	1900	
600	Macroscopic VB_2	2.09	0.64	2200	55	1300	1.2
	Nanoscopic VB_2	2.39	0.75	2300	56	1600	
200	Macroscopic VB_2	0.71	0.60	1600	40	690	1.1
	Nanoscopic VB_2	0.61	0.66	1600	40	730	

the lighter region. The primary VB_2 particle size is in the 10–100 nm range. The thickness of the zirconia coating layer varies from ca. 3 to 40 nm. The representative EDS spectrum of nanoscopic VB_2 particles with ZrO_2 coating layer is shown in Fig. 3B. The presence of V and Zr was determined by EDS analysis of the area shown within the inset TEM image of Fig. 3B. The EDS data supports that the coating layer contains Zr.

Fig. 4A shows the representative TEM image of nanoscopic VB_2 coated with a thicker ZrO_2 layer (10 wt% $ZrCl_4$). For this sample, a higher amount of $ZrCl_4$ precursor was used to obtain a higher degree of coating. For the sample imaged, the primary VB_2 particle size is slightly larger, and the VB_2 base material and the ZrO_2 coating layer are not as distinguishable as the 3.5 wt% $ZrCl_4$ sample. The EDS spectrum of nanoscopic VB_2 particles with ZrO_2 coating layer (10 wt% $ZrCl_4$) is shown in Fig. 4B. The presence of V and Zr was determined by means of EDS. However, for this region probed the Zr content was lower since the image may have probed a significant portion of the base VB_2 in addition to the coating. As evident in Figs. 3 and 4, the zirconia coating appears to coat the entire VB_2 particles, and the coating thickness varies over the material. Interestingly, the coating is not just for discrete particles, but also results in a coating over aggregates.

3.3. Nitrogen physisorption analysis

Nitrogen physisorption measurements were obtained to determine the effect of the zirconia coating on the surface area, pore volume, and the pore size and compare the macroscopic and nanoscopic VB_2 materials. The results presented in Table 2 show that the coating affected the surface area of both the macroscopic and nanoscopic materials. For both materials, the application of the zirconia coating lowered the Brunauer, Emmett and Teller (BET) surface area compared to the uncoated materials. The results also show that the uncoated nanoscopic material prepared using high energy ball milling has a significantly larger surface area (2.84 $m^2\ g^{-1}$) compared to that of the uncoated macroscopic material (0.089 $m^2\ g^{-1}$). Similarly, the surface area of the coated nanoscopic material (0.854 $m^2\ g^{-1}$) was approximately two orders of magnitude higher compared with the surface area of the macroscopic material (0.0089 $m^2\ g^{-1}$). The data also shows that the application of the zirconia coating does reduce the surface area, as expected. For the macroscopic material, the coating decreases the surface area by an order of magnitude, while for the nanoscopic material the coating decreases the surface area by a factor of about three. For the nanomaterial, further analysis was performed to determine the effect of the coating on cumulative pore volume and pore width. Both the cumulative pore volume and average pore width decrease upon application of the coating to the base nano-VB_2. It may be significant that the cumulative surface area and cumulative pore volume between 1.7 nm and 300 nm are relatively small for the coated nano-VB_2 as well as for the macro-VB_2. Within the cumulative pore volume measurement, both mesopores (>2–50 nm) and the lower end of macropores (50 nm–500 μm) are included. In particular, high degrees of mesoporosity contribute to electrolyte access at electrochemically accessible timescales [13]. The small cumulative pore volume within the meso- and macropores may limit rapid discharge performance based on restricting electrolyte access, although the degree to which electrolyte access to the surface may be affected is not clear from present analysis. The accessibility of the underlying VB_2 to the electrolyte will also depend on the permeability of the zirconia coating to the ions within the electrolyte [14].

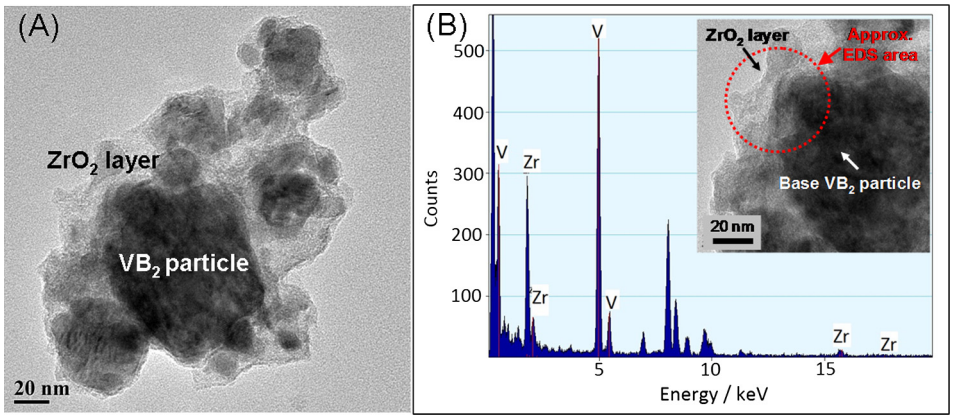

Fig. 3. (A) High resolution TEM and (B) EDS of the LT nanoscopic VB_2 particles with ZrO_2 coating layer. The inset of (B) shows the approximate EDS area which is an enlarged part of (A).

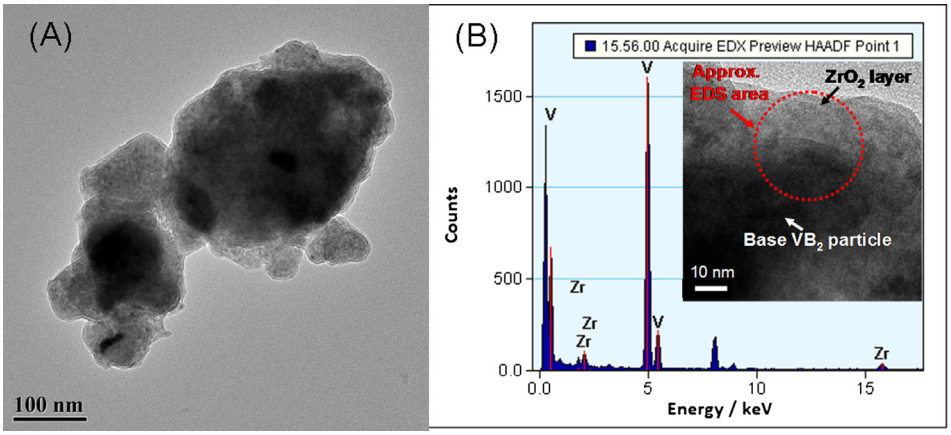

Fig. 4. (A) High resolution TEM and (B) EDS of the nanoscopic VB_2 particles with ZrO_2 coating layer. The inset of (B) shows the approximate EDS area which is an enlarged part of (A).

3.4. Electrical conductivity

Electrical conductivity measurements were obtained to determine the properties of the materials, the effect of the coating, and provide further insight into the differences between the performance of the macro-VB_2 and nano-VB_2. The electrical conductivity of the macroscopic coated, nanoscopic coated, and uncoated VB_2 materials is presented in Table 3. For comparison, the conductivities of the starting materials, elemental boron and vanadium powders, were also obtained. For the VB_2 precursors, elemental vanadium powder is highly conductive in contrast to the elemental boron powder. The coated materials show lower electrical conductivities compared with the base materials, which is expected based on the application of an electronically insulating ZrO_2 material. The results also show that the nanoscopic material has a significantly higher electronic conductivity compared to the macroscopic material, both for the uncoated and coated material, presumably related to the improved conductive matrix due to the tighter packing and larger number of interparticle contacts assessable to smaller particles. Interestingly, X-ray diffraction shows that the nanomaterial is not as highly crystalline as the macroscopic material [7]. To our knowledge, the electrical conductivity of nanoscopic VB_2 has not been previously reported. The VB_2 electrical conductivities (67–230 S cm^{-1}) are higher than the electrical conductivity of carbons typically used for electrochemical cells (ca. 0.3–2.0 S cm^{-1}) [15,16]. The higher electrical conductivity of the nano-VB_2 compared with the macro-VB_2 likely contributes to the higher voltage (i.e. lower resistance) observed within the electrochemical testing.

Table 2
Nitrogen physisorption measurements of macroscopic uncoated VB_2, macroscopic-coated VB_2, nanoscopic uncoated VB_2 and nanoscopic-coated VB_2.

Category	Parameter	Macroscopic		Nanoscopic	
		Uncoated	Coated	Uncoated	Coated
Surface area	BET surface area (m^2 g^{-1})	0.089	0.0089	2.84	0.854
	t-plot micropore area (m^2 g^{-1})	0.828	0.469	0.870	0.123
	Cumulative surface area (m^2 g^{-1}) [a]	N/A	N/A	2.57	0.251
Pore volume	Cumulative pore volume (cm^3 g^{-1}) [b]	N/A	N/A	4.29×10^{-3}	4.62×10^{-4}
Pore size	Average pore width (nm) [c]	N/A	N/A	1.8	1.1

[a] Barrett, Joyner and Halenda (BJH) adsorption; pores between 1.7 nm and 300 nm diameter.
[b] BJH adsorption; between 1.7 nm and 300 nm diameter.
[c] Adsorption (4V/A by Brunauer, Emmett and Teller (BET)).

3.5. Electrochemical impedance analysis

Electrochemical impedance spectroscopy was performed of the VB_2/air cells to allow comparison of the cell impedance in the charged state and after discharge and permit comparison of the macroscopic and nanoscopic VB_2. Shown in Fig. 5 is the complex (Nyquist) impedance plot of a representative charged VB_2/air cell containing nanoscopic VB_2 material. The complex impedance plot shows three regions of interest: (i) the high frequency x-axis intercept (Fig. 5B), (ii) the high frequency semicircle (Fig. 5B), and (iii) the low frequency region (Fig. 5A).

Based on the observed features, the equivalent circuit shown in Fig. 6 was used for fitting the experimental electrochemical impedance data. Similar equivalent circuits have been used to describe the impedance response of Zn/air batteries and related systems [17–19]. Within this equivalent circuit, R_s describes the series resistance, which includes contact resistances and the bulk electrolyte resistance. The dominant contribution to R_s is the electrolyte resistance, and the value for R_s can be determined from the point of intersection of the high frequency semicircle and the x-axis.

The mid-frequency semicircle (Fig. 5B) can be described by a resistor (R_1) in parallel with a constant phase element (Q_1). The resistance R_1 is attributed to the charge transfer resistance [20]. In this case, R_1 includes the resistances associated with ion transport through the coating and VB_2. The capacitive element indicates charge polarization coupled with the charge transfer process and has been attributed to a double layer capacitance [20]. A constant phase element was used rather than a single capacitor to account for the distribution of capacitances, which may result from the distribution of particle sizes. This combination of a resistor and capacitor in parallel is characteristic of a kinetically controlled reaction [21]. There may be multiple parallel R–C elements associated with the various elements of the charge transport process that may not be frequency resolved.

The low frequency region exhibited features similar to a Warburg element (Z_w) that describes semi-infinite diffusion. However

Table 3
Electrical conductivity of VB_2 materials and starting materials.

Sample		Electrical conductivity (S cm^{-1})
Vanadium powder		430 ± 77
Boron powder		$7 \pm 3 \times 10^{-4}$
Macroscopic VB_2	Uncoated	97 ± 5
	Coated	67 ± 14
Nanoscopic VB_2	Uncoated	230 ± 33
	Coated	90 ± 32

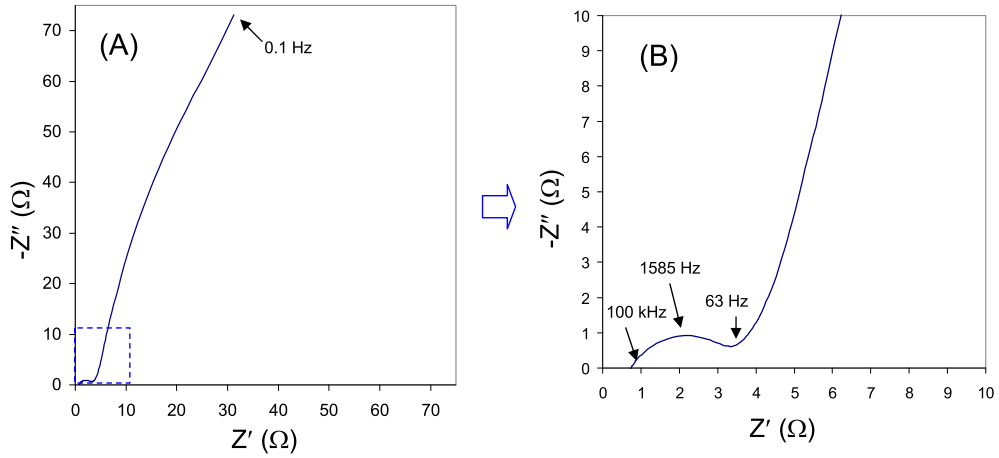

Fig. 5. Electrochemical impedance of nanoscopic, charged VB_2/air battery: (A) full frequency region; (B) expanded view of high frequency region.

in fitting the low frequency region, a Warburg element alone was not sufficient to obtain a reasonable fit of the experimental data. As observed with the Fig. 6, the low frequency region is not entirely a straight line, but also shows some curvature. The low frequency region was therefore fit with a combination of a resistor (R_2), a constant phase element (Q_2), and a Warburg element.

The resistance R_2 is attributed to resistances within the air cathode [17–19,22]. A constant phase element was also used for this region rather than a capacitor based on the distribution of capacitances within the air electrode. The Warburg element may be influenced by processes within the air cathode as well as the VB_2 anode. Previous work supports that diffusion of ions within the air electrode contributes to the Warburg element [17]. Within Zn–alkaline cells, the Warburg element has been also attributed to diffusion of soluble ionic species from the electrode surface to the bulk of solution [20]. The understanding of the processes associated with the various elements of the equivalent circuit (Fig. 6) was used to interpret the experimental data.

The electrochemical impedance data was obtained for the VB_2/air cells in charged and discharged states. Shown in Fig. 7 are the complex (Nyquist) impedance plots of (a) VB_2/air cells containing macroscopic VB_2 in the charged state and after discharge, and (b) VB_2/air cells containing nanoscopic VB_2 in the charged state and after discharge. From the experimental impedance data and the equivalent circuit described above, the values for R_s, R_1, Q_1, R_2, Q_2, and Z_w were obtained from fitting and are presented in Table 4.

The series resistances, R_s, for the charged cells containing either macroscopic or nanoscopic VB_2 are similar. This is consistent with our understanding that the electrolyte resistances within these two configurations are similar based on the same electrolyte composition (4 M NaOH/4 M KOH) and the cell configuration being utilized. The value of R_s for the charged cells is similar to the value obtained from the fitting of impedance data for Zn/air cells containing alkaline electrolytes [18]. The series resistance, R_s, increases from charge to discharge for both the macroscopic and the nanoscopic materials. The increase in R_s from charge to discharge is consistent with the formation of soluble discharge products in the electrolyte that increase the resistivity of the electrolyte [5,6]. The discharged

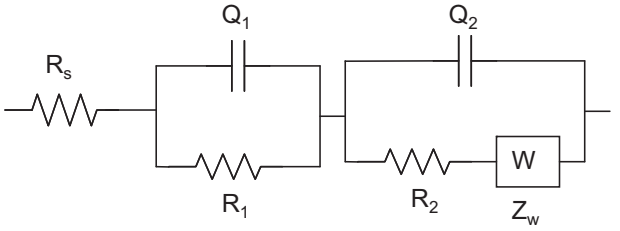

Fig. 6. Equivalent circuit used for fitting electrochemical impedance.

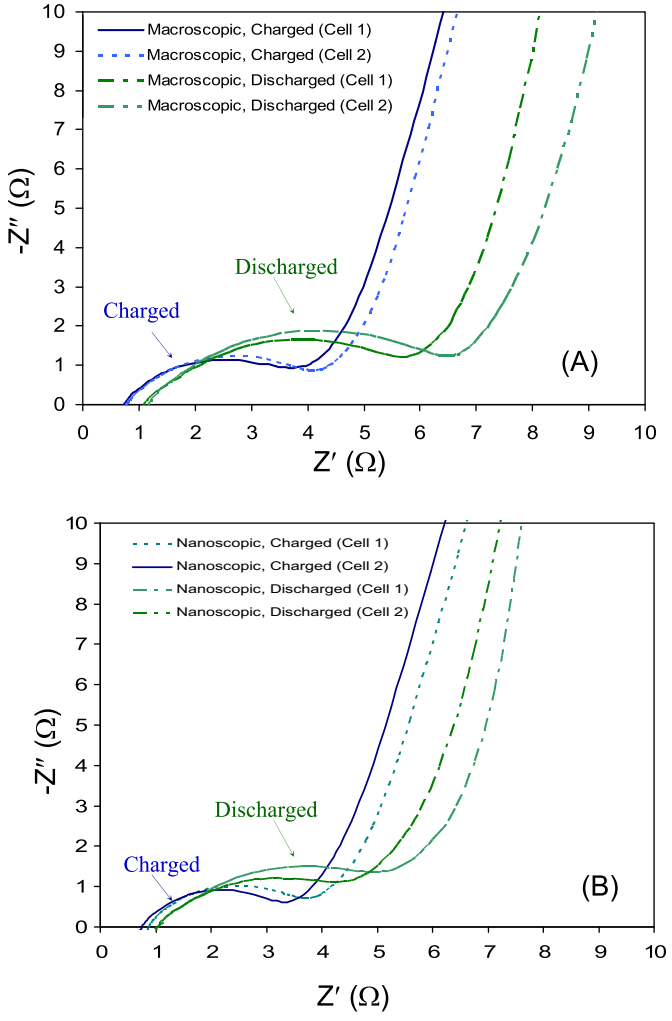

Fig. 7. Electrochemical impedance in the high frequency region of 5 mAh VB_2–air cells discharged at a constant load of 1000 Ω; (A) cells containing macroscopic 1.9% ZrO_2-coated VB_2 before and after discharge; (B) cells containing nanoscopic 1.9% ZrO_2-coated VB_2 before and after discharge.

Table 4
Parameters obtained from fitting of electrochemical impedance of VB_2–air cells using equivalent circuit as described in the text. *R* is resistance, *Q* denotes a constant phase element with the frequency power *n*, and Z_w is a Warburg element.

Sample		R_s (Ω)	R_1 (Ω)	Q_1 (S s^n) (n)	R_2 (Ω)	Q_2 (S s^n) (n)	Z_w (Ω^{-1} $s^{1/2}$)
Macroscopic VB_2	Charged	0.74	3.6	1.2×10^{-2} (0.9)	4770	6.3×10^{-4} (0.7)	7.1×10^{-7}
	Discharged	0.94	5.9	7.0×10^{-3} (0.9)	720	5.3×10^{-4} (0.7)	3.3×10^{-7}
Nanoscopic VB_2	Charged	0.68	3.5	1.7×10^{-2} (0.8)	1000	7.1×10^{-4} (0.7)	6.1×10^{-7}
	Discharged	0.99	5.9	3.7×10^{-3} (0.9)	3900	9.9×10^{-4} (0.6)	1.2×10^{-5}

nanoscopic VB_2 and macroscopic cells show similar values for the series resistance, R_s, upon discharge which suggests that similar discharge products and concentrations of discharge products may be present in the electrolyte.

Comparing the charge transfer resistances (R_1) for the nanoscopic and macroscopic materials, the nanoscopic material shows slightly lower resistances for the charged cells. The lower resistance may be attributed to the higher conductivity of the nanoscopic VB_2 material compared with the macroscopic VB_2 material. The clear trend from the impedance data is that the charge transfer resistance, R_1, increases from charge to discharge for cells containing both the macroscopic and the nanoscopic materials. The increase in the charge transfer resistance from charge to discharge indicates that the resistance associated with the charge transfer process changes as a function of the state of discharge, which may be due to material, surface, and/or electrolyte changes occurring during the discharge process. It is likely that the conductivity of the discharge product is substantially less than that of the VB_2 as will be probed in an upcoming study.

The additional resistor, R_2, is attributed primarily to resistances within the air cathode including resistance associated with ion transport to the catalyst sites. Within the experimental data, this resistance occurs in the low frequency region and captures the curvature present at low frequencies. The relatively high value of R_2 may be influenced by the electrolyte wetting, the ambient humidity, and the electrode architecture. Alkaline air cathodes, typically contain carbon and a catalyst such as manganese dioxide (MnO_2) and related compounds. Previous work involving impedance analysis of MnO_2 nanoarchictectures showed that the low frequency impedance response and the Warburg element were affected by the humidity [23]. The Warburg element can be correlated with the ion diffusion coefficient, however further analysis of the low frequency impedance region of the commercial air cathode was not performed based on the primary focus on the VB_2 anode material.

3.6. Towards practical VB_2/air batteries

In all batteries, the capacity of a practical cell is considerably less than the intrinsic, theoretical cell capacity. In our prior estimate of practical (compared to intrinsic) VB_2/air cell capacities, we extrapolated the similar case of zinc/air batteries that have achieved over 18% of the intrinsic capacity [6]. The practical capacity of air batteries is less than the intrinsic capacity for several reasons, such as inclusion of the cell casing, the air cathode current collector volume, and the volume expansion as the anode material combines with oxygen. This latter expansion is normally either designed within the anode compartment volume [3] or is part of the volume used to contain the electrolyte and can include the degree of hydration of the discharge products. For example, in discharging a Zn/air battery, the relative inverse density of the active anode material and its products are respectively: 0.14 cm^3 g^{-1} (Zn), 0.18 cm^3 g^{-1} (ZnO) and 0.33 cm^3 g^{-1} ($Zn(OH)_2$). The molar volume change of an air battery can be even greater, which for Zn/air changes from 9 cm^3 mol^{-1} (Zn) to 15 cm^3 mol^{-1} (ZnO) to 33 cm^3 mol^{-1} ($Zn(OH)_2$). For VB_2 and its oxidation products the relative densities are: 5.1 g cm^{-3} (VB_2), 3.36 g cm^{-3} (V_2O_5), and 2.55 (crystalline) or 1.84 (amorphous) g cm^{-3} (B_2O_3). Volume expansion of the VB_2/air cell is expected based on the addition of oxygen within the cell and the lower density of the discharge products, and the cell can be designed to accommodate the volume expansion in a manner similar to the construction of Zn/air batteries [3]. The discharge products are soluble species, [5,6] and the hydroxides of these V_2O_5 and B_2O_3 salts have been less characterized. We are currently exploring the degree of hydration and volume of the VB_2/air discharge products with the depth of discharge, and these will be the topic of a future publication.

4. Conclusions

The demands of emerging technologies have resulted in the need for a high capacity battery that can be rapidly discharged. The VB_2/air system provides extremely high energy density batteries. This work furthers our understanding of the performance of VB_2/air batteries at rapid discharge times and provides insight into the factors influencing the electrochemical properties and performance.

The data obtained in this work shows that for all discharge times evaluated, cells containing nanoscopic VB_2 anodes provide significantly higher voltages than cells containing macroscopic VB_2 anodes. For discharge times of ca. 4 h and longer, cells containing nanoscopic VB_2 show higher capacities than cells containing macroscopic VB_2. From the comparison of the nitrogen physisorption, electrical conductivity measurements and electrochemical performance, we determined that the higher performance of the VB_2 nanoscopic material compared with the macroscopic VB_2 material may result from the combination of the nanomaterial's higher surface area and higher electronic conductivity. The higher voltages may be attributed to the higher conductivity of the nanoscopic material, and the higher capacities may result from the higher surface area of the nanoscopic material, which allows a greater degree of material utilization. The coated nanoscopic VB_2 material has a surface area that is two orders of magnitude higher than the coated macroscopic VB_2 material. The higher voltage of the nanoscopic materials may also result from a more disordered structure, as supported by the broader X-ray diffraction peaks compared with macroscopic VB_2 [7]. At high discharge times of ca. $\leq$2 h, nanoscopic VB_2 and macroscopic VB_2 show similar capacities. This observation may point to a surface area limited discharge reaction process.

Transmission electron microscopy and energy dispersive X-ray spectroscopy were used to determine that the VB_2 nanomaterial is coated with a nanoscale zirconia layer, which may allow rapid discharge through the coating. Electrochemical impedance spectroscopy was used to analyze the cells before and after discharge and corroborated the lower resistance of the nano-VB_2 electrodes. The impedance results indicated that the charge transfer resistance changes during the discharge processes which suggests that the anode structure and properties change during the discharge.

These results provide a basis for further development of the unique multi-electron discharge process of VB_2, and the development of high energy and power density VB_2/air batteries. This work points to the development of higher surface area

materials to further improve the rate capabilities of VB_2/air batteries. Higher surface area materials may also be more susceptible to corrosion by the electrolyte, so developing an optimal protective and conductive coating will also be necessary. In addition to higher surface area materials, the design of electrode surfaces and electrolyte compositions may facilitate controlling the charge transfer resistances during the discharge process. Additional analysis of the discharge process and surface structure will facilitate the further development of high performance VB_2/air batteries for numerous applications.

Acknowledgements

The authors would like to gratefully acknowledge funding from the National Science Foundation (Award 1006568) and the Air Force Research Laboratory (Contract No. FA8650-11-M-5170) for support of this research.

Appendix A. Supplementary material

Supplementary material associated with this article can be found, in the online version, at http://dx.doi.org/10.1016/j.jpowsour.2013.03.071.

References

[1] Z. Rogulski, A. Czerwiński, J. Solid State Electrochem. 7 (2003) 118–121.
[2] V. Neburchilov, H. Wang, J.J. Martin, W. Qu, J. Power Sources 195 (2010) 1271–1291.
[3] D. Linden, T.B. Reddy, Handbook of Batteries, 3rd ed., McGraw-Hill, New York, 2002.
[4] X.-P. Gao, H.-X. Yang, Energy Environ. Sci. 3 (2010) 174–189.
[5] H.X. Yang, Y.D. Wang, X.P. Ai, C.S. Cha, Electrochem. Solid-State Lett. 7 (2004) A212–A215.
[6] S. Licht, H.M. Wu, X.W. Yu, Y.F. Wang, Chem. Commun. 3257–3259 (2008).
[7] S. Licht, C. Hettige, J. Lau, U. Cubeta, H. Wu, J. Stuart, B. Wang, Electrochem. Solid-State Lett. 15 (2012) A1–A3.
[8] S. Licht, S. Ghosh, B. Wang, D. Jiang, J. Asercion, H. Bergmann, Electrochem. Solid-State Lett. 14 (2011) A83–A85.
[9] S. Licht, X. Yu, D. Zheng, Chem. Commun. (2006) 4341.
[10] S. Licht, C. Hettige, J. Lau, U. Cubeta, H. Wu, J. Stuart, B. Wang, J. Electrochem. Soc. 155 (2008) 3257–3259.
[11] S. Licht, C. Hettige, J. Lau, U. Cubeta, H. Wu, J. Stuart, B. Wang, J. Electrochem. Soc. 155 (2008) A297–303.
[12] B.A. Holmberg, Y. Yan, J. Electrochem. Soc. 153 (2006) A146–A149.
[13] M.J. Bleda-Martinez, D. Lozano-Castello, D. Cazorla-Amoros, E. Morallon, Energy Fuels 24 (2010) 3378–3384.
[14] S. Licht, X. Yu, Y. Wang, J. Electrochem. Soc. 155 (1) (2008) A1–A7.
[15] E. Frackowiak, Phys. Chem. Chem. Phys. 9 (2007) 1774–1785.
[16] F. Pico, C. Pecharroman, A. Anson, M.T. Martinez, J.M. Rojo, J. Electrochem. Soc. 154 (2007) A579–A586.
[17] G.Q. Zhang, X.G. Zhang, H.L. Li, J. Solid State Electrochem. 10 (2006) 995–1001.
[18] S.M. Zhu, Z. Chen, B. Li, D. Higgins, H.J. Wang, H. Li, Z.W. Chen, Electrochim. Acta 56 (2011) 5080–5084.
[19] Z. Chen, A.P. Yu, R. Ahmed, H.J. Wang, H. Li, Z.W. Chen, Electrochim. Acta 69 (2012) 295–300.
[20] A. El-Sayed, H.S. Mohran, H.M. Abd El-Lateef, Metall. Mater. Trans. A 43 (2012) 619–632.
[21] M. Metikos-Hukovic, S. Omanovic, J. Electroanal. Chem. 455 (1998) 181–189.
[22] D. Thiele, A. Züttel, J. Power Sources 183 (2008) 590–594.
[23] M.S. Doescher, J.J. Pietron, B.M. Dening, J.W. Long, C.P. Rhodes, C.A. Edmondson, D.R. Rolison, Anal. Chem. 77 (2005) 7924–7932.

The Net Discharge Mechanism of the VB_2/Air Battery

Jessica Stuart,[a,*] Amelia Hohenadel,[a] Xuguang Li,[b] Han Xiao,[b] Jeff Parkey,[b] Christopher P. Rhodes,[c,z] and Stuart Licht[a,,z]**

[a]*Department of Chemistry, George Washington University, Washington, D.C. 20052, USA*
[b]*Lynntech, College Station, Texas 77845, USA*
[c]*Department of Chemistry and Biochemistry, Texas State University, San Marcos, Texas 78666, USA*

The electrochemical discharge of VB_2 is a unique process that involves the multiple electron per molecule oxidation of the tetravalent transition metal ion, V ($+4 \rightarrow +5$), and each of the two borons $2\times$B ($-2 \rightarrow +3$), corresponding to a net 11 electron discharge mechanism of the VB_2/air cell as described by the overall cell reaction: $VB_2 + 11/4O_2 \rightarrow B_2O_3 + \frac{1}{2}\ V_2O_5$. However, in the presence of alkaline electrolytes, the discharge products include alkali salts associated with vanadaic and boric acid. In this study, we used FTIR, XRD, and coulombic efficiency measurements to probe the discharge products of high capacity cells and isolate KVO_3 as the principal vanadium discharge product. Additionally, we show that $K_2B_4O_7$ is the probable borate product. From FTIR analysis in KOH electrolyte, it is evident that the alkaline VB_2/air discharge reaction is: $VB_2 + 11/4O_2 + 2KOH \rightarrow \frac{1}{2}\ K_2B_4O_7 + KVO_3 + H_2O$. XPS shows that the surface structure of nanoscopic VB_2 is very different from macroscopic VB_2, which may contribute to the improved electrochemical properties of the nanoscopic material. The understanding of the discharge process and factors affecting performance contribute to furthering the development of extremely high capacity VB_2/air batteries that utilize multi-electron processes.

 [DOI: 10.1149/2.0801501jes] All rights reserved.

Manuscript submitted October 6, 2014; revised manuscript received November 11, 2014. Published November 26, 2014.

Metallic zinc has been used as an anode material in the majority of aqueous primary systems due to zinc metal's high two-electron oxidation capacity and effective discharge. The zinc-carbon battery, known as the Leclanché cell, was first introduced in the 19th century as a low-cost solution for early energy storage needs. The zinc cell, which produced approximately 65 Wh kg^{-1}, was ideal only for low-rate discharges.[1,2] Until the development of the zinc/alkaline/manganese dioxide battery and the zinc/air cell, there was little improvement in primary batteries. The alkaline Zn/MnO_2 cell has since dominated primary electrochemical storage, providing 145 Wh kg^{-1}. Although more expensive than the zinc-carbon battery, the alkaline cell improved performance by increasing energy densities and power capabilities. The zinc/air battery, using external O_2 as the battery active cathode reactant further improves the energy density of primary battery systems. It would be useful for electronic devices to have even higher energy storage densities than that available with zinc/air batteries.[3] Most metal/air batteries to date have been unsuccessful in reaching the high-energy densities that are made possible by multi-electron oxidations, due to material passivation or chemical instabilities.[4]

To provide high energy density cells, there has been an effort to develop high-capacity multi-electron per molecule charge storage processes.[5–21] Vanadium diboride (VB_2) undergoes a multiple electron oxidation process, which to its completion involves an extraordinary 11 electron per molecule oxidation, including oxidation of the tetravalent transition metal ion, V($+4 \rightarrow +5$), and each of the two borons 2xB($-2 \rightarrow +3$). VB_2 has an intrinsic gravimetric capacity of 4060 Ah kg^{-1}, which is five-fold higher than that of the Zn anode electrode (820 Ah kg^{-1}). The intrinsic volumetric anodic capacity of the VB_2 anode (20.7 kAh L^{-1}) is tenfold higher than that of the lithium anode (2.06 kAh L^{-1}).[13–21]

A VB_2 anode within a battery can be coupled with oxygen from external air to provide extremely high energy density VB_2/air batteries.[17] The anode half cell, cathode half cell, and full cell reactions based on generalized discharge products[19] are as follows:

$$\text{Anode}: VB_2 + 11OH^- \rightarrow 1/2V_2O_5 + B_2O_3 + 11/2\ H_2O + 11e^- \quad [1]$$

$$\text{Cathode}: 11/4O_2 + 11/2\ H_2O + 11e^- \rightarrow 11OH^- \quad [2]$$

$$\text{Cell}: VB_2 + 11/4O_2 \rightarrow B_2O_3 + 1/2\ V_2O_5 \quad E_{cell} = 1.55\ V \quad [3]$$

The VB_2/air battery has a theoretical discharge potential of 1.55 V, as calculated from the thermodynamic free energy of the cell reactants and products.[19] The VB_2/air battery's intrinsic volumetric energy density of 32 kWh L^{-1} is substantially greater than that of gasoline (<10 kWh L^{-1}) and has an intrinsic specific energy of 5,300 kWh kg^{-1}, which is four times higher than the theoretical specific energy of zinc/air batteries (1,353 kWh kg^{-1}). The VB_2/air couple uses an alkaline electrolyte, such as aqueous KOH or NaOH. Oxygen from the air reacts at the cathode in a manner similar to that of the zinc/air cell.[3] Concentrated aqueous hydroxide electrolytes ranging from 8 molar to saturated KOH or NaOH yield a similar electrochemical discharge in the VB_2/air cell.[18,19] The VB_2/air cell shows an experimental open circuit potential of ~1.3 V, and under load, the cell can release its capacity over a flat, highly singular discharge potential plateau.

Self-discharge is of paramount important for the practical operation of a battery, and similar to Zn anodes, the VB_2 anode can react with the electrolyte under open circuit potential. In Zn/air batteries, the self-discharge loss was until recently mitigated by the addition of several percent mercuric oxide. More recently, the mercury additives have been replaced with compounds such as polyacrylic acid (i.e. Carbopol), and other Zn/air self-discharge mitigation strategies include alloying, coating with Al_2O_3 and various organic corrosion inhibitors.[22] Our prior efforts to stabilize VB_2 have involved using a zirconia overlayer to prevent corrosion of the boride surface while also allowing charge transfer during the anodic discharge process. Using this approach for macroscopic VB_2, we have been able to largely mitigate the VB_2 self-discharge through using a zirconia overlayer.[12,17] Stored at 45°C for one week, an uncoated VB_2 alkaline anode loses 10% of its original charge capacity, however with a 1% ZrO_2 coating the anode retains 100% of that capacity.[17]

Synthesis of nanoscopic VB_2 has been explored,[18,19,23] and can improve anode performance in VB_2/air batteries.[18,19,21] Its preparation from elemental vanadium and boron powders in a planetary ball mill is straightforward, and this nano-VB_2 is anodically active in electrochemical media.[19] As reported, the planetary ball mill synthesis reaction of elemental vanadium and boron yields VB_2 as characterized by XRD (X-ray diffraction).[19] Recently, we reported on the improved voltage and 11 electron discharge efficiency of 5 mAh VB_2/air batteries using this nanoscopic compared to macroscopic particle sized VB_2 within the anode construction.[19–21] As seen in Figure 1, nanoscopic VB_2 cells discharged to 70–74% coulombic efficiency over a load 3000 Ω and exhibited an initial potential of 0.9 V. This compares to

*Electrochemical Society Student Member.
**Electrochemical Society Active Member.
zE-mail: cprhodes@txstate.edu; slicht@gwu.edu

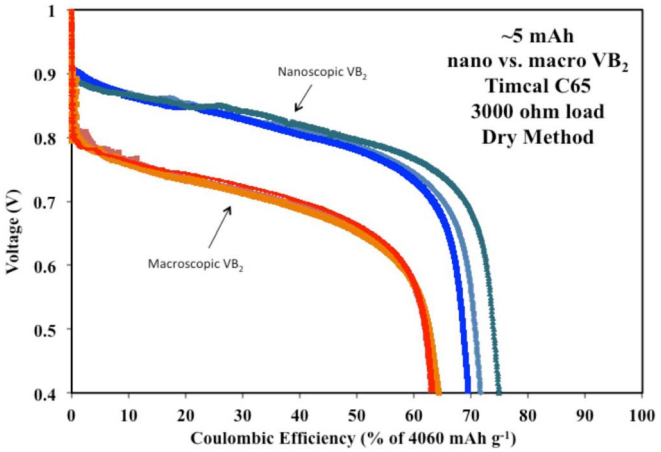

Figure 1. Comparison of VB_2/air cells containing either macroscopic or nanoscopic VB_2 with a capacity of 5 mAh discharged at a constant load of 3000 Ω.[21]

only 63% coulombic efficiency and an initial potential of 0.8 V for the macroscopic VB_2 cells. The Equation 1 oxidation products are generalized as B_2O_3 and V_2O_5, which are the respective anhydride salts of boric acid (H_3BO_3, pK1,2,3 = 9.1, 12.7 and 13.8) and vanadaic acid (H_3VO_4, pK1,2,3 = 3.8, 7.8 and 13.0). In solution, the products will vary with hydroxide concentration and depth of discharge, including hydrogen and metal cation containing species, such as in either a KOH or NaOH electrolyte: $K_xH_zBO_3^{3-x-z}$ or $Na_xH_zBO_3^{3-x-z}$ (where x ranges from 0 to 3, and z from 0 to 3 - x), as well as polymeric species, such as related to the boric condensation reaction forming borax species: $Na_yB_4O_7^{2-y}$, $K_yB_4O_7^{2-y}$, and analogous vanadium species. In this study, we isolated the vanadium active discharge product from a potassium hydroxide electrolyte as well as the boron discharge product formed in a potassium hydroxide electrolyte of the VB_2/air cell to advance understanding of this high-energy capacity battery.

We had initially been unsuccessful in scaling the battery to thicker anodes to allow for higher intrinsic capacity. This limited the quantity of extractable discharge product for analysis. In this study, this limitation is overcome yielding larger quantities of the VB_2/air battery discharge product. This provides a path to analyzing speciation of the product and a net alkaline discharge mechanism of the battery. In this paper, we also introduce XPS measurements that compare the macroscopic to nanoscopic vanadium diboride and provide strong evidence for a VB_2 surface-based understanding of the higher observed discharge voltage of the nanoscopic VB_2/air batteries.

Experimental

Nanoscopic VB_2 synthesis.— Nanoscopic VB_2 was synthesized mechanochemically using vanadium powder (Alfa Aesar) and boron powder (Alfa Aesar) based on methods previously published by Licht et al. [8]. In a controlled argon atmosphere glove box system (Vacuum Atmospheres, Nexus-II), 0.500 g of vanadium and 0.212 g of boron power were measured and transferred into a tungsten carbide milling chamber along with ten tungsten carbide balls, ten millimeters in diameter. The milling vessel was sealed, removed from the glove box, and placed into a Retsch PM 100 planetary ball mill set to 600 rpm and allowed to run for four hours. After the vanadium diboride cooled to room temperature, the material was then collected in the glove box and the mass was measured.

The electrochemical performance of the VB_2 anode, as well as the composite anode, was investigated. Coulombic efficiency is the percentage of the measured capacity compared to the theoretical (intrinsic) anode discharge capacity of the VB_2 anode.

Anode fabrication.— Anodes were prepared using nanoscopic VB_2, synthesized in-laboratory as described above, or commercially available, macroscopic VB_2 (American Elements Organo-Metallics), carbon black (TIMCAL C-NERGY SUPER C65), and KOH pellets (Alfa Aesar). Panasonic PR675H batteries were used as a test bed for electrode fabrication to perform electrochemical tests. The cell fabricated is as previously delineated.[21] In brief, the air electrode from the Panasonic battery is kept intact and reused. The Zn anode of the Panasonic cells was removed by opening the existing cell, removing the anode active material, and using the separator and cathode as received for the VB_2/air battery. VB_2 electrodes were prepared first by mixing 70 wt% active material (VB_2) and 30 wt% carbon black, then measuring the appropriate amount of dry material, and lastly spreading the mixture with isopropyl alcohol and allowing the working electrode to dry. An 8M KOH electrolyte solution was used. The cell was then closed with the cap in reverse so that the anodic material was in contact with the electrolyte.

Once the fabrication process had been completed, cells were discharged at constant loads as indicated in the results and discussion. The change in voltage with time during discharge was measured using NI LabVIEW 2010 and NI USB-6210 multifunction data acquisition.

XRD analysis.— X-ray diffraction (XRD) measurements were performed with a Rigaku MiniFlex. Samples were prepared by loading the crushed powders on a round zero background holder containing a depression in the middle and spread by either isopropyl alcohol or petroleum jelly. Spectra were obtained using the Rigaku powder diffraction analysis package, PDXL. Further analysis was completed with comparison of the obtained spectra to the Inorganic Crystal Structure Database (ICSD) online.

XPS analysis.— X-ray photoelectron spectroscopy (XPS) measurements were obtained at the University of South Carolina on a Kratos AXIS Ultra DLD XPS system equipped with a hemispherical energy analyzer and a monochromatic Al K source, which was operated at 15 keV and 150 W. XPS fitting was carried out by using XPSPEAK Version 4.1 software. Anodic material of the macroscopic and nanoscopic VB_2 was tested prior to and after discharging at a load of 3,000 ohm. The anodic composite consisted of a mixture of 70% VB_2, equivalent to a capacity of 5 mAh, and 30% C65 carbon. Cells used for XPS analysis were discharged using an Arbin Instruments battery tester controlled by MITS software.

Solubility measurements.— 5 mL of 8 molar KOH were transferred to two 10 mL beakers and placed on a stir plate under constant stirring. Potassium metavanadate, KVO_3, or boron oxide, B_2O_3, were weighed and periodically transferred to either beaker, and dissolved until the two solutions became saturated. Both beakers were covered and left to stir for 48 hours. Vacuum filtration was used to collect KVO_3 (Alfa Aesar 99.9%) and B_2O_3 (Alfa Aesar 99%) that remained undissolved. Filter papers with the solid excess were left overnight to dry in a hood then weighed. The solubility was determined by subtracting the undissolved KVO_3 and B_2O_3 from the total mass added to each solution then dividing by volume of KOH. FTIR were measured for the salts and for $K_2B_4O_7{\cdot}4H_2O$ (Alfa Aesar 99%), KVO_3 (Alfa Aesar 99.9%) and K_3VO_4 (Alfa Aesar 99.9%).

FTIR analysis.— Characterization of spent battery material and battery discharge products was completed via Fourier-Transform Infrared Spectroscopy (FT-IR). Weighed samples to be analyzed were ground thoroughly with KBr by mortar and pestle. By means of a hydraulic press, 150 mg of the sample mixture was pressed under 7 tons of pressure for 5 minutes using a Perkin-Elmer 13 mm die set to form a KBr pellet containing the sample for analysis. Composition of the KBr pellets varied between 0.1 weight percent and 1 weight percent of the sample depending on the opaqueness of the sample. Filtrates for B_2O_3 in KOH and H_2O were measured using attenuated total reflectance infrared spectroscopy (ATR-FTIR), as an alternative method to transmission spectroscopy. FTIR spectra were measured by Perkin-Elmer Spectrum 100 with a resolution of 4 cm^{-1} and between 16 and 32 scans per spectrum. A baseline correction was performed with the automatic baseline correction tool offered with the Perkin-Elmer Spectrum software package.

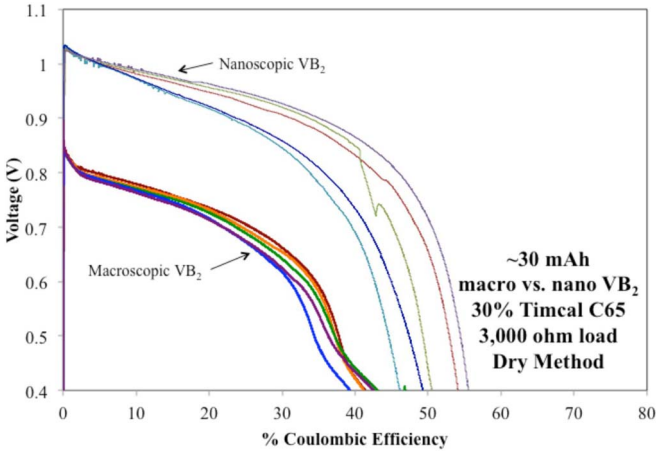

Figure 2. Comparison of higher capacity ~30 mAh anode, compared to the 5 mAh in Figure 1. Macroscopic (bottom curves) or nanoscopic (top curves) 1 cm diameter VB_2/air batteries discharged over a 3000 Ω load. Discontinuity in the green colored discharge curve is symptomatic of an infrequent, but observed poor electrical contact to data acquisition rather than an intrinsic property of the cell.

Results and Discussion

Utilizing high capacity VB_2 anode/air batteries.— The unusually high gravimetric anodic capacity coupled with the characteristic high density of VB_2, 5.10 g cm^{-3}, results in a large volumetric capacity of 20,700 mAh cm^{-3}. Hence, only small quantities of VB_2 are required for extended battery discharge. A five mAh (1 cm diameter) button cell contains only ~1 mg of VB_2, which yields little discharge product. This small amount of discharge product is a direct result of the attractive high capacity of the anode. However, the small quantities posed challenges to effective characterization of that discharge product. Initial attempts to scale-up were ineffective resulting in rapid decreases in coulombic efficiency as the anode thickness was increased several fold.

Recent improvements to the cell fabrication process including upgrades to the gas regeneration in the glove box to better exclude oxygen and better control of the ball mill process have significantly improved scaled-up cell performance. Here, we show that a 6-fold increase in the packed capacity of the 1 cm diameter cell results in a reproducible cell with a relatively small decrease in coulombic efficiency, and further enhancement in the initial cell discharge potential for that of the nanoscopic VB_2 anode (greater than 1.0 V) as shown in Figure 2. The coulombic efficiency of the nanoscopic material has fallen from ~70 to ~52% with scale-up; however, the 600% increase in packed anode post-discharge provides sufficient discharge product for analysis. Using the 30 mAh cells that contained thicker anodes, the nanoscopic material still showed significantly higher voltages and capacities compared with the macroscopic material.

XPS of the macroscopic and nanoscopic VB_2/air battery anodic active material.— To further understand the significant difference in the electrochemical discharge of the nanoscopic and macroscopic material, XPS measurements were carried out to characterize the concentrations and oxidation states of the elements at the surface region (top ~10 nm of the surface) of the unreacted macroscopic and nanoscopic VB_2 materials (prior to discharge).

The XPS showed clear differences in the atomic concentration of V, B, and O at the surface region of the macroscopic and nanoscopic VB_2, as shown in Table I. From the data, comparable amounts of V were observed for both macroscopic and nanoscopic VB_2. However, the concentration of B at the surface of macroscopic VB_2 is much lower than that on nanoscopic VB_2. In contrast, the oxygen concentration on macroscopic VB_2 is much higher compared to nanoscopic VB_2.

The V2p, B1s, and O1s regions of the XPS spectra were evaluated to determine the specific species present at the surface region of the macroscopic and nanoscopic VB_2 materials, as presented in Figure 3. The peak positions from fitting, their relative concentrations, and assignments for the V, B, and O species are shown in Table II.

Table I. Surface concentrations of macroscopic and nanoscopic VB_2 from XPS analysis.

Sample	Element (Region)	Atomic concentration (%)
Macro VB_2	Vanadium ($V2p^{3/2}$)	19.8
	Boron (B1s)	12.0
	Oxygen (O1s)	68.2
Nano VB_2	Vanadium ($V2p^{3/2}$)	17.3
	Boron (B1s)	46.3
	Oxygen (O1s)	36.4

The V2p, B1s, and O1s regions of the XPS spectra show significant differences in the type and relative concentration of species present at the surface of macroscopic and nanoscopic VB_2. As shown in Figure 3a, in the V2p region, the spectra are composed of a pair of $V2p^{1/2}$ and $V2p^{3/2}$ peaks due to spin-orbit peak splitting. As presented in Figure 3c, the $V2p^{3/2}$ peak of the macroscopic VB_2 can be fitted to two peaks at 516.3 eV and 517.6 eV, which are attributed to VO_2/V_2O_4 (V^{4+}) and V_2O_5 (V^{5+}) species respectively.[24] In contrast, the $V2p^{3/2}$ peak of nano-VB_2 contains three peaks from fitting analysis as shown in Figure 3b, and the peak positions of 512.5 eV, 513.6 eV, and 515.4 eV are attributed to elemental vanadium, VB_2, and a V_2O_3 (V^{3+}) species respectively.[24] The peak position of 513.6 eV attributed to VB_2 is similar to the reported value of 513.7 eV for VB_2 prepared from a high temperature synthesis process.[23] The existence of elemental V at the surface of nano-VB_2 is due to the un-reacted vanadium precursor. Interestingly, while the V-containing species at the surface of macroscopic VB_2 are vanadium oxides, nanoscopic VB_2 contains VB_2 at the surface in addition to elemental vanadium and a vanadium oxide species.

As shown in Figures 3d and 3f, the XPS spectra of macroscopic VB_2 in the B1s region can be fitted to peaks at 193.9 eV and 192.8 eV, assigned to H_3BO_3 and B_2O_3, respectively.[24] For nano-VB_2, shown in Figure 3e, the B1s spectra can be fitted to three peaks at 187.3 eV, 187.8 eV, and 192.3 eV, which are attributed to B(0), VB_2, and B_2O_3, respectively. The B1s peak position of 187.8 eV for boron in VB_2 is in the same range but slightly lower than the peak position reported for VB_2 (188.2 eV),[23] which indicates a slightly different chemical environment for boride at the surface of nano-VB_2. The existence of boron in nano-VB_2 is due to the un-reacted boron precursor.

The XPS spectra in the O1s region was also analyzed and is shown in Figures 3g–3i. Oxygen detected by XPS on the surface of VB_2 may be introduced by surface oxidation of B and V, as well as the adsorption of H_2O. As shown in Figure 3i, fitting analysis of macroscopic VB_2 shows three peaks at 530.3 eV, 531.0 eV, and 532.7 eV attributed to oxygen in VO_2(V^{4+}) oxide, V_2O_5 (V^{5+}) oxide, and B_2O_3 respectively.[24] Nano-VB_2 exhibits peaks at 530.5 eV and 532.1 eV attributed to oxygen within VO_2(V^{4+}) oxide or V_2O_3(V^{3+}) oxide, and B_2O_3 respectively.[24] It should be noted that, the O1s peak of oxygen from H_2O has a binding energy of 534.4 ± 1.8 eV, which is not observed in our case. Therefore, the oxygen present in both macroscopic and nanoscopic VB_2 is not from adsorbed water.

As shown in Figure 3 and Tables I and II, it is clear from the XPS analysis that nanoscopic VB_2 has a very different surface structure compared with macroscopic VB_2. Interestingly, the macroscopic VB_2 does not show the presence of VB_2 on the surface, but rather it shows oxides. In contrast, the nanoscopic VB_2 shows the presence of VB_2 at the surface region.

The surface structure of both macroscopic and nanoscopic VB_2 is related to the synthetic conditions, additional surface treatments, and atmospheric storage conditions (oxygen and/or water). The low observed surface oxygen content of nanoscopic VB_2 is related to the synthesis and storage conditions used: elemental vanadium and boron were combined in a glove box with ≤10 ppm H_2O and O_2, sealed and transferred to the ball mill, and then transferred back into the glove

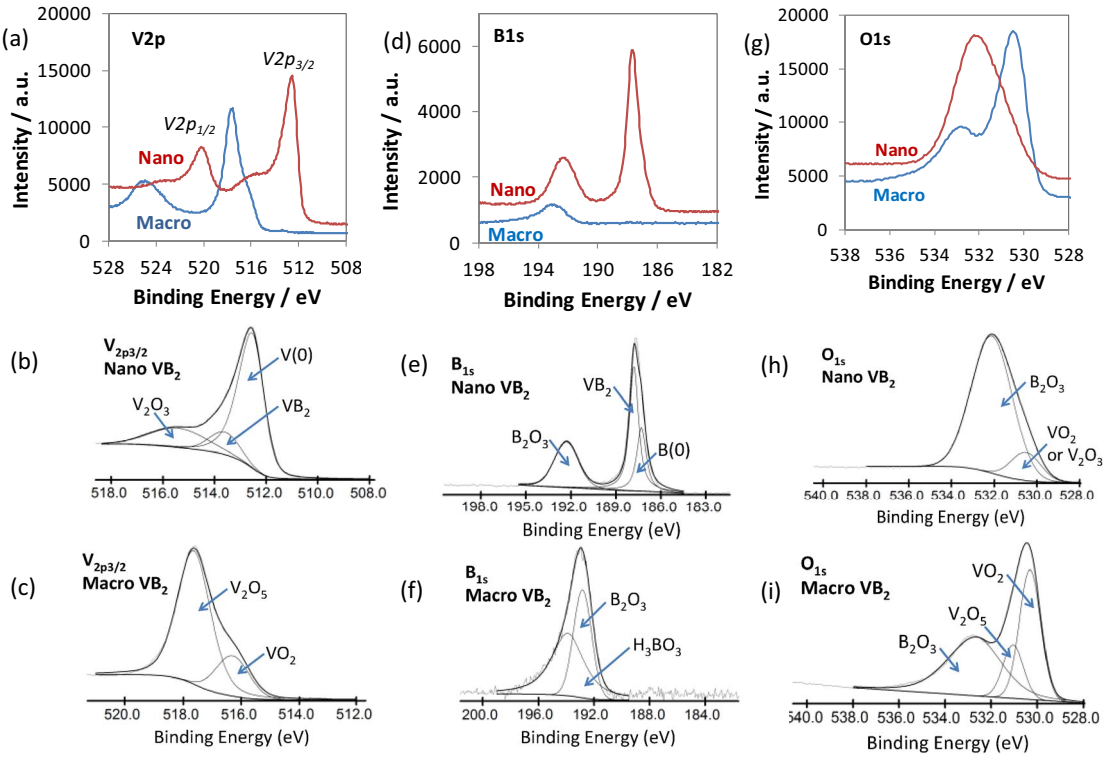

Figure 3. XPS spectra and fitted peaks for macroscopic and nanoscopic VB_2 in the V2p (a,b,c) B1s (d,e, f) and O1s (g, h, i) regions.

box. Although handled in our laboratory in the glove box similar to nanoscopic VB_2, commercial macroscopic VB_2 may have higher surface oxygen content due to synthetic or prior storage conditions.

The data and analysis shows that the as-prepared materials have very different surface structures, which in turn affects the electrochemical properties. Since the macroscopic VB_2 has a significantly higher concentration of oxides present at the surface region compared with nanoscopic VB_2, this may result in an additional resistive layer that affects the ability of hydroxides to interact with the underlying VB_2 structure. The additional resistance resulting from the oxide layer is supported by our prior work, which showed that the interfacial charge transfer resistance of the macroscopic material was higher for the macroscopic VB_2 compared to nanoscopic VB_2.[20]

Table II. Relative concentrations of surface V, B and O species for macroscopic and nanoscopic VB_2 obtained from fitting of XPS spectra.

Element	Sample	Binding Energy (eV)	Relative concentration (%)	Assigned Species[24]
V	Nano	512.5	70.7	V (elemental)
	VB_2	513.6	11.7	VB_2
		515.4	17.6	V_2O_3 (V^{3+})
	Macro	516.3	20.8	VO_2/V_2O_4 (V^{4+})
	VB_2	517.6	79.2	V_2O_5 (V^{5+})
B	Nano	187.3	23.2	B(0)
	VB_2	187.8	44.2	VB_2
		192.3	32.6	B_2O_3
	Macro	192.8	41.5	B_2O_3
	VB_2	193.9	58.5	H_3BO_3
O	Nano	530.5	13.0	VO_2 (V^{4+})or V_2O_3(V^{3+})
	VB_2	532.1	87.0	B_2O_3
	Macro	530.3	36.1	VO_2 (V^{4+})
	VB_2	531.0	14.4	V_2O_5 (V^{5+})
		532.7	49.5	B_2O_3

XRD of the VB_2/air discharge product.— The ~30 mAh cells yield sufficient discharge product for effective FTIR and XRD characterization. For these analyses, a pure 8 M KOH electrolyte was employed, rather than the previous 8 M electrolyte containing 4 M KOH and 4 M NaOH.[21] This change of electrolyte leads to no discernable change in the discharge voltage or to the coulombic efficiency, but provides a simpler (single cation) basis for the discharge product analysis. Effective XRD of the product requires a slow 2Θ scan (6 hours from 2Θ = 5 to 80) due to the high carbon (30% Timcal) content. Additionally, the data is sequentially averaged every 10 data points, which does not result in any peak loss and improves the signal to noise ratio.

The XRD of the deeply discharged 30 mAh VB_2/air cell product does not exhibit remaining VB_2 and provides a strong match to the Inorganic Crystal Structure Database (ICSD) online spectra of KVO_3 shown as the blue curve in Figure 4. It is clear that as predicted in the initial discharge mechanism, pentavalent vanadium is present, V(V), and in this case takes the form of the salt KVO_3. Interestingly, the boron product is not evident, presumably existing as an amorphous

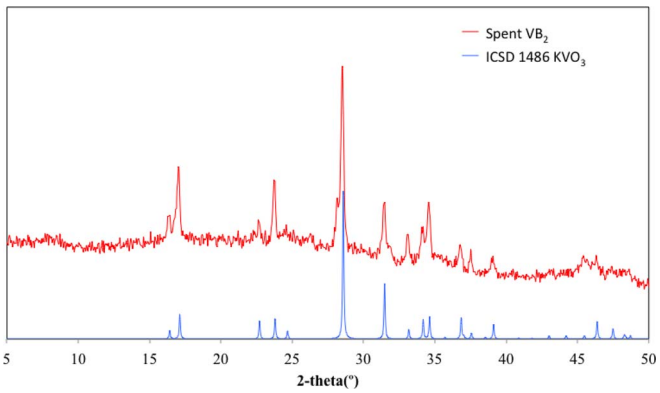

Figure 4. XRD comparison of the data point averaged VB_2/air 35 mAh discharge product as extracted from 3000 Ω discharged 1 cm diameter VB_2/air battery (top curve, red) and the library XRD spectra of KVO_3 (bottom curve, blue).

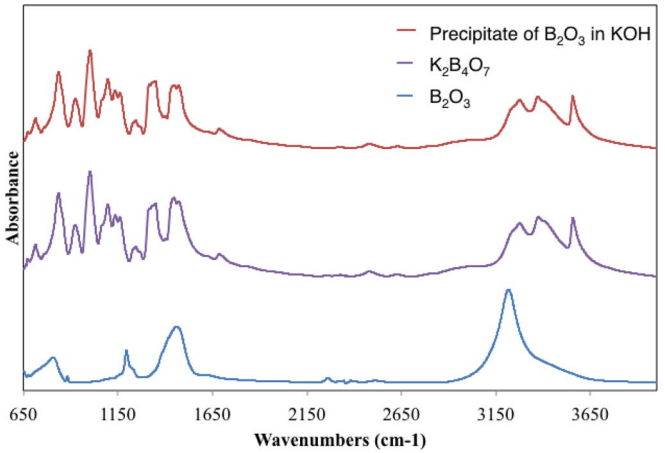

Figure 5. FTIR absorption (KBr pellet) spectra comparison of the precipitate formed from dissolving B_2O_3 in an 8M KOH solution to the initial solute, B_2O_3 while providing evidence of the predicted salt, $K_2B_4O_7$.

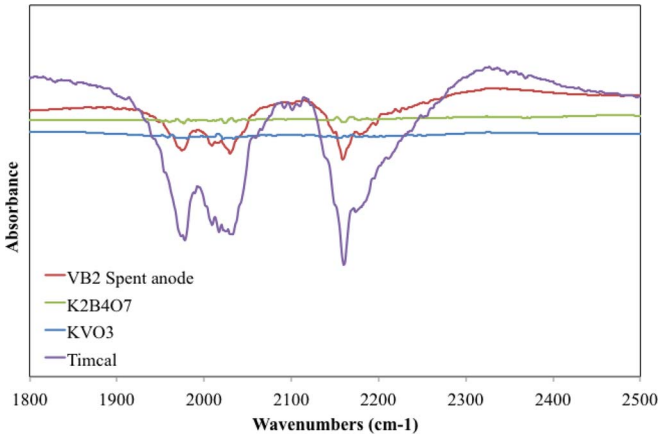

Figure 7. ATR FTIR comparison of Timcal C65 to the spent anodic material exhibiting features between 1900–2300 cm^{-1}.

rather than a crystalline product. In the subsequent section the boron product will be characterized by IR spectroscopy.

Solubility and IR of the VB_2/air discharge product.— The XRD analysis provides useful information of the vanadium product of the VB_2/air cell discharge. In order to determine the predominate boron species, further testing was performed via solubility analysis. Interestingly, one viable product, KVO_3, was found to be highly soluble (5.3 molar), whereas a boron product was found to exhibit a solubility behavior similar to zincate discharged in zinc/air batteries. In that latter case the solubility is dynamic, initially dissolving and then precipitating. Similarly, the equation 3 generalized predicted boron product, B_2O_3, was initially soluble in an 8M KOH, but after 48 hours had precipitated back out from solution. In order to determine the predominate boron species, further testing was performed prior to FTIR analysis. Vacuum filtration was used to collect the precipitate that was identified, via FTIR absorption analysis, to be potassium tetraborate tetrahydrate, $K_2B_4O_7$, shown in Figure 5. The formation of the precipitate from the battery electrolyte suggests that $K_2B_4O_7$, and not B_2O_3, is the principal B(+3) product when the VB_2/air cell is discharged in the KOH electrolyte.

Figure 6 compares FTIR absorption of the 30 mAh VB_2/air battery discharge product. As seen in Figure 6, the discharge product spectrum contains a mix of the separate pure component spectra of pure KOH, $K_2B_4O_7$ and KVO_3 (figure top), and the battery discharge product is a poor fit to the alternate alkali cation free and B_2O_3 and V_2O_3 products (figure bottom). The $K_2B_4O_7$ and KVO_3 products strongly overlap in the 650 to 1650 cm^{-1} domain. In the next section ATR FTIR is used to distinguish between these two product species.

ATR FTIR of the VB_2/air discharge product.— Although absent from the XRD pattern of the discharge product in Figure 4, ATR FTIR provides further evidence (in addition to the IR absorption evidence of Figures 5 and 6) of the boron product from the original VB_2 reactant. We hypothesize that the boron product is highly amorphous in character and it is therefore difficult to characterize with XRD. This hypothesis is supported by results comparing the ATR FTIR spectrum of the VB_2 discharged anode with that measured for KOH, B_2O_3, $K_2B_4O_7$, V_2O_5 and KVO_3. The ATR FTIR spectra in Figure 7 show the dominant feature between 1900 cm^{-1} and 2300 cm^{-1} is from the carbon added to the anode to improve electrical conductivity. The spectrum of this carbon, Timcal C65, is observed before the discharge and with or without mixing 70% by weight nanoscopic VB_2. Similarly as with the XRD analyses the high degree of absorption by this carbon black additive adds noise.

ATR FTIR over a broader frequency range was used for further comparison of the spent anodic material. The data shown in Figure 8 presents evidence for KVO_3 and $K_2B_4O_7$ as the primary discharge products extracted from an approximate 30 mAh discharged nanoscopic VB_2/air battery. Despite large variations to the baseline, due to Timcal there are notable absorption peaks, which provide evidence of the isolated discharge products. Spectral features located at approximately 825 cm^{-1}, 910 cm^{-1}, and 995 cm^{-1} show strong correlations between the spent battery material and $K_2B_4O_7$. Specifically, peaks at 680 cm^{-1} and 970 cm^{-1} may be attributed to KVO_3, rather

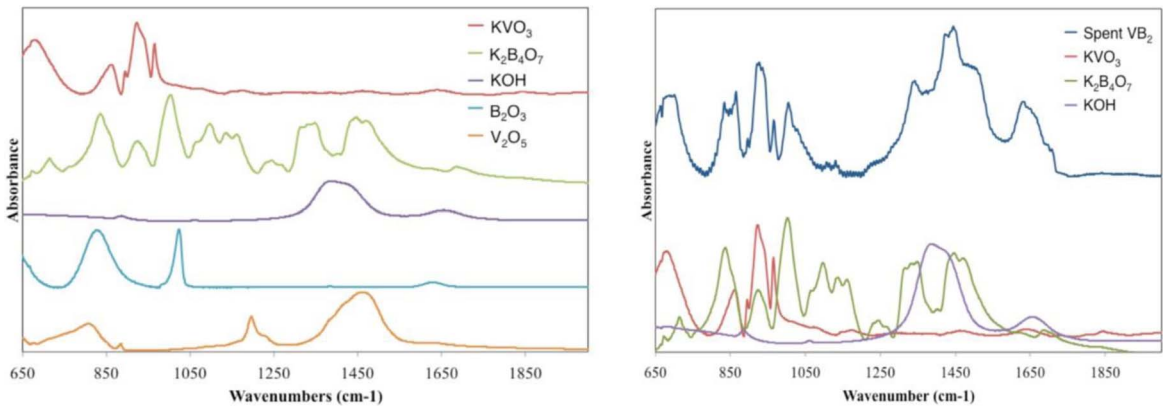

Figure 6. Left: FTIR absorption spectra comparison of the possible discharge products and 35 mAh VB_2/air battery discharge (spent) product. Right: FTIR absorption spectra of the product of the 35 mAh VB_2/air battery discharge compared to the individual FTIR of the has been suggested products $K_2B_4O_7$, KVO_3, and KOH.

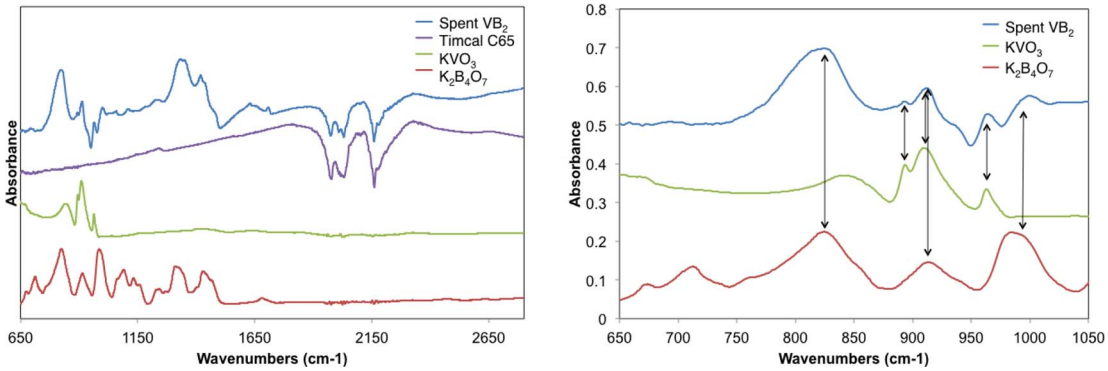

Figure 8. ATR FTIR analysis of the discharged VB_2/air battery anodic material to the expected discharge products, $K_2B_4O_7$ and KVO_3. (left) and (right) figures show region of 750–2800cm^{-1} and enlarged region 650–1050cm^{-1}, respectively.

than $K_2B_4O_7$. Additionally, features attributed to KVO_3 are located at 895 cm^{-1} and 910 cm^{-1}. This provides corroboration to the XRD evidence that KVO_3 is the principal vanadium discharge product of the VB_2/air battery, and is separate from the principal boron product, $K_2B_4O_7$.

There is little evidence for the IR absorption of B_2O_3 in the discharge product as shown in Figure 8, while the V_2O_5 spectrum in the figure exhibits general features evident in the discharge product. Absorption peaks in the 825 cm^{-1} and 995 cm^{-1} region overlap with features attributed to KVO_3 and $K_2B_4O_7$, respectively. Specific absorption peaks observed in the discharge product at 895 cm^{-1} and 910 cm^{-1} are not evident in the V_2O_5 spectrum. Despite uncertainties in the absorption baseline of the spent anodic material due to the large global IR absorption of the Timcal, these additional features are accounted for when KVO_3 is considered as the vanadium discharge product. From FTIR and ATR FTIR analysis of the spent anodic material and expected discharge products, it is evident that the VB_2/air discharge reaction is:

$$VB_2 + 11/4O_2 + 2KOH \rightarrow 1/2\ K_2B_4O_7 + KVO_3 + H_2O \qquad [4]$$

XPS probe of macroscopic VB_2 anode discharge.— Future work will show analysis of XPS measurements of charged and spent macroscopic VB_2. The discharged VB_2 samples are obtained from anodes equivalent to a capacity of 5 mAh of VB_2 and discharged at a load of 3000 ohm.

Conclusions

A mechanism for the net discharge process of the VB_2/air battery in the presence of a KOH electrolyte is presented. First experiments resulted in identification of KVO_3, a salt of the initial theorized V_2O_5 product. Solubility measurements provide significant evidence that the $K_2B_4O_7$ is the most probable borate product. From ATR FTIR analysis in KOH electrolyte, it is evident that the VB_2/air discharge products are $K_2B_4O_7$ and KVO_3. Our understanding of the discharge products of the electrooxidation of VB_2 provides a basis for further development of the unique multi-electron discharge processes of transition metal borides and related compounds.

In addition, the analysis of the unreacted (prior to discharge) VB_2 provides a better understanding of the higher observed discharge voltage of the nanoscopic compared to macroscopic anode VB_2/air batteries. X-ray photoelectron spectroscopy (XPS) measurements show that macroscopic and nanoscopic VB_2 materials have significantly different surfaces. The macroscopic VB_2 does not show the presence of VB_2 on the surface, but rather oxides. In contrast, the nanoscopic VB_2 shows the presence of VB_2 at the surface region. The surface oxides on the macroscopic VB_2 may result in an additional resistive layer, and this observation appears to be consistent with the lower voltage and capacity observed with those anodic materials. This work shows the significant impact of surface structure on electrochemical properties, and additional work will be aimed at understanding the factors that contribute to surface structure (e.g. synthetic conditions, particle size, surface coatings, atmospheric exposure time and temperature, etc.).

Coulombic efficiency of the VB_2 is high, but falls with increasing discharge current density. We have previously shown improvements and retention of high coloumbic efficiency using a zirconia coating of the VB_2.[12,17] We are currently investigating (i) solution phase additives, and (ii) an enhanced current collector conductive matrix to further advance the coulombic efficiency and maintain high stability for the VB_2/air battery. We are also exploring molten electrolytes to transition VB_2/air from a primary to a rechargeable battery.[25,26]

Acknowledgments

The authors are grateful for support of this study by the National Science Foundation (Award 1006568), the Air Force (SBIR award FA8650-13-C-5174), and the Welsh Foundation (AI-0045).

References

1. D. Linden and T. B. Reddy, *Handbook of Batteries*, 3rd edition. New York: McGraw-Hill (2002).
2. Z. Rogulski and A. Czerwiński, *J. Solid State Electrochem.* **7**, 118 (2003).
3. V. Neburchilov, H. Wang, J. J. Martin, and W. Qu, *J. Power Sources*, **195**, 1271 (2010).
4. X.-P. Gao and H.-X. Yang, *Energy Environ. Sci.* **3**,174 (2010).
5. S. Licht, G. Hodes, R. Tenne, and J. Manassen, *Nature*, **326**, 863 (1987).
6. D. Peramunage and S. Licht, *Science*, **261**, 1029 (1993).
7. S. Licht, B. Wang, and S. Ghosh, *Science*, **285**, 1039 (1999).
8. S. Licht, *Electrochem. Comm.*, **1**, 33 (1999).
9. R. Tel-Vered, G. Levitin, and S. Licht, *J. Electrochem. Soc.*, **147**, 496 (2000).
10. G. Levitin, C. Yarnitzky, and S. Licht, *Electrochem. Solid-State Lett.*, **5**, A160 (2002).
11. S. Licht, Y. Wang, and G. Gourdin, *J. Phy. Chem., C*, **113**, 9884 (2009).
12. S. Licht, X. Yu, and Y. Wang, *J. Electrochem. Soc.*, **155**, A1 (2008).
13. S. Licht, X. Yu, and D. Qu, *Chem. Comm.*, 2753 (2007).
14. S. Licht, X. Yu, Y. Wang, and H. Wu, *J. Electrochem. Soc.*, **155**, A297 (2008).
15. H. Yang, Y. Wang, X. Ai, and C. Cha, *Electrochem. Sol. State. Lett.*, **7**, A212 (2004).
16. Y. Wang, X. Ai, Y. Cao, and H. Yang, *Electrochem. Comm.*, **6**, 780 (2004).
17. S. Licht, H. Wu, X. Yu, and Y. Wang, *Chem. Comm.*, 3257 (2008).
18. S. Light, S. Ghosh, B. Wang, D. Jiang, J. Asercion, and H. Bergmann, *Electrochem. Solid State Lett.* **14**, A83 (2011).
19. S. Licht, C. Hettige, J. Lau, U. Cubeta, H. Wu, J. Stuart, and B. Wang, *Electrochem. Solid-State Lett.* **15**, A1 (2012).
20. C. Rhodes, J. Stuart, R. Lopez, X. Li, M. Waje, M. Mullings, J. Lau, and S. Licht, *J. Power Sources*, **239**, 244 (2013).
21. J. Stuart, R. Lopez, J. Lau, X. Li, M. Waje, M. Mullings, C. Rhodes, and S. Licht, *JOVE, J. Vis. Exp.*, 78, e50593 (2013).
22. V. Caramia and B. Bozzini, *Mater. Renew. Sustain. Energy*, **3**(28), 12 (2014).
23. L. Shi, Y. Gu, L. Chen, Z. Yang, J. Ma, and Y. Qian, *Mat. Lett.*, **58**, 2890 (2004).
24. C.D. Wagner, A.V. Naumkin, A. Kraut-Vass, J.W. Allison, C.J. Powell, and J.R. Rumble Jr., NIST Standard Reference Database 20, Version 4.1 (web version) (http:/srdata.nist.gov/xps/) 2012.
25. S. Licht, B. Cui, J. Stuart, B. Wang, and J. Lau, *Energy Environ. Sci.* **6**, 3646 (2013).
26. B. Cui and S. Licht, *J. Mat. Chem. A*, **2**, 10577 (2014).

High Energy Capacity TiB_2/VB_2 Composite Metal Boride Air Battery

Jessica Stuart,[a,*] Matthew Lefler,[a] Christopher P. Rhodes,[b,c,z] and Stuart Licht[a,,z]**

[a]*Department of Chemistry, George Washington University, Washington, DC 20052, USA*
[b]*Lynntech, College Station, Texas 77845, USA*
[c]*Department of Chemistry & Biochemistry, Texas State University, San Marcos, Texas 78666, USA*

Transition metal borides, such as VB_2 and TiB_2, are studied as battery anode materials both individually and as a composite anode for an air cathode battery. The combination of VB_2 and TiB_2 is shown to enhance anodic battery performance. In alkaline media, VB_2 and TiB_2 anodically discharge to yield respectively 11 and 6 electrons per molecule with VB_2 intrinsic gravimetric charge capacity of 4,060 mAh/g and 2,314 mAh/g for TiB_2, 3 to 5 fold higher than a conventional zinc anode. With an air cathode using external O_2, these boride/air batteries discharge at ~1 V, and exhibit unusually high, primary battery energy capacities. We show that the coulombic efficiency attained by the TiB_2 anode in boride/air batteries is not a strong function of the anode capacity per unit area (cm^2) of anode, while the efficiency of the VB_2 anode decreases with increasing anode capacity. The discharge of VB_2 shows a unique singular voltage plateau, indicating that the 11 electrons discharge at a similar potential. Two voltage plateaus are observed during the TiB_2 discharge indicating the possibility of a two-step anodic oxidation. The combination of VB_2 and TiB_2 exhibits evidence of a synergistic increase of the capacity and discharge voltage of boride/air batteries.

Manuscript submitted October 3, 2014; revised manuscript received December 8, 2014. Published January 2, 2015.

The development of improved energy density battery systems is driven by emerging technological demands of longer operational time and lighter weight for medical, military and consumer electronic devices. A principal focus of battery research in the past decade has been the advancement of the energy capacity of rechargeable Li-ion batteries, which have a capacity of 100 to 200 Wh/kg. Despite this, the capacity of rechargeable batteries remains approximately 5-fold lower than that of primary batteries. The highest commercial primary battery energy capacity is exhibited by zinc/air batteries.[1] Replacement of the air battery's zinc electrode by a higher capacity anode material has the potential to further increase the energy capacity. New materials, such as metal borides, have been studied due to their demonstrated high capacities as anodes for primary alkaline batteries. Of the large number of borides that have been investigated as anodes in alkaline media, TiB_2 and VB_2 exhibit the highest stability and demonstrated anodic capacity.[2–9] Although Zn, TiB_2, and VB_2 have similar formula weights (65.39, 69.49. 72.56 g/mol), the Zn oxidative discharge releases only two electrons, whereas TiB_2 and VB_2 are observed to discharge up to 6 and 11 electrons, respectively. While the conventional Zn anode has an intrinsic capacity of 820 mAh/g (2*FW/Faraday*mAh), TiB_2 and VB_2 have respective intrinsic capacities of 2,314 and 4,060 mAh/g. Coupled with an air cathode, vanadium diboride has been reported to have among the highest energy density of any primary battery (5,300 kWh/kg).[9] The 11 electron discharge reaction of the VB_2/air battery is given by the following half cell and full cell reactions:[9]

$$\text{Anode}: VB_2 + 11OH^- \rightarrow 1/2V_2O_5 + B_2O_3 + 11/2\,H_2O + 11e^- \quad [1]$$

$$\text{Cathode}: O_2 + 2H_2O + 4e^- \rightarrow 4OH^- \quad [2]$$

$$\text{Cell}: VB_2 + 11/4O_2 \rightarrow B_2O_3 + V_2O_5 \quad [3]$$

It is interesting to note that VB_2 discharges each of its 11 electrons at a singular discharge voltage plateau.[9]

Self-discharge is also of paramount important for the practical operation of a battery, and similar to Zn anodes, the VB_2 anode can react with the electrolyte under open circuit potential. In Zn/air batteries, the self-discharge loss was until recently mitigated by the addition of several percent mercuric oxide. More recently, the mercury additives have been replaced with compounds such as polyacrylic acid (i.e. Carbopol), and other Zn/air self-discharge mitigation strategies include alloying, coating with Al_2O_3 and various organic corrosion inhibitors.[10] Our prior efforts to stabilize VB_2 have involved using a zirconia overlayer to prevent corrosion of the boride surface while also allowing charge transfer during the anodic discharge process. Using this approach for macroscopic VB_2, we have been able to largely mitigate the VB_2 self-discharge through using a zirconia overlayer.[3,9] Stored at 45 °C for one week, an uncoated VB_2 alkaline anode loses 10% of its original charge capacity, however with a 1% ZrO_2 coating the anode retains 100% of that capacity.[9]

Preparation of nanoscopic VB_2 has been investigated,[11–16] and the straightforward synthesis of anodically active nanoscopic VB_2 from elemental vanadium and boron in a planetary ball mill using a mechanochemical process has been reported.[13–16] The voltage and rate advantages of nanoscopic compared to macroscopic VB_2 anodes in VB_2/air batteries has been characterized, providing 10 to 20% higher voltage as well as higher coulombic efficiency under low and moderate discharge loads.[15]

While there have been few prior characterizations of the anodic properties of TiB_2, the high conductivity of the material makes it a strong candidate for a potential anodic active material.[2] The 6 electron discharge reaction of the TiB_2/air battery is in accord with following half cell anodic (eq. 4) and full cell reactions (eq. 5), with the half cell cathodic reaction of eq. 2:

$$\text{Anode}: TiB_2 + 6OH^- \rightarrow Ti + B_2O_3 + 3H_2O + 6e^- \quad [4]$$

$$\text{Cell}: TiB_2 + 3/2O_2 \rightarrow Ti + B_2O_3 \quad [5]$$

Room temperature measurements of the resistivity of TiB_2 9–28 $\mu\Omega$ cm have been reported to be lower than the 16–38 $\mu\Omega$ cm range reported for VB_2.[17] In comparison to vanadium diboride, TiB_2 has a lower theoretic capacity of 2,314 mAh/g, nonetheless this capacity is three fold greater than the commercially established alkaline zinc anode. In addition to examining TiB_2 or VB_2 anodes individually, composites of TiB_2 and VB_2 were examined to determine if the combination of these materials would provide improved electrochemical properties.

Experimental

Anodes were prepared using commercially available TiB_2 (Alfa Aesar, 325 mesh powder), macroscopic VB_2 (American Elements Organo-Metallics), and carbon black (TIMCAL C-NERGY SUPER C65). Nanoscopic VB_2 was synthesized via ball milling using

*Electrochemical Society Student Member.
**Electrochemical Society Active Member.
zE-mail: cprhodes@txstate.edu; slicht@gwu.edu

vanadium powder (Alfa Aesar) and boron powder (Alfa Aesar) as previously reported detailed.[14] In a controlled argon atmosphere glove box system (Vacuum Atmospheres, Nexus-II), vanadium and boron powers were measured and transferred into a tungsten carbide milling chamber along with ten tungsten carbide balls, ten millimeters in diameter. The milling vessel was sealed, removed from the glove box, and placed into a Retsch PM 100 planetary ball mill, which was set to 600 rpm and allowed to run for four hours. After the vanadium diboride cooled to room temperature, the material was then collected in the glove box into a round bottom flask, and the mass was measured.

Panasonic PR675H batteries were used as a test bed for electrode fabrication to perform electrochemical tests as previously reported.[15] In brief, the Panasonic cell was opened (the anode cap was removed from the cathode bottom), and the Zn anode material was cleaned out of both parts. We have recently detailed cell fabrication of composite anodes of Zn and VB_2 which demonstrate that zinc has been removed from the commercial (Panasonic PR675H) Zn/air battery shells.[15] The Zn/VB_2 composite clearly demonstrates two distinguishable plateaus at the normal Zn discharge voltage of 1.4 V and the lower VB_2 discharge voltage. Therefore based on the lack of a Zn plateau, we conclude that that all Zn has been effectively removed from the anode compartment.

TiB_2 and VB_2 electrodes were prepared first by mixing 70 wt% active material (TiB_2, VB_2, or a composite as described in the text) and 30 wt% carbon black, then measuring the appropriate amount of dry material onto the top of the anode cap, and lastly spreading the mixture with isopropyl alcohol and allowing the working electrode to dry under ambient conditions. An 8 M KOH (Alfa Aesar) electrolyte solution was used. The cell was then closed with the cap in reverse so that the anodic material was in contact with the electrolyte, and glued shut with a fast-drying epoxy. Once the fabrication process was completed, cells were placed on a holder and discharged at constant loads as indicated in the results and discussion. The change in voltage with time during discharge was measured using NI LabVIEW 2010 and NI USB-6210 multifunction data acquisition.

The electrochemical performance of the individual VB_2 or TiB_2 anodes, as well as the composite anode, was investigated and reported as specific capacity (mAh/g) and coulombic efficiency, the percentage of the measured capacity was compared to the theoretical (intrinsic) anode discharge capacity of the TiB_2 or VB_2 or composite mixture anodes. The theoretical capacities for the composites were determined from the theoretical capacities from each individual component and the relative mass.

Scanning electron microscopy is conducted with a PHENOM Pro-X SEM.

Results and Discussion

TiB_2/air battery discharge.— The incorporation of an appropriate conducting material into the electrode matrix is needed to provide continuous electron-conducting pathways to the active boride material. We had previously found that Timcal C65 carbon black powder provides an effective conductive matrix for the VB_2 anode.[15,16] Discharges of the TiB_2/air cell were studied to determine a preferred Timcal C65 composition for the anode mix by studying the discharge of cells with various weight ratios of TiB_2 compared to the Timcal carbon additive. Figure 1 compares four sets of 10 mAh cells containing various amounts of carbon black to determine which composition would be used for further testing. The TiB_2/air battery discharges at an initial plateau at ~1 V followed by a minor shorter duration secondary plateau at ~0.85 V for anodes with capacities ranging from 2.5–10 mAh. The extent of this smaller, secondary, lower voltage plateau varies from 0 to 30% of the observed total discharge. The presence of two distinct voltage plateaus suggests that the discharge of TiB_2 may occur in stages, and the discharge voltage is related to a different local chemical potential for the reaction over these voltage ranges. Changes in the conductivity of the material during discharge may also contribute to the presence of two voltage plateaus. While the emphasis of this effort was on the effect of combining TiB_2 and VB_2, the

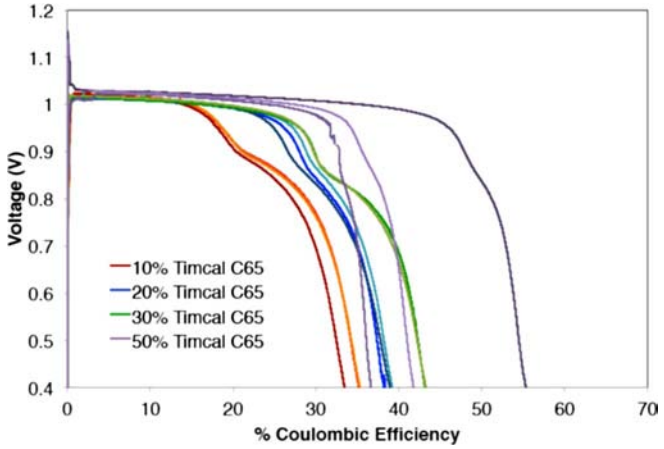

Figure 1. The effect of various carbon ratios (the weight percent of Timcal C65) in the TiB_2 anode mix on the discharge efficiency of the TiB_2/air cell; 10 mAh capacity TiB_2 cells, 3000 Ω load.

further investigation of the discharge process of TiB_2 is needed. Our recent study of the discharge mechanism of VB_2 determined specific discharge products and provided an updated reaction for the anodic discharge process.[18]

From the data in Figure 1, it is evident in the figure that the specific capacity of the TiB_2/air cell improves with increasing carbon content in the anode mix. Using the 30 wt% carbon mixture, a coulombic efficiency (experimental specific capacity/theoretical specific capacity) of ~40% was obtained. However, the highest examined anode composition of 50 wt% TiB_2 and Timcal was not used in subsequent measurements due to (i) the large variation observed between multiple samples of the same composition as observed from the data in Figure 1, and (ii) the large fraction of anodically inactive (carbon) material in the anode mix, which diminishes the total capacity, despite the higher coulombic efficiency. The anode composition of 70 wt% TiB_2 with 30 wt% carbon black was selected for further analysis of this anode candidate due to the relatively high observed reproducibility and specific capacity, as well as to maintain the same percentage of carbon black also used in our prior measurements with the analogous VB_2 anode.[8,14,18]

The effect of the capacity of the anode (either 2.5, 5, or 10 mAh) on the specific capacity (mAh/g) and coulombic efficiency of the active TiB_2 anode material was determined by measuring the discharge of the TiB_2/air battery with 70% TiB_2 and 30% Timcal C65 as presented in Figure 2 and Table I. As observed from the data in Figure 2 (bottom), the observed specific capacities of the TiB_2/air battery are largely unrelated to the cell capacity. This is particularly important since higher capacity anodes are needed for practical commercial cells.

In comparison, for macroscopic VB_2 anodes as the cell capacity increases, the specific capacity and percent coulombic efficiency rapidly diminishes. For example, discharged under the same 3,000 Ω load, a 2.5 mAh VB_2 anode air cells discharges to over 80% columbic efficiency, while 5, 10 or 30 mAh VB_2 anode cells discharge to only ~60%, 50% or 40% columbic efficiency respectively.[16,18] In contrast to VB_2, the experimental capacity of TiB_2 anodes is maintained at higher material loadings which is significant since obtaining thicker electrodes that maintain high coulombic efficiencies is needed for developing practical cells.

The performance of the TiB_2 anode was also evaluated at various rates using constant resistive loads ranging from 1,000 to 10,000 ohms in order to evaluate the anode performance under various discharge rates. Typically, as seen in Figure 3, there is an onset time to full discharge voltage that increases at higher initial discharge currents (at smaller resistive discharge loads). This onset time diminishes (not shown) when the cell sits for a day or more prior to discharge, allowing the electrolyte to more fully permeate throughout the cell. The results of these tests, shown in Figure 3, exhibit a substantial decrease in

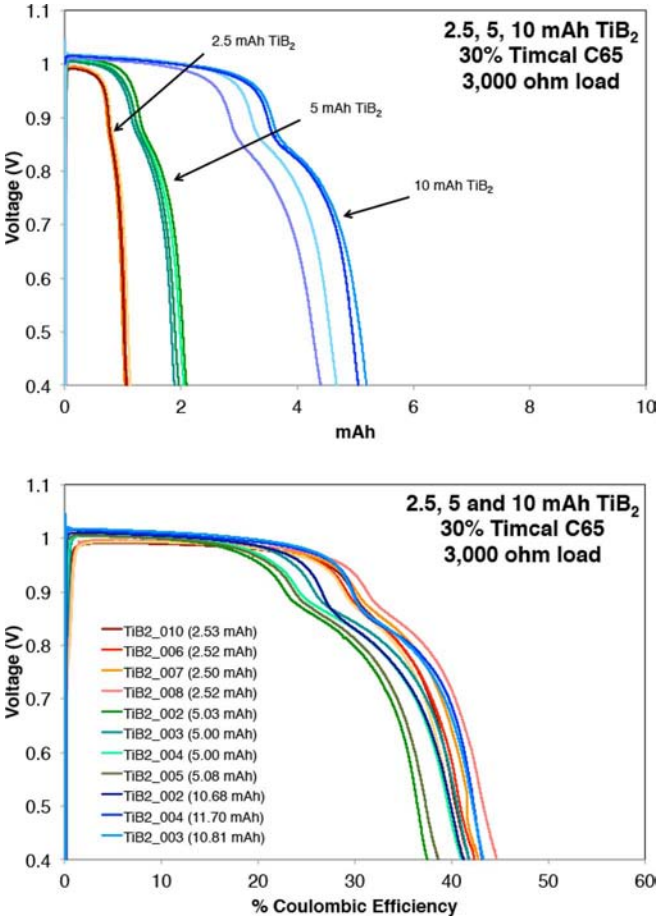

Figure 2. Top: Discharge capacity of 2.5, 5, and 10 mAh TiB_2/air battery anodes containing 30% Timcal C65 and 70% active material. Bottom: Specific capacity of TiB_2 anodes with different cell capacities.

the specific capacity and voltage as the discharge rate increases, in a manner previously reported for the VB_2 anode.[15]

Composite TiB_2-VB_2/air discharge.— We investigated composite TiB_2 and VB_2 anodes to determine if the combination of these materials would result in a synergistic effect to improve (i) the coulombic efficiency of higher capacity (thicker) VB_2-containing anodes, (ii) the TiB_2 coulombic efficiency, and (iii) the VB_2 discharge voltage. Figure 4 presents a scanning electron microscopy (SEM) image of the

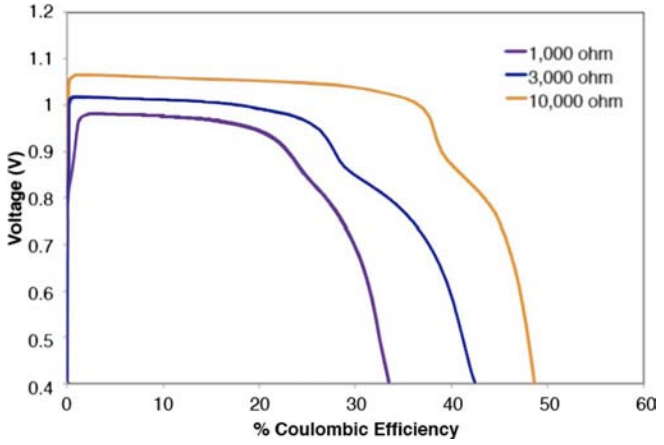

Figure 3. Discharge curves of 10 mAh TiB_2 cells over constant resistive loads ranging from 1,000 ohm to 10,000 ohm; 10 mAh TiB_2 anodes prepared with 30 wt% carbon.

composite anode (30 wt% VB_2; 70 wt% TiB_2) without the presence of Timcal C65. In the SEM the macroscopic VB_2 consists of the 1–5 μm particles, and the TiB_2, consists of particles primarily in the μm 5–25 range. As seen in the SEM the VB_2 is well dispersed and generally in contact with some TiB_2.

In order to observe the discharge effects of the composite TiB_2 and VB_2 anode in the boride/air battery, a 10 mAh capacity anode was prepared that was comprised of 5 mAh of VB_2 (30 wt% VB_2; intrinsic capacity 4,060 mAh g^{-1}) and 5 mAh of TiB_2 (70 wt% TiB_2; intrinsic capacity 2,314 mAh g^{-1}). The resultant composite anode boride/air discharge curves and the comparison to pure VB_2 or TiB_2 anode air batteries is shown in Figure 5. In the batteries containing a composite anode, the voltage is substantially higher for the initial plateau region when compared to the VB_2 discharge curve, and is characteristic of the TiB_2 (alone) discharge effects.

Table I compares the experimental and theoretical capacities of the individual and composite electrodes. For the 10 mAh cells: the macroscopic VB_2:TiB_2 (50:50) had a higher experimental specific capacity relative to the theoretical specific capacity (55% of theoretical) compared to the individual 10 mAh VB_2 (50% of theoretical) or TiB_2 electrodes (40% of theoretical). The effective higher specific capacity also results in a higher capacity for the composite, as shown in Figure 5. The higher ratio of the specific capacity to theoretical capacity for the VB_2:TiB_2 composite compared to individual VB_2 and TiB_2 electrodes supports that there is a synergistic effect occurring between the materials which contributes to increasing the capacity. It is possible that one of the products of TiB_2 discharge may contribute to increased electrical connectivity to the VB_2 particles.

Table I. Comparison of theoretical and experimental capacities and specific capacities of VB_2, TiB_2, and composite VB_2-TiB_2/air cells.

Category	Sample ID	Wt% VB_2	Wt% TB_2	Wt% Carbon	Ratio of VB_2:TiB_2 (mAh:mAh)	Theoretical capacity (mAh)	Experimental capacity (mAh)	Theoretical specific capacity (mAh/g)	Experimental specific (mAh/g)	Percentage of experimental/ theoretical specific capacity (%)
TiB_2	T100-2.5 mAh	0	70	30	–	2.5	1.0	2,314	967	42
	T100-5 mAh	0	70	30	–	5	2.0	2,314	914	40
	T100-10 mAh	0	70	30	–	10	4.0	2,314	965	42
	T100-30 mAh	0	70	30	–	30	12	2,314	926	40
VB_2	VM100-10 mAh	70	0	30	–	10	5.0	4,060	2030	50
	VN100-15 mAh	70	0	30	–	15	7.2	4,060	2071	51
	VM100-30 mAh	70	0	30	–	30	12	4,060	1624	40
	VN100-30 mAh	70	0	30	–	30	15	4,060	1949	48
VB_2: TiB_2 composites	VM50-T50-10 mAh	26	46	28	50–50	10	5.9	3,187	1753	55
	VM90-T10-30 mAh	63	7	30	90–10	30	14.8	3,885	1826	47
	VN50-T50-30 mAh	25	45	30	50–50	30	15.1	3,187	1657	52

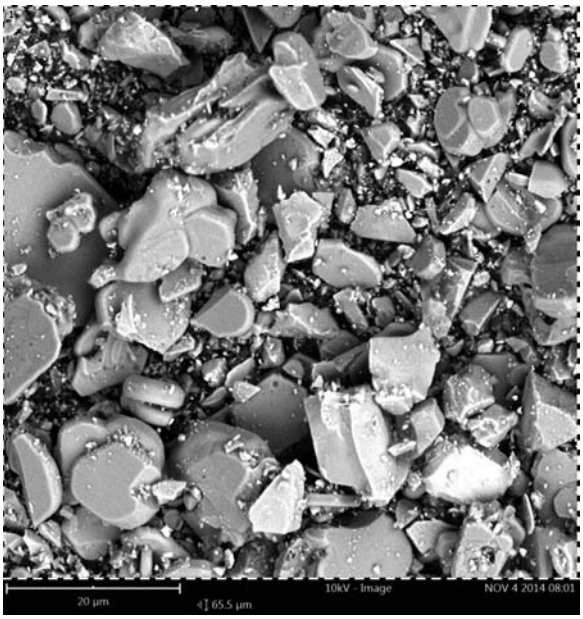

Figure 4. SEM image of macroscopic TiB_2 and VB_2 anodic composite without the presence of Timcal C65.

Further work is needed to determine the specific structural and electrochemical changes occurring during the discharge of the composite electrode.

Higher capacity boride/air battery discharge.— The synergistic effect, in which the composite TiB_2/VB_2 anode of the boride/air battery discharges to a higher energy than either of the TiB_2 or VB_2 cells alone, was additionally probed for larger capacity batteries. This is of particular importance due to the fact that the VB_2 anode exhibits a significant loss of coulombic efficiency with increasing capacity and anode thickness.[16] Figure 6 presents characteristics of ∼30 mAh intrinsic capacity cells, in which the discharge exhibits an average coulombic efficiency of ∼40%.

To further investigate the benefits of the composite cell, a small amount of the TiB_2 anode, approximately 4% of the total capacity (1:9 TiB_2 to VB_2 by weight), was added to the larger capacity macroscopic VB_2 anode. As presented in Figure 6, this relatively small addition of TiB_2 resulted in significant increase in the coulombic efficiency (to ∼50%), as well as a 0.2 V increase to the initial voltage of 0.8 V

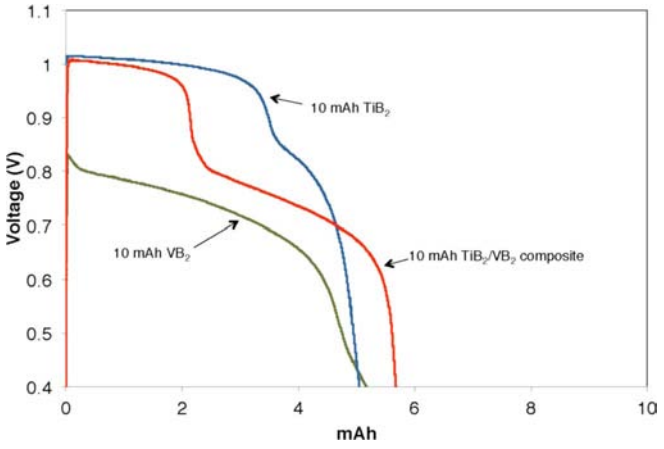

Figure 5. Discharge curves of 10 mAh TiB_2 (without VB_2) or VB_2 (without TiB_2) cells compared to that of the same 10 mAh composite (with TiB_2 and VB_2).

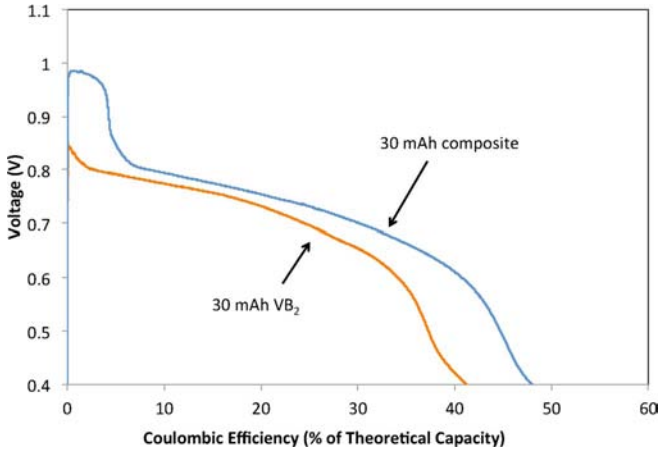

Figure 6. 30 mAh VB_2/air discharge compared to a 30 mAh composite anode of 90% VB_2 and 10% TiB_2 by weight.

due to the first plateau of TiB_2. The increase in the net capacity is further supported by analysis of the experimental and theoretical specific capacities for the composite and the individual electrode materials. As presented in Table I for the high capacity 30 mAh cells, the composite of macroscopic VB_2:TiB_2 (90:10) had a higher experimental specific capacity (1826 mAh/g, 47% of theoretical) compared with the individual 30 mAh VB_2 (1624 mAh/g, 40% of theoretical) or TiB_2 electrodes (926 mAh/g, 40% of theoretical).

In addition to using macroscopic VB_2, we also investigated the effect of composites prepared using nanoscopic VB_2 based on our previous work that demonstrated that that nanoscopic VB_2 resulted in higher voltages and specific capacities.[13,16] Our recent work supports that the higher specific capacity and voltage of nanoscopic VB_2 compared to macroscopic VB_2 is related to the higher degree of vanadium and boron at the surface region for nanoscopic VB_2 compared to predominately oxide species at the surface region of macroscopic VB_2 based on X-ray photoelectron spectroscopic analysis.[18] Shown in Figure 7 are high capacity (30 mAh) VB_2 anodes prepared with either nanoscopic or macroscopic vanadium diboride, which were used as a baseline for comparison with the composites. It is evident from the data in the figure that for the 30 mAh cells, the nanoscopic VB_2 discharges at a higher voltage and to a higher discharge capacity than the comparable cell prepared with the macroscopic VB_2. The nanoscopic

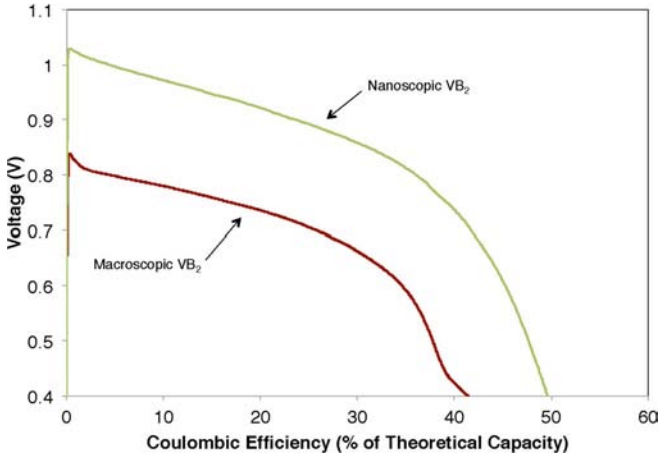

Figure 7. Characteristic discharge curves of higher capacity anodes containing either macroscopic VB_2 or mechanochemical synthesized VB_2 (from elemental vanadium and boron in a planetary ball mill). An increased VB_2 air battery capacity to ∼30 mAh is presented.

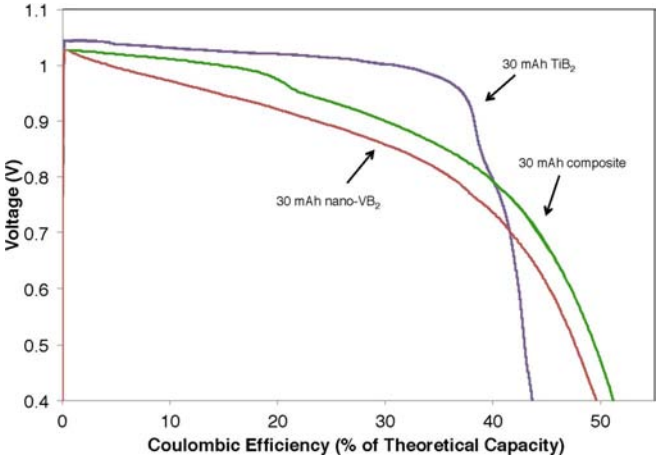

Figure 8. Comparison of the 30 mAh (15 mAh nanoscopic VB_2 and 15 mAh TiB_2) composite discharge to 30 mAh nanoscopic VB_2 and TiB_2 air battery discharges.

VB_2 anodic discharge voltage is not only high, but is also comparable to the discharge voltage of the TiB_2 cells in Figures 1 and 2.

Unlike the VB_2 analogy, attempts at synthesizing a nano-TiB_2 from the titanium and boride elements have been unsuccessful to date. However, an interesting composite anode has been formulated from a mix of the nano-VB_2 and commercial (macroscopic) TiB_2. Figure 8 presents the discharge of a composite cell prepared with this TiB_2 and the nanoscopic, rather than macroscopic VB_2. This alternative composite anode cell exhibits an advantageous, higher voltage that is higher than that observed for the pure nanoscopic VB_2 anode. The composite anode discharge occurs at predominately smooth discharge voltage plateau, although a minor discharge voltage slope is evident at ~1 V, and the 2nd discharge plateau evident at ~0.8 V for pure TiB_2 is not evident.

Similar to the 10 mAh and 30 mAh composites with macroscopic VB_2, as presented in Table I the 30 mAh composite of nanoscopic VB_2:TiB_2 (50:50) had a higher experimental specific capacity relative to the theoretical specific capacity (52% of theoretical) compared with the individual 30 mAh nanoscopic VB_2 (48% of theoretical) or TiB_2 electrodes (40% of theoretical).

Conclusions

This study establishes that the addition of TiB_2 to the anode of VB_2/air batteries improves performance by increasing the battery discharge voltage as well as the coulombic efficiency of the cell. We have found that TiB_2 anodes comprised of various capacities (2.5, 5, and 10 mAh TiB_2) attained similar coulombic efficiencies. The titanium diboride anode discharges exhibit an initial plateau at ~1 V followed by a minor, secondary plateau at ~0.85 V, achieving an average discharge efficiency of 40–50%. From the comparisons of a composite cell containing 50% VB_2/50% TiB_2 to both 5 and 10 mAh TiB_2 capacity anodes and to 5 and 10 mAh VB_2 capacity anodes, a synergistic effect of the composite $VB_2 + TiB_2$ anode cell is evident in enhanced coulombic efficiency compared to either pure (VB_2 or TiB_2 anode) cell alone.

The VB_2: TiB_2 composite anode exhibits improvement in both smaller (10 mAh) and larger (30 mAh) cells, as well as for composites containing either large or small (70 or 10) wt% of TiB_2 relative to VB_2. There is an observed coulombic increase of the characteristic first (higher voltage) plateau of TiB_2. Furthermore, there is an increase in the overall efficiency of the cell. Additionally, we report a substantial increase in the initial plateau region for the composite cell when compared to the macroscopic VB_2 discharge curve, characteristic of the TiB_2 discharge effects. The higher voltage may be attributed to the higher conductivity of the titanium based anodic material. This observed trend continues into the larger capacity cells where a typically ~30 mAh VB_2 cell discharges to an average percent coulombic efficiency of ~40%. With the addition of only 10% TiB_2 by weight to the VB_2 anode composition, an increase in coulombic efficiency from 40 to 50% was observed, as well as a 0.2 V increase to the initial voltage of 0.8 V. These results provide evidence for an improved VB_2 anode by the addition of TiB_2. Further work is needed to understand the specific changes that occur during discharge of the composite that result in increased capacities. We are also currently investigating (i) solution phase additives, and (ii) an enhanced current collector conductive matrix to further advance the coulombic efficiency and maintain high stability for the boride/air battery. We are also exploring molten electrolytes to transition boride/air from a primary to a rechargeable battery.[19,20]

Acknowledgments

The authors are grateful for support of this study by the National Science Foundation (Award 1006568) and the Air Force (SBIR award FA8650-13-C-5174).

References

1. Y. Li and H. Dai, *Chem. Soc. Rev.*, **43**, 5257 (2014).
2. S. Licht, X. Yu, and D. Qu, *Chem. Comm.*, 2753 (2007).
3. S. Licht, X. Yu, Y. Wang, and H. Wu, *J. Electrochem. Soc.*, **155**, A297 (2008).
4. H. Yang, Y. Wang, X. Ai, and C. Cha, *Electrochem. Sol. State. Lett.*, **7**, A212 (2004).
5. M. Pourbaix, *Atlas d'Equilibres Electrochimiques*, p. 219, 243, Gauthier-Villars, Paris (1963).
6. Y. Wang, X. Ai, Y. Cao, and H. Yang, *Electrochem. Comm.*, **6**, 780 (2004).
7. X. Yu and S. Licht, *Electrochim. Acta*, **52**, 8138 (2007).
8. X. Yu and S. Licht, *J. Power Sources*, **179**, 407 (2009).
9. S. Licht, H. Wu, X. Yu, and Y. Wang, *Chem. Comm.*, 3257 (2008).
10. V. Caramia and B. Bozzini, *Mater. Renew. Sustain. Energy*, (2014).
11. L. Shi, Y. Gu, L. Chen, Z. Yang, J. Ma, and Y. Qian, *Mat. Lett.*, **58**, 2890 (2004).
12. J. W. Kim, H. Shim, J. Ahn, Y. Cho, J. Kim, and K. Oh, *Mat. Lett.*, **62**, 2461 (2008).
13. S. Licht, S. Ghosh, B. Wang, D. Jiang, J. Asercion, and H. Bergmann, *Electrochem. Solid-State Lett.*, **14**, A83 (2011).
14. S. Licht, C. Hettige, J. Lau, U. Cubeta, H. Wu, J. Stuart, and B. Wang, *Electrochem. Solid-State Lett.*, **15**, A1 (2012).
15. J. Stuart, R. Lopez, J. Lau, X. Li, M. Waje, M. Mullings, C. Rhodes, and S. Licht, *JOVE, J. Vis. Exp.*, http://www.jove.com/video/50593, (78), e50593, (2013).
16. C. Rhodes, J. Stuart, R. Lopez, X. Li, M. Waje, M. Mullings, J. Lau, and S. Licht, *J. Power Sources*, **239**, 244 (2013).
17. B. Emrich, Literature Survey on Synthesis Properties and Applications of Selected Boride Compounds, *Air Force Tech. Rep. no. ASD-ATR-62-873* (1962).
18. J. Stuart, A. Hohenadel, X. Li, H. Xiao, J. Parkey, C. Rhodes, and S. Licht, *J. Electrochem. Soc*, **162**(1) A192 (2015).
19. S. Licht, B. Cui, J. Stuart, B. Wang, and J. Lau, *Energy Environ. Sci.* **6**, 3646 (2013).
20. B. Cui and S. Licht, *J. Mat. Chem. A*, **2**, 10577 (2014).

VOLUME 285

Science

www.sciencemag.org

Energetic Iron(VI) Chemistry: The Super-Iron Battery

Stuart Licht,* Baohui Wang, Susanta Ghosh

Higher capacity batteries based on an unusual stabilized iron(VI) chemistry are presented. The storage capacities of alkaline and metal hydride batteries are largely cathode limited, and both use a potassium hydroxide electrolyte. The new batteries are compatible with the alkaline and metal hydride battery anodes but have higher cathode capacity and are based on available, benign materials. Iron(VI/III) cathodes can use low-solubility K_2FeO_4 and $BaFeO_4$ salts with respective capacities of 406 and 313 milliampere-hours per gram. Super-iron batteries have a 50 percent energy advantage compared to conventional alkaline batteries. A cell with an iron(VI) cathode and a metal hydride anode is significantly (75 percent) rechargeable.

Improved batteries are needed for various applications such as consumer electronics, communications devices, medical implants, and transportation needs. The search for higher capacity electrochemical storage has focused on a wide range of materials, such as carbonaceous materials (*1*), tin oxide (*2*), grouped electrocatalysts (*3*), or macroporous minerals (*4*). Of growing importance are rechargeable (secondary) batteries such as metal hydride (MH) batteries (*5*), which this year have increased the commercial electric car range to 250 km per charge. In consumer electronics, primary, rather than secondary, batteries dominate. Capacity, power, cost, and safety factors have led to the annual global use of approximately 6×10^{10} alkaline or dry batteries, which use electrochemical storage based on a Zn anode, an aqueous electrolyte, and a MnO_2 cathode, and which constitute the vast majority of consumer batteries. Despite the need for safe, inexpensive, higher capacity electrical storage, the aqueous MnO_2/Zn battery has been a dominant primary battery chemistry for over a century. Contemporary alkaline and MH batteries have two common features: Their storage capacity is largely cathode limited and both use a KOH electrolyte.

We report a new class of batteries, referred to as super-iron batteries, which contain a cathode that uses a common material (Fe) but in an unusual (greater than 3) valence state. Although they contain the same Zn anode and electrolyte as conventional alkaline batteries, the super-iron batteries provide >50% more energy capacity. In addition, the Fe(VI) chemistry is rechargeable, is based on abundant starting materials, has a relatively environmentally benign discharge product, and appears to be compatible with the anode of either the primary alkaline or secondary MH batteries.

The fundamentals of MnO_2 chemistry continue to be of widespread interest (*6*). The storage capacity of the aqueous MnO_2/Zn

Department of Chemistry and Institute of Catalysis Science, Technion—Israel Institute of Technology, Haifa 32000, Israel.

*To whom correspondence should be addressed. E-mail: chrlicht@techunix.technion.ac.il

battery is limited by the charge capacity of MnO_2 [308 milliampere hours per gram (mA·hours/g)], compared to that of Zn (820 mA·hours/g). Alternative cathodes, such as Ag or air, have found only limited application because of their cost and power density limitations, respectively. Unusual cathodes, such as aqueous S (*7*), can inhibit the discharge behavior of conventional anodes such as oxidation of Zn to zincates. The aqueous MnO_2/Zn battery continues to contain either an ammonium chloride electrolyte (developed around 1860), an acidic chloride electrolyte, or, more recently, an alkaline electrolyte. In the latter, the electrolyte is not consumed during discharge, which increases the energy storage capacity. Additionally, the high alkaline conductivity can improve battery performance in the high-power domain (*8*). An attractive replacement will have higher capacity than MnO_2, but will remain compatible with the Zn anode and the alkaline electrolyte. Alternative cathodes that we studied use Fe(VI) compounds. Because of their highly oxidized Fe basis, multiple electron transfer, and high intrinsic energy, we refer to the new cell containing these compounds as a "super-iron" battery.

Iron typically occurs as a metal, or in the valence states Fe(II) or Fe(III). Although the Fe(VI) species has been known for more than a century, its chemistry remains relatively unexplored (*9*), evidently due to a misperception that the Fe(VI) species is intrinsically highly unstable. The decomposition of Fe(VI) occurs in reactions such as those presented in Eq. 1. Indeed, the rapid decomposition of Fe(VI) to the environmentally benign ferric oxide product via Eq. 1 has been the basis for suggesting the use of Fe(VI) as a safer alternative to the chlorination purification of water (*10*)

$$FeO_4^{2-} + 3/2H_2O \rightarrow FeOOH + 3/4O_2 + 2OH^- \quad (1)$$

Similarly, the strong oxidizing nature of Fe(VI) has been suggested for the oxidative preparation of a variety of organic compounds (*11*), including conditions for the oxidation of benzyl alcohol to benzaldehyde at 100% yield (*12*)

$$3C_6H_5OH + 2K_2FeO_4 \rightarrow 3C_7H_6O + Fe_2O_3 + 4KOH + H_2O \quad (2)$$

The reduction of Fe(VI) represents an energetic and high-capacity source of cathodic charge. We have investigated a variety of salts, including those with the following theoretical three-electron charge capacities determined as $3F \times MW^{-1}$, from the salt molecular weight, MW(g/mol) and the Faraday constant (F = 96,485 coulomb/mol = 26,801 mA·hours/mol): K_2FeO_4 (406 mA·hours/g), Na_2FeO_4 (485 mA·hours/g), Li_2FeO_4 (601 mA·hours/g), Cs_2FeO_4 (209 mA·hours/g), $SrFeO_4$ (388 mA·hours/g), Ag_2FeO_4 (240 mA·hours/g), $MgFeO_4$ (558 mA·hours/g), $CaFeO_4$ (503 mA·hours/g), $BaFeO_4$ (313 mA·hours/g), and $ZnFeO_4$ (434 mA·hours/g). The discharge of these solid materials as battery cathodes has not been previously reported. In particular, pure K_2FeO_4 and $BaFeO_4$ are readily synthesized (*13*). The K_2FeO_4 cathodic charge capacity is 32% greater than the equivalent MnO_2. The full 406 mA·hours/g storage capacity of K_2FeO_4 is obtained during discharge (Fig. 1), in accord with

$$FeO_4^{2-} + 3H_2O + 3e^- \rightarrow FeOOH + 5OH^- \quad (3)$$

or as the anhydrous product

$$FeO_4^{2-} + 5/2H_2O + 3e^- \rightarrow 1/2Fe_2O_3 + 5OH^- \quad (4)$$

The $BaFeO_4$, although of lower capacity than K_2FeO_4, discharges a higher fraction of this charge at higher current densities (Fig. 1 legend). Both Fe(VI) materials were used as synthesized. As exemplified by the history of MnO_2 optimization, Fe(VI) coulombic efficiency will be further affected by additives other than graphite, and control of packing, electrolyte, and particle size (*14*). The average discharge potential of the K_2FeO_4 cathode of 1.58 V versus Zn is 24% greater than the average for the equivalent MnO_2 cell (1.27 V), both determined to 90% depth of discharge (Fig. 1). Combined with the increased charge capacity, this potential also leads to a further increase in comparative energy capacity.

The fundamental solubility and stability constraints on FeO_4^{2-} chemistry are not well established. The $BaFeO_4$ and K_2FeO_4 Fe(VI) salts both combine attributes of very low alkaline solubility (Fig. 2, data inset) and high stability. Alternatively, Li_2FeO_4 and Na_2FeO_4 exhibit high solublities (~1 M) in alkaline hydroxide. The synthesized K_2FeO_4 is stable in a dehumidified environment and is readily mixed with graphite and molded as a cathode under pressure. The synthesized $BaFeO_4$ is highly stable in a humid environment and may be either pressed or formed as a paste.

The view of Fe(VI) species as intrinsically unstable is not correct. For example, an excess of K_2FeO_4 in contact with a concentrated KOH solution has a calculated stability of many years. Veprek-Siska and Ettel demonstrated that at elevated temperatures, the rapid decomposition of Fe(VI) is due to trace catalysis by Ni(II) and concluded "the rate of non-catalyzed decomposition is immeasur-

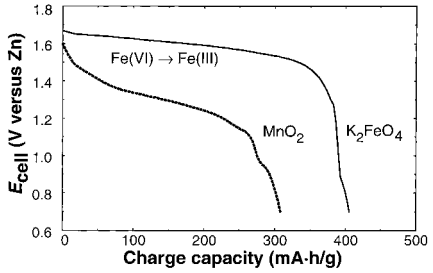

Fig. 1. Galvanostatic discharge at 0.5 mA/cm^2 of a K_2FeO_4 cathode compared to a MnO_2 cathode-limited Zn cell. Cell discharge was measured with Labview Software–interfaced Pine model AFCBP1 bipotentiostat at 22°C. The cathode consisted of either 17.3 mg (7 mA·hours) K_2FeO_4 or 22.7 mg (7 mA·hours) MnO_2, mixed with 30% graphite by weight. In each case, a commercial 1.1-cm-diameter button cell containing excess Zn was opened, and the cathode was removed and replaced with the 7-mA·hours cathode. Under these conditions, but at a higher current density of 5 mA/cm^2, the faradaic efficiency of a K_2FeO_4 cathode, discharged to 1 V, falls to 66% of the theoretical capacity of 406 mA·hours/g, whereas a $BaFeO_4$ cathode generates 85% of its theoretical capacity (313 mA·hours/g).

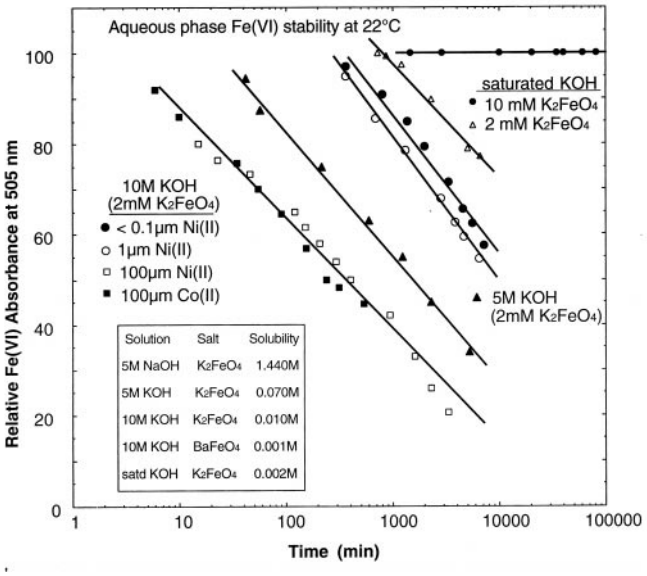

Fig. 2. Stability of Fe(VI) (1 week = 10,800 min), as measured by variation of the aqueous FeO_4^{2-} absorption occurring at 505 nm, and our measured 505-nm extinction coefficient $\varepsilon_{505nm}(FeO_4^{2-})$ of 1.1 mM^{-1} cm^{-1}. A relative absorption of 100 (as a percentage) refers to the initial FeO_4^{2-} concentration. Colloidal ferric oxide is generated if Fe(VI) decomposes. This interference is minimized by a 385-nm baseline correction and solution centrifugation before spectroscopic analysis. The indicated Ni(II) and Co(II) concentrations are prepared as added nitrate salts.

ably low" (*15*). We studied stability at room temperature (Fig. 2), by measuring the 505-nm wavelength peak absorption of FeO_4^{2-}. In 10 M KOH, the stability of K_2FeO_4 is increased by orders of magnitude, from hours to weeks, when the concentration of Ni(II) is decreased from 100 μM to <0.1 μM. The K_2FeO_4 exhibits similiar stability in KOH or NaOH (*16*) electrolytes. We observed that the catalyzed kinetics are first order for FeO_4^{2-} concentration. Hence, the half life of 0.001 M is the same as for 0.01 M K_2FeO_4, in solutions containing constant Ni(II) and OH^- concentrations.

The catalytic acceleration of Fe(VI) decomposition in solution is evident with <1 μM Ni(II). At the lowest Ni(II) concentrations, solution pretreatment (such as inducing decomposition of 2 mM K_2FeO_4 in KOH solution at 60° to 80°C, followed by removal of the decomposition products) can improve the subsequent Fe(VI) stability. Nickel(II) and Co(II) exhibit similiar catalytic effects (Fig. 2). However, we observed no other significant catalytic activity for salts not containing Ni(II) or Co(II), including the nitrates of added Cu(II), Fe(III), Zn(II), Pb(II), Ba(II), Sr(II), Ca(II), Mg(II), or other salts including $K_2Zn(OH)_4$, KIO_4, $K_2B_4O_9$, K_3PO_4, $Na_4P_2O_7$, Na_2SiF_6, Na_2SiO_3, Na_2MoO_4, or Na_2WO_4.

The observed stability of Fe(VI), as FeO_4^{2-}, is an order of magnitude greater in 10 M KOH compared to 5 M KOH. Continuing this trend, Fe(VI) is further stabilized in saturated (~13.5 M) KOH (Fig. 2). We correlate this phenomenon to a decrease in Ni(II) and Co(II) activity with an increase in hydroxide activity, as determined from the solubility product $K_{sp}[Ni(OH)_2] \approx K_{sp}[Co(OH)_2] \approx 10^{-15}$ and the tendency toward formation of these metal ions as the tri- and tetra-hydroxymetallates in concentrated hydroxide solutions. In this saturated KOH solution, Fe(VI) decomposes at a rate of 10^{-9} M/s. This rate is equivalent, in 1 ml of this solution, to a monthly loss of 0.0005 g K_2FeO_4. Hence in this solution, excess 10 mM (solubility 2 mM) K_2FeO_4, exhibits no change in absorbance at 505 nm for the measured period of 3 months (Fig. 2). This solution is prepared with 0.002 g/ml K_2FeO_4. However, a battery contains a much larger fraction of cathode mass, typically >1 g cathode per milliliter electrolyte. Extension of the data collected over a few months to predict behavior in 10 years is risky, but based on the measured solution-phase Fe(VI) decomposition rate, after 10 years there will be less than a 10% loss of 1 g K_2FeO_4 in contact with 1 ml concentrated KOH solution.

In a Zn alkaline battery the Zn anode generates a distribution of zinc oxide and zincate products, and similarly, the final Fe(VI) product will depend on the depth of discharge. For the respective K and Ba super-iron batteries, the cell discharge reaction may be generalized with M = K_2 or Ba as

$$M\text{Fe(VI)}O_4 + 3/2\text{Zn} \rightarrow 1/2\text{Fe(III)}_2O_3 + 1/2\text{ZnO} + M\text{Zn}O_2 \quad (5)$$

Equation 5 shows that OH^- generated during reductive discharge closely balances that consumed by a Zn anode. This is compatible with our observation that little electrolyte is required in the complete Fe(VI) storage cell.

A variety of super-iron Zn batteries have been prepared and discharged. The open-circuit potential observed in the super-iron Zn battery is modified by ±0.05 V with variation of packing conditions and electrolyte. Generally, the $BaFeO_4$ potential, at 1.85 V, is 0.1 V higher than the K_2FeO_4 battery at 1.75 V. On the basis of these open-circuit potentials and Eq. 5, the K_2FeO_4/Zn and $BaFeO_4$/Zn batteries have a respective maximum energy capacity of 475 W·hours/kg, and 419 W·hours/kg, both higher than the maximum of 323 W·hours/kg for a MnO_2/Zn battery; other Fe(VI) compounds suggest further storage capacity increases.

The energy capacities of several Fe(VI) and conventional MnO_2 cathode, alkaline primary batteries with a Zn anode have been measured and compared (Fig. 3). In both the low- (6000 ohm, current density $J \cong 0.25$ mA/cm^2) and high- (500 ohm, $J \cong 3$ mA/cm^2) discharge domain, the K_2FeO_4 cell generates significantly higher capacity than does the MnO_2 cell. Of the three cells examined, the $BaFeO_4$ cathode cell exhibits the highest coulombic efficiency at high discharge rates ($J > 10$ mA/cm^2), resulting in the observed higher energy capacity despite the lower intrinsic charge capacity of $BaFeO_4$ compared to K_2FeO_4.

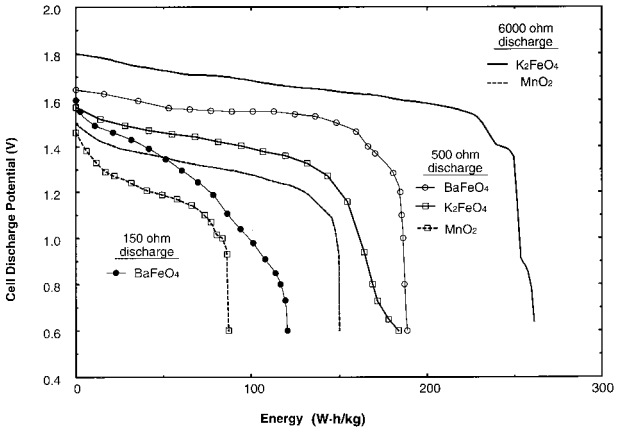

Fig. 3. Energy capacity of several super-iron and conventional MnO_2 cathode alkaline primary batteries with a Zn anode. In each case, a constant discharge load is used of either 150, 500, or 6000 ohms. The MnO_2 cells consist of conventional (commercial) 1.1-cm-diameter alkaline button cells rated at 31 mA·hours capacity. Super-iron cells were prepared by opening alkaline button cells and replacing the cathode with 31 mA·hours of either (i) 90% (76.3 mg) K_2FeO_4, 10% (9 mg) graphite, and 12 mg concentrated KOH, or (ii) 90% (106 mg) $BaFeO_4$, 10% (12 mg) graphite, and 30 mg concentrated KOH. Energy capacity is calculated from the mass of the anode, wet separator, and total cathode mass.

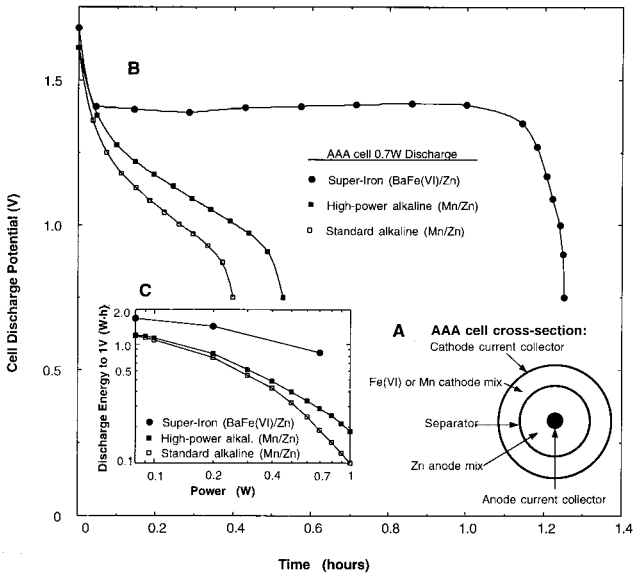

Fig. 4. The discharge of super-iron ($BaFeO_4$) compared to the discharge of standard or high-power alkaline MnO_2, each in AAA (cylindrical) cell configuration. (**A**) Cell cross-section. Total diameter is 10.1 mm, and height (*16*) of the cathode current collector is 42 mm. In the super-iron AAA experiments, components were removed from the standard alkaline cell, and the outer MnO_2 mix was replaced with a pressed $BaFeO_4$ mix (containing 90% $BaFeO_4$, 10% conductor, and 0.4 ml saturated KOH). This was followed by inclusion of the separator, Zn anode mix, and anode collector. (**B**) The cell potential measured during constant power discharge. (**C**) Measured energy capacity (watt-hour) versus power (watt) for the super-iron, high-power, or standard alkaline MnO_2 AAA cells. The data for the latter two cells is from (*17*).

The benefit of the facile charge-transfer capabilities of the conductive $BaFeO_4$ salt is evident in a cylindrical cell configuration (Fig. 4). Discharged to 1 V at 0.7 W high constant power, the $BaFeO_4$ cell provides 200% higher energy compared to advanced MnO_2 alkaline cylindrical AAA cells (0.86 W·hours compared to 0.285 W·hours). Common cylindrical cells range in volume from approximately 3 to 50 cm^3 for AAA up to D-type configurations. This geometry requires an increase in material scale by two orders of magnitude compared to the simple "button" configuration, and provides an ongoing challenge in cell optimization. Industry regularly reports incremental increases in alkaline cylindrical MnO_2/Zn energy density and, most recently, has reported advances in the high-power discharge domain. One recent posted advanced result is determined at constant power discharge (Fig. 4, inset) (*17*). Compared to these conventional advanced alkaline cells, the $BaFeO_4$ cell provides a 200% higher energy capacity under high-drain (0.7 W discharge) and a 40% increased capacity under low-drain (0.08 W) conditions. The cylindrical $BaFeO_4$ cell uses the conventional cell Zn anode mix, anode current collector, and separator. In future experiments, with specific optimization for the super-iron cell, further energy capacity increases are expected.

Conventional MH batteries, with a capacity up to 95 W·hours/kg (*5*), compared to 40 W·hours/kg for NiCd, have advanced to where further energy storage improvements are largely limited by the cell's heavy nickel oxyhydroxide (NiOOH) cathode. This situation is analogous to the limitations of MnO_2 for primary Zn batteries and is accentuated by the lower limiting NiOOH cathode capacity of ~290 mA·hours/g. These important secondary (rechargeable) batteries use alkaline KOH electrolyte.

We have also probed the reversible nature of Fe(VI) chemistry. An Fe(VI) charge-limited open-cell experiment provides fundamental evidence that the Fe(VI) cathode is significantly rechargeable. The cell has been discharged to 75% cathode capacity depth of discharge (DOD) for several cycles and more than 400 cycles at 30% DOD. The cell consists of an excess of MH anode (35 mA·hours, removed from a GP 35BVH button cell), and a limiting Fe(VI) cathode (9 mA·hours based on 406 mA·hours/g K_2FeO_4, using a Teflon mesh pressed over the K_2FeO_4 mix), in excess 12 M KOH electrolyte. The cell potential varies from 1.3 V (open circuit) to 1.1 V (at 5 mA/cm^2) and is cycled at 2.5 mA charge and 1 mA discharge. This cell has a characteristic voltage similar to the conventional MH battery because of the similarity of the Fe(VI) potential to the 0.5 V formal potential of NiOOH.

In the primary-battery studies, the AAA cell configuration has been used only to provide a clear comparison to existing optimized electrochemistries. The engineering of MnO_2 into a conventional cylindrical cell is an ongoing process which has taken many decades. Engineering studies of the new Fe(VI) cathode will also be an ongoing process. Further research probing, stabilizing, and releasing the substantial storage of other Fe(VI) cathodes will be needed. For example, a composite high-capacity Fe(VI) cathode containing several Fe(VI) salts also exhibits efficient discharge in the high-current domain, and, as in the K_2FeO_4 and $BaFeO_4$ cells in this study, generates significantly greater energy capacity than in conventional alkaline batteries.

References and Notes

1. J. R. Dahn, T. Zheng, Y. Liu, J. S. Xue, *Science* **270**, 590 (1995).
2. Y. Idota, T. Kubota, A. Matsufuji, Y. Maekawa, T. Miyasaka, *ibid.* **276**, 1395 (1997).
3. E. Reddington *et al.*, *ibid.* **280**, 1735 (1998).
4. B. T. Holland, C. F. Blanford, A. Stein, *ibid.* **281**, 538 (1998).
5. S. R. Ovshinsky, M. A. Fetcenko, J. Ross, *ibid.* **260**, 176 (1993); S. K. Dhar *et al.*, *J. Power Sources* **65**, 1 (1997).
6. Z. Rong *et al.*, *Science* **276**, 926 (1997).
7. D. Peramunage and S. Licht, *ibid.* **261**, 1029 (1993).
8. S. Licht, D. Peramunage, N. Myung, *J. Phys. Chem. B.* **102**, 6780 (1998).
9. M. D. Johnson and J. F. Read, *Inorg. Chem.* **35**, 6795 (1996).
10. J. D. Carr *et al.*, Proceedings of the 5th Conference, *Water Chlorination*, Williamsburg, VA, 3 to 8 June 1984, R. L. Jolley, Ed., (Lewis, Chelsea, MI, 1985), pp. 1285–1298; V. K. Sharma, J. O. Smith, F. J. Millero, *Environ. Sci. Technol.* **31**, 2486 (1997).
11. M. D. Johnson and B. Hornstein, *Chem. Commun.* **1996**, 965 (1996).
12. L. Delaude and P. A Laszlo, *J. Org. Chem.* **61**, 6360 (1996).
13. Using analytical grade reagents of 97 to 99% purity, K_2FeO_4 was synthesized from alkaline hypochlorite treatment of $Fe(NO_3)_3$ as described in (*12*). The dried product is stable in time. The $BaFeO_4$ was synthesized from 0.25 M (97 to 99% pure) K_2FeO_4 dissolved in 2% KOH solution at 0°C, and filtered into an equivalent volume of 0.39 M (analytical grade) $Ba(C_2H_3O_2)_2$ solution at 0°C. Solutions were prepared without CO_2 in deionized water. The precipitate was filtered, washed with water, and freeze dried (using a Labconco Lyph-Lock Freeze Dry System), producing 98.5 ± 0.5% purity $BaFeO_4$. The Li_2FeO_4, Na_2FeO_4, and Cs_2FeO_4 were prepared in a manner similar to K_2FeO_4 (hypochlorite oxidation) but yielded lower purity. The $SrFeO_4$, Ag_2FeO_4 $MgFeO_4$, $CaFeO_4$, and $ZnFeO_4$ were investigated in a manner similar to $BaFeO_4$ (precipitation from a K_2FeO_4 solution) but yielded lower purity.
14. J. Chen and H. Y. Che, *J. Electrochem. Soc.* **140**, 1205 (1993).
15. J. Veprek-Siska and V. Ettel, *Chem. Ind.* **1967**, 548 (1967).
16. S. Licht, B. Wang, S. Ghosh, data not shown.
17. Duracell Web site, file MX2400.pdf (ULTRA vs. Standard AAA) downloaded 24 June 1999. (www.duracell.com/OEM/Primary/Alkaline/alkaline_manganese_data.html.)

18. We thank V. Naschitz, J. Li, S. Shesternin, and V. Nair, who participated in synthesis of the Fe(VI) compounds, and G. Xu, V. Goldstein, O. Khaselev, and E. Kvashnina who participated in cell discharges.

25 May 1999; accepted 2 July 1999

Energies **2010**, *3*, 960-972; doi:10.3390/en3050960

OPEN ACCESS

energies

ISSN 1996-1073

www.mdpi.com/journal/energies

Review

A High Capacity Li-Ion Cathode: The Fe(III/VI) Super-Iron Cathode

Stuart Licht

Department of Chemistry and Institute of Basic Energy Science and Technology, George Washington University, Washington, DC 20052, USA; E-Mail: slicht@gwu.edu; Tel.: +1-703-726-8225

Received: 31 March 2010 / Accepted: 12 April 2010 / Published: 6 May 2010

Abstract: A super-iron Li-ion cathode with a 3-fold higher reversible capacity (a storage capacity of 485 mAh/g) is presented. One of the principle constraints to vehicle electrification is that the Li-ion cathode battery chemistry is massive, and expensive. Demonstrated is a 3 electron storage lithium cathodic chemistry, and a reversible Li super-iron battery, which has a significantly higher capacity than contemporary Li-ion batteries. The super-iron Li-ion cathode consists of the hexavalent iron (Fe(VI)) salt, Na_2FeO_4, and is formed from inexpensive and clean materials. The charge storage mechanism is fundamentally different from those of traditional lithium ion intercalation cathodes. Instead, charge storage is based on multi-electron faradaic reduction, which considerably enhances the intrinsic charge storage capacity.

Keywords: cathode; Li-ion; super-iron; battery; electric vehicle; lithium battery

1. Introduction

Vehicle electrification provides significant advantages of fuel efficiency, which will decrease greenhouse gas emission, decrease the dependence on fossil fuel resources, and facilitate the transition to the renewable energy economy. However the rate of societal transition to electric vehicles is constrained by the low travel range and high battery cost of these vehicles. One of the principle constraints to vehicle electrification is that the Li-ion cathode battery chemistry is massive, and expensive. Demonstrated here is a transformative 3e- storage lithium cathodic chemistry, and a reversible Li super-iron battery with 3-fold higher capacity than contemporary cathodes. This super-iron Li-ion cathode has a storage capacity of 485 mAh/g, consists of the hexavlanent iron (FeVI)) salt, Na_2FeO_4, and is formed from inexpensive and clean materials. The charge storage mechanism is fundamentally different from those of traditional lithium ion intercalation cathodes.

Instead, charge storage is based on multi-electron faradaic reduction, which considerably enhances the intrinsic charge storage capacity.

The introduction of Li-ion systems has substantially increased electrochemical energy storage capacity [1]. Yet, contemporary rechargeable lithium batteries have only one fifth the volumetric energy density of gasoline, and require five times the gas tank volume to travel the same distance [2]. The cathode comprises the main mass component of contemporary Li-ion batteries. For example, the commonly used $LiCoO_2$ cathode and Li-Co-Mn-Ni variants have capacities of 80–150 mAh/g, but are cost limited by the relative scarcity and high price of cobalt (which is up two orders of magnitude more expensive than iron). The cobalt is associated with significant toxicity hazards.

An alternative to $LiCoO_2$ cathode, $LiMn_2O_4$, has an even lower capacity of 100 mAh/g. A popular new cathode $LiFePO_4$, contains divalent iron, Fe(II), and can store up to 170 mh/g [3,4]. An attraction of this cathode is the availability and low cost of the source reagents (iron is the most common metal in the earth's crust). $LiFePO_4$ can sustain higher power densities than equivalent cobalt or manganese cathodes. However, Li-ion $LiFePO_4$ batteries operate at lower voltage than those with cobalt and manganese based cathodes, and also have approximately 20% lower energy storage density.

Development of 3e- Fe(VI) charge storage. An unusual class of iron salts was pioneered by our group as inorganic charge storage salts in 1999, and named super-irons due to their highly oxidized hexavalent iron state [5,6].

Key milestones in the super-iron battery development to date are of Table 1.

Table 1. Timeline of Fe(VI) charge storage development.

Year	Development	Reference
1999	introduction of super-iron charge storage & super-iron alkaline battery	[5]
2000**	introduction of super-iron lithium primary (single discharge) battery	[7]
2001	demonstration of the solid state stability of the hexavalent iron	[8]
1999-5	chemical syntheses of an array of super-iron salts	[5,7,9-16]
2000-4	inexpensive, electrochemical syntheses of super-iron salts	[17-26]
2003-5**	electrolyte optimization for super-iron lithium batteries	[27,28]
2003	reversibility of alkaline, nanothick (3 nm) Fe(VI) cathodes	[29]
2006	rechargeable alkaline super-iron battery	[30]
2006**	reversibility of non-aqueous, nanothick (3 nm) Fe(VI) cathodes	[31]
2007-8	zirconia encapsulation–stabilization of alkali super-irons	[32-35]
2009**	rechargeable super-iron lithium battery, 4 V cathode	[6]

**=lithium super-iron battery development.

2. Results and Discussion

2.1. The challenge of facile Fe(VI) charge transfer

The principal limitation to facile Fe(VI) charge transfer has been passivation of the couple due to resistive buildup of low-conductivity ferric (Fe(III)) salts, as schematically represented in the lower left corner of Scheme 1 [32,36,37]. We have demonstrated that the addition of simple transition metal

oxides, such as manganese or silver oxide (shown in the scheme), to form a composite with alkali or alkali earth super-irons, considerably facilitates the rate of super-iron charge transfer through chemical and mediation of charge transport mechanisms [38-42].

Chemical mediation acts to displace passivating Fe(III) centers into the bulk and away from the current collectors, while the electronic mediation provides alternative, more conductive pathways for charge transport. We have also demonstrated that a zirconia overlayer facilitates alkal Fe(VI) charge transfer in alkali media [32-35]. Most recently, we have also shown that an external conductive matrix, such as platinized, platinum considerably enhances reversible, non-aqueous Fe(VI) charge transfer [5].

Scheme 1. Modes of Fe(VI) charge transfer and passivation. Bottom: middle-Chemical mediated, and right-electronic mediated, Fe(VI) charge transfer. Bottom-left: Fe(III) inhibition and passivation of charge transfer. Top: Nanofilm enhanced reversible Fe(VI) charge transfer.

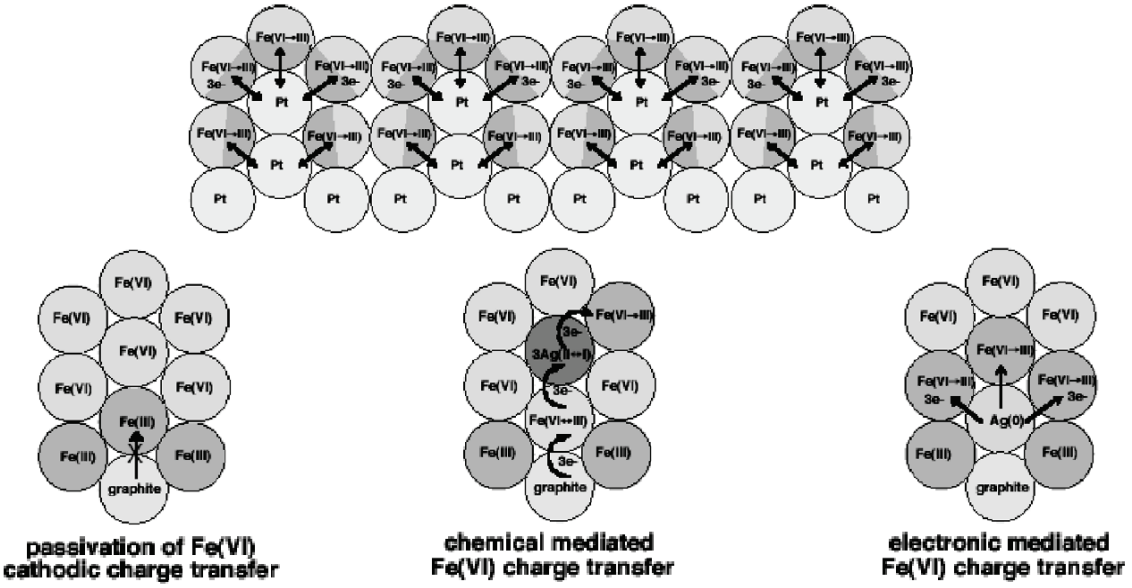

2.2. Reversible non-aqueous 3e- Fe(VI) charge storage

The basis for improved electrochemical storage capacity using the super-iron Li battery:

(i) Fe(VI) nonaqueous charge transfer is constrained by reduction, not intercalation.
(ii) Fe(VI) cathodes store the charge equivalent to 3 electrons per iron center,
(iii) an extended conductive matrix facilitates reversible Fe(VI) reduction,
(iv) the redox Fe(VI) potential is 0.25 V larger than that of Li-Mn or Li-Co cathodes.

The Fe(VI) redox storage potential *versus* lithium has increased from an observed 3 V, to over 4 V, in the past 3 years. With advent of the 485 mAh/g lithium non-aqueous cathode, and with use of the conductive matrix, the reversible, non-aqueous super-iron has increased 200 fold in thickness (from 3 nm to over 600 nm).

In 2009, we presented the first reversible super-iron Li batteries, cells operating at high voltage (over 4 volt) and a cathode capacity of 485 mAh/g, several fold higher than the cathodes in contemporary Li-ion batteries [6]. The capacity is based on the intrinsic three electron storage of

Na_2FeO_4, 50 nm thick cathodes were cycled at over 90% DOD (depth of discharge), and 191 and 573 nm thick cathodes were cycled at over 80% (400 mAh/g). Charge and discharge voltage during 300 recharge cycles are shown in Figure 1.

Figure 1. Extended galvanostatic cycling charge-transfer behavior for a super-iron Li battery containing a 191-nm thick Fe(III/VI) Na_2FeO_4 cathode film. (a) Cell potential during charge and (b) cell potential during discharge. Charge/discharge cycle numbers are indicated. Results are detailed in Licht, Wang, Gourdin, Enhancement of Reversible Nonaqueous Fe(III/VI) Cathodic Charge Transfer, *Journal of Physical Chemistry*, *C*, *133*, 9884–9891 (2009).

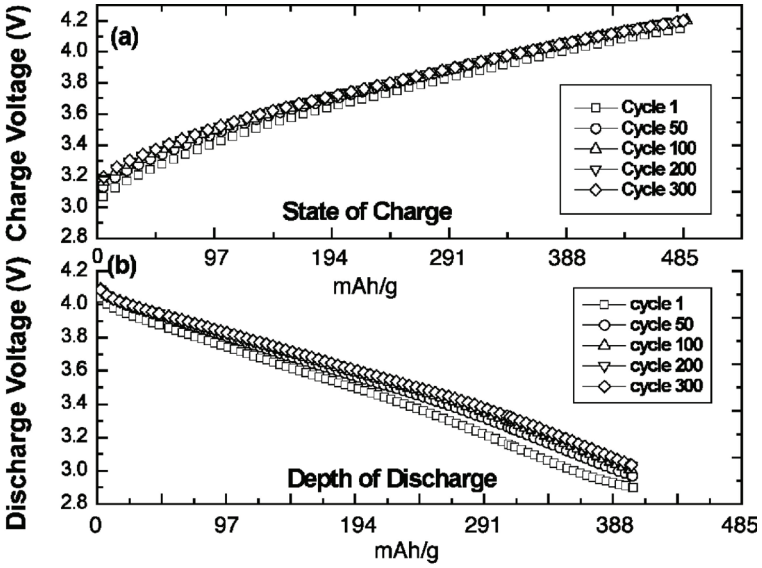

Rather than the typical intercalation mechanism of conventional Li and Li-ion cathodes, the super-iron discharge involves reduction from Fe(VI to III), as confirmed by AA, Mossbauer and charge measurements in the electrochemical processes. To date this was demonstrated as 3 Faraday per mole of Na_2FeO_4 (an intrinsic 485 mAh/g capacity), K_2FeO_4 (an intrinsic 408 mAh/g capacity) or $BaFeO_4$ (314 mAh/g) in accord with the discharge mechanism [6]:

$$MFe(VI))O_4 + 3e^- + 3Li^+ \rightarrow MO + 3/2Li_2O + 1/2Fe(III)_2O_3,\ M= K_2,\ Na_2 \text{ or } Ba \quad (1)$$

2.3. Preparation of Super-Iron Cathode Films

The electrochemical preparation of Fe(III/VI) super-iron thin films cathodes on an extended conductive matrix significantly facilitates such film's nonaqueous, reversible charge transfer. Fe(VI) salts can exhibit higher cathodic capacity and environmental advantages, and the films are of relevance toward the next generation charge storage chemistry for reversible cathodes. These films were electrochemically deposited by electrochemical reduction of Na_2FeO_4, which retains an intrinsic 3 e^- cathodic charge storage capacity of 485 mAh g^{-1}. The influence on cathode reversibility, capacity and charge retention was probed as function of film deposition conditions (including the deposition potential and stirring rate, and the concentration of NaOH and K_2FeO_4, in the deposition electrolyte).

Initially to optimize deposition conditions, super-iron films were electrodeposited from various alkaline K_2FeO_4/NaOH solutions at an applied potentiostatic voltage of 0.11 V *vs.* Ag/AgCl in a voltammetric Plexiglas cell, and optimized as a function of solution composition. Subsequently, super-iron films were consistently electrodeposited from 50 mM K_2FeO_4 dissolved in stirred (magnetic bar), 8.0 M NaOH in a voltammetric Plexiglas cell at a galvanostatic current of 10.0 mA. The working electrode was a 1 cm^2 platinum disc or a 1 cm^2 platinized, platinum disc. The auxiliary electrode was a platinum rod, and the reference electrode was an Ag/AgCl/ KCl (sat) encased in a 0.1 M $NaNO_3$ jacket. Solutions were initially de-aerated with nitrogen gas for a minimum of 5 min prior to the electro-deposition. A N_2 gas atmosphere was maintained over the solution during the electrodeposition. The film electrode was carefully rinsed with 8.0 M NaOH solution, air dried for 30 minutes, and then vacuum dried for 2 days prior to use.

During the optimization of the electrodeposition process, the surface of the working electrode was rinsed at each end of the experiment by an oxidative linear potential scan in 1.0 M HCl solution. Employed voltammetric Plexiglas cells were consistently, cleaned by soaking overnight in a solution of 10^{-2} M nitric acid, followed by DI water rinse, and results presented are the average of three replicate measurements. For Fe(III/VI) film formation, at the optimized deposition potential employed, the electrodeposition via the 3 electron reduction of Fe(VI) to Fe(III) substantially dominates, permitting the current efficiency to be assumed as 100%. Hence, the intrinsic capacity of the super-iron films determined by integrating the current-time response curve, Q(C = coulombs = ampere seconds), provides a quantitative measure of the intrinsic charge capacity of the super-iron films and, for convenience, a relative (not absolute) measure of the film thickness. The relative comparison of film thicknesses, T, is quantitative for all compared electrodes. For example a 19 nm Fe(III/VI) films contains 69 nanaomole of Fe per cm^2, and is capable of storing 20 mC of intrinsic capacity per cm^2 (based on the observed 3 electrons of storage per Fe(III/VI) center). Similarly, thicker deposited 57, 191 and 573 nm Fe(III/VI) films used in this study, have an intrinsic storage capacity respectively of 60, 202 and 605 mC per cm^2.

The solid state stability (stable to > 99.9% year retention of the Fe(VI) valence state), and storage time, for K_2FeO_4 is much greater than for Na_2FeO_4, and hence it has been our chemical dissolution salt of choice. In this study, the effects on Fe(III/VI) charge storage on smooth platinum were conducted by varying the concentrations of [K_2FeO_4], [NaOH], electrodeposition potential and magnetic stirring rate, respectively.

Figure 2a presents the effect of the electrolyte, NaOH, concentration on charge storage in 50 mM K_2FeO_4. It is seen that the Fe(III/VI) charge storage capacity increased with increasing the concentration of NaOH from 1.0 to 8.0 M, while an increase beyond 8.0 M NaOH led to a decrease of Fe(III/VI) charge storage. Increasing NaOH concentration (from 1.0 to 8.0 M) will inhibit the K_2FeO_4 solution phase decomposition process (Equation 7), stabilizing the $MFeO_4^-$ or FeO_4^{2-} species (Equations 12 and 13), and as a result, the Fe(III/VI) charge storage is increased. In competition with this is the decrease in equivalent ionic conductivity of hydroxide with increasing concentration. For the NaOH electrolyte, this decrease is significant. For example at 18°C the equivalent conduction of NOH solutions, decrease from 160 to 108 S cm^2/equivalent, as concentration increases from 1 to 3 M, and the decrease is precipitous in more concentrated NaOH (decreasing to 69 S cm^2/ equivalent in 5 M NaOH). Consistent with the observed decrease in charge storage at 8 M NaOH, this decrease in

mobility at higher concentrations appears to dominate over the stabilization enhancement. Therefore, in order to obtain a favorable charge storage, a compromise between decomposition and ion mobility needs to be considered. Figure 2b presents the concentration effect of K_2FeO_4 on charge storage in 8.0 M NaOH. It was found that the storage charge increased with increasing the concentration of K_2FeO_4 until a plateau was formed about 45 mM of K_2FeO_4, which approaches the saturation point of K_2FeO_4 in 8.0 M NaOH. In subsequent experiments in this study, 8.0 M of NaOH and 50.0 mM of K_2FeO_4 were used in the following experiments, except in noted special cases. In this concentrated alkaline environment diffusion processes should be facilitated. Hence, variation of the (magnet bar) stirring rate was also probed, and generally, the higher the stirring rate, the greater the charge storage which can be obtained in the deposited Fe(III/VI) films; this is consistent with the expected compression of the diffusion layer with an increase in solution turbulence.

Figure 2. Electrodeposition optimization of a Fe(III/VI) film. Deposition conditions—applied potential: 110 mV *versus* Ag/AgCl; deposition time 10 s on a smooth platinum electrode; stirring rate: maximum, without disruptive turbulence: (a) the effect of NaOH concentration on charge storage in 50 mM K_2FeO_4 and (b), the effect of K_2FeO_4 concentration on charge storage in 8.0 M NaOH.

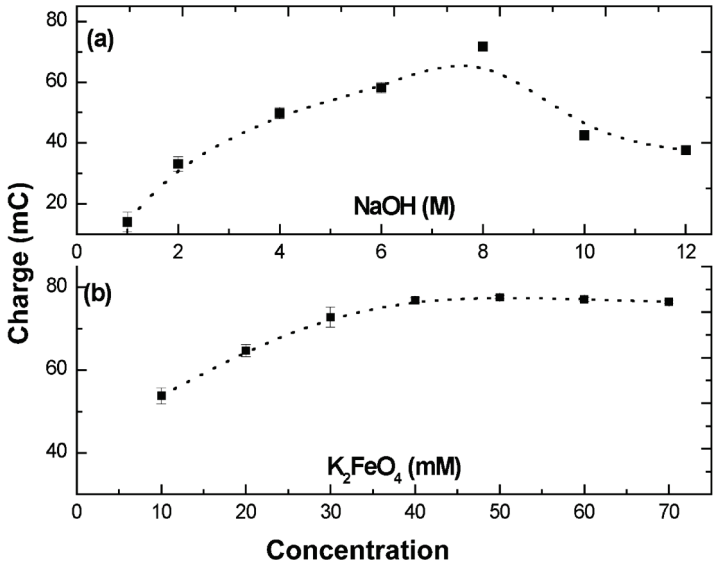

2.4. Characterization of Super-Iron Cathode Films

The 3-electron reduction of Fe(VI) can produce a variety of Fe(III) oxide and oxyhydroxide species such as (α,γ Fe_2O_3) and (α,γ,β,δ FeOOH). Sodium, over potassium, species will dominate in the 8 M N^+, 0.01 M K^+ deposition solution, and a variety of cation-containing ferric salts such $NaFeO_2$ are also possible in the film. Well-defined Fe_2O_3 particles gave three fundamental bands ranged from 500 cm^{-1}, 400 cm^{-1} to 300 cm^{-1} respectively, and the bands shifted with varying in size, shape, internal structure and aggregation of particles. In our experiment, the surface morphologies of thin Fe(III) film on smooth platinum were examined by a Nicolet Nexus 670 Fourier Transform Infrared Spectrophotometer.

Figure 3a presents the FTIR diffuse reflectance spectra (in absorbance mode) of a 191 nm thin Fe(III) film which was freshly electrodeposited on a 1 cm^2 platinum disk. A single peak at ~429 cm^{-1},

and a shoulder near 538 cm^{-1} are observed (far infrared spectra less than 400 cm^{-1} was not examined due to the instrumental limitations). For comparison, nanocrystalline γ-Fe_2O_3 particles was synthesized, and the FTIR absorption spectra of this particle is showed in Figure 3b. Two adjacent peaks near 1500 cm^{-1} appear to be associated with residual free hydroxide. The strong similarity between our Fe(VI) electrodeposited film Fe(III) and the nanocrystalline γ-Fe_2O_3 particles indicates this as a principal component of the Fe(III) film. In ongoing investigations, we continue to probe the identity of the Fe(III) centers in the reduced form of the film Fe(III/VI) films.

Figure 3. FTIR diffuse reflectance spectrum (in absorbance mode) of (a) a Pt/Fe(III) electrode and (b) a Fe_2O_3 sample. The electrodeposition conditions of Pt/Fe(III) are the same as above with 50 mM K_2FeO_4 in 8.0 M NaOH. The Fe_2O_3 samples are freshly synthesized.

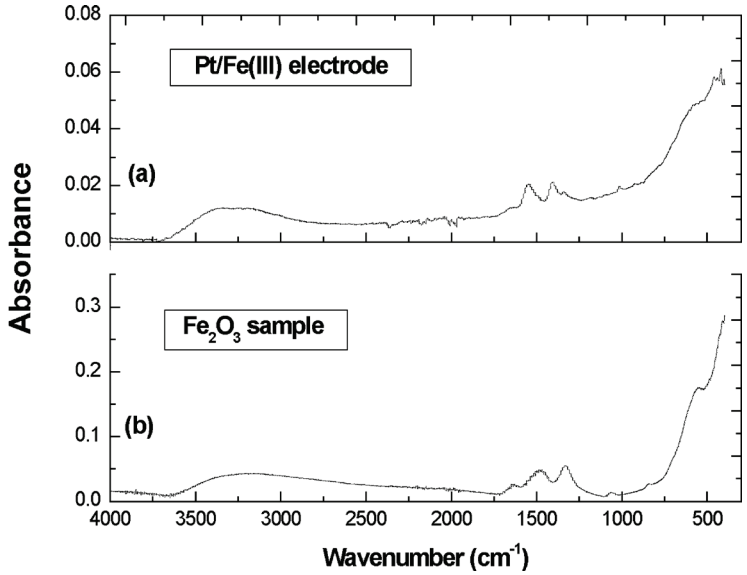

The Fe(III/VI) films were placed in a lithium cell with 1M LiPF6 in PC: DME (1:1) electrolyte, and their quasi-reversibility characterized as a function of hydroxide and Fe(VI) concentrations in the deposition solution. Specifically, a 191 nm Fe(III/VI) on smooth platinum was galvanostically deposited (at 10 mA, for 10s) in either 10, 50 or 80 mM K_2FeO_4. The film was placed in a lithium cell with 1M $LiPF_6$ in PC: DME (1:1) electrolyte, and cycled through periodic, galvanostatic charge/discharge cycles. Specifically, each cell was repeatedly subject to a 0.02 mA cm^{-2} charge, followed by a deep 0.01 mA cm^{-2} discharge.

Figure 4 presents the discharge voltage during the 20th discharge cycle as a function of the intrinsic, (100 mC , 3 electron) depth of discharge of these films. Figure 4a,b, respectively presents discharge cycle behavior for films prepared from either 8.0 M (4a) or 12.0 M (4b) deposition solutions. It is evident in Figure 4 that the average discharge voltage, and the depth of discharge are significantly higher for films deposited in 8 M, rather than 12 M, NaOH. Furthermore, in the preferred 8 M NaOH deposition solution, the average discharge voltage, and the depth of discharge are significantly higher for films deposited from 50 mM, rather than 10 or 80 mM K_2FeO_4 solutions. It is evident that the charge storage and transfer behavior of Fe(III/VI) thin-film cells are significantly influenced by the electrochemical deposition conditions. In the 50.0 mM K_2FeO_4, 8.0 M of NaOH prepared film,

the 20th discharge cycle commenced at 4.1 V and decayed to 3.1 V through an 80% depth of discharge, and no sharp decline of potential was observed within 20 cycles.

Figure 4. The discharge behavior of a 191 nm Fe(VI) film on a Pt electrode with various deposition conditions at 20th cycle. Films are deposited at a constant current of 10 mA for 10 s from electrolytes containing various [K_2FeO_4] in 8.0 M (a) or 12.0 M NaOH (b). Subsequent nonaqueous galvanostatic cycling consists of charge at 0.02 mA cm^{-2} to 100% of the intrinsic $3e^-$ Fe capacity, as limited by a maximum cut0ff voltage of 4.2 V, followed by discharge at 0.01 mA cm^{-2} to 90% DOD of this capacity as limited by a 1.5 V minimum voltage cutoff.

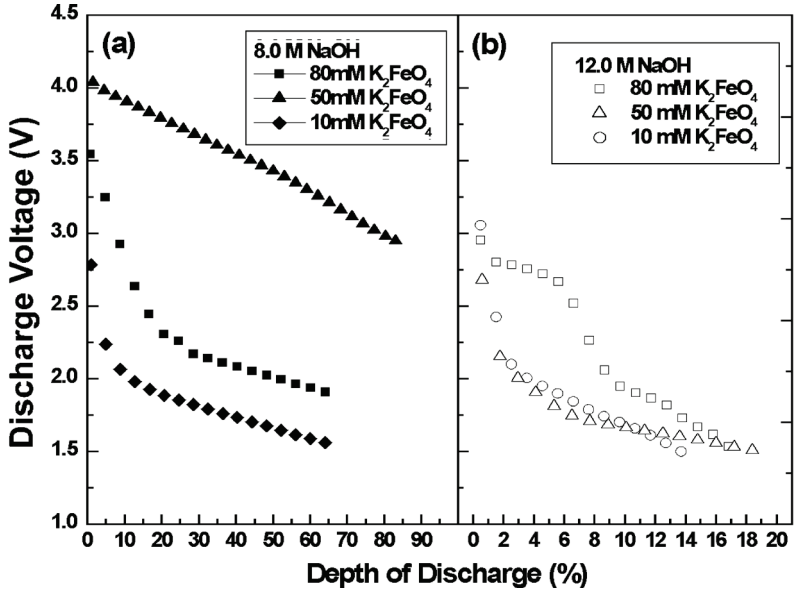

FTIR provides not only a specific "fingerprint" distinguishing the various Fe(VI) oxides, as shown in Figure 5, but importantly we have also developed it as a quantitative technique to determine the Fe(VI) salt purity through the addition of a standardized $BaSO_4$ salt [8]. Discharge of cathode replaced, commercial alkaline button cells provides rapid screening of the redox activity of alternative salts [6,10,11,14,15,19,27-35].

X-ray powder diffraction and Mössbauer are used to distinguish the variation of crystal structure and definitive nature of the iron state of super-iron oxides as a function of the state of charge/discharge of the cycled new cathode salts. As seen in Figure 6, we used these techniques to probe alkali and alkali earth super-iron oxides, and x-ray characterization of these salts has provided specific lattice parameters of their orthorhombic β-K_2SO_4 analogue structure.

As seen in Figures 1 and 6(right), we have the fascinating case of a cathode which can be reversibly, reformed by faradaic charge transfer, as in aqueous cells, but with the high voltage advantage of the nonaqueous environment.

Figure 5. IR absorption of solid K_2FeO_4, Rb_2FeO_4, Cs_2FeO_4, $BaFeO_4$, and $SrFeO_4$, mixed with a $BaSO_4$ standard. From Licht, S.; Naschitz, V.; Rozen, D.; Halperin, N. Cathodic charge transfer and analysis of Cs_2FeO_4, K_2FeO_4 and mixed alkali Fe(VI), ferrate, super-irons. *J. Electrochem. Soc*. **2004**, *151*, A1147–A1151.

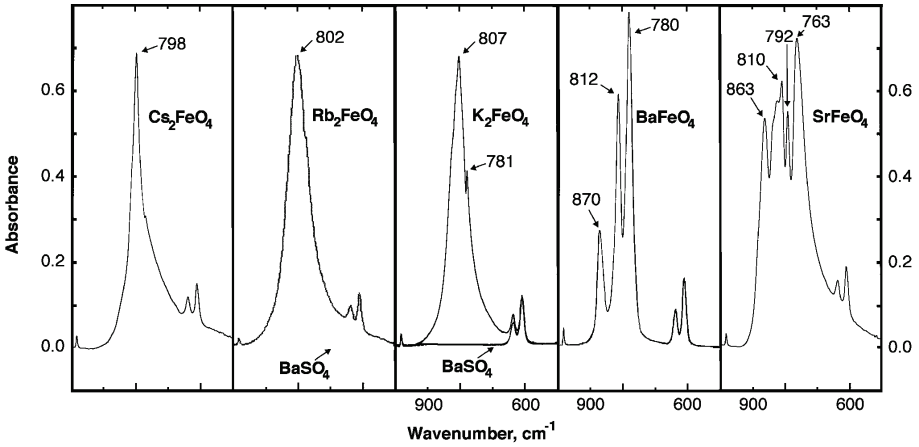

Figure 6. Left: X-ray analysis of Fe(VI) compounds, evidence of their orthorhombic β-K_2SO_4 analogue structure, from "Recent advances in the synthesis and analysis of Fe(VI) cathodes." Licht, *et al.*, *J. Solid State Electrochem.* **2008**, *12*, 1523. Right: Mössbauer spectra of K_2FeO_4: (a) pristine electrode, (b) polarized to 1.5V *vs.* Li/Li^+, and (c) after one complete lithiation cycle. From "Study of Various ("super iron") $MeFeO_4$ compounds in Li salt solutions as cathode materials for Li batteries." *J. Electrochem Soc.* **2006**, *153*, A32.

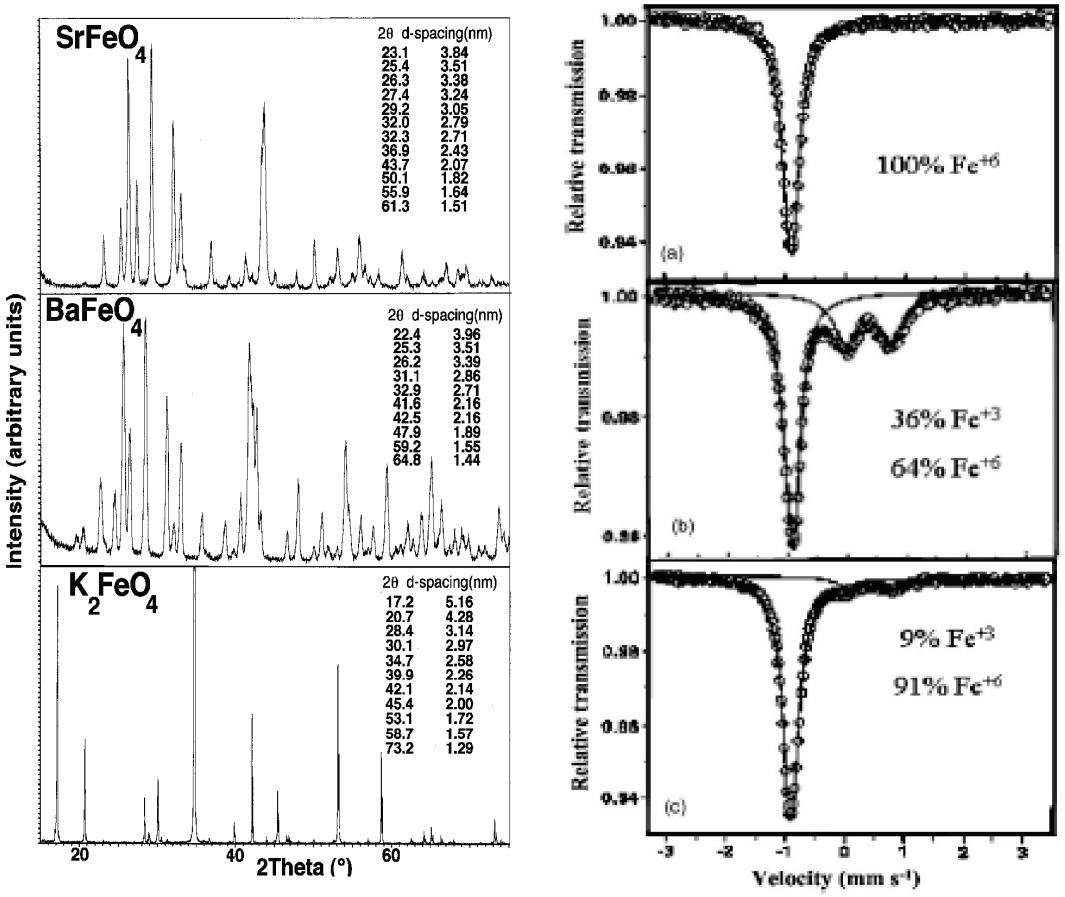

3. Conclusions

Vehicle electrification provides significant advantages of fuel efficiency, which will decrease greenhouse gas emission, decrease the dependence on fossil fuel resources, and facilitate the transition to the renewable energy economy. Principle constraints to vehicle electrification include that the Li-ion cathode battery chemistry is massive and costly. Limited battery capacity (vehicle range) and cost are hurdles to implementation. This is exemplified in a recent evaluation of Li-ion batteries for use in electrified vehicles, which concludes that after yield economies of scale, the "most significant cost component at the cell-level is the cathode active material", and which is three times more expensive than the anode material [43].

The super-iron cathode addresses the cathode challenge with a transformative $3e^-$ Fe(VI) storage Li-ion chemistry, with a capacity several fold higher than observed in conventional lithium-ion cathodes. Continued research will further advance these systems. For example, new nm-architectures need to be explored which preserve the high recharge voltage efficiency observed for the thin layer Fe(III/VI) films. As super-iron films are increased in thickness by a factor of two orders of magnitude, from a thickness of several nm [29] to a thickness approaching 1 μm [6], impedance losses increase, and impair the recharge voltage of efficiency. The thicker films retain a high coulombic efficiency, but exhibit a charge/discharge potential variation similar to super-capacitor, rather than battery, behavior. The super-iron lithium-ion battery is a Li-ion chemistry in which the cathode does not weigh down the battery, with a *transformative potential in terms of range increase of electric vehicles*.

Acknowledgements

S. Licht is grateful to the US Department of Energy and the George Washington University Institute of Basic Energy Science and Technology for partial support of this research. Yufei Wang, Gerald Gourdin and Lan Yang participated in the results reported in Figure 1 and Reference 6.

References and Notes

1. *Advances in Lithium-ion Batteries*; van Schalkwijk, W.A., Scrosati, B., Eds.; Springer: Berlin, Germany, 2002.
2. Licht, S.; Wu, H.; Yu, X.; Wang, Y. Renewable highest capacity VB_2/air energy storage. *Chem. Comm.* **2008**, *28*, 3257–3259.
3. Li, Z.; Zhang, D.; Yang, F. Developments of lithium-ion batteries & challenges of $LiFePO_4$ as one promising cathode material. *J. Mater. Sci.*, **2009**, *44*, 2435–2443.
4. Padhi, A.K.; Nanjundaswamy, K.S.; Goodenough, J.B. Phospho-olivines as positive-electrode materials for rechargeable lithium-ion batteries. *J. Electrochem. Soc.* **1997**, *144*, 1188–1194.
5. Licht, S.; Wang, B.; Ghosh, S. Energetic iron (VI) chemistry: The super-iron battery. *Science* **1999**, *285*, 1039–1042.
6. Licht, S.; Wang, Y.; Gourdin, G. Enhancement of reversible nonaqueous Fe(III/VI) cathodic charge transfer. *J. Phys. Chem. C* **2009**, *113*, 9884–9891.
7. Licht, S.; Wang, B. Non aqueous Iron(VI) chemistry: The lithium super-iron battery. *Electrochem. Solid State Lett.* **2000**, *3*, A 209–A212.

8. Licht, S.; Naschitz, V.; Halperin, L.; Halperin, L.; Lin, L.; Chen, J.; Ghosh, S.; Lui, B. Analysis of Ferrate(VI) compounds & super-Iron battery cathodes, FTIR, XRD, UV/Vis, ICP, electrochemical & chemical characterization. *J. Power Sources*, **2001**, *99*, 7–14.
9. Licht, S.; Wang, B.; Ghosh, S.; Jun, Li; Naschitz, V. Insoluble Fe(VI) compounds: Effects on the super-iron battery. *Electrochem. Comm.* **1999**, *1*, 522–526.
10. Licht, S.; Naschitz, V.; Ghosh, S.; Liu, B.; Halperin, N.; Halperin, L.; Rozen, D. Chemical synthesis of battery grade super-iron barium and potassium Fe(VI) ferrate compounds. *J. Power Sources* **2001**, *99*, 7–14.
11. Licht, S.; Naschitz, V.; Ghosh, S.; Lin, L.; Lui, B. $SrFeO_4$: synthesis, Fe(VI) characterization and the strontium super-iron battery. *Electrochem. Comm.* 2001, *3*, 340–345.
12. Yang, W.; Wang, J.; Pan, T.; Xu, J.; Xhang, J.; Cao, C. Studies on electrochem. characteristics of $K_2Sr(FeO_4)_2$ electrode. *Electrochem. Comm.* **2002**, *4*, 710–715.
13. Licht, S.; Naschitz, V.; Wang, B. Rapid chemical synthesis of barium ferrate, $BaFe(VI)O_4$. *J. Power Sources* **2002**, *109*, 67–70.
14. Licht, S.; Naschitz, V.; Rozen, D.; Halperin, N. Cathodic charge transfer and analysis of Cs_2FeO_4, K_2FeO_4 and mixed alkali Fe(VI), ferrate, super-irons. *J. Electrochem. Soc*. **2004**, *151*, A1147–A1151.
15. Licht, S.; Yang, L.; Wang, B. Synthesis and analysis of Ag_2FeO_4 Fe(VI) ferrate super-iron cathodes. *Electrochem. Comm.* 2005, *7*, 931–936.
16. Xu, Z.; Wang, J.; Shao, H.; Tang, Z.; Zhang, J. Preliminary investigation on the physiochemical properties of calcium ferrate. *Electrochem. Comm.* **2007**, *9*, 371–377.
17. Licht, S. Electrolytic production of solid Fe(VI) salts, PCT application No. LI00588. Patent No. WO0,121,856, 2000.
18. Lapique, F.; Valentin, G. Direct electrochemical preparation of solid potassium ferrate. *Electrochem. Comm.* **2002**, *4*, 764–766.
19. Licht, S.; Tel-Vered, R.; Halperin, L. Direct electrochemical preparation of solid Fe(VI) compounds and super-iron battery compounds. *Electrochem. Comm.* **2002**, *4*, 933–937.
20. Lee, J.; Tryk, D.; Fujishima, A.; Park, S. Electrochemical generation of ferrate in acidic media at boron-doped diamond electrodes. *Chem. Comm.* **2002**, *5*, 486–487.
21. De Koninck, M.; Brousse, T.; Belanger, D. The electrochemical generation of ferrate at pressed iron powder electrode: Effect of different parameters. *Electrochim. Acta* **2003**, *48*, 1425–1433.
22. Licht, S.; Tel-Vered, R.; Halperin, L. Towards efficient electrochemical synthesis of Fe(VI) ferrate, and super-iron battery compounds. *J. Electrochem. Soc*. **2004**, *151*, A31–A39.
23. Zhang, F.C.; Liu, Z.; Wu, F.; Lin, L.; Qi, F. Electrochemical generation of ferrate on SnO_2-Sb_2O_3/Ti electrodes in strong concentration basic condition. *Electrochem. Comm.* **2005**, *6*, 1104–1109.
24. Cañizares, P.; Arcís, M.; Sáez, C.; Rodrigo, M.A. Electrochemical synthesis of ferrate using boron doped diamond anodes. *Electrochem. Comm.* **2007**, *9*, 2286–2290.
25. Xu, Z.; Wang, J.; Mao, W.; He, W.; Chen, Q.; Zhang, J. The effects of ultrasound on the direct electrosynthesis of solid K_2FeO_4 and the anodic behaviors of Fe in 14 M KOH solution. *J. Solid State Electrochem* **2008**, *11*, 413–420.

26. Yu, X.; Licht, S. Advances in electrochemical Fe(VI) synthesis and analysis. *J. Appl. Electrochem.* **2008**, *38*, 731–742.
27. Licht, S.; Rozen, D.; Tel-Vered, R.; Halperin, L. Enhancement of nonaqueous Fe(VI) super-iron primary cathodic charge transfer. *J. Electrochem. Soc.* **2003**, *150*, A1671–A1675.
28. Koltypin, M.; Licht, S.; Tel-Vered, R.; Nashitz, V.; Aurbach, D. The Study of Licht, S.: Various ("super iron") $MeFeO_4$ (F^{6+}-super iron) compounds in Li salt solutions. *J. Power Sources* **2005**, *146*, 723–726.
29. Licht, S.; Tel-Vered, R. Rechargeable Fe(III/VI) super-iron cathodes. *Chem. Comm.* **2004**, *6*, 628–629.
30. Licht, S.; DeAlwis, C. Conductive matrix mediated charge transfer in Fe(III/VI): Three electron storage, reversible super-iron thin film cathodes. *J. Phys. Chem. B* **2006**, *110*, 12394–123404.
31. Koltypin, M.; Licht, S.; Nowik, I.; Levi, E.; Gofer ,Y.; Aurbach, D. The study of various ("super-iron") $MeFeO_4$ compounds in Li salt solutions as potential cathode materials for Li batteries. *J. Electrochem. Soc* **2006**, *153*, A32–A41.
32. Licht, S.; Yu, X.; Dhong, Z. Cathodic chemistry of high performance Zr coated alkaline materials. *Chem. Comm.* **2006,** *2006*, 4341–4343.
33. Licht, S.; Yu, X.; Qu, D. A novel alkaline redox couple: Chemistry of the Fe^{6+}/B^{2-} super-iron boride battery. *Chem. Comm.* **2007**, *2007*, 2753–2755.
34. Licht, S.; Yu, X.; Wang, Y.; Stabilized alkaline Fe(VI) charge transfer: Zirconia coating stabilized super-iron alkaline batteries. *J. Electrochem. Soc.* **2008**, *155*, A1–A7.
35. Licht, S.; Yu ,X.; Wang, Y.; Wu, H.; The super-iron boride battery. *J.Electrochem. Soc.* **2008**, *155*, A297–A303.
36. Ghosh, S.; Wen, W.; Urian, R.C.; Heath, C.; Srinivasamurthi, V.; Reiff, W.M.; Mukerjee, S.; Naschitz, V.; Licht, S. The reversible behavior of K_2FeO_4. *Electrochem. Solid State Lett.* **2003**, *6*, A260–A264.
37. Yu, X.; Licht, S. Recent advances in synthesis and analysis of Fe(VI) cathodes: solution phase and solid-state Fe(VI) syntheses, reversible thin-film Fe(VI) synthesis, coating-stabilized Fe(VI) synthesis. *J. Solid State Electrochem.* **2008**, *12*, 1523–1540.
38. Licht, S.; Ghosh, S.; Naschitz, V.; Halperin, N.; Halperin, L. Fe(VI) catalyzed manganese redox chemistry: Permanganate and super-iron batteries. *J. Phys. Chem. B* **2001**, *105*, 11933–11936.
39. Licht, S.; Naschitz, V.; Ghosh, S. Silver mediation of Fe(VI) charge transfer: Activation of the K_2FeO_4 super-iron cathode. *J. Phys. Chem. B* **2002**, *106*, 5947–5955.
40. Yu, X.; Licht, S. Advances in Fe(VI) charge storage: Part II. Reversible alkaline super-iron batteries and nonaqueous super-iron batteries. *J. Power Sources* **2007**, *171*, 1010–1022.
41. Licht, S.; Ghosh, S. High power $BaFe(VI)O_4$ /MnO_2 composite cathode alkaline super-iron batteries. *J. Power Sources* **2002**, *109*, 465–468.
42. Licht, S.; Naschitz, V.; Ghosh, S. Hydroxide activated $AgMnO_4$ alkaline cathodes, alone, and in combination with Fe(VI) super-iron, $BaFeO_4$. *Electrochem. Solid State Lett.* **2001**, *4*, A209–A212.

43. Anderson, D.L. *An evaluation of current and future costs for lithium-ion batteries for use in electrified vehicle powertrains*. Master Thesis, Duke University, Durham, NC, USA, May 2009. Available online: http://dukespace.lib.duke.edu/dspace/bitstream/10161/1007/1/Li-Ion%20Battery%20Costs%20-%20Anderson%20-%20MP%20Final.pdf (accessed on 25 April 2010).

THE JOURNAL OF PHYSICAL CHEMISTRY C

Article

pubs.acs.org/JPCC

Studying the Reversibility of Multielectron Charge Transfer in Fe(VI) Cathodes Utilizing X-ray Absorption Spectroscopy

Maryam Farmand, Stuart Licht,* and David Ramaker*

Department of Chemistry, George Washington University, 725 21st Street N.W., Washington D.C. 20052, United States

ABSTRACT: The superiron salts $BaFeO_4$ and K_2FeO_4 when utilized as battery cathodes both undergo a three electron charge transfer; however, they exhibit significantly different physical and electrochemical properties. K_2FeO_4 exhibits higher solid-state stability and higher intrinsic $3e^-$ capacity (406 mAh/g) than $BaFeO_4$ (313 mAh/g); however, the rate of cathodic charge transfer is considerably higher for $BaFeO_4$. To understand these differences, primary coin cells of alkaline batteries containing either μm-$BaFeO_4$, μm-K_2FeO_4, or nm-K_2FeO_4 (nm = nanometer, or μm = micrometer size particles) were constructed and discharged to various depths under a constant load. Discharged cathode composite were studied by ex-situ X-ray absorption measurements. The oxidation state of discharge product of the Fe local symmetry was followed by the magnitude of K-edge and pre-edge Fe 1s to 3d peak. To track structural changes, the extended X-ray absorption fine structure (EXAFS) χ functions of the partially discharged cathodes were subject to linear combination fitting. The expanded $BaFeO_4$ lattice, or the much larger surface-electrolyte interface in the nm-K_2FeO_4 materials, significantly increased their capacities compared to μm-K_2FeO_4. In the case of nm-K_2FeO_4, electron density is more distributed by water intercalation about the Fe hydrous environment, which relieves the "stress" of full Fe^{6+} to Fe^{3+} reduction. The stronger Ba−FeO_4 anion−cation interaction and increased lattice size apparently slows the rate of lattice rearrangement into the discharge product.

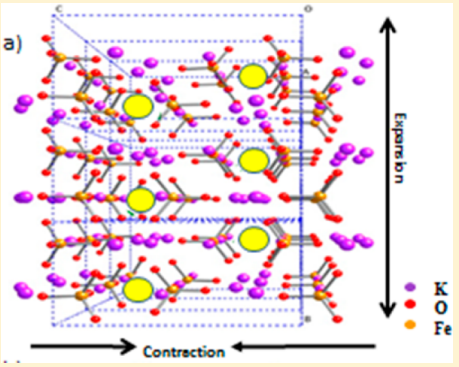

1. INTRODUCTION

The sharp increase in energy demands of modern portable electronics devices, such as laptops, and the critical need in future electric automobiles, necessitates the search for new materials that can potentially offer higher storage capacities beyond that of current Li ion batteries.[1] Current lithium and lithium-ion anode batteries are limited by the cathode capacity, as the anodes generally have higher capacity and suffer less potential loss with capacity. Therefore, there is a vital need for higher capacity cathode materials. Other important characteristics that an improved cathodic material should possess are, stability, facile charge transfer, high oxidative electrochemical potential, and low solubility in the electrolyte, attributes that would allow long battery life and high energy output.[2]

The most common cathode materials for secondary and primary batteries utilize redox reactions that undergo a single (or partial) electron transfer per redox atom within their working potential. Cathode materials that can offer multi-electron charge transfer generally offer higher energy densities. Hexa-valent iron salts, or "superiron" salts, contain highly oxidized iron (Fe^{6+}) that can theoretically undergo a three electron reduction to Fe^{3+} in a relatively narrow electropositive cathodic potential range, offering intrinsic capacities much higher than current cathodic compounds (e.g., 406 mAh/g for K_2FeO_4 compared to 274 mAh/g for commercially available $LiCoO_2$, calculated as the intrinsic number of Faradays normalized by the molecular weight). Furthermore, the resultant Fe^{3+} discharge product is environmentally benign. A main challenge associated with the superiron salts is that the Fe^{3+} discharge product (nominally Fe_2O_3)[6] is highly resistive impeding reversible charge transfer.[3,4]

To alleviate the poor reversibility issue with superiron salts, various approaches have been taken to either provide a more conductive path or a reduced charge carrier path length. Thin films of the Fe(VI) salt have been electrochemically deposited on a conductive matrix such a smooth Pt surface or on a "platinized" rough surface. These show relatively high reversibility in both aqueous and non-aqueous solvents.[4,5] Recently, a new low-heat and gentle mechano-synthesized (ball mill) approach was taken to reduce the micrometer super-iron particle size to the nano domain. The decreased particle size can potentially offer a higher reversibility by decreasing the electron and/or ion path length as well.[6] In highly basic aqueous KOH electrolyte, the reversibility of Fe(VI) is attributed to a hydrogen intercalation mechanism.[7] For K_2FeO_4, the reversible reaction can be written as

$$K_2FeO_4 + xH_2O + xe^- \rightleftarrows H_xK_2FeO_4 + x\ OH^- \qquad (1)$$

Therefore increased reversibility requires a more conductive path for both the electrons as well as for the protons, which move in and out of the ferrate salt matrix with charge/discharge.

Previously, the chemistry of the three-electron redox Fe(VI)/Fe(III) couple has been studied by various electrochemical

Received: July 4, 2013
Revised: September 6, 2013
Published: September 9, 2013

techniques and a limited number of spectrochemical techniques; namely, Fourier Transform Infrared (FTIR), in-situ and ex-situ Mossbauer spectroscopy and X-ray diffraction (XRD).[8−11] Although providing partial insight into the charge/discharge mechanism and the nature of the less conductive final discharge product, the exact structural transformations and their relation to the valence state changes and reversibility have not yet been fully elucidated. In this work X-ray absorption spectroscopy will be used to gain further information on the final discharge state and the structural transformations that occur during charge/discharge.

The intercalation of H^+ ions during discharge induces reduction in the Fe valence state and leads to ferrate lattice expansion, $\delta a = a_c - a_d$ where a_c and a_d indicate the "effective" lattice constant of the charged and partially discharged state. If this lattice expansion, δa, becomes too large to be accommodated, severe instabilities and even phase transitions and phase separation, such as that indicated by eq 2:

$$2K_2FeO_4 + 6H^+ + 6e^- \rightarrow \gamma\text{-}Fe_2O_3 + 4KOH + H_2O \quad (2)$$

can occur in the crystal structure.[12,13] The change in crystal structure, such as a change from the tetrahedral ferrate salt structure to the nonconducting Fe_2O_3 discharge state, is detrimental to the reversibility of the super iron battery, as conversion back to the ferrate salt structure is apparently not facile both because of the resistive nature of Fe_2O_3 and the regional separation into the Fe_2O_3 and KOH phases.

To prevent the structural changes and accommodate lattice expansion in the superiron salts, two different paths are examined in this work:

1. Accommodating the Lattice Expansion. Reducing the ferrate salt particle size to the nanodomain facilitates the electron transport rate and diffusion rate of the intercalating H^+ ions by providing a shorter diffusion length, and has other advantages. The higher surface area provided by the decrease in particle size increases the contact with the electrolyte interface, it also provides shorter diffusion pathways for the OH^- byproduct. Further, the lattice expansion is more easily accommodated in smaller nanoparticles, thereby relieving the stress that can lead to the unwanted structural and spatial variations in the discharge product.[14]

2. Decreasing the Lattice Expansion. A second path is to expand the "effective" lattice constant of the ferrate salt in the initial charged state, so that the lattice expansion, δa, is reduced. Thus this work focuses on the effect of the cation in M_nFeO_4 on the lattice constant, hydrogen diffusivity, intercalation mechanism, and ultimate conservation of electrode microstructure.

Here, the salts studied are $BaFeO_4$ and K_2FeO_4. $BaFeO_4$ and K_2FeO_4 exhibit significantly different electrochemical properties. K_2FeO_4 shows a higher solid-state stability (0.1% decomposition per year) and higher intrinsic $3e^-$ capacity compared to pure $BaFeO_4$; however, the rate of charge transfer under similar external load is higher in the latter. The solubility of K_2FeO_4 decreases with KOH concentration, while $BaFeO_4$ is considerably less soluble, 2×10^{-4} M in 5 M KOH containing $Ba(OH)_2$, and nearly insoluble in $Ba(OH)_2$.[9] The low $BaFeO_4$ solubility is beneficial, decreasing the possibility of self-discharge in the superiron battery. Although $BaFeO_4$ has a lower theoretical capacity (313 mAh/g) compared to K_2FeO_4 (406 mAh/g), it has exhibited higher experimental capacity.[15] Both of these compounds can be synthesized by several routes with high purity as previously described by Licht et al. in several publications.[9,16,17]

Figure 1a illustrates a comparison of electrochemical performance of micrometer-sized K_2FeO_4 and $BaFeO_4$; when

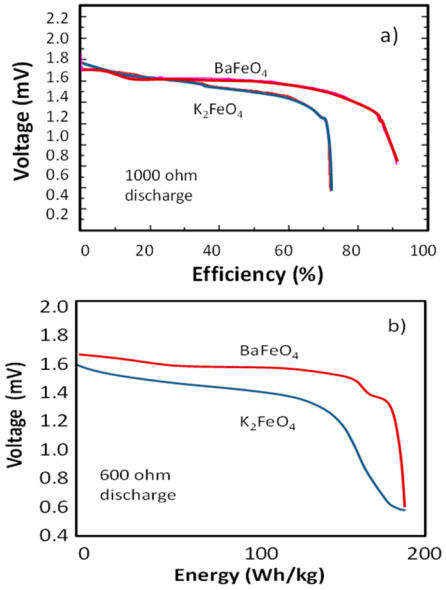

Figure 1. (a) Comparative discharge of micrometer-sized K_2FeO_4 and $BaFeO_4$ cathodes mixed with 10% carbon black in a 1 cm diameter coin cell, Zn anode, and saturated KOH electrolyte. Discharged under constant load of 1000 Ω. (b) Energy capacity comparison of micrometer-sized $BaFeO_4$ and (the improved capacity of) nanometer-sized K_2FeO_4 with a Zn anode. Discharged under constant load of 600 Ω.

discharged under a constant load of 1000 Ω, $BaFeO_4$ discharges to more than 90% of the $3e^-$ columbic efficiency compared to 70% from K_2FeO_4. As illustrated in Figure 1b, the $BaFeO_4$ cathode also exhibits a higher columbic efficiency at higher discharge rates (now with a load of 600 Ω and $J > 10$ mA/cm^2), providing a higher experimental energy capacity for this compound despite the lower intrinsic charge capacity of $BaFeO_4$ compared with K_2FeO_4. Although these two compounds have only a different "spectator" cation with otherwise very similar crystal structure, they exhibit significantly different electrochemical behavior. This suggests that a detailed comparison of their spectroscopic properties might shed new light on the reversibility issue.

In this work, the objective is to investigate the relationship between the structural and valence state properties and the reversibility of this class of novel cathodic materials in aqueous media utilizing X-ray absorption spectroscopy (XAS). XAS is an element specific technique; this means that the chemical environment of a specific element in a complex material such as a cathode can be probed, and this can be performed in situ during charge/discharge. We will take advantage of both the structural information obtained from the extended X-ray absorption fine structure (EXAFS) and the electronic information in the X-ray absorption near edge structure (XANES) parts of an XAS spectrum utilizing the Fe K edge. The EXAFS will give us structural information, such as Fe−O bond distances, coordination numbers, and Debye−Waller "disorder" factor, etc., and the XANES provides information on the electronic valence state of Fe. XAS is a short-range order

dx.doi.org/10.1021/jp406626x | J. Phys. Chem. C 2013, 117, 19875−19884

technique; therefore, it can be used to study amorphous materials and small particles.

In our previous paper,[6] it was illustrated that a gentle and low-heat milling procedure, consisting of six 5 min intervals with 300 rpm, improves the electrochemical activity of K_2FeO_4 by decreasing the K_2FeO_4 particle size from the micrometer to the nanometer domain. As measured from the scanning electron microscopy (SEM) image in Figure 6 of that paper (ref 6), the micrometer-sized K_2FeO_4 has an average particle size of 31 μm with a rather large standard deviation in the dispersion of σ = 12 μm, while the nanometer-sized K_2FeO_4 is 2 orders of magnitude smaller with a particle size of 205 nm (0.205 μm), σ = 97 nm. The reduction of particle size successfully increases the columbic efficiency of the discharge in an alkaline medium from about 20−30% to about 60−80% when discharged under a constant load of 600 Ω. Thus the charge/discharge of μm- and nm-K_2FeO_4 will be observed with XAS, along with that of μm-$BaFeO_4$.

2. EXPERIMENTAL SECTION

2.1. Synthesis. μm-K_2FeO_4 was chemically synthesized as previously reported,[16] recrystallized by dissolution in cold 2.67 M KOH, then filtered into cold 12 M KOH and stirred for 15 min. The product was filtered, and washed in turn with hexane, isopropanol, methanol, and ether, and then dried under vacuum for 1 h. To prepare nm-K_2FeO_4, the chemically synthesized and recrystallized K_2FeO_4 was carefully ball milled in a RetschPM100 planetary ball mill with a steel vessel and steel grinding balls. A gentle and low-heat ball milling procedure was carefully carried out in short segments, consisting of six 5 min intervals with 300 rpm as described previously to avoid thermochemical and heat related restructuring and chemical decomposition of the ferrate material. The ball milling procedure resulted in reduction of the particle size from 20−200 μm to ∼100 nm as confirmed by SEM imaging reported previously.[6]

$BaFeO_4$ was synthesized using the chemical synthesis procedure also described previously.[16] In brief, the $BaFeO_4$ is obtained directly from the recrystallized K_2FeO_4 utilizing the higher alkaline insolubility of $BaFeO_4$ relative to K_2FeO_4. A sample of 20.1 g of $Ba(OH)_2.8H_2O$ (98%, Sigma Aldrich) was dissolved in 500 mL of doubly deionized water, while argon was bubbled through the solution at 0 °C to remove CO_2. This solution was then filtered through GF/A filter paper (150 mm). A second solution containing 8 g of K_2FeO_4 in 160 mL of 2% KOH was prepared, and CO_2 was removed with flow of argon at 0 °C and then filtered through 150 mm GF/A filter paper into the first solution at 0 °C. The resulting mixture was then stirred at 0 °C for 20 min. The $BaFeO_4$ precipitate was filtered and washed with 4 L of cold distilled water and dried under vacuum for 24 h.

The μm-$BaFeO_4$ synthesized using this method is relatively pure, but suffers from low solid state stability. This does not permit for ball milling of this salt without thermal decomposition to γ-Fe_2O_3, thus nm-$BaFeO_4$ could not be prepared. In the dry state, $BaFeO_4$ was also found to decompose to γ-FeO_4 in about 3 h under the X-ray beam. Thus extreme care is required, even for micrometer size particles, to maintain the ferrate structure in the $BaFeO_4$.

2.2. XAS Ex-Situ Measurements. XAS data for $BaFeO_4$ and the Fe_2O_3 standard were taken at room temperature at the Fe K edge at the X-3B beamline (National Synchrotron Light Source, Brookhaven National Laboratory, Upton, NY) with a Si (111) double crystal monochromator, and collected in fluorescence mode, with the sample placed between two gas ionization detectors and a Canberra 13-element Germanium solid state detector, which was collecting X-rays at a 90 degree angle relative to the incident beam. To account for the drift in the incident beam, a Fe reference foil (7 μm thickness) was positioned between the second and third ionization chamber detectors in all measurements.

The superiron primary cells were prepared in conventional 1.1 cm diameter A76 button cells. The zinc anode of the commercial button cells was retained, and concentrated (16 M) KOH was added as electrolyte. The nm- and μm-K_2FeO_4 and μm-$BaFeO_4$ were mixed with 10% carbon and replaced in the cathodic compartment and discharged under a constant load of either 600 or 1000 Ω. The cells were discharged to various percentages of the $3e^-$ Columbic efficiency, then opened, and the cathode composite removed, placed between two layers of Kapton tape, and studied with XAS. As noted above, $BaFeO_4$ is relatively unstable, so if the initial XANES spectra did not show the characteristic Fe(VI) 1s to 3d pre-edge peak (such as that shown in Figure 4 below), the sample was discarded, and another sample was prepared.

2.3. The Δμ-XANES Technique. The IFEFFIT suite (version 1.2.11 IFEFFIT, Copyright 2008, Mathew Newville, University of Chicago, http://cars9.uchicago.edu/ifeffit) of programs was used for the Δμ-XANES data analysis including the background subtraction (AUTOBK algorithm) and normalization. The Δμ results for K_2FeO_4 undergoing various degrees of electrochemical discharge (cathodic reduction) are presented below. This Δμ analysis technique has been described in detail elsewhere.[6] In summary, the raw spectra from different XAS scans were merged together for each single potential. To account for the drift in beam energy over the beam lifetime, these normalized foil spectra were then aligned to one standard foil spectrum. This energy correction is automatically transferred to the sample spectra as well. The success of the Δμ technique is very much dependent on the precision of this energy alignment step. A postedge normalization procedure (25 to 150 eV above the edge, for Δμ analysis) is then applied to the sample spectra. The Δμ signatures are then obtained by subtracting the μ for γ-Fe_2O_3 as reference:

$$\Delta\mu = \mu(V) - \mu(\mathrm{Ref}) \tag{3}$$

The completely discharged product has been shown previously[6] to be γ-Fe_2O_3 for nm-K_2FeO_4, and we will show below that this is only nominally true for $BaFeO_4$ but we will use the same reference for all salts.

2.4. EXAFS Analysis. Using the IFEFFIT suite (version 1.2.11 IFEFFIT, Copyright 2008, Matthew Newville, University of Chicago, http://cars9.uchicago.edu/ifeffit/) linear combination fitting was conducted on the cathodic composites discharged to various depths after initial data analysis to extract the $\chi(k)$. In this method, the $\chi = [\mu(k) - \mu_o]/\mu_o$, of each partially discharged cathode is fit to the χ for the undischarged M_nFeO_4 cathode material and the discharge material, γ-Fe_2O_3:

$$\chi(t) = A^*\chi_{M_nFeO_4} + (1 - A)^*\chi_{\gamma-Fe_2O_3} \tag{4}$$

where A is the fraction of the initial ferrate structure (M_nFeO_4) present in each partially discharged cathode. Equation 4 assumes that only the two "end" structures are possible, the fully charge and discharged, and this of course is not necessarily

dx.doi.org/10.1021/jp406626x | J. Phys. Chem. C 2013, 117, 19875−19884

the case, as possible partial discharge products are also certainly present. Further, eq 2 shows that even the final discharge product contains regions of MOH. Nevertheless, we will show below that the fit of eq 4 to the experimental $\chi(k)$ obtained from the cathode material at a particular time during the discharge effectively identifies the point where the rather sharp decomposition and/or phase transformation occurs, causing the increase in internal resistance, and hence decline in current flow (i.e., the sharp drop in A in eq 4 appears to strongly correlate with the current drop in a discharge profile such as those shown in Figure 1).

3. RESULTS AND DISCUSSION

3.1. EXAFS Results. It is important to establish the nature of the fully discharged product of either the K_2FeO_4 or $BaFeO_4$ when discharged as cathodes in zinc anode alkaline cells. Here we compare the discharge products of ball-milled nm-K_2FeO_4 to that of $BaFeO_4$ (as described in the prior synthesis section, the latter salt was too sensitive toward solid state decomposition to be ball milled). Both nm-K_2FeO_4 and $BaFeO_4$ exhibit facile charge transfer to a large fraction of their intrinsic $3e^-$ storage capacity. Comparison of the EXAFS spectrum of final discharged cathodes, $\chi_{FD}(k)$, with various iron oxide standards, $\chi_{Stand}(k)$, reveals in Figure 2 that the final discharge

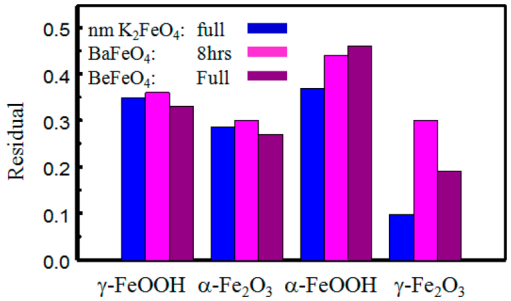

Figure 2. Residuals defined as described in the text between the full discharge product for nm-K_2FeO_4 and that after 8 h and the full discharge of μm-$BaFeO_4$ compared to the standards indicated.

product of both K_2FeO_4 and $BaFeO_4$ is "mainly" γ-Fe_2O_3; that is, the residual Res = Σ $(\chi_{FD} - \chi_{Stand})^2/\Sigma$ χ_{FD}^2) between the standard γ-Fe_2O_3 and the final discharge product is 2−3 times less with γ-Fe_2O_3 (at least for K_2FeO_4) than that with other standards. In the expression Res, $\chi(k)$ was summed over points in the range $3 < k < 10$ and the χ_{FD} and χ_{Stand} are the EXAFS χ functions of the fully or 8 h discharged cathode (as indicated in Figure 2) and the standard that is being examined. These results suggest that for nm-K_2FeO_4, the discharge product is indeed more like γ-Fe_2O_3, but for the $BaFeO_4$, it may be partially hydrated at least initially, since the residual with γ-Fe_2O_3 is only slightly less than for the hydrated oxides after just 8 h, but then dehydrates some after longer periods.

The change in crystal structure during discharge is from that of a ferrate, to a partially discharged ferrate but still in its ferrate ionic lattice, and ultimately to full lattice rearrangement with regions of more extended Fe−O−Fe covalent bonding existing in γ-Fe_2O_3 oxide along with regions of KOH, as suggested by eq 2. The sizes of the alkaline hydroxides and the iron oxide regions are not known, but this is certainly one reason why the comparison of the $\chi(k)$'s in Figure 2 cannot give significantly lower residuals; we are comparing the discharge product (interspersed iron oxide + K or Ba hydroxide regions of unknown size) with a pure iron oxide standard. In contrast with that of previously reported FT-IR studies and in situ Mossbauer spectroscopy[8] on $BaFeO_4$, which could not point to a specific ferric oxide or hydroxide as the main discharge product, the EXAFS features for the $BaFeO_4$ discharge product do show slightly better agreement with the γ-Fe_2O_3 form of the oxide, similar to that clearly found for K_2FeO_4. However, conclusive evidence for the discharge produce in the case of $BaFeO_4$ is not indicated here either, because the residual is not sufficiently small compared with the other iron oxyhydroxides or oxides.

To study the structural and morphological properties of the cathode through the course of the discharge, linear combination EXAFS fitting with the procedure described above was conducted on each partially discharged cathode (for μm- and nm- K_2FeO_4 and $BaFeO_4$) in the k range of 3−12. Example fits for two of the partially discharged nm-K_2FeO_4 cathodes are shown in Figure 3, as well as the constituent components and

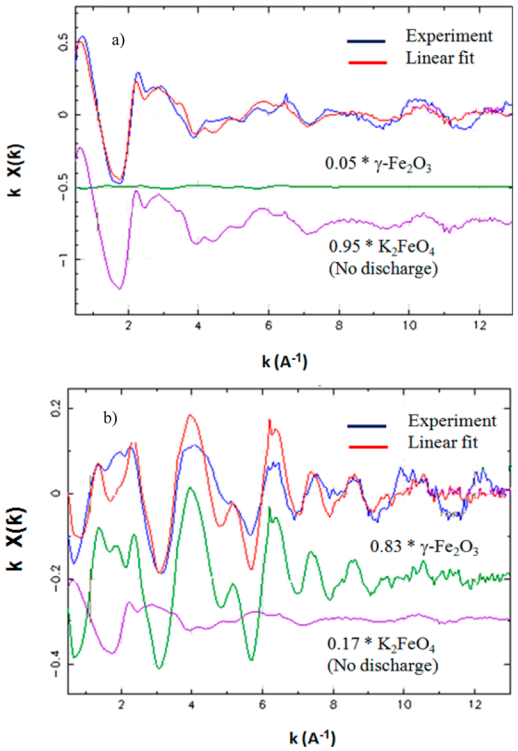

Figure 3. Linear EXAFS component fits for two nm-K_2FeO_4 discharged cathodes: (a) cathode discharged for 3 h; (b) cathode discharged for 16 h.

their contribution to the final fit. As the discharge progresses from 3 h (figure top) to 16 h (figure bottom), the composition of the cathode changes from 95% to only 17% undischarged K_2FeO_4. The quality of the fits are acceptable for the undischarged and partially discharged cathodic composites; however the quality of the fits decreases for the deeply discharged cathodes. Fit R-factors increase from 0.000744 for a 3 h discharged cathode (when comparing mostly undischarged product with completely undischarged material) to 0.002753 for 16 h of discharge and to 0.171459 for a completely discharged nano-K_2FeO_4 cathode as shown in Figure 3. We emphasize again that the full $3e^-$ discharge radically disrupts the lattice and forms a two phase (metal hydroxide and iron oxide) material that is structurally nonreversible; i.e., it cannot return to the initial charged Fe(VI) ionic ferrate state.

dx.doi.org/10.1021/jp406626x | J. Phys. Chem. C 2013, 117, 19875−19884

Nevertheless, the linear combination fit provides a tool to quantify the level of discharge, or discharge time, when this structural change occurs in the cathode.

3.2. $\Delta\mu$ Results. Identifying the nature of the main discharge product using the EXAFS procedure above to follow the structural change is useful, but it also useful to follow the Fe oxidation state in the cathode material with discharge time. This can be done with the XANES part of an XAS spectrum utilizing the Fe K edge. Figure 4 shows the significant difference

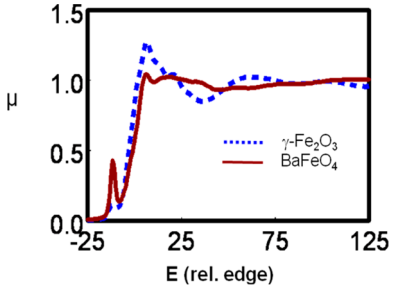

Figure 4. XAS data, $\mu(E)$ for $BaFeO_4$ and γ-Fe_2O_3 as standard, where the data for $BaFeO_4$ is for the undischarged micrometer sized cathode.

between the XAS data, $\mu(E)$, for $BaFeO_4$ and γ-Fe_2O_3 (similar large differences for K_2FeO_4 occur). The $BaFeO_4$ in Figure 4 has the strong pre-edge peak from the nondipole allowed 1s to 3d transition, and the higher energy "whiteline" resulting from the 1s to np excitation. This whiteline moves up in energy with higher oxidation state of the iron as expected. Figure 5 presents

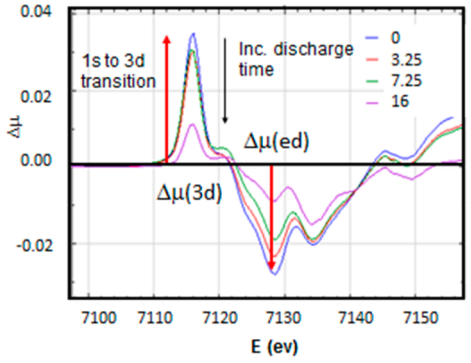

Figure 5. $\Delta\mu$ results for μm K_2FeO_4 at the indicated discharge times in hours under 600 Ω load. The magnitudes of the $\Delta\mu(3d)$ and $\Delta\mu(ed)$ are indicated by the red arrow.

the $\Delta\mu$ results for μm K_2FeO_4 at various depths of cathodic electrochemical discharge. The 1s to 3d transition is only visible in the XAS spectrum because of 4p and 3d orbital mixing, and this can strongly occur only in a non-octahedral environment, such as the tetrahedral environment around the Fe atoms in the FeO_4 structure present in the ferrates. The 1s to 3p peak is mostly absent in γ-Fe_2O_3, due to the FeO_6 near octahedral environment existing in γ-Fe_2O_3, which does not allow p-d orbital mixing.[20] The intensity of the pre-edge feature decreases upon reduction in part due to the increased electron population of the 3d state, namely, from approximately d^2 in Fe^{6+} to d^5 in Fe^{3+} (i.e. less empty d states exist for the photoelectron to be excited into in the XAS process); however, this alone cannot account for the factor of 4−6 decrease in the pre-edge peak with reduction of the iron, as the number of vacant d slots only decreases from about 8 to 5, a factor of 1.6. Thus the decrease in the pre-edge feature apparently also comes from a symmetry change about the Fe atom, namely, from a tetrahedral to a more octahedral environment.

This change in coordination and hence average symmetry about the Fe atoms can be accounted for via two possible mechanisms as summarized in Figure 6: (I) assuming that

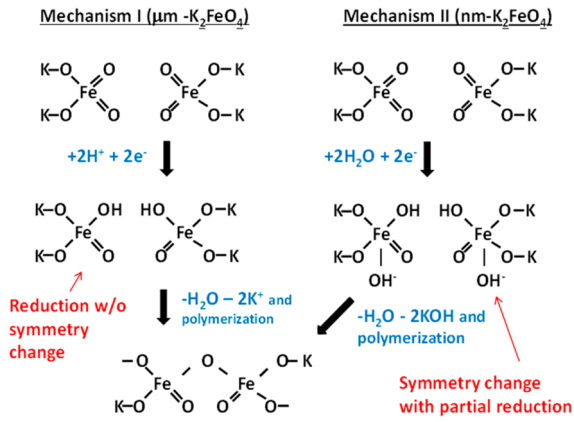

Figure 6. Schematic showing different reduction sequences for the um- and nm-K_2FeO_4 as discussed in the text.

discharge of the ferrate cathode involves intercalation of a proton through the electrolyte and an electron via the circuit along with some atom rearrangement, and (II) intercalation of a water molecule and an electron, $H_2O + e^-$, so that reduction involves M_nFeO_4 going to $M_nFeO_4(H_2O)_n^{n-}$. In this mechanism, the separation of the OH^- assumed in eq 1 does not occur, rather the OH^- group remains with the Fe atom. In mechanism I, addition of H atoms ($H^+ + e^-$ with OH^- remaining behind) may result in the formation of a Fe−O−Fe "cross-link" between neighboring ferrate anions with formation of edge or face touching FeO_6 octahedra (appearing as a dimer-like species in Figure 6):

$$2M_nFeO_4 + 2H^+ \rightarrow M_n[(OH)O_2Fe{<}_{O}^{O}{>}_{O}FeO_2(OH)]M_n$$

In γ-Fe_2O_3, each O atom is coordinated to 4 Fe atoms with tetrahedral symmetry around the O atoms (i.e., all O existing in a Fe−O−Fe linkage with edge or face touching FeO_6 octahedra). This is in contrast to K_2FeO_4, where the O atoms are coordinated to just one Fe atom. Thus the Fe coordination increases from 4 (tetrahedral) to 6 (octahedral), but the O coordination increases even more from 1 to 4 upon reduction. The dimer-like specie in Figure 6 with one O coordination increasing from 1 to 2 (and experimentally trimer, tetramer, to ultimately polymer with further discharge) serves as a precursor to the fuller lattice rearrangement and separation into hydroxide and iron oxide region mapped by the EXAFS fitting. It is likely that O coordination much great than 2 or 3 cannot occur unless the full lattice rearrangement occurs. After formation of the polymer-like precursors, the coordination around the Fe atoms has increased to 5 or 6, and this will result in the loss of some 3d intensity, as the symmetry changes from tetrahedral to more octahedral-like symmetry.

In mechanism II (water intercalation), the Fe coordination can change from 4 with tetrahedral symmetry, $(FeO_4)^{2-}$, in the ferrate, to 6 in $FeO_2(OH)_4^{5-}$ with near octahedral symmetry, but without significant increase in the O coordination. In this way, a hydrated ferric oxide is initially formed, which ultimately

dx.doi.org/10.1021/jp406626x | J. Phys. Chem. C 2013, 117, 19875−19884

converts to iron(III) oxide upon dehydration and separation into metal hydroxide and iron oxide regions as shown in Figure 6 for just two FeO_n groups.

In the two mechanisms described above, the oxidation state can change with or without increase of the Fe and O coordination's and resultant symmetry, even if the total crystal structure has not yet changed. The Fe oxidation state can be tracked by following the shift in the Fe k-edge, as it is reflected in the magnitude of the peak in the $\Delta\mu$ signal at photon energy 7124−7129, or just 2−3 eV from the edge around 7126.5 eV. We will show below that $|\Delta\mu(\mathrm{ed})|$ does vary nearly linearly with time during the discharge and changes very differently than the magnitude of the pre-edge peak, $|\Delta\mu(\mathrm{3d})|$, because the latter involves the local geometric symmetry around the Fe, while $\Delta\mu(\mathrm{ed})$ involves only the electronic oxidation state. By following both as a function of time, we can gain significant insight into how the reduction and resultant change in structure is taking place.

3.3. .Comparison of nm- versus μm-K_2FeO_4. Figure 7 shows the $\Delta\mu$ amplitudes, $|\Delta\mu(\mathrm{ed})|$ and $|\Delta\mu(\mathrm{3d})|$, which track

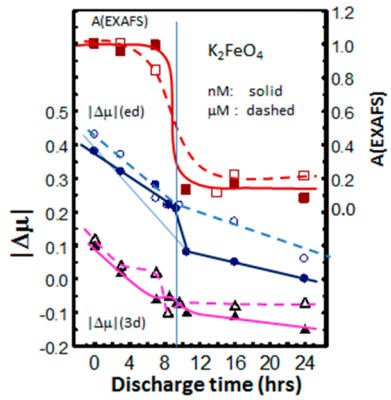

Figure 7. Plot of the indicated $\Delta\mu$ amplitudes (at the edge and pre-edge peaks) and A(EXAFS) for the nm- and μm-K_2FeO_4 as a function of discharge time. The light solid blue line on the $|\Delta\mu(\mathrm{ed})|$ plot suggest how it would change if just H^+ was intercalated. Measurements were taken on 50 mAh cells with cathodes composed of 10% carbon black, 90% of K_2FeO4 and 16 M KOH electrolyte and discharged under constant load of 600 Ω. Vertical line drawn at rearrangement.

the Fe oxidation state and change of symmetry about the Fe atom, respectively, and the A(EXAFS) coefficient from the EXAFS linear fit, which tracks the fraction of ferrate still remaining in the cathode with discharge time. We report the discharge profiles in Figure 1 with discharge using a 1000 Ω load, but Figure 7 shows XAS data with the smaller 600Ω load. The A(EXAFS) coefficient shows that the rearrangement of the crystal structure from mostly ionic ferrate-like to γ-Fe_2O_3 is rather sharp on a 20 h time scale, and occurs after 9 h into the discharge, for both the nm- and μm-K_2FeO_4 particles (i.e., ground and unground). However, note that this transition is much sharper for the much smaller nm particles as might be expected.

Figure 7 shows that $|\Delta\mu(\mathrm{ed})|$ varies linearly with time from 0 to about 9 h, and then quite abruptly changes slope above 9 h, i.e., right after the crystal structure rearrangement. The slope of the decline in $|\Delta\mu(\mathrm{ed})|$, i.e., $\mathrm{d}|\Delta\mu(\mathrm{ed})|/\mathrm{d}t$, should track with the current, and the current sharply decreases at 9 h when the rearrangement occurs, because at this point the resistivity of the cathode material (R_{int}) sharply increases; and $I = V/(R_{int} + R_{load})$. Note that the slope, $\mathrm{d}|\Delta\mu(\mathrm{ed})|/\mathrm{d}t$, (light blue line for the nm particles) is larger for the nanometer particles than for the micrometer particles, consistent with the greater conductivity of the nanometer material. The crystal rearrangement happens to occur around the same discharge time, but because of the larger current flow in the nanometer material, the discharge capacity prior to rearrangement is much greater for the nanometer particles, consistent with the current versus voltage discharge curves reported previously.[6] The capacity can be predicted from Figure 7 by the total drop in $|\Delta\mu(\mathrm{ed})|$ from 0.45 to 0.1, a 75% drop for the nm material, versus a 50% drop (0.45 to 0.23) for the μm material. These are consistent with the capacities reported for these materials previously under a 600 Ω load (these capacities are somewhat larger under a 1000 Ω load as shown in Figure 1a). Note that the $\mathrm{d}|\Delta\mu(\mathrm{ed})|/\mathrm{d}t$ slope above 9 h is lower in the nm material, consistent with the greater conversion to the resistive γ-Fe_2O_3 in the nanometer material as shown by the A(EXAFS) magnitude; i.e., the lattice conversion is more complete in the nanometer materials, but occurs at a larger capacity.

Figure 7 shows a very large $\mathrm{d}|\Delta\mu(\mathrm{ed})|/\mathrm{d}t$ slope in a narrow region around 9 h in the nanometer material. This can best be understood in the context of the behavior in $|\Delta\mu(\mathrm{3d})|$. Recall that $|\Delta\mu(\mathrm{3d})|$ tracks the local symmetry change around the Fe atom. In the micrometer material, the decrease in $|\Delta\mu(\mathrm{3d})|$ with time is delayed between 3 and 8 h, then sharply increases between 8 and 9 h. This suggests that that H^+ is primarily intercalated between 3 and 8 h, i.e., Fe reduction but without significant change in Fe−O coordination and symmetry. This difference in the drop between $\Delta\mu(\mathrm{ed})$ and $\Delta\mu(\mathrm{3d})$ can be regarded as an indication of "stress" build-up, as the lattice wants to rearrange and allow the symmetry around the Fe to change but cannot under the constraints of the lattice. The stress is relieved only when the Fe symmetry is allowed to change during the lattice rearrangement. Thus the changes in $|\Delta\mu(\mathrm{3d})|$ in the micrometer material occur as expected, i.e., as H^+ intercalation proceeds, a lag in $|\Delta\mu(\mathrm{3d})|$ drop occurs prior to the lattice rearrangement, followed by a steep drop during the rearrangement.

The nanometer material exhibits a significantly different behavior. Except for a slight "bump" at 9 h, $\Delta\mu(\mathrm{3d})$ decreases rather uniformly with time, and now $\Delta\mu(\mathrm{ed})$ shows a lag and then sudden drop at 9 h. How do we account for this significantly different behavior? These results are consistent with much more H_2O intercalation (i.e., mechanism II when the OH^- stays with the Fe as illustrated in Figure 6), and therefore increase in Fe−O coordination with gradual change in symmetry from tetrahedral to octahedral symmetry. This intercalation of H_2O then apparently allows the incoming electrons to be distributed more evenly about the $FeO_4(H_2O)_n$ [or $FeO_{4-n}(OH)_{2n}$] environment, thus delaying the reduction in the Fe valence state. At 8−9 h the lattice rearrangement separates the water and KOH from the γ-Fe_2O_3, so that the Fe oxidation state now falls quickly as the OH^- separates from the Fe forcing the electrons onto the Fe atoms.

These results reveal the most important reason why the ground nm material has increased capacity compared to the μm material. Not only is the conductivity (to electrons) increased, but apparently more important, the greater K_2FeO_4-electrolyte interface area in the nanometer material increases the ability of the larger H_2O species to intercalate at, and near, the surface of the smaller particles, and thereby decrease the reduction of the Fe valence by distributing some of the electrons onto the OH

dx.doi.org/10.1021/jp406626x | J. Phys. Chem. C 2013, 117, 19875−19884

or waters. The reduction of the Fe is the apparent "stress", which induces the unwanted lattice rearrangement, and intercalation of H_2O, rather than H, enables reduction in this stress by distribution of the electrons more about the intercalated H_2O and/or OH coordinating with the Fe. Thus, as might be expected, H_2O intercalation is as important, or more so, than the electron conductivity for increasing capacity.

3.5. Comparison of $BaFeO_4$ with K_2FeO_4. Figure 8 shows results for μm-$BaFeO_4$, which are quite different from those for

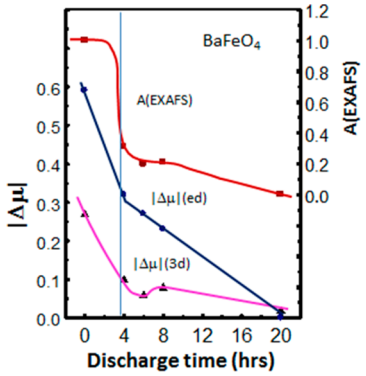

Figure 8. Plot of $\Delta\mu$ at the 3d pre-edge and edge and A(EXAFS) versus discharge time for $BaFeO_4$. Vertical line drawn at rearrangement.

K_2FeO_4. In $BaFeO_4$, $|\Delta\mu(ed)|$ tracks remarkably similarly with $|\Delta\mu(3d)|$, and both decrease uniformly with time; i.e., there is no apparent lag in either. Note that $|\Delta\mu(ed)|$ varies linearly again, but with much larger slope before the lattice rearrangement than after the lattice rearrangement. Here we note another significant difference with the K_2FeO_4 results. The slope prior to 4 h is much larger for $BaFeO_4$ compared with even the nm-K_2FeO_4, consistent with the greater charge transfer rate exhibited by $BaFeO_4$ as discussed in the Introduction. This also accounts for the rearrangement occurring already after 3.8 h compared with around 9 h for the K_2FeO_4. However, even at times longer than 3.8 h, i.e., after the lattice rearrangement, the slope is still relatively large at about 0.025/h, comparable to what it is for K_2FeO_4 before the rearrangement. Note that the capacity at 3.8 h is only about 50%, so that indeed the larger capacity (about 70−80%) exhibited in CV plots for $BaFeO_4$ with 600 Ω load apparently extends beyond the initial lattice rearrangement visible from the EXAFS fit.

What can account for the high current in $BaFeO_4$ even after the apparent lattice rearrangement at 3.8 h as indicated by the EXAFS? We suggest a possible two-step lattice rearrangement process, or more gradual slow change over to γ-Fe_2O_3 if at all, beyond 10 h. Unfortunately, we do not have any points between 8 h and the nominal full discharge at 20 h in Figure 7, and the difficulties with acquiring synchrotron time, etc. do not allow us readily return and get more points in this region, but other data are consistent with a two-step rearrangement process. Figure 1b shows a small initial drop in V around 160 Wh/kg followed by the major drop somewhat later. Further, Figure 2 indicates that the discharge products at 8 h and at full discharge are different (at least the Res is very different in these two cases). Clearly the rearrangement into separate $Ba(OH)_2$ and γ-Fe_2O_3 regions does not occur as quickly in time and as fully as the separation into the KOH and γ-Fe_2O_3 regions evident in the nm-K_2FeO_4 material. This is perhaps not surprising considering the bigger micrometer-sized $BaFeO_4$ particle; the rearrangement also occurs slower in the μm-K_2FeO_4 material, beginning already after 4 h and extending to 16 h. However, even after 20 h (nominally full discharge), the discharge product does not reflect full γ-Fe_2O_3 conversion as suggested by the larger Res in Figure 2, but rather a more hydrated structure with the OH groups still present near the Fe atoms.

In all cases, the XAS data simply reflect the "average" conditions existing in the small volume (i.e., cross-sectional area times path length) sampled by the transmitted light beam. In the nm-K_2FeO_4 material, some particles could completely undergo the lattice rearrangement into separated regions of γ-Fe_2O_3 and metal hydroxide, while other particles remain partially or even fully charged. In the micrometer-sized particles ($BaFeO_4$ or K_2FeO_4), it is more probable that individual particles have both regions existing at the same time, i.e., more fully discharged lattice rearranged regions and still charged regions in the same μm-sized particle, arranged in some unknown core−shell or mosaic-like structure similar to that evident in other battery materials.[27−29] This would explain the slower lattice changeover with time evident in the A(EXAFS) seen with the micrometer-sized particles. However, in all cases, the drop-off in A(EXAFS) occurs simultaneously with a significant change in slope of the $\Delta\mu$(ed) line, and these two data indicators come from the same XAS scan (i.e., exactly the small volume sampled by the light beam). Thus at least on the scale of the XAS sampled volume (millimeters), the discharge appears to be occurring rather uniformly, and the EXAFS data is indeed representative of the final discharge product.

The above results strongly suggest that the final discharge product with $BaFeO_4$ is not the same as in K_2FeO_4, i.e., the separation into KOH and γ-Fe_2O_3 appears to be much more complete, and the separated regions are spatially larger in the case of K_2FeO_4 than for $BaFeO_4$. This less complete separation makes the discharge product much more conductive to both electrons and protons, so that the discharge can continue even after the lattice rearrangement indicated by the EXAFS fitting. Thus both the charged and discharged end materials are more conductive in $BaFeO_4$ than in K_2FeO_4.

3.3. Intercalation Channels and Lattice Expansion. At higher discharge rate, both nm-K_2FeO_4 and μm-$BaFeO_4$ exhibit higher capacities than μm-K_2FeO_4. However, the mechanism by which the intercalation tolerance is increased differs for these two cases.

Others[21−25] have previously observed that nanometer-size particles can enable electrode reactions that do not occur in the micrometer-size domain. The rate and ability of intercalant diffusion (here H_2O) is increased in nanoparticles, due to the shorter diffusion length and increased electrode/electrolyte interface (SEI) as compared to larger particles. Here the decreased diffusion length required for the H_2O in the nanometer particles decreases the Fe reduction as noted above, and therefore better "accommodates" the stress induced in the lattice.

XRD measurements[26] indicate that one-dimensional intercalation channels exist in the 'a' and 'b' directions of the K_2FeO_4 unit cell with a radius of 0.93 Å. The sharpening of the diffraction peaks observed in the (002), (004) and (006) planes along with the broadening of other features indicates that the intercalants move along these existing one-dimensional channels. Figure 9 shows the unit cell for K_2FeO_4 as viewed from the 'a' and 'b' directions. The channels are situated along

dx.doi.org/10.1021/jp406626x | J. Phys. Chem. C 2013, 117, 19875−19884

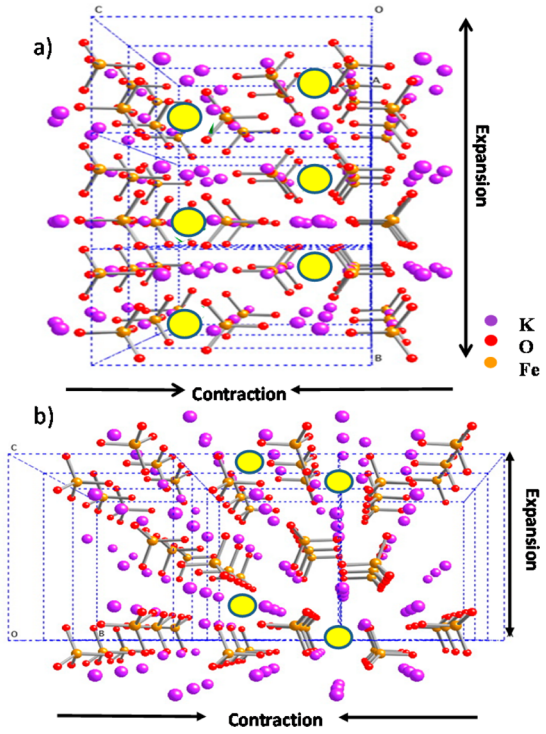

Figure 9. Unit cell of crystalline K_2FeO_4 along (a) *x* and (b) *y* axes. Circles in yellow highlight some of the diffusion channels. Images generated using CrystalMaker: a crystal and molecular structure program for Mac and Windows. CrystalMaker Software Ltd., Oxford, England (www.crystalmaker.com).

the Fe−O bonds, and this is where the diffusion of intercalating ions occurs. Diffusion of H^+ along these channels leads to their association with the oxygens of the ferrate anion. The stability of the initial structure (which is related directly to the stability of the intermediate species) and the ease of diffusion of the intercalating ions are the two factors that determine the rate capabilities and reversibility of the cathode material under study.

In the $BaFeO_4$ lattice, every Ba atom is associated with two ferrate anions, compared to one K associated with each ferrate anion. The different interaction between cation and anion leads to different lattice parameters in these two compounds: $BaFeO_4$ has an expanded lattice compared to K_2FeO_4. Table 1 shows XRD data previously obtained,[18,19] for both K_2FeO_4 and $BaFeO_4$. The unit cell of $BaFeO_4$ is expanded in the 'a' and 'b' directions compared to that of K_2FeO_4 (9.13 and 5.85 Å for $BaFeO_4$ and 7.70 and 5.46 Å for K_2FeO_4). In contrast, the unit cell in the 'c' direction is contracted in $BaFeO_4$ (7.3232 Å) compared to that of K_2FeO_4 (10.3506 Å). Hence, the channels along the 'a' and 'b' axes are enlarged and more symmetrical in $BaFeO_4$. The expanded lattice and more symmetrical diffusion channels facilitate the diffusivity of the H^+ along the channels enabling higher current densities and capacity. The expanded lattice of $BaFeO_4$, and the stronger anion−cation interaction apparently also causes less variation in the microstructure of $BaFeO_4$ and less separation into $BaOH_2$ and γ-Fe_2O_3 after discharge.

The Fourier transform XAS data shown in Figure 10 confirm that both the Fe−O and Fe−Fe bond distances are increased in

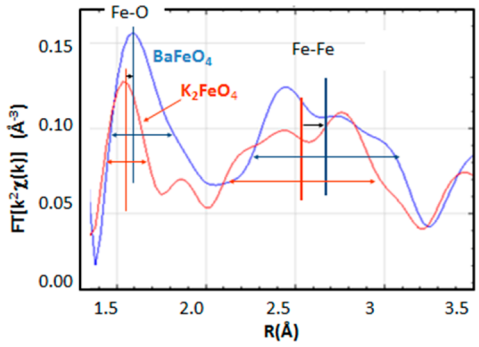

Figure 10. K_2FeO_4 and $BaFeO_4$ Fourier transform prior to discharge; $BaFeO_4$ shows increased Fe−O and Fe−Fe bond lengths and large Fe−O peak width.

our $BaFeO_4$ samples compared to K_2FeO_4. EXAFS data have been reported previously for many different iron oxides showing a Fe−O peak around 1.5−2 Å and a Fe−Fe peak around 2−3 Å.[30,31] Indeed plots have been given previously of the Fe−O bond length and how it shrinks with oxidation state, as obtained from EXAFS or XRD; including that for Fe(VI).[31,32] Thus the assignment in Figure 11 of the peaks

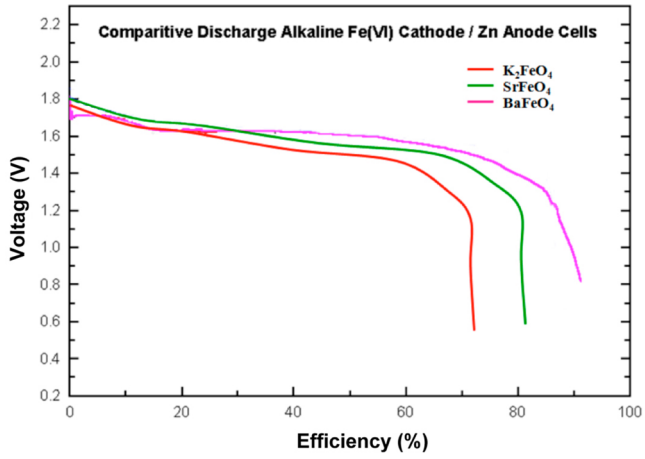

Figure 11. Comparative discharges of various Fe(VI) salt cathodes versus Zn anodes. One centimeter diameter coin cells were utilized, 300 mg of dry cathodes was mixed with 10 wt % of 1 μm graphite, electrolyte was saturated KOH, and all cells were discharged with constant load of 1000 Ω.

Table 1. XRD K_2FeO_4 and $BaFeO_4$ Crystal Data from Ref 18 and 19

compound	space group	*a*, Å	*b*,Å	*c*,Å
K_2FeO_4	*Pnma*	7.7010 ± 0.0070	5.8520 ± 0.0064	10.3506 ± 0.0136
$BaFeO_4$	*Pnma*	9.1260 ± 0.0110	5.4563 ± 0.0067	7.3232 ± 0.0083
Cs_2FeO_4	*Pnma*	8.3998 ± 0.0166	6.2737 ± 0.0105	11.064 ± 0.0230
$SrFeO_4$	*Pnma*	9.1826 ± 0.0580	5.3980 ± 0.0263	7.2256 ± 0.0386

dx.doi.org/10.1021/jp406626x | J. Phys. Chem. C 2013, 117, 19875−19884

to the Fe−O and Fe−Fe distances is without question, and the short Fe−O bond distance here again confirms the Fe(VI) oxidation state. Further, the widening of the Fe−O peak around 1.6 Å indicates a larger variation in the Fe−O bond lengths in $BaFeO_4$; this is mostly likely caused by a larger interaction between the ferrate anion and the Ba cation. Clearly, $BaFeO_4$ undergoes a smaller lattice expansion as a result of the intercalation process. The smaller lattice expansion, combined with more symmetrical intercalation channels, increases the reversibility of the intercalation process in $BaFeO_4$. The larger ferrate-Ba cation interaction may also make it more difficult for the $BaOH_2$ hydroxide and γ-Fe_2O_3 segregation to occur in the discharge product.

A comparison of the XRD data in Table 1 and electrochemical data previously obtained from constant load discharges of other M_nFeO_4 salts as cathodes in alkaline coin cells given in Figure 11 confirms that an initial expanded lattice leads to a higher charge transfer rate (and as a result higher reversibility) in the cathode. $SrFeO_4$ and $BaFeO_4$ each discharge to more than 80% of the 3 e^- transfer columbic efficiency under a constant load of 1000 Ω, whereas K_2FeO_4 only discharges up to 70%. The XRD data in Table 1 shows that the unit cell in the 'a' direction for $SrFeO_4$ (8. 9.1826 Å) is larger than that of K_2FeO_4. This correlation between XRD data and electrochemical data strengthens the correlation of the importance of an initial expanded lattice for increased discharge efficiency, charge transfer rate, and reversibility.

4. CONCLUSIONS

XAS provides a valuable, highly specific technique to study materials used as novel electrodes in high capacity batteries. The $\Delta\mu$ technique allows one to follow the Fe oxidation state (hence capacity) and average local symmetry about the Fe atom, and the EXAFS can be used to study the structural rearrangements and lattice variations of the electrode at any charge state. Ex situ XAS measurements conducted on nanometer and micrometer-sized K_2FeO_4 and comparison to $BaFeO_4$ at various states of charge reveal the significance of minimizing the structural variations of the salt lattice and its effects on the increased reversibility of the cathode. Micron-size $BaFeO_4$ particles hold their initial super iron salt structure to about 50% of the three-electron discharge similar to the behavior observed for the μm-K_2FeO_4 particles, but the discharge product remains more conductive enabling further discharge. Relieving the stress induced in the electrode's structure, caused by intercalation processes during charge/discharge cycles, is critical for increasing the cathode's charge transfer rate and electrochemical reversibility. Reduction of this intercalation-induced stress is achieved either by accommodation of the lattice expansion and increase of the surface interface area (such as that enabled by decrease in particle size to the nano domain) or by minimization of the lattice expansion through the use of an initially enlarged lattice (such as $BaFeO_4$, $SrFeO_4$, etc.) and keeping the discharge product more uniform and less separated into hydroxide and iron oxide regions.

AUTHOR INFORMATION

Corresponding Authors

*E-mail: slicht@gwu.edu; Phone: 703-726-8215.
*E-mail: ramaker@gwu.edu; Phone: 703-451-4495.

Notes

The authors declare no competing financial interest.

ACKNOWLEDGMENTS

The authors are grateful for the use of the X3-B and X-11A beam lines at the National Synchrotron Light Source (NSLS), Brookhaven National Laboratory, Upton NY, which is supported by the U.S. Department of Energy, Office of Science, Office of Basic Energy Sciences. S.L. acknowledges partial support of this work by the U.S. National Science Foundation (Award 1006568), and D.R. acknowledges that by the U.S. Department of Energy.

REFERENCES

(1) Gao, X. P.; Yang, H. X. Multi-electron reaction materials for high energy density batteries. *Energy Environ. Sci.* **2010**, *3*, 174−189.
(2) Licht, S. Super-Iron Batteries. Garche, J.; Dyer, C.; Moseley, P.; Ogumi, Z.; David Rand, D.; Scrosati, B. *Encyclopedia of Electrochemical Power Sources 4*; Elsevier: Amsterdam, 2009; pp 262−284.
(3) Licht, S. A High Capacity Li-Ion Cathode: The Fe(III/VI) Super-Iron Cathode. *Energies* **2010**, *3*, 960−972.
(4) Licht, S.; Wang, Y.; Gourdin, G. Enhancement of Reversible Nonaqueous Fe(III/VI) Cathodic Charge Transfer. *J. Phys. Chem. C* **2009**, *113*, 9884−9891.
(5) Licht, S.; De Alwis, C. Conductive-Matrix-Mediated Alkaline Fe(III/VI) Charge Transfer: Three-Electron Storage. *J. Phys. Chem. B* **2006**, *110*, 12394−12403.
(6) Farmand, M.; Jiang, D.; Wang, B.; Ghosh, S.; Ramaker, D. E.; Licht, S. Super-iron nanoparticles with facile cathodic charge transfer. *Electrochem. Commun.* **2011**, *13*, 909−912.
(7) Licht, S.; Wang, B.; Ghosh, S. Energetic Iron(VI) Chemistry: The Super Iron Battery. *Science* **1999**, *285*, 1039−1042.
(8) Ghosh, S.; Wen, W.; Urian, R. C.; Heath, C.; Sirinvasmurthi, V.; Reiff, W. M.; Mukerjee, S.; Naschitz, V.; Licht, S. Reversible Behavior of $K_2Fe(VI)O_4$ in Aqueous Media. *Electrochem. Solid-State Lett.* **2003**, *6*, A260−a264.
(9) Licht, S.; Naschitz, V.; Halperin, L.; Halperin, N.; Lin, L.; Chen, J.; Ghosh, S.; Liu, B. Analysis of ferrate(VI) compounds and super-iron Fe(VI) battery cathodes: FTIR, ICP, titrimetric, XRD, UV/VIS, and electrochemical characterization. *J. Power Sources* **2001**, *101*, 167−176.
(10) Ayersa, K. E.; White, N. C. Characterization of Iron(VI) Compounds and Their Discharge Products in Strongly Alkaline Electrolyte. *J. Electrochem. Soc.* **2005**, *152*, A467−A473.
(11) Wang, Y. L.; Ye, S. H.; Wang, Y. Y.; Cao, J. S.; Wu, F. Structural and electrochemical properties of a K_2FeO_4 cathode for rechargeable Li ion batteries. *Electrochim. Acta* **2009**, *16*, 4131−4135.
(12) Whittingham, M. S. Lithium Batteries and Cathode Materials. *Chem. Rev.* **2004**, *104*, 4271−4301.
(13) Fergus, J. W. Recent developments in cathode materials for lithium ion batteries. *J. Power Sources* **2010**, *195*, 939−954.
(14) Bruce, P. G.; Scrosati, B.; Tarascon, J. M. Nanomaterials for Rechargeable Lithium Batteries. *Angew Chem., Int. Ed.* **2008**, *47*, 2930−2946.
(15) Licht, S.; Yu, X. Recent advances in synthesis and analysis of Fe(VI) cathodes: Solution phase and solid-state Fe(VI) syntheses, reversible thin-film Fe(VI) synthesis, coating-stabilized Fe(VI) synthesis, and Fe(VI) analytical methodologies. *J. Solid State Electrochem.* **2008**, *12*, 1523−1540.
(16) Licht, S.; Naschitz, V.; Liu, B.; Ghosh, S.; Halperin, N.; Halperin, L.; Rozen, D. Chemical synthesis of battery grade super-iron barrium and pottasium Fe(VI) ferrate compounds. *J. Power Sources* **2001**, *99*, 7−14.
(17) Licht, S.; Tel-Vered, R.; Halperin, L. Direct electrochemical preparation of solid Fe(VI) ferrate, and super-iron battery compounds. *Electrochem. Commun.* **2002**, *4*, 933−937.

(18) Herber, R. H.; Johnson, D. Lattice Dynamics and Hyperfine Interactions in M_2FeO_4 ($M = K^+$, Rb^+, Cs^+) and $M'FeO_4$ ($M' = Sr^{2+}$, Ba^{2+}). *Inorg. Chem.* **1979**, *18*, 2786−2790.
(19) Audette, R. J.; Quail, J. W. Crystal Structures of M,FeO, (M = K, Rb, Cs). *J. Solid State Chem.* **1973**, *8*, 39−43.
(20) Newville, M. IFEFFIT: Interactive XAFS analysis and FEFF fitting. *J. Synchrotron Radiat.* **2001**, *8*, 322−324.
(21) Newville, M.; Livina, P.; Yacoby, Y.; Stern, E. A.; Rehr, J. Near-edge X-ray-absorption fine structure of Pb: A comparison of theory and experiment. *J. Phys. Rev. B* **1993**, *47*, 14126−14131.
(22) Shulman, R. G.; Yafet, Y.; Eisenberger, P.; Blumberg, W. E. Observations and interpretation of X-ray absorption edges in iron compounds and proteins. *Proc. Natl. Acad. Sci. U.S.A.* **1976**, *73*, 1384−1388.
(23) Bruce, P. G.; Jiao, F. Mesoporous Crystalline β-MnO_2—A Reversible Positive Electrode for Rechargeable Lithium Batteries. *Adv. Mater (Weinheim, Ger.)* **2007**, *19*, 657−660.
(24) Bruce, P. G. Energy storage beyond the horizon: Rechargeable lithium batteries. *Solid State Ionics* **2008**, *179*, 752−760.
(25) Meethong, N.; Huang, H. Y. S.; Carter, W. S.; Chiang, Y. M. Size-Dependent Lithium Miscibility Gap in Nanoscale $Li_{1-x}FePO_4$. *Electrochem. Solid-State Lett.* **2007**, *10*, A134.
(26) Wanga, Y. L.; Yea, S. H.; Wanga, Y. Y.; Caoa, J. S.; Wu, F. B. Structural and electrochemical properties of a K_2FeO_4 cathode for rechargeable Li ion batteries. *Electrochim. Acta* **2009**, *54*, 4131−4135.
(27) Singh, G. K.; Ceder, G.; Bazant, M. Z. Intercalation dynamics in rechargeable battery materials: General theory and phase-transformation waves in $LiFePO_4$. *Electrochim. Acta* **2008**, *53*, 7599−7613.
(28) Bai, P.; Cogswell, D. A.; Bazant, M. Z. Suppression of Phase Separation in $LiFePO_4$ nanoparticles during battery discharge. *Nano Lett.* **2011**, *11*, 4890−4896.
(29) Roscher, M. A.; Vetter, J.; Sauer, D. U. Characterization of charge and discharge behavior of lithium ion batteries with olivine based cathode active material. *J. Power Sources* **2009**, *191*, 582−590.
(30) Onyszko, A.; Kapusta, Cz.; Sieniawski, J. *Arch. Mater. Sci. Eng.* **2007**, *28*, 597−600.
(31) Kemner, K. M.; Kelly, S. D.; Orlandini, K. A.; Tsapin, A. I.; Goldfeld, M. G.; Perfiliev, Y. D.; Nealson, K. H. *J. Synch. Rad.* **2001**, *8*, 949−951.
(32) Berry, J. F.; Bill, E.; Bothe, E.; George, S. D.; Mienert, B.; Neese, F.; Wieghardt, K. *Science* **2006**, *312*, 1937−1941.

ISSN 0036-8075
20 AUGUST 1993
VOLUME 261
NUMBER 5124

SCIENCE

AMERICAN
ASSOCIATION FOR THE
ADVANCEMENT OF
SCIENCE

A Solid Sulfur Cathode for Aqueous Batteries

Dharmasena Peramunage and Stuart Licht*

Because of its high resistivity and subsequent low electroactivity, sulfur is not normally considered a room-temperature battery cathode. An elemental sulfur cathode has been made with a measured capacity of over 900 ampere·hours per kilogram, more than 90 percent of the theoretical storage capacity of solid sulfur at room temperature, accessed by means of a lightweight, highly conductive, aqueous polysulfide interface through the electrocatalyzed reaction $S + H_2O + 2e^- \rightarrow HS^- + OH^-$. This solid sulfur cathode was first used in a battery with an aluminum anode for an overall discharge reaction $2Al + 3S + 3OH^- + 3H_2O \rightarrow 2Al(OH)_3 + 3HS^-$, giving a cell potential of 1.3 volts. The theoretical specific energy of the aluminum-sulfur battery (based on potassium salts) is 910 watt·hours per kilogram with an experimental specific energy of up to 220 watt·hours per kilogram.

There is a critical need for new electrochemical storage concepts that address future societal needs for consumer batteries and the propulsion of electric vehicles (*1*, *2*). The search for contemporary batteries has blurred the conventional distinctions of electrochemical storage systems. For example, candidates for electrochemical propulsion include mechanically rechargeable primary batteries, secondary batteries, and fuel cells (*2*). There has been considerable interest in nonaqueous electrolytes (such as chloroaluminate), ambient-temperature molten

*To whom correspondence should be addressed.

salt electrolytes (3), and a variety of lithium batteries. However, when compared to aqueous systems, these have certain environmental and cost disadvantages; consequently, aqueous batteries continue to dominate both the consumer and electric vehicle market (1). There have been few high-capacity aqueous cathodes introduced in the last half century, with the exception of the metal hydrides (4) and oxygen or air cathodes, for which many challenges remain (5). Of the older aqueous cathodes, lead oxide, manganese dioxide (theoretical capacity, 280 A·hour/kg), and nickel hydroxide predominate (6).

The low weight and cost of sulfur make it an attractive candidate for electrochemical energy storage. Molten sulfur systems, such as the sodium sulfur battery, are operated at temperatures of 300° to 350°C, maintaining the components in a liquid state for adequate electrolyte conductivity. However, material and safety constraints associated with high temperatures, corrosion, thermal cycling, and cell fabrication have slowed their development (2, 6).

At low (room) temperatures, elemental sulfur is a highly insoluble, insulating solid and is not expected to be a useful cathode material. Sulfur will, however, dissolve in aqueous sulfide solutions, which may be used, for example, in a reversible, low-concentration aqueous polysulfide (cathode)–tin (anode) battery (7). In 1987, we (8) presented an aqueous cathode based on highly concentrated polysulfide solution reduction

$$S_4^{2-} + 4H_2O + 6e^- \rightarrow 4HS^- + 4OH^- \quad (1)$$

where $E° = -0.51$ V versus a standard hydrogen electrode (SHE). The high capacity of this cathode is a result of the anomalously high solubility of potassium polysulfide salts. In excess of 25 molal (*m*) reducible sulfur can be added to saturated aqueous K_2S at room temperature (8). The resultant electrolyte can contain more total sulfur than water, yet operates at room temperature and is highly conductive. In accordance with Eq. 1, at 25°C, the solubility of K_2S_4 is consistent with a maximum charge capacity of 500 A·hour per kilogram of solution. This led to the introduction of an aluminum-sulfur aqueous battery with a specific energy of up to 170 W·hour/kg (9).

We report a cathode capable of the direct reduction of elemental sulfur at room temperature (Fig. 1). The maximum storage capacity is substantially increased and is given by the limit as all solid sulfur is reduced

$$S + H_2O + 2e^- \rightarrow HS^- + OH^- \quad (2)$$

for which $E° = -0.51$ V versus SHE. The theoretical storage capacity of the solid sulfur cathode [1070 A·hour/kg (10)] is several times larger than that of conventional aqueous cathodes, including PbO_2, NiOOH, MnO_2, HgO, and AgO (6).

The cathode features solid sulfur in contact with a polysulfide solution saturated in sulfur (Fig. 1A). Initiation of reductive discharge of the cell will generate polysulfide species with shorter chain lengths (Fig. 1B)

$$3S_4^{2-} + 2e- \rightarrow 4S_3^{2-} \quad (3)$$

Further reactions proceed with dissolution and continued reduction of available solution and solid-phase sulfur

$$S_3^{2-} + S \rightarrow S_4^{2-} \quad (4)$$

Discharge continues until all available zero-valent sulfur (both solid and dissolved) is reduced in accordance with Eq. 1. The solid sulfur maintains longer chain polysulfide species in solution, which positively shift and maximize the cell voltage (8). This elemental (solid-solution phase) sulfur cathode has the theoretical advantage of higher storage capacity and higher cell voltage.

Direct evidence supporting the proposed mechanism of solid sulfur cathode discharge (Eqs. 2 to 4) is found in the solubility limit [three (zero-valent) sulfurs per dissolved K_2S in saturated polysulfide solutions (8)] and the measured discharge of sulfur cathodes. The solid sulfur cathode exhibits an experimental discharge capacity in excess of 900 A·hour/kg (Fig. 2), an increase of 80% over that of the polysulfide cathode (9). To ensure that the majority of the coulombic capacity resides in the solid sulfur rather than the polysulfide, one uses an aqueous K_2S_2 rather than an aqueous K_2S_4 interface. The experimental cathode (Fig. 2, circles) consists of 50% sulfur and 50% disulfide solution interface by mass. The cathode contained a theoretical capacity of 836 A·hour/kg attributable to solid sulfur and 81 A·hour/kg attributable to the interfacial aqueous disulfide (containing two electrons per molecule of K_2S_2). The experimental discharge capacity of 903 A·hour/kg includes the mass of the polysulfide interface but not the additional mass contributions of the electrical contacts, the cell container, or the electrocatalytic current collector [the latter has a mass of 0.038 g/cm² for a thin film of CoS deposited on a 25-μm brass electrode (9), equivalent to 33 g of electrode per kilogram of solid sulfur cathode]. The addition of 4.9 *m* KOH to the disulfide interface can diminish the cathodic potential (Fig. 2, inset) but also compensates for

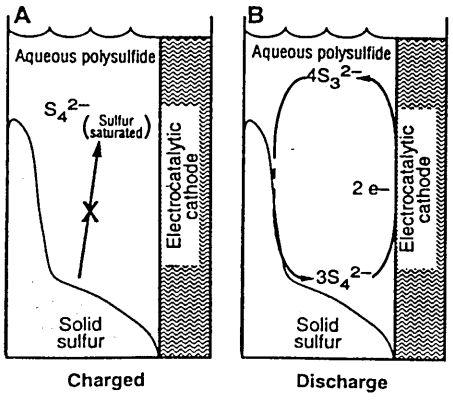

Fig. 1. Schematic representation of the solid sulfur cathode in its (**A**) charged state and (**B**) discharging state.

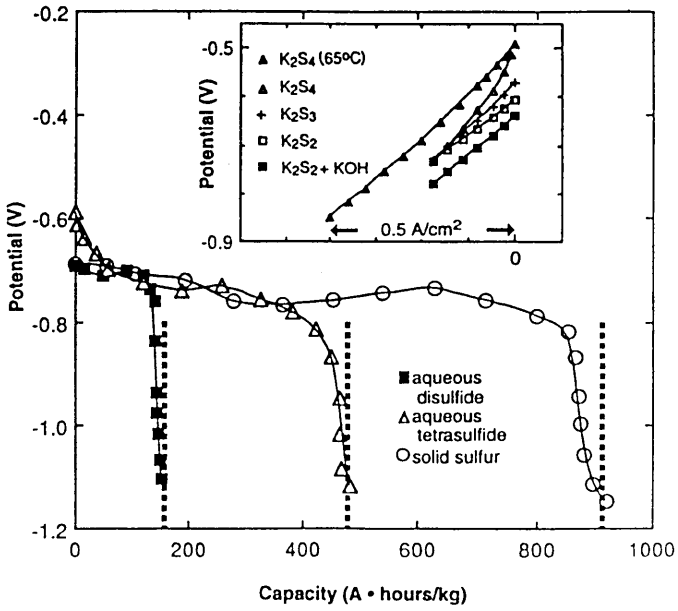

Fig. 2. Comparison of the storage capacity of the solid sulfur or polysulfide cathodes (26). Potentials measured versus SHE. Cathodes galvanostatically discharged at 60 mA and 35°C, each weighing 3.45 g: aqueous disulfide (squares), 2.28 ml of 6.5 *m* K_2S_2 and 4.9 *m* KOH; aqueous tetrasulfide (triangles), 2.25 ml of 7.7 *m* K_2S_4; solid sulfur (circles), 1.72 g sulfur and 1.73 g (1.14 ml) of 6.5 *m* K_2S_2 and 4.9 *m* KOH. The dashed lines refer to the theoretical charge capacities of the respective cathodes. (**Inset**) Discharge polarization of several aqueous concentrated polysulfide electrolytes at a thin-film CoS electrode and at 50°C or as indicated.

the highly alkaline anolytes that were used in the separated anode half-cell during these discharge tests. Each of the polysulfide or sulfur-polysulfide cathodes may be reduced at faradaic efficiencies approaching 100% (Fig. 2, dashed lines); thin films of CoS provide effective electrocatalysts for polysulfide reduction (*11*).

Further evidence for the dominant role of trisulfide and tetrasulfide species in Eqs. 3 and 4 is found in the electrochemistry of tetrasulfide (*12, 13*), in the enhanced rate of sulfur dissolution in solutions containing high rather than low ratios of (dissolved) sulfur to sulfide (*14, 15*), and in the near ultraviolet–visible absorption spectroscopy of aqueous polysulfide solutions. Aqueous solutions containing sulfur and a sulfide salt, M_xS_y, result in extensive speciation and a complex equilibrium of $M^{(2y/x)+}$, H_2S, HS^-, S^{2-}, S_2^{2-}, S_2^-, S_3^{2-}, S_4^{2-}, S_5^{2-}, H_2O, H^+, and OH^-. The associated equilibria have been investigated and described (*16–21*). Spectroscopic evidence shows that upon sulfur dissolution or pH modification, several distinguishable absorption peaks appear, in particular, a disulfide peak at 354 nm that diminishes with the formation and growth of a 302-nm trisulfide peak. Further sulfur addition diminishes the trisulfide peak with the formation of a 372-nm tetrasulfide peak and a 296-nm pentasulfide peak (*20*). The variation of polysulfide species during cathode discharge can therefore be determined (Table 1). During the majority of the discharge, solid sulfur is in contact with the polysulfide interface, the cell becomes saturated in sulfur, and the tetrasulfide species is predominant (Table 1, first column). However, in the latter portions of the cell discharge, the trisulfide species is predominant. Near completion of the discharge, (Table 1, columns 2 to 4), the catholyte is nominally a K_2S_3, K_2S_2, and then a $K_2S_{1.2}$ solution.

Table 1. The distribution of polysulfide species in increasingly discharged cathodic solutions at 35°C. Calculated with the previously described computer iterative model (*20*) and equilibria constants (*18*). The final column is an expression of the alternative electrolyte in Fig. 2.

Species	Concentration (moles per liter)				
K_2S	4.5	4.5	4.5	4.5	4.5
Sulfur	13.5	9.0	4.5	1.0	4.5
KOH	0.0	0.0	0.0	0.0	3.38
$[S_2^{2-}]$	4×10^{-4}	0.07	0.2	0.1	0.7
$[S_3^{2-}]$	0.4	2.7	1.9	0.2	1.8
$[S_4^{2-}]$	3.7	1.2	0.2	0.003	0.06
$[S_5^{2-}]$	0.4	0.005	2×10^{-4}	4×10^{-7}	2×10^{-5}

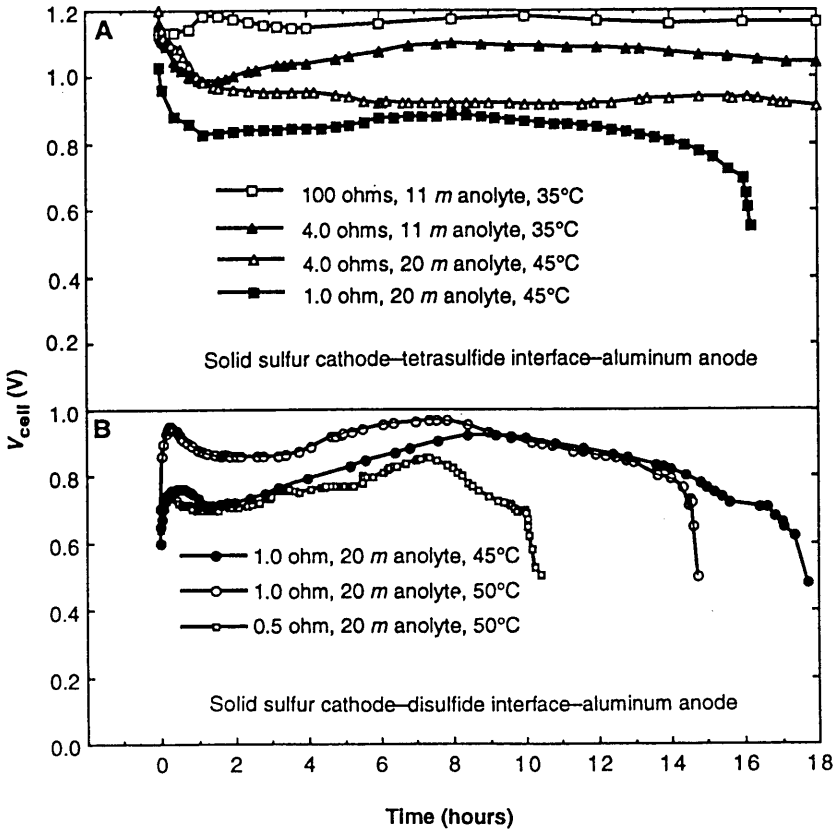

Fig. 3. Solid sulfur–aluminum discharge using a rectangular "D" cell configuration (*24*). The discharges were made through 1% precision resistors at the values indicated in ohms. The temperature was controlled with a thermostatic bath. In (**A**), the cathode contains 8.13 g of sulfur, the tetrasulfide interface consists of 0.006 liter of 7.7 *m* K_2S_4 catholyte without added KOH, and the anolyte is 0.040 liters of either 11 or 20.4 *m* KOH with 0.010 *m* $In(OH)_3$. In (**B**), the cathode utilizes a 0.006-liter interface of 6.5 *m* K_2S_2 catholyte and 4.9 *m* KOH.

Saturated sulfur-polysulfide solutions stored at room temperature for several months are stable (*21*). Furthermore, those solutions specifically measured for degradation at 45°C [with a previously described barium precipitation procedure (*22*)] show no measurable sulfur loss (to within the ±0.3% detection limits) over several days, although longer term testing is required. Giggenbach (*23*) has measured the reversible reaction of polysulfide solutions at elevated temperatures (over 150°C) and has shown that they spontaneously disproportionate to thiosulfate

$$S_5^{2-} + 3OH^- \rightarrow S_2O_3^{2-} + 3HS^- \quad (5)$$

This reaction will be parasitic to the solid sulfur cathode but is slow at moderate temperatures (*21*).

The solid sulfur cathode was incorporated into an aluminum cell analogous to the aluminum-polysulfide battery recently described (*9*). The discharge of aluminum in aqueous medium is accompanied by the formation of several aluminum species combined in the simplified anodic oxidation

$$Al + 3OH^- \rightarrow Al(OH)_3 + 3e^- \quad (6)$$

where $-E^\circ = -2.30$ versus SHE. From Eqs. 2 and 6, discharge of the aluminum–solid sulfur battery is expressed as

$$2Al + 3S + 3KOH + 3H_2O \rightarrow 2Al(OH)_3 + 3KHS \quad (7)$$

where $E_{cell} = 1.8$ V. Faradaic capacity of the Al-S battery (based on potassium salts) is 505 A·hour/kg, and the theoretical specific energy is 1.8 V × 505 A·hour/kg = 910 W·hour/kg, about 40% higher than that of the aluminum-polysulfide battery (*9*) and two to five times larger than that of conventional aqueous batteries. Utilization of lighter cations than K^+ may further improve the Al-S energy capacity.

In support of the proposed mechanism for discharge of the high-capacity solid sulfur cell given in Eqs. 2 through 4, Fig. 3 presents graphs of the discharge, at various

rates, temperatures, and conditions, of a battery with a solid sulfur cathode, a polysulfide interface, and an aluminum anode. Typical open circuit voltages are 1.28 to 1.30 V. Under moderate to high rate conditions [1-ohm load over a "D" cell configuration (*24*)], the discharge time of 15 to 18 hours (Fig. 3) is over twice the 6.5-hour discharge obtainable in conventional alkaline batteries (*6*) and an increase of 30% compared with the previously described aluminum-polysulfide cell (*9*). The measured specific energy capacity of the Al-S battery (1-ohm discharge) is 220 W·hour/kg on the basis of active materials. Highly concentrated anolytes induce cathodic polarization losses (Fig. 3), a phenomenon that one can minimize by increasing cell temperature, increasing the ionic strength, or substituting disulfide for tetrasulfide in the catholyte interface.

The measured specific energy of 220 W·hour/kg of this cell can only provide an approximate comparison with the capacities of aqueous batteries in a more mature state of development. Conventional aqueous batteries typically achieve an experimental specific energy of 10 to 25% of the theoretical. The mechanically rechargeable Zn-air battery is considered to have a high measured specific energy of up to 110 W·hour/kg, and alkaline batteries with low discharge rates (Zn-MnO_2) have a specific energy of up to 95 W·hour/kg (*2*, *5*).

A further increase in Al-S power and specific energy may be accessible with a recently described Al-redox, mechanically rechargeable flow cell configuration with a high power density in which solvent may be recycled while electrolyte flows into and through the cell (*25*). The solid sulfur cathodes can support the requisite current densities for this configuration (Fig. 2, inset). This configuration, as modeled with an Al-ferricyanide battery, took advantage of the high currents sustainable for the reduction of ferricyanide (up to 0.5 A/cm^2 on planar electrocatalysts, and in excess of 2 A/cm^2 on porous electrocatalysts) and permitted better utilization of anode materials (*25*). Replacement of ferricyanide with a solid sulfur cathode may considerably enhance the energy capacity of this configuration.

REFERENCES AND NOTES

1. *Workshop on Advanced Battery Technology Research and Development*, Division of Chemical Sciences, Office of Basic Energy Science (U.S. Department of Energy, Washington, DC, 1992).
2. E. J. Cairns and F. R. McLarnon, in *Proceedings of the Symposium on Batteries and Fuel Cells for Stationary and Electric Vehicle Applications*, A. R. Landgrebe and A. Takehara, Eds. (Electrochemical Society, Pennington, NJ, 1993), vols. 93–98.
3. C. Scordilis-Kelley, J. Fuller, R. R. Carlin, J. S. Wilkes, *J. Electrochem. Soc.* 139, 694 (1992).
4. N. Kuriyama, T. Sakai, H. Miyamua, I. Uehara, H. Ishikaras, *ibid.*, p. L72.
5. K. Y. Chu and R. F. Savinell, *ibid.* 138, 1976 (1991).
6. D. Linden, *Handbook of Batteries* (McGraw-Hill, New York, 1984).
7. S. Licht, G. Hodes, R. Tenne, J. Manassen, *Nature* 326, 863 (1987).
8. S. Licht, *J. Electrochem. Soc.* 134, 2137 (1987).
9. _____ and D. Peramunage, *ibid.* 140, L4 (1993).
10. From Eq. 2, 2 faradays of electrons are present for each mole of S and H_2O (0.032 + 0.018 kg). We can get the appropriate charge units per kilogram using standard conversions: 1 faraday = 96,500 C, 3600 C = 1 A·hour.
11. G. Hodes, J. Manassen, D. Cahen, *J. Electrochem. Soc.* 127, 544 (1980).
12. P. Lessner, J. Winnick, F. R. McLarnon, E. J. Cairns, *ibid.* 133, 2517 (1986).
13. S. Licht, *Nature* 330, 148 (1987).
14. D. Lando, J. Manassen, G. Hodes, D. Cahen, *J. Am. Chem. Soc.* 101, 3969 (1979).
15. N. Hartler, J. Libert, A. Teder, *Ind. Eng. Chem. Process Des. Dev.* 6, 398 (1967).
16. _____, *Sven. Papperstidn.* 72, 245 (1969); *Acta Chem. Scand.* 25, 1722 (1971).
17. W. Giggenbach, *Inorg. Chem.* 11, 1201 (1972).
18. _____, *ibid.* 13, 1724 (1974).
19. S. Licht *et al.*, *J. Electroanal. Chem.* 318, 111 (1991); S. Licht *et al.*, *Anal. Chem.* 62, 1356 (1990); S. Licht *et al.*, *J. Electrochem. Soc.* 135, 2971 (1988); S. Licht *et al.*, *ibid.* 134, 918 (1987); S. Licht *et al.*, *ibid.* 133, 277 (1986); S. Licht *et al.*, *ibid.* 132, 1077 (1985).
20. S. Licht, G. Hodes, J. Manassen, *Inorg. Chem.* 25, 2486 (1986).
21. S. Licht, J. Manassen, G. Hodes, *J. Electrochem. Soc.* 133, 272 (1986).
22. S. Licht, *J. Phys. Chem.* 90, 1096 (1986).
23. W. Giggenbach, *Inorg. Chem.* 13, 1730 (1974).
24. The "D" cell configuration of 0.05 liter volume is described in (*9*) and contains a 60-cm^2 DH50V ALCAN aluminum anode in anolyte separated by a 60-cm^2 Raipore HD2291 membrane from solid sulfur in a catholyte polysulfide interface containing a 60-cm^2 thin-film CoS electrocatalytic cathode.
25. S. Licht and C. Marsh, *J. Electrochem. Soc.* 139, L109 (1992).
26. A conventional three-electrode cell configuration and a Pine Instrument (Grove City, PA) RDE4 potentiostat-galvanostat were used to supply a constant current in the galvanostatic reduction of the cathodes. The cell contained cathode and counter (anode) compartments separated by a 3-cm^2 R1010 Raipore (Long Island, NY) cation-selective membrane. The cathode compartment consisted of solid (powdered) sulfur separated by a polypropylene mesh or polysulfide solution, or both. The 3-cm^2 CoS electrode (*9*) and a double-junction AgCl reference electrode were immersed in the polysulfide solution. The counter electrode compartment contained a DH50V ALCAN (Warren, NJ) aluminum electrode immersed in 13 *m* KOH, 0.010 *m* $In(OH)_3$, and 0.003 *m* $Hg(NO_3)_2$.

27. Supported in part by the National Science Foundation and the Clark University Carl Julius and Anna (Kranz) Carlson Chair in Chemistry.

16 April 1993; accepted 24 June 1993